DEPARTAMENTO DE FÍSICA TEÓRICA Y DEL COSMOS

Universidad de Granada

Star Formation in Galaxies of Nearby Clusters: a Deep Hα Imaging Survey

Memoria que presenta
Don Daniel Reverte Payá
para optar al grado de
Doctor en Astrofísica.

INSTITUTO DE ASTROFÍSICA DE ANDALUCÍA
Consejo Superior de Investigaciones Científicas
2008

Editor: Editorial de la Universidad de Granada
Autor: Daniel Reverte Payá
D.L.: Gr. 1264-2008
ISBN: 9788469143643

A mi mujer, Carmen

Agradecimientos

Doy gracias a Dios en quien creo, y a cuyo Hijo único confieso como Señor. Durante toda mi vida se ha mostrado como un Padre bueno, con una pedagogía excelente, llena de misericordia y de amor que se me ha dado a conocer en su iglesia.

Creo sinceramente que Dios Padre omnipotente es creador del cielo y de la tierra. Y todo el conocimiento que ha puesto a mi alcance dentro de mi historia, con mis limitaciones, no me lleva sino a darle gloria y gracias infinitas por el don de la vida.

Deseo expresar mi agradecimiento a todos aquellos que han compartido conmigo una parte de este camino de madurez recorrido a lo largo de los últimos años. Para ello nombraré explícitamente a mis compañeros de despacho que lo han sido: José Antonio, Daniel Espada, Miguel y Valentina, Maia, José Luis, Vicente, Daniel Cabrera y David. A mis tutores y profesores: D. Antxón Alberdi, D. Antonio Claret dos Santos, D. Emilio Alfaro, D. Enrique Pérez, D. Mariano Moles y D. Eduardo Battaner, a quien además agradezco su gran cercanía y eterna disponibilidad.

Si, hoy por hoy, deseo seguir en el ámbito de la investigación es porque he conocido a dos personas que me hacen anhelar este ambiente de trabajo, y porque me he sentido apreciado y querido tanto en las correciones como en las felicitaciones. Por ello, quiero manifestar mi más profundo agradecimiento a mis directores de tesis, el profesor Don José Manuel Vilchez Medina y el doctor Don Jorge Iglesias Páramo, por quienes he conocido la calidad científica, y, sobre todo, la calidad personal.

Gracias, Pepe, por la excelencia en lo científico y más aún si cabe en lo personal. Gracias por el trato, por las consideraciones hacia mí dignas de un hijo. Por tus consejos y por tu tiempo. Gracias a tu esposa y tus hijos a quienes te he robado en tantas ocasiones.

Gracias, Jorge, por todo tu esfuerzo impagado para conmigo. Gracias por estar tan cerca y compartir tus alegrías. Por enseñarme a relativizar la importancia de las cosas.

Gracias a los dos por vuestra paciencia conmigo. Gracias por ser, además de magníficos directores, mis amigos.

Doy gracias por la familia en que he nacido y que me ha criado. A mi padre cuyas palabras, sacrificio y trabajo por todos nosotros, me han educado, enseñado y alimentado en la fe hasta la edad adulta. A mi madre, la alegría de la huerta, cuyo empuje, optimismo y fe inquebrantable me ha animado tantas veces. A mi hermano Pablo por su cariño y escucha. A mis hermanos Mariano,

Beatriz, Alejandro, Ana Dolores, Rocí y Fuensanta por vuestras oraciones.

También recuerdo aquí de mi familia a mi padrino, que en gloria esté y que bien me ha protegido como ángel de la guarda, y, por supuesto, a mi madrina que me es tan querida y que tantas velas ha consumido junto con mis primas Antonia, Juana y Merche y mi tía Amalia "haciendo palanca".

A mis hijos Inmaculada, Carmen María, Lucía y Daniel, y a los que vendrán - ya faltan sólo 2 meses, Zenaida -, gracias por existir; por darme ese respiro de frescura, a veces como un oasis en medio del desierto.

Pero, por encima de todos, quiero agradecer a mi mujer, Carmen. Ella ha hecho posible la consecución de este trabajo entregando su vida por mí, en todos los aspectos, en un anonadamiento digno de Cristo. Me ha esperado y desesperado. Me ha sostenido y apoyado. Me ha querido, corregido, escuchado, soportado y perdonado veces incontables en estos pocos años. Con mi amor para ti. Te quiero.

Summary

Recent investigations have revealed that the Universe as a whole has been more actively forming stars in the past than in recent epochs. The activity of star formation in galaxies located in groups, rich clusters and in the general field is enhanced as redshift increased; the evolution of star formation seems to hold for all the environments, from the low galaxy density up to clusters of galaxies.

However, the quantification of this evolution has proven to be hard, especially in the case of clusters, for which the properies of cluster galaxies show substantial variation from cluster to cluster for a given redshift. Therefore, a systematic work intended to investigate the role played by the cluster environment on the activity of star formation, including all the range of galaxy luminosity and morphology, is much needed. Also, such a study is useful in order to estimate the degreee of cosmic evolution of star formation on top of the cluster to cluster variations, as sampled by the component of statistical variance observed within a fixed interval of redshift.

The determination of the contribution of the cosmic evolution to the observed change in the star formation activity of galaxies with the redshift can benefit from the study of the star formation of a sample of galaxies in nearby clusters. In this Thesis, a sample of nearby northern clusters of galaxies located within the same interval of redshift ($0.02 \leq z \leq 0.03$) has been constructed in order to carry out a deep search for star formation activity. The flux in the line of Hα has been widely used as a powerful indicator of the masssive star content in actively star forming galaxies. In this sense, the evaluation of the present star formation rate will be determined from the observations carried out in this Thesis assuming the scenario of a burst of star formation, in the line of previous work in the literature. In this work, a deep search for star forming galaxies has been performed in the light of the Hα line, reaching values of Hα flux of 10^{-16} ergs s^{-1} cm^{-2} for the completeness in flux detection (5σ) and typical values of the minimum Hα equivalent width measured of $\sim$ 3 Å. The survey has been designed to gather deep Hα imaging, so as to provide new bidimensional information of the cluster star-forming galaxies, in addition to the high photometric accuracy and sensibility.

The sample of clusters studied comprises five Abell clusters, # 400, 539, 634, 779 and 2666, observed in this Thesis, plus other two, Abell 1656 (Coma) and Abell 1367, already observed by our group. The observational results obtained for this sample of clusters have been used in the analysis and the discussion of the present work.

The observations were carried out with the 2.5m INT telescope of the ING

at the Observatorio del Roque de los Muchachos (La Palma) using the Wide Field Camera (WFC) with a sytem of a narrow band filter tuned to the wavelength of Hα at the redshift of the clusters, plus broad and/or narrow band filters to measure the level of the continuum flux adjacent to the Hα line. Typically, each cluster was mapped with the WFC camera producing a mosaic with radial limits close to the Abell radius. Over four square degrees of sky have been mapped in the Hα line and in continuum emission. Subsequent data reduction, apart of the standard steps, has included the realization of precise astrometric solutions improving previous findings, plus a refined spectro-photometric calibration based on a set of observed spectrophotometric standard stars and complemented by SDSS calibration references.

Hα flux measurements have been obtained making use of the Sextractor package and of *ad hoc* written software to handle with the different morphologies of the Hα emission observed in an appropriate manner. A battery of computational tests were carried out in order to examine the detection procedure, limiting magnitude and flux, as well as the completeness of the study. An exhaustive detection process has produced a census of the population of Hα emitting source candidates for each cluster. From this census, the new catalogue of star-forming galaxies for the sample of nearby clusters has been completed. The cataloge comprises 4782 galaxies with line fluxes between $5{\cdot}10^{-17}$ and 10^{-12} ergs s^{-1} cm^{-2} corresponding to star formation rates between 0.001 and 22 M$\odot$ yr^{-1} for the assumed redshifts. The statistical distributions of Hα source fluxes and equivalent widths for the sample of clusters have been compared with the corresponding distribution for field galaxies, implying that the distributions show a clear, statistically significant difference between field and cluster galaxies, with field galaxies always presenting the larger Hα fluxes and equivalent widths. The spatial distribution of star-forming galaxies within each cluster has been derived; the results have revealed the presence of a widespread star-forming galaxy population, especially noticeable for the lower luminosity galaxies –i.e. the dwarfs–, which, in most cases, are found extending beyond the loci traced by the higher luminosity component –i.e. the giants. This findings have demonstrated that the spatial distribution of star-forming galaxies in nearby clusters does not seem to follow any especial isotropical pattern; rather, though the bulk of star-forming galaxies appear to be associated to the overall distribution of cluster galaxies, as indicated by 2MASS isodensity contours, the dwarf star-forming population seems to avoid the maxima traced by brighter galaxies.

The distribution of the fraction of star-forming galaxies for each cluster has been found to be well correlated with global parameters of the clusters, such as the velocity dispersion, σ_v, and the luminosity in X-rays, for example. The

incidence of these factors on the role played by the cluster environment on the evolution of the activity of star formation observed for these galaxies has been analysed. Specifically, the presence of a given degree of stripping of the gas in the outer parts of the spirals in our sample has been analysed by the comparison of the normalized Hα radial profiles of these galaxies with the corresponding profiles of Virgo spirals from the sample of R. Koopmann's Thesis. All in all, the evolution of the fraction of star-forming galaxies per cluster has been analysed for a sample constructed including the results obtained for the seven nearby clusters of this study, plus from a set of clusters at two different redshifts taken from the literature. This analysis shows that the fraction of star-forming galaxies per cluster does not seem to follow a one-to-one function with lookback time, for a large range of values of cluster σ_v. In the light of this result we suggest a possible conexion between the evolutionary stage of a cluster and the presence of a strongly structured distribution of star-forming galaxies, as revealed in this work for a significant fraction of our nearby clusters.

Resumen

Un buen número de estudios han revelado que el Universo como un todo fue más activo formando estrellas en el pasado que en épocas más recientes. La actividad de formación estelar en galaxias ubicadas en grupos, cúmulos ricos y en el campo en general se ve potenciada para redshift mayores y este resultado parece repetirse para cualquier tipo de entorno; en particular para cúmulos de galaxias. Sin embargo ningún trabajo sistemático ha sido analizado aún que investigue el rôle jugado por el cúmulo como entorno sobre la actividad de formación de estrellas, incluyendo galaxias de todo el rango de luminosidades y morphologías; ni que, notablemente, establezca el intervalo preciso de variación cósmica de la formación estelar y que sirva para ser comparado con los cambios estadísticos observados en un intervalo dado de desplazamientos al rojo.

La determinación precisa de la contribución de la evolución cosmológica al cambio observado en la actividad de formación estelar puede beneficiarse del estudio de la formación estelar en galaxias de una muestra de cúmulos cercanos. En esta Tesis, una muestra de cúmulos del norte cercanos situados en el mismo intervalo de desplazamientos al rojo se ha construido para llevar a cabo una búsqueda profunda de formación estelar en cúmulos. El flujo en la línea de Hα ha sido ampliamente usado como buen indicador del contenido en estrellas masivas de una galaxia con formación estelar activa. En este sentido, la evaluación de la Razón de Formación Estelar (RFE) presente puede ser determinada de las observaciones asumiendo que el escenario que enmarca dicha formación estelar se limita a un único brote de formación de estrellas, en la línea de los trabajos similares y relacionados de la bibliografía. En este proyecto de Tesis se ha desarrollado la búsqueda profunda de galaxias con formación de estrellas a la luz de la línea de Hα, alcanzando valores del flujo del orden típicamente de 10^{-16} ergs s^{-1} cm^{-2} para la completitud en detección y mínimos anchos equivalentes del orden de 3-4 Å.

La muestra comprende 5 cúmulos de Abell, # 400, 539, 634, 779 y 2666, que han sido observados durante la Tesis, más otros 2 a saber, Abell 1656 (Coma) y Abell 1367 que fueron ya observados por nuestro grupo y que se han rescatado en el análisis y en la discusión del presente trabajo.

Las observaciones fueron realizadas con el telescopio Isaac Newton de 2.5m del ING en el Observatorio del Roque de los Muchachos (La Palma), usando la cámara de campo ancho (Wide Field Camera - WFC) con un sistema de filtros incluyendo un filtro estrecho correspondiente a la línea de Hα para el desplazamiento al rojo de los cúmulos considerados, e incluyendo un filtro ancho y/o estrecho adecuados para medir la altura del "continuo espectral" adyacente a la línea de Hα. Tipicamente se ha mapeado cada cúmulo con la WFC

produciendo un mosaico que cubra aproximadamente el radio virial. Más de 4 grados cuadrados de cielo han sido cubiertos en Hα y en continuo. La reducción de datos, aparte de los pasos estándares, ha incluido la realización de una astrometría precisa, por debajo del segundo de arco, más una refinada calibración espectro-fotométrica basad en una serie de estrellas de calibración con espectro conocido complementadas con referencias de la búsqueda de Sloan.

La medida a los flujos de Hα ha sido obtenida haciendo uso tanto de SExtractor como de un "software" basado en IDL y escrito *a*d hoc para tratar en la manera apropiada las diferentes morfologías de la emisión Hα. Una batería de pruebas se llevaron a cabo para examinar el procedimiento de detección, la magnitud límite y el flujo así como la "completitud" del estudio. Un proceso de detección exhaustiva ha dado como producto un censo global de la población de fuentes brillantes en Hα para cada cúmulo, y el nuevo catálogo de galaxias con FE para la muestra de cúmulos se ha completado. Dicho catlogo contiene 4782 fuentes con flujos comprendidos entre $5{\cdot}10^{-17}$ and 10^{-12} ergs s^{-1} cm^{-2} correspondientes a tasas de formación estelar (RFE) de entre 0.001 and 22 M$\odot$ yr^{-1}. La distribución estadísitica de los flujos de las fuentes Hα y de sus anchos equivalentes en la muestra de cúmulos se ha comparado con la correspondiente distribucion para galaxias del campo, llegándose a que existe una significativa diferencia estadistica entre las distribuciones de la muestra y el campo, presentando siempre las galaxias del campo flujos y razones de formación estelar típicas mayores. La distribución espacial de las galaxias con FE para cada cúmulo se han calculado; el resultado ha revelado la presencia de un población prevalente de galaxias con FE, especialmente de galaxias con baja luminosidad, enanas, para las que se encuentra que se extienden a lugares próximos o disjuntos a los preferidos por las de alta luminosidad.

Este hallazgo ha demostrado que la distribución espacial de las galaxias con FE en cúmulos no parece seguir un patrón de distribución isotrópica; más aún, el grueso de las enanas con FE no aparece asociado a una distribución global del cúmulo de galaxias como indica los isocontornos del 2MASS.

Se ha encontrado que la fracción de galaxias con FE está bien correlada para cada cúmulo con los parámetros globales del mismo, como la dispersión de velocidades (σ_v) o la luminosidad bolométrica de rayos X. La incidencia de estos factores en el papel jugado por el entorno sobre la evolución de la formación estelar observada para estas galaxias ha sido analizada. Particularmente, la presencia de un grado de "arranque de gas" de las partes externas de las espirales en nuestra muestra se ha enfatizado comparando los perfiles radiales de Hα normalizados a r_{24} con los perfiles así producidos por Rebecca Koopmann en su trabajo tesis. Con todo, el análisis de la evolución de la fracción de galaxias con FE de los cúmulos de esta muestra (7 cúmulos), dentro de una muestra

que considera cúmulos a 2 desplazamientos al rojo procedentes de la bibliografía enseñan que este observable (la fracción de galaxias con formación estelar) no responde a una función uno a uno con el tiempo cosmológico, para cualquier valor de la σ_v del cúmulo, un resultado que podría sugerir una relación con la distribución fuertemente estructurada de las galaxias con formación para los cúmulos observados en este trabajo, y sus estados evolutivos.

CONTENTS

CHAPTER

1

INTRODUCTION

1.1 Evolution of galaxies in dense environments: star formation in clusters.

The universe as a whole was more actively forming stars in the past than today (Lilly et al. 1996; Madau et al. 1998; Hopkins 2004). Studies of galaxies in clusters, groups, and the general field indicate an increased star formation activity at higher redshifts, in all environments. However, a complete mapping of the average star formation activity with redshift as a function of environment has still not been achieved.

A large number of studies, during the last 30 years, have shown that distant clusters generally contain many star-forming galaxies. In fact, the first evidence for galaxy evolution in clusters, and for galaxy evolution in general, has been the detection of evolution in the star formation activity of cluster galaxies, as revealed by photometry and spectroscopy.

Historically, the higher incidence of star-forming galaxies in distant clusters compared to nearby clusters was first discovered by photometric studies of the proportion of blue galaxies, the so-called Butcher-Oemler effect (Butcher & Oemler 1978, 1984), subsequently confirmed by several author (Smail et al. 1998; Margoniner & de Carvalho 2000; Margoniner et al. 2001; Kodama & Bower 2001).

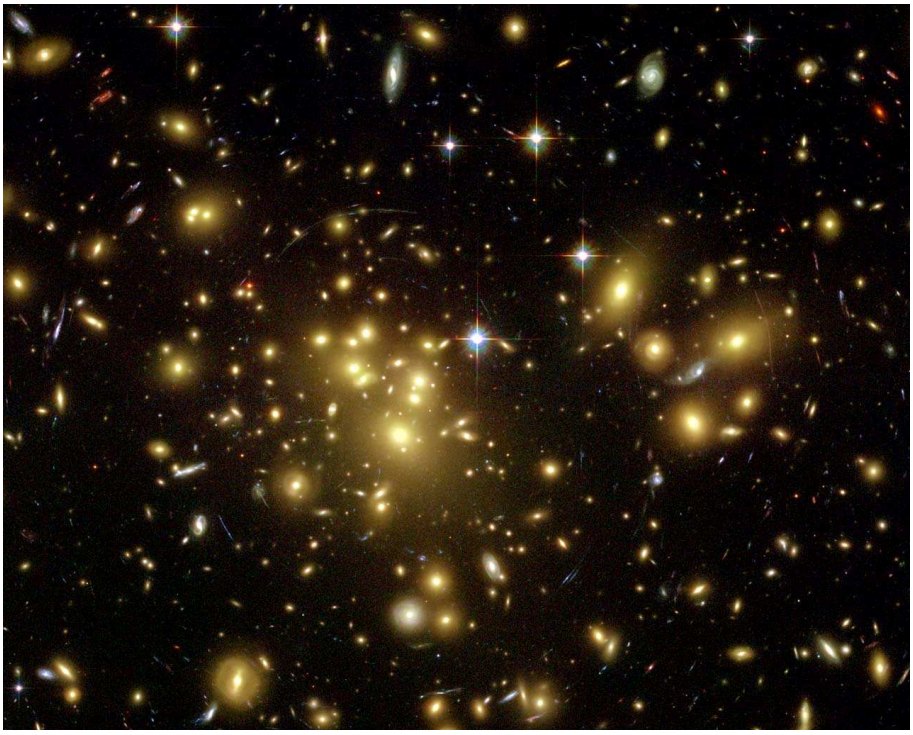

Figure 1.1:: Illustrative picture of a Cluster of galaxies. (Abell 1689; z = 0.18)

In agreement with the photometric results, spectroscopic studies of distant clusters have found significant populations of emission-line galaxies (Dressler & Gunn 1982, 1983, 1992; Couch & Sharples 1987; Dressler et al. 1999; Balogh et al. 1997, 1998; Poggianti et al. 1999; Moran et al. 2005). In contrast, is widely accepted that nearby rich clusters generally have relatively few emission-line galaxies. Increased star formation activity in distant clusters is also indicated by the emission properties of composite cluster-integrated spectra (Dressler et al. 2004). In parallel to the cluster studies, the fraction of star-forming galaxies has been found to be higher at z = 0.3-0.5 than at z = 0 also in poorer aggregates of galaxies like groups (Wilman et al. 2005).

While these observations have qualitatively shown that star-forming galaxies were more common in the past than today, quantifying this evolution has proved to be very hard. At any given redshift, the properties of cluster galaxies display a large cluster-to-cluster variance. Disentangling cosmic evolution from cluster-to-cluster variations in a quantitative way has not been possible to date due to the relatively small samples of clusters studied in detail at different

redshifts. This difficulty in measuring how the fraction of star-forming galaxies evolves with redshift as a function of the cluster properties has affected all types of studies, photometric and spectroscopic (multislit) surveys cluster-wide studies (Couch et al. 2001; Finn et al. 2004, 2005; Kodama et al. 2004; Umeda et al. 2004; Homeier et al. 2005). This might be the reason why a quantitative detection of a clear evolution with redshift in the fraction of star-forming galaxies has been elusive so far (Nakata et al. 2005).

On the field side, an easier path to describe the past to present day variation of the SFR for galaxies outside a stated denser environment, was found early by Lilly et al. (1996); Madau et al. (1998). Fig. 1.2 is known as the Lilly-Madau plot. In it, the peak of the SFR density at z∼1 is marked by several surveys (see Hopkins, Irwin, & Connolly 2001).

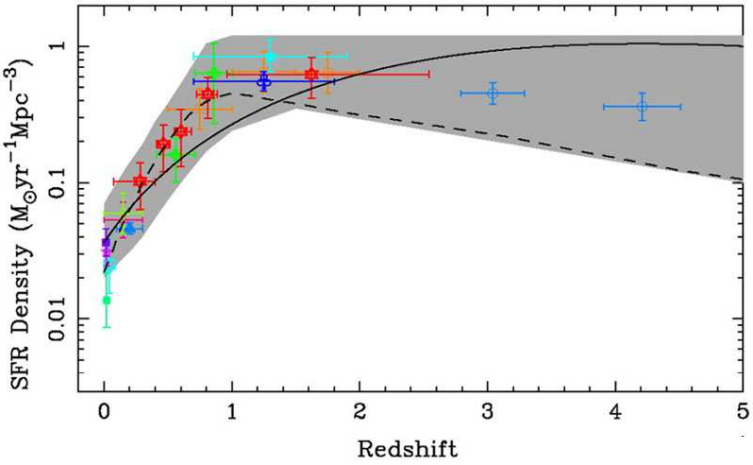

Figure 1.2:: SFR density versus the redshift. The different coloured points come from several surveys (see Hopkins et al. 2001 for details.)

Understanding the role of environmental conditions in determing how galaxies are and evolve is especially important in the context of a hierarchical cosmological scenario. As structures grow, galaxies assemble in more massive structures and experience different environmental conditions during their history. Two different environment-dominated paths for galaxy evolution, at least in spent-time for particular processes (e.g. star formation), can be remarked here, an evolution into the field and an evolution into the cluster, conditioning this scenario, since a cluster galaxy today may have been a group or field galaxy during the earlier phases of its evolution. The physical mechanisms that are

usually considered when trying to assess the influence of the environment on galaxy evolution can be grouped in four main families (see Boselli & Gavazzi 2006 for a review):

- Mergers and strong galaxy-galaxy interactions (Toomre&Toomre 1972, Hernquist& Barnes 1991, see Mihos 2004 for a review). They are most efficient when the relative velocities between the galaxies are low, thus are expected to be especially efficient in galaxy groups, relatively efficient in the cluster infall region and much less efficient within the inner part of clusters. About the gas we should declare a wide variability of effects on gas by triggering (ring galaxies, ...) or inhibiting the star formation depending on the timescale of the interaction (see picture 1.3)

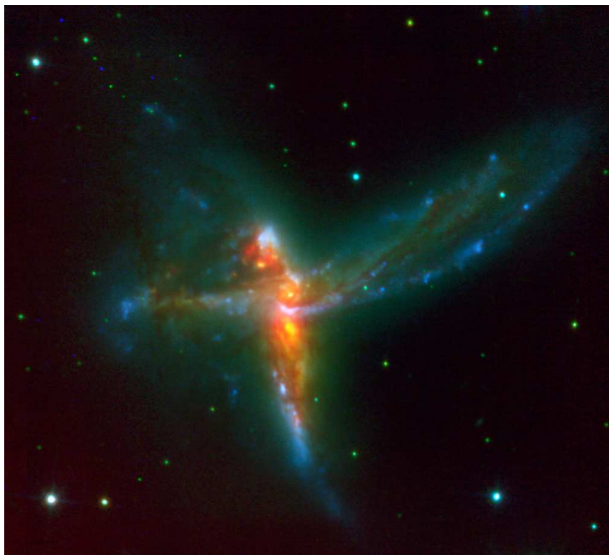

Figure 1.3:: Image (from the European Southern Observatory) shows a three-galaxy merger known as the Cosmic Bird or the Tinker Bell Triplet. Three band (BIK) pseudo-colour composition where K (yellow) is tracing the dust and indirectly the star formation. This interaction has already trigger that burst of SF and it could lead to morphological transformation into a elliptical galaxy. Photo credits: Väisänen et al. 2008

- Tidal forces due to the cumulative effect of many weaker encounters (also known as harassment) (Richstone 1976, Moore et al. 1998). This process is the fruit of the combined action of high relative motion interactions between galaxies and the interaction with the cluster potential well. The

result of a series of multiple interactions is the increase of the velocity dispersion of the stellar component and thus, the consequent leak of not neglectable fraction of stars can lead to a morphological transformation. They are expected to be especially important in clusters, and particularly on smaller/lower mass galaxies.

- Gas stripping - Interactions between the galaxy and the inter-galactic medium (IGM) (Gunn & Gott 1972, Quilis et al. 2000) which consists of the removal of cold gas from external parts of spiral galaxies. The component usually more affected is the neutral gas (HI), since the gas in the molecular phase use to occupy inward regions of discs where stripping does not reach . The interstellar medium of a galaxy can be stripped via various mechanisms, including viscous stripping, thermal evaporation and the most famous member of this family ram pressure stripping. Ram pressure can be efficient when the IGM gas density is high and the relative velocity between the galaxy and the IGM is high. These conditions are expected to be found especially in the very central regions of cluster cores (see an example on fig. 1.4 of the inner part of Abell 1367 where stripped gas tail are conspicuous indeed (Gavazzi et al. 2001a)).

- Strangulation (also known as starvation, or suffocation) (Larson, Tinsley & Caldwell 1980, Bower & Balogh 2004). Assuming galaxies possess an envelope of hot gas that can cool and feed the disk with fuel for star formation, the removal of such reservoir of gas is destined to inhibit further activity once the disk gas is exhausted. In semi-analytic models, for example, the gas halo is assumed to be removed when a galaxy enters as satellite in a more massive dark matter halo.

  Note that while stripping gas from the disk induces a truncation of the star formation activity on a short timescale ($\sim 10^7$ yrs), strangulation is expected to affect a galaxy star formation history on a long timescale (1 Gyr) provoking a slowly declining activity which consumes the disk gas after the supply of cooling gas has been removed. In turn, it requires less ICM densities to be effective.

Some of these processes have empirical motivation (e.g. ram pressure stripping and mergers can be observed at work), while others have a more theoretical ground (e.g. strangulation and harassment).

It is obvious that if the gaseous component is affected in a galaxy embedded in denser environments, then the structure, the rate and the life time of its star

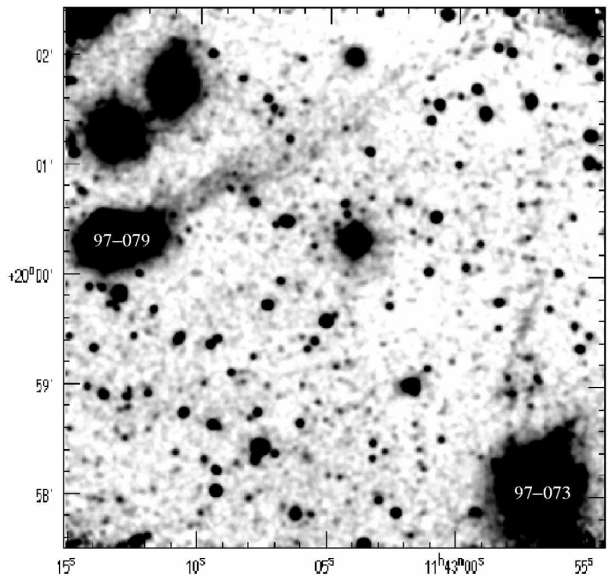

Figure 1.4:: Hα + [NII] image of the region of Abell 1367 containing the two CGCG galaxies 97-073 and 97-079 showing at a high contrast to enhance the extended tails of gas forming stars. Gavazzi et al. 2001a

formation will be modified. The way in which that variation/modification does take place have several (to much to cite or remark one over the rest here) attempts to be answered, but always attacking those questions separately. The knowledge of the history of star formation together with the 2D structure info of the star forming region based on the Hα emission for a galaxy in a determined environment drives to find more rapidly the path followed in its recent past and how it have evolved. Up to date it is still easy to study deeply the nearby universe with the current facilities (telescopes, ccd's,...) that allow us to explore galaxies throughout their physical limits and to reach fainter limits in a survey of magnitude coverage.

Another argument in favor of local clusters is that they are ideal laboratories for studying interaction mechanisms at high resolution. Prototypes of all the relevant mechanisms can be found in nearby clusters. Abell 1367, for example, contains perhaps the best known example of currently ongoing ram pressure stripping (CGCG 97-073 studied by Gavazzi et al. 2001a, presented here on fig. 1.4), a rare example of a merging system in a cluster (UGC 6697 seen in the paper of Gavazzi et al. 2001b), and even a local prototype of an infalling group where preprocessing occurs at the present cosmological epoch. Infall was

much more effective but unfortunately was hard to observe in the past ($z \sim 0.5$), when it probably contributed much more to the shaping of the S0 galaxies (preprocessing).

So far, we have insisted on the importance of observing nearby clusters. Among them, we selected for the present work a set of clusters Abell 400, Abell 539, Abell 634, Abell 779 and Abell 2666, together with and extending the previous studies on Abell 1367, and Coma, which have a wealthy and broad range of global properties. The variety of their conditions (e.g., X-ray luminosity, richness, velocity dispersion) makes them suitable "laboratories" for comparing clusters in different evolutionary stages: near formation (Abell 2666), still accreting (Abell 1367), and near virialization (Coma).

The natural extension of such a work is to complete with other broad band colours or even 2D spectroscopic studies that would constrain strongly the parallel effects on the SF given by the metallicity, the underlying population, or the contamination by active nuclei. Such a project would take up the equivalent time of a couple of thesis (!), but the final prize is to establish the firmest point to compare with more distant galaxies. The alternative more accepted is to consider the already existing huge amount of data with slit and fiber spectroscopy.

Unfortunately, comparisons of the spectroscopic properties of nearby galaxies with those at higher redshifts can be severely hindered by aperture effects. The combination of a fixed-size aperture and radial gradients, plus variations in metallicity, star formation, and extinction can lead to a bias in these properties that may mimic or hide evolution as a function of redshift. Typical fiber diameters are 3 arcsec; for the SDSS and 2 arcsec; for the 2dFGRS. Spectra of nearby galaxies taken through such small apertures cover only a small portion of the nearest galaxies and capture a small fraction of their integrated light.

Early studies of the effect of aperture size on apparent galaxy properties were carried out decades ago. De Vaucouleurs (1961) and Hodge (1963) used various aperture sizes to show that early-type galaxies are redder in their galaxy centers. Tinsley (1971) pointed out that the color-aperture relation seen in early-type spiral galaxies leads to the observation of bluer colors at higher z in an aperture with a small, fixed angular size.

Recent investigations into aperture effects have focused on spectral classification and SFRs. Zaritsky et al. (1995) showed that galaxies in the Las Campanas Redshift Survey at redshifts $z < 0.05$ could be misclassified, because the 3 arcsecs fibers capture only the central fraction of the galaxies' light.

The Hα emission line is commonly used to estimate SFRs in galaxies with redshifts $z < 0.3$. Prez-Gonzlez et al. (2003) analyzed the Hα emission in a sample of local star-forming galaxies selected from the Universidad Complutense

de Madrid Survey. Prez-Gonzlez et al. concluded that long-slit or fiber spectra of nearby galaxies can miss substantial fractions of the emission-line flux (typically 50%∼ 70%). They suggest supplementing emission-line fluxes with direct emission-line imaging to overcome this bias. However, for large samples covering a range of redshifts, H imaging of every galaxy is not currently viable.

Flux calibration of spectra in fiber-based surveys is difficult. Thus, Hα emission-line equivalent widths (EWs) are often used along with an r-band magnitude to estimate SFRs. Gmez et al. (2003) pointed out that aperture bias may result in a systematic increase in the observed Hα EW for higher redshift galaxies relative to lower redshift galaxies in the SDSS. Gmez et al. analyzed SDSS galaxies within three equal-volume redshift bins between 0.05 ¡ z ¡ 0.095. They found no evidence of an increase in the median and 75th percentile of the H EW distribution among these three bins.

Hopkins et al. (2003) investigated aperture effects on Hα-based SFRs in the SDSS by comparing the Hα SFRs with those derived from radio observations. They found that the H SFRs are overestimated for galaxies requiring the largest aperture corrections. The galaxies requiring the largest aperture corrections are either the closest or the most massive galaxies. Because of the large scatter between the two SFRs, Hopkins et al. (2003) were unable to quantify this aperture effect.

1.2 The Hα emission as SF tracer.

The Hα emission trustworthy traces the ongoing (less than 10 Myr) star formation activity in galaxies. But for inferring indirect figures from measurements of this emission line, few assumptions are needed (Hunter & Elmegreen 2004). First: when stars form from a gas cloud, this last one should be as big as needed not to lose radiation. Second: the number of stars formed follows a power law on the star masses, the Initial Mass Function (IMF).

$$\xi(m) \quad \propto \quad m^{\gamma} \tag{1.1}$$

where the γ is the power-law index related to the "slope of the stellar initial mass function" Γ as $\Gamma = \gamma + 1$. Traditionally, the most simple IMF considered is a Salpeter (Salpeter 1955), see fig. 1.5, with $\Gamma = -1.35$ and the assumption of an upper mass limits of 100 $M_{\odot}$ and of a lower mass limit of 0.1 $M_{\odot}$.

Third: we need to assume an efficiency factor η for the absorption of ionizing photons by the nebulae. Now, knowing the quantity of photons absorbed and re-emitted as the first of Balmer lines series based on the expression of the recombination equilibrium by means of that number of ionizing photons (Osterbrock 1974) we can write a direct relation between the Hα-luminosity and the

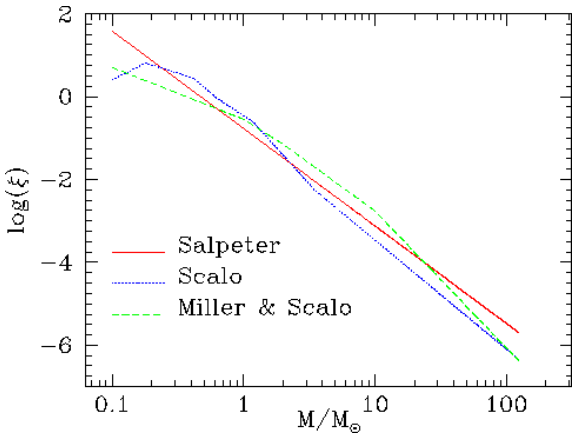

Figure 1.5:: Form of the most common Initial Mass Functions. Number/fraction of stars on Y-axis, versus de mass of the star on X-axis.

amount of stars inside the Hα-shining region. Only stars with masses of > 10 $M_\odot$ and lifetimes of < 20 Myr contribute significantly to the integrated ionizing flux, so the emission lines provide a nearly instantaneous measure of the SFR, independent of the previous star formation history. After, by conserving the relative proportions of massive to dwarf stars according to the IMF assumed it shall be inferred the star formation within the whole interval of masses. And finally, it is obtained

$$SFR[M_\odot year^{-1}] = 7.9 \cdot 10^{-42} L(H\alpha)[ergss^{-1}] \quad (1.2)$$
$$= 1.08 \cdot 10^{-53} Q(H_0)[s^{-1}] \quad (1.3)$$

where $Q(H_0)$ is the ionizing photon luminosity and the Hα calibration is computed for Case B recombination at T_e D 10,000 K (Kennicutt 1998).

1.3 Framework and Scope of the thesis.

Knowing how galaxy properties depend on cluster and group properties at different redshifts is therefore a necessary condition to assess the amount of evolution with redshift, even before attempting to shed some light on how this evolution depends on environment. General trends were soon discovered by the early studies of nearby clusters, such as the fact that richer, more centrally concentrated, relaxed clusters tend to have proportionally fewer star-forming galaxies than less rich, irregular, unrelaxed clusters. However, an exact portrait

of how the star formation activity in galaxies depends on the cluster characteristics is still lacking. For example, apparently contrasting results have been found in the literature regarding the presence (Martinez et al. 2002; Biviano et al. 1997; Zabludoff & Mulchaey 1998; Margoniner et al. 2001; Goto et al. 2003) or absence (Smail et al. 1998; Andreon & Ettori 1999; Ellingson et al. 2001; Fairley et al. 2002; De Propris et al. 2004; Goto 2005; Wilman et al. 2005a) of a relation between galaxy properties and global cluster/group properties such as velocity dispersion, X-ray luminosity, and richness.

Increasing literature on the SF trends with interest on cluster environment is nowdays available. All of it improving our knowledge and broadening the investigation on this issue, but with lack in one, flux limited coverage, or other aspects, aperture affected/biassed/... Getting to the point of which news are offered by the present research, how it is adapted and how it replies to the current neccesities of the scientific community.

We expect to carry out a large deep Hα survey searching for the Star Forming Galaxy population up to the Abell radius in five nearby clusters with a lower restriction in logarithm of Hα flux of -15.5. From this we go to obtain a complete census of SF sources and its Luminosities and Equivalent Widths of Hα in every cluster. Analysing the main figures obtained (F(Hα), EW(Hα), R_{mag}, position [Right Ascension, Declination]) is desired go further and find basic relationship between those properties and between the distribution of those properties. Beside that brand-new catalogue and relationships, a set of morphological parameter (Asymmetry, Compactness, Radial profiles) for every significative Hα emitting galaxy will be computed, completing the description of Intensity and 2D Shape of the Hα emission. Once the individual, for every galaxy, whole parameters derivation were achieved we will be interested in comparing the clusters (between them, and with field characteristics). We go to wonder if we are able to relate the efficiency of stripping with the cluster properties as well as to probe whether a theoretical scenario, already published, is preferred as a result of our analysis.

CHAPTER

2

DEFINITION OF THE SAMPLE

2.1 Selection criteria

Present days have experimented an explosion in number of surveys (2dF, SDSS, 2MASS, GALEX,...). Given this (bountiful) wealth of data, an important number of databases resulting from those surveys have been published via web. However on Hα related subjects, like star formation, the amount of data on those databases is not relevant and, if exists, it does not enter deeply on environment distinctions: specially orphan are the clusters of galaxies. In this context, our survey comes to open a new study way in the near universe.

The sample of clusters which present survey is composed of, was carefully selected, by only limiting two observational parameters: the declination (visible from northern hemisphere $\delta \gtrsim -25^o$); and the redshift ($0.02 < z < 0.03$). Within this semispheric shell (see fig. 2.1) of the universe 7 clusters can be found: Abell 400, Abell 539, Abell 634, Abell 779, Abell 1367, Abell 1656 (Coma), and Abell 2666. Hα based star formation activity on Abell 1367 and Coma clusters were observed and studied previously through their spirals to peculiar types in several publications starting by the earlier works of Kent 1979 and subsequents papers, xsKennicutt & Kent 1983; Kennicutt et al. 1984, also the objective prism survey of Moss et al. 1988; Moss & Whittle 1993 went

over them, but it has been at the present century when the relative proportion of dwarf to luminous Hα emission lines galaxies in clusters where write down numerically for the first time through the Hα Luminosity Function in Iglesias-Páramo et al. (2002). These two clusters from the nearby universe (Gavazzi et al. 1998, 2001a) together with the Virgo cluster (Gavazzi et al. 2002; Koopmann & Kenney 2004b; Gavazzi et al. 2003a; Koopmann & Kenney 2004a), are probably the most relevant in the environment-star formation tandem related works in galaxies due to their population and richness, and hence the most studied. Our sample including these two massive clusters, Abell 1367 and Coma, extend the basic cluster characteristics to a low densities, and a variety of ranges in X-ray luminosities, velocity dispersion and others. This work will run over a wide range of properties of the hosting clusters that makes of it, a firm basis for the comparison with more distant clusters, as well as, it supposes a neccesary counterpoint for comparison with nearby star forming galaxies in the field.

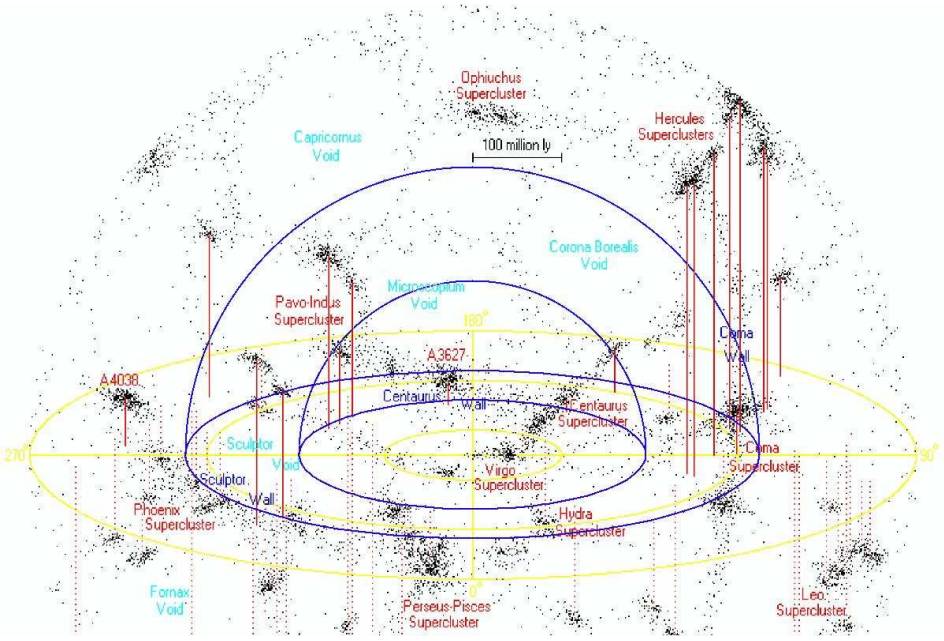

Figure 2.1:: Ilustration of a universe shell such as the covered by our survey

Given the proximity of the clusters, a detailed study of the morphology of the emission could be viable. Any previous attempt to introduce a Hα morphological classification/segregation has produced a strong bias because the majority of the works are precisely focused on late type galaxies. Here we

can afford an unbiassed description of what is happening in a relative extended region of the clusters, where processes acting on individual-grouped galaxies in the two ways (enhance/trigger or inhibit/exhaust the SF) are expected.

2.2 Catalogue of nearby clusters

In the past section, the clusters where we go to search for star forming galaxies have been introduced, and although the point of view in this work will be referred rather to individual galaxies than to the cluster, nowadays, there is no doubts about that the environment, local and global, takes a major role on the evolution of a single galaxy. Thus we would like to devote this section to put forward those "global" properties of the selected sample of cluster. Table 2.1 expounds the main properties of the selected cluster of galaxies.

Cluster name Abell name	**RA** h m s	**Dec** ^{o} ' "	V_r (km s^{-1})	$\sigma_{\mathbf{v}}$ (km s^{-1})	**Cluster Diamet.** (arcmin)	**BM type**	$\mathbf{L}_X$**(Bol)** x 10^{43} (ergs s^{-1} cm^{-2})
(1)	(2)	(3)	(4)	(5)	(6)	(7)	(8)
Abell 400	$02^h\ 57^m38^s.6$	$+06^o$ 02'00"	7315	610	157	II-III	7.6 ± 0.7
Abell 539	$05^h\ 16^m35^s.1$	$+06^o$ 27'14"	8514	629	355	III	13.0 ± 0.3
Abell 634	$08^h\ 14^m33^s.7$	$+58^o$ 02'52"	7945	391	96	III	0.006:
Abell 779	$09^h\ 19^m50^s.8$	$+33^o$ 46'17"	6742	339	90	I-II	2.00± 0.19
Abell 1367	$11^h\ 44^m29^s.5$	$+19^o$ 50'21"	6595	879	266	II-III	17.6 ± 0.5
Abell 1656	$12^h\ 59^m48^s.7$	$+27^o$ 58'50"	6925	1008	319	II	156. ± 8.
Abell 2666	$23^h\ 50^m56^s.2$	$+27^o$ 08'41"	8042	518	50	I	0.095:

Table 2.1:: Relevant properties of sample of clusters of galaxies. Description to the columns: (1) Abell name of clusters of sample; (2) and (3) Right Ascension and Declination[1]; (4) and (5) radial velocity and velocity dispersion; (6) Cluster diameter[1] in arcmin; (7) Bautz-Morgan type[1] - a system of classification based on cluster morphology dependent on the brighter/dominant galaxy morph. type - ; and (8) X-Ray bolometric luminosity[2]

Looking at the table 2.1 one can see that pretty all Bautz-Morgan types[1] are represented, X-ray luminosity ranges from those values which other surveys do not consider clustering of galaxies to the large value of the prototypical viri-

[1]Source: NASA Extragalactic Database (NED)

[2]Data taken from White et al. (1997).

[1]A system for classifying clusters of galaxies based on morphology. It recognizes three main types. Type I has a single supergiant cD galaxy, type III (for example, Virgo Cluster) has no members significantly brighter than the general bright population, and type II (for example, Coma Cluster) is intermediate between the other two.

Cluster Name	Redshift	D_L (Mpc)	D_A (Mpc)	Size (Kpc/")
A400	0.02440	106.5	101.4	0.492
A539	0.02840	124.3	117.5	0.570
A634	0.02650	115.8	109.9	0.530
A779	0.02249	98.0	93.72	0.454
A2666	0.02629	117.3	111.2	0.539

Table 2.2:: Cosmological parameters to be applied for Luminosities, derived using Ned Wright's Comology Calculator (*http://www.astro.ucla.edu/%7Ewright/CosmoCalc.html*) with $\Omega_M = 0.3$ and a flat universe. 1st column: Abell name; 2nd: redshift; 3rd: luminosity distance in Mpc; 4th: angular distance in Mpc; 5th: size in Kpc subtended by one arcsec.

alized cluster, Coma. The same thing happens to the velocity dispersion and to the cluster diameter. We could include here other characteristic properties as richness, virial radius, always with the early conclusion: in respect to the cluster selection we do not introduce any significant bias.

Abell 1367 and Coma clusters have been deeply observed and already studied, so in this observational part, data-reducing, and measuring we go to focus on the five Abell clusters # 400, 539, 634, 779 and 2666. That two clusters, Abell 1367 and Coma, are invoked during the stage of analysis and discussion.

Cosmology assumed is a flat universe with $\Omega_M = 0.3$ and a Hubble constant $H_0 = 70$ km·s^{-1}·Mpc^{-1}. Table 2.2 provide useful numbers to derive Luminosities and angular sizes for individual objects under this asumption. Those numbers were computed using the Ned Wright's web tool[2].

2.3 Properties of the sample

We move on a brief description of the clusters through their images collected for our survey. Images offered are exposed on the continuum band (red continuum).

2.3.1 Abell 400

Abell 400 is a medium size cluster of galaxies with a morphology II-III in the Bautz-Morgan (BM) classification. Two elliptical galaxies instead of a cD dominant galaxy are placed at the central region of the X-ray potential. On

[2]First of the Cosmology Calculators among the available on NASA Extragalactic webpage. URL: *http://www.astro.ucla.edu/%7Ewright/CosmoCalc.html*

fig. 2.6 a 60x60 arcmin Digital Sky Survey (DSS) image of the centre of cluster is shown.

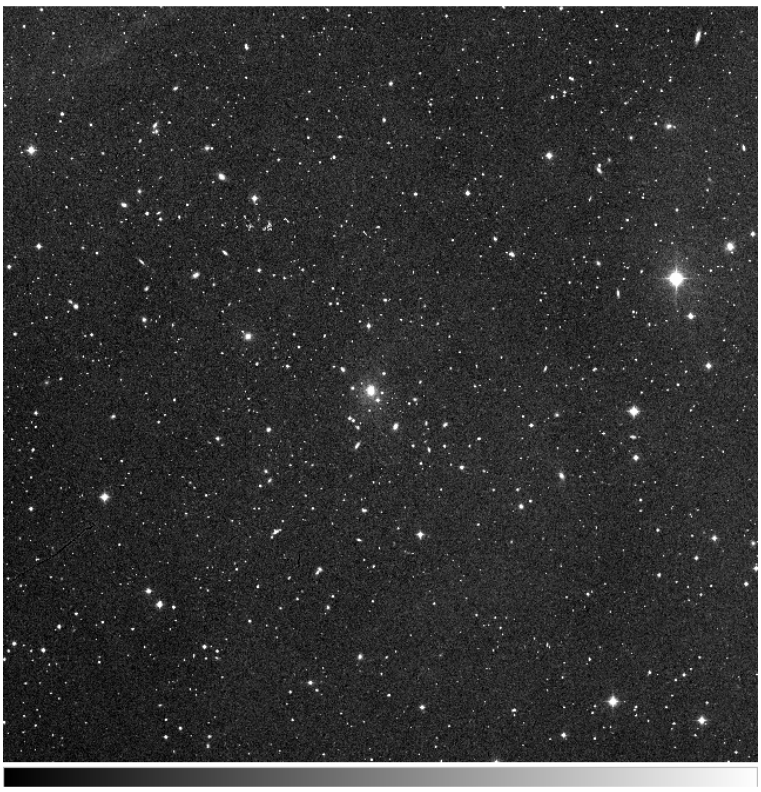

Figure 2.2:: DSS image of the Abell 400 sky region. North is to the top and East to the left (60'x60').

Pointings in the sky were designed to cover the cluster along the Right Ascension direction, but for few problems with the guiding, two pointings were taken in the east position, configuring a final design as can be seen on fig. 4.5. Covered area is almost a 1 degree x 1 degree.

2.3.2 Abell 539

The cluster of galaxies Abell 539 is near the galactic plane. Its population is numerous and it has got a well defined X-ray potential coincident with a spatial density contouring constructed from 2MASS galaxies. An apparent concentration of galaxies to the southwest of the center is not conspicuous neither in 2MASS contours nor in X-ray from ROSAT. Nevertheless, pointings all over the sample were designed in some way following these apparent substructures because interactions, "precooking", and other interesting processes take place within them.

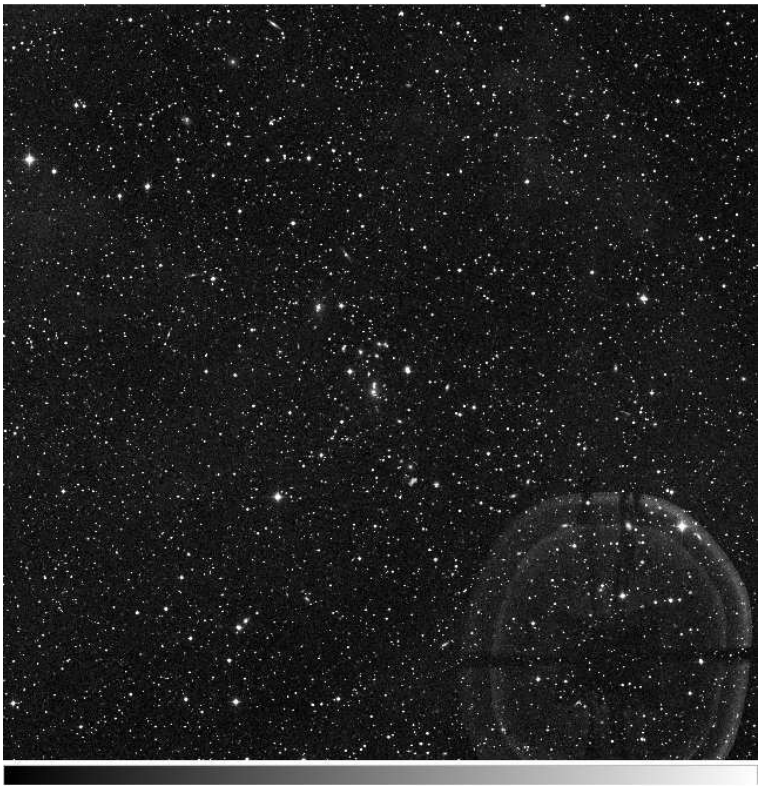

Figure 2.3:: DSS image of the Abell 539 sky region. North is to the top and East to the left (60'x60').

2.3.3 Abell 634

Abell 634, a galaxy cluster in Lynx, which has a low velocity dispersion and a X-ray luminosity below the ROSAT detection limits. Nonetheless, a good number of member galaxies have been declared, occupying a wide (spread) sky region. From a preliminary analysis on the spatial-velocity structure, no substructure were found.

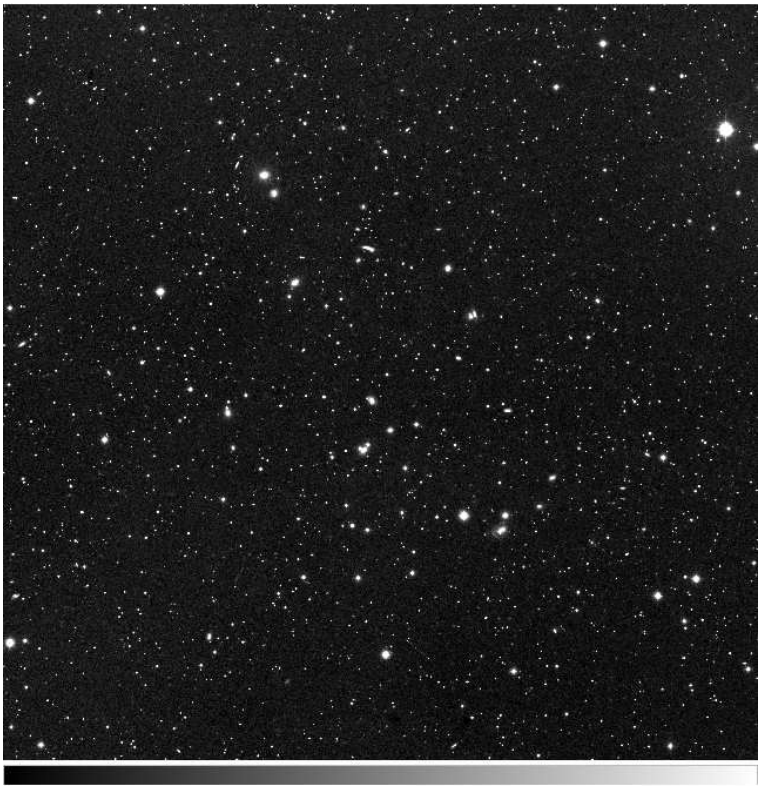

Figure 2.4:: DSS image of the Abell 634 sky region. North is to the top and East to the left (60'x60').

2.3.4 Abell 779

The cluster of galaxies Abell 779 has in common with Abell 634 a low velocity dispersion published. However, Abell 779 presents a conspicuous wells potential defined by a circular X-ray emission detected by ROSAT. A well know cD galaxy dominates the centre of the cluster, NGC 2832. The optical extension

in the sky is as wide as 50 arcmin, shaped up elongated in the North-South direction.

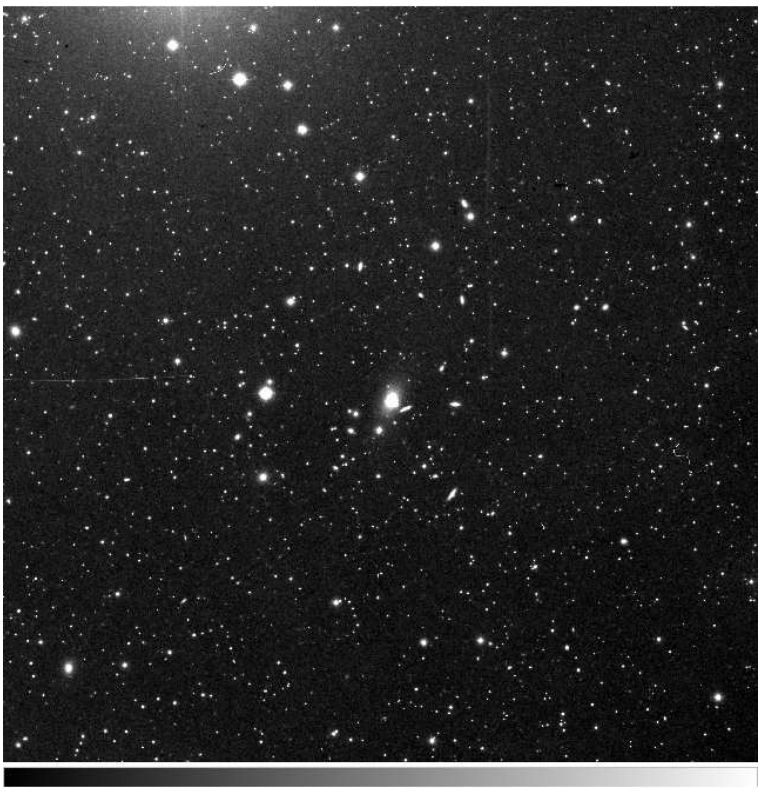

Figure 2.5:: DSS image of the Abell 779 sky region. North is to the top and East to the left (60'x60').

2.3.5 Abell 2666

Nearby Abell 2666 was less populous than Abell 779 and more compact. This cluster together with the Abell 400 are the most separated from the galactic plane, so for them the guiding operation have presented more difficulties. This cluster features four NGC galaxies within a 5 arcminute field. By far the brightest, at 12th magnitude, is NGC 7768. No more than a handful of bright galaxies can be observed at first sight, testifyin the shortness of population. Nevertheless, Abell 2666 has a esteemable velocity dispersion which make it clearly different from another structure.

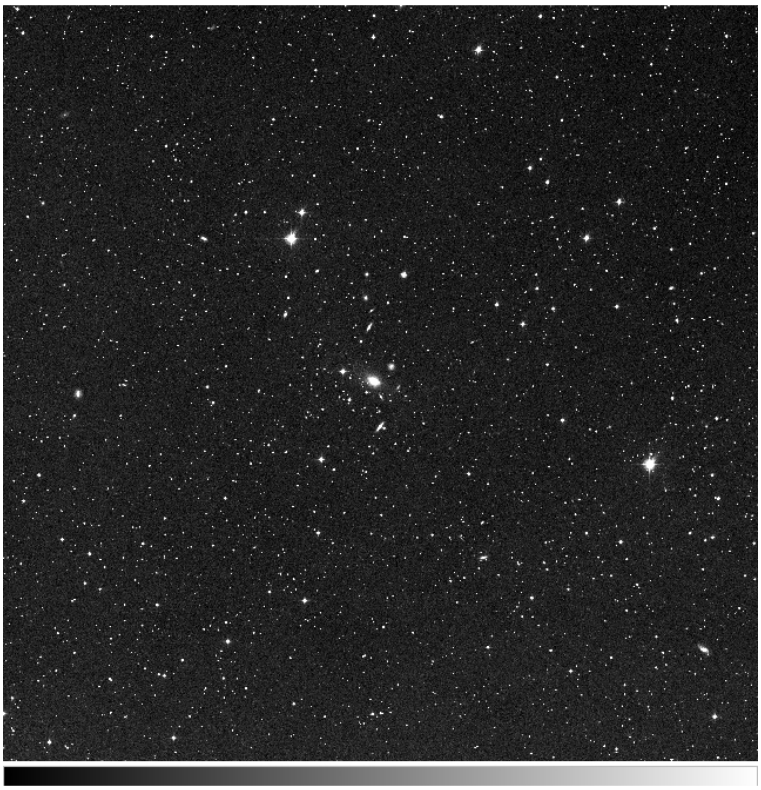

Figure 2.6:: DSS image of the Abell 2666 sky region. North is to the top and East to the left (60'x60').

CHAPTER

3

OBSERVATIONS

3.1 Imaging

Carrying out a survey, whatever it would be focus in, implies a great effort in working time and human resources. But, undoubtedly, the fisrt extra effort required comes when it has being planified. Thus, for observing a big sky extension, firstly, we must consider carefully the use of a wide field in front of a big telescope. Nowadays big telescopes supply small field of view with very good spatial resolution by construction. Therefore *Wide Field Camera* attached to the *Isaac Newton Telescope* supposes the perfect match for our requests. This two instrument ensemble will cover our necessities.

A complete log of imaging observations for each cluster can be found in table 3.3 in section 3.2

3.1.1 Isaac Newton Telescope: Wide Field Camera

The Isaac Newton Telescope (INT) is a 2.5m equatorial Newton type telescope located at the *Observatorio del Roque de los Muchachos* (ORM). This Observatory, suited by an unbeatable weather conditions, number of clear nights along the year, seeing and others, is in La Palma at the Canary Island, an extraordinary and valuated observing place. The Wide Field Camera (WFC)

is science array of four thinned AR coated EEV 4k×2k devices attached to the prime focus of the INT. The pixel scale is 0.33 arcsec pixel^{-1} which gives a total field of view of 34'×34'. Due to its special arrangement, a useless square area of 11'×11' is lost at the North West corner (see fig.3.1). A variety of effects must be declared here related to the chips camera spatial distribution, coplanarity, vignetting and linearity. First of all it is worth noting that a big science ccd camera like this is not to easy to be constructed. Hence a list of first step corrections together with the reduction process are needed on every WFC science image. Gaps between chips make of the array a non-parallel spatial distribution, being the number 3 the most and the number 4 the least tilted of them. In addition, there is not a unique physical plane definition for the whole set. Chip number 4 is the only one ortogonal to the light path from the primary mirror. Chips 1 and 3 are roughly coplanar with the chip number 4. Nonetheless the chip number 2 deviates a bit more of the plane defined by the fourth one. All of these effects are taken into account in the astrometry calibration described in sect 4. Due to extension of the array, the field of view produce a small vignetting effect on chips 1 and 2, and in a more noticeable way on chip number 3. Different linearities are quoted for each ccd, affecting to the photometry calibration.

Spectrophotometric technique make use of narrow band filter, hereinafter referred to as ON-band, to capture a range for a spectral line, in our case Hα. This together with another filter to register the adjacent continuum of the line, referred to as OFF-band, put us in conditions to measure the amount of Hα emission or absorption, its equivalent width and subsequent properties for a determined source. This is possible under the supposition that both filter are seeing the same continuum level since in that case we can estimate the continuum level with the OFF-band filter and the Hα emission with the ON-band. For our purpose we selected an ON-band narrow filter ([S II] filter: $\lambda_0 =$ 6725 Å, $\Delta\lambda = 80$ Å) that allow us to isolate the Hα emission and an OFF-Band (Hα filter: $\lambda_0 = 6563$ Å, $\Delta\lambda = 95$ Å) to measure the continuum emission corresponding to the redshifted Hα line. Further details on the profile of the filters are showed in sects. 5.2 and 5.1.

A total of 5 campaigns were carried out in order to collect the data for the cluster of the sample. Last run, on 2004 September, was totally rejected because of the bad weather conditions and data quality. Now, I move on a short description about each run.

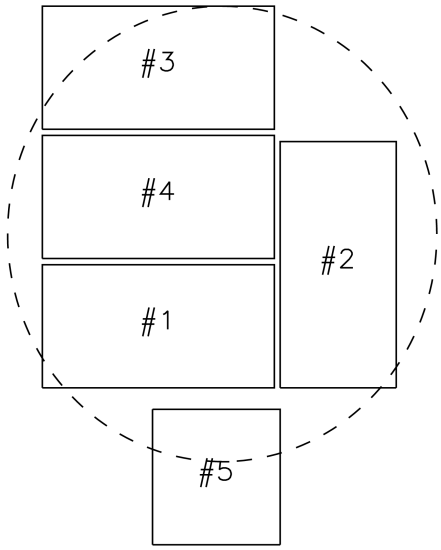

Figure 3.1:: Wide Field Camera array scheme. As explained in the text the total field of view is about a quarter of square degree. Please note the different orientation for the CCD number 2 versus the rest of them. FOV is indicated with the dashed line. Vignetting slightly affects to the first and second EEV, being noticeable for the third one.

	Date		**Number of Nights**	**Cluster of Objects observed**
Month	**Days**	**Year**	**-**	
February	18-21	1999	4	Abell 634
December	1- 4	2002	4	Abell 400, Abell 539, Abell 634, Abell 2666
February	25-28	2003	4	Abell 634, Abell 779, Abell 1367, Abell 1656
December	18-22	2003	5	Abell 539, Abell 2666

Table 3.1:: Imaging dates observation log.

February 1999 run

A first observational campaing took place on 1999 February. The weather during the run was clear and dry except for one night. The seeing was about 1.5". Central half abell radius of the cluster of galaxies Abell 634 was covered by pointing a total of 4×1200 s exposure integration on each band (ON and OFF). This fact allow us to start the study on 2002 August.

December 2002 run

The observing granted time for the project extended since 1st to 4th December. During this run, the four clear nights were devoted to collect images for the sample. Although the nights were clear, just one of them, 3rd December, could be calibrated. Therefore the corresponding spectrophotometrical standard stars were taken and measures of the extinction from Mercator and Carlsberg telescopes have been used. Every winter clusters Abell 400, Abell 634, Abell 539 and Abell 2666, was imaged in two or more bands[1] covering mean area of 1 square degrees. See table 3.2 for the total area covered for each cluster. Pointings were registered at least 3 times offset by a 20" dithering shift in order to avoid bad column. Seeing was varying between 2" (1st Dec) and 0.7" (4th Dec).

February 2003 run

Excellent observing conditions characterized the 2003 February campaing. Four clear dry calibrated nights allowed us to point Abell 634, Abell 779, Abell 1367 and Abell 1656 also known as Coma cluster, completing around an hour of observation in 0.75 square degree mean area by cluster. The seeing stood on average at 1.2".

December 2003 run

Three dry but uncalibrated plus one wet nights compound this campaing. The seeing was all the time above 1.5". Despite of this circumstances few images of Abell 539 and Abell 2666 were obtained.

Having into account the quality of data, last run from December 2004 campaing was totally rejected.

Please, see table 3.1 for a summarized chart.

[1]Broad band r', g', B and V were included in the filter wheel

Cluster	**Pointings**	**Area** (± 0.05) (degree square)
Abell 400	C,W,E and SE	0.85
Abell 539	C,N,W and SW	0.95
Abell 634	NE,NW,SE,SW and C	1.00
Abell 779	C, N and S	0.80
Abell 2666	C,N and E	0.73

Table 3.2:: Covered areas for every cluster in the sample.

3.2 Imaging Observations log

Counting for the selected reduced and analized data images we can built a general imaging observation log that will allow us to have an idea of the dimensions of the work.

Table 3.3:: Imaging observations log.

Name of Cluster	**(Pointing)**	**R.A.** hh:mm:ss.s	**Dec** ^{o} ' "	**N$_{exp}$ × T (s)**	**Filter**	**Date** MM.DD.YYYY
Abell 400	Centre	2:57:38.6	+6:01:59.8	7 × 300	OFF	12.01.2002
				6 × 300	ON	12.01.2002
				3 × 300	r'	12.01.2002
				3 × 300	ON	12.03.2002
				3 × 300	OFF	12.03.2002
				3 × 100	r'	12.03.2002
				1 × 900	ON	12.04.2002
				1 × 300	g'	12.04.2002
				1 × 900	OFF	12.04.2002
		2:56:54.0	+6:01:59.0	3 × 300	r'	12.18.2003
				3 × 200	r'	12.18.2003
				6 × 300	ON	12.18.2003
		2:57:38.9	+6:01:59.9	2 × 200	r'	12.18.2003
				1 × 500	r'	12.18.2003
				6 × 300	ON	12.18.2003
				2 × 600	ON	12.21.2003
				1 × 300	ON	12.21.2003
				1 × 500	ON	12.21.2003
				1 × 250	ON	12.21.2003
Abell 400	West	2:56:27.5	+6:17:14.9	1 × 900	ON	12.21.2003
				1 ×1200	ON	12.21.2003
				1 × 300	ON	12.21.2003
				2 × 600	ON	12.21.2003
				8 × 300	r'	12.21.2003
Abell 400	East	2:59:10.5	+6:11:38.3	7 × 600	ON	12.21.2003
				4 × 300	r'	12.21.2003
Abell 400	SouthEast	2:59:10.5	+5:47:38.0	3 × 300	r'	12.21.2003
				2 × 600	ON	12.21.2003
				3 × 300	ON	12.21.2003
Abell 539	Centre	5:16:35.1	+6:27:14.0	5 × 600	ON	12.03.2002
				3 × 300	r'	12.03.2002
				1 ×1200	ON	12.04.2002
				1 ×1200	OFF	12.04.2002
				1 × 300	r'	12.04.2002
				1 × 250	g'	12.04.2002
				2 ×1200	OFF	02.28.2002
				5 × 600	OFF	02.28.2002
				2 × 500	OFF	02.28.2002
Abell 539	North	5:16:35.0	+6:57:14.0	2 ×1250	ON	02.26.2003
				2 ×1250	OFF	02.26.2003
				2 × 350	r'	02.26.2003
				1 × 500	ON	12.18.2003
				5 × 300	ON	12.18.2003
Abell 539	West	5:14:47.0	+6:26:12.0	5 × 300	ON	12.18.2003

Continued on next page.

Table 3.3 – continued from previous page

Name of Cluster	**(Pointing)**	**R.A.** hh:mm:ss.s	**Dec** ^{o} ' "	**N$_{exp}$ × T (s)**	**Filter**	**Date** MM.DD.YYYY
				2 × 300	r'	12.18.2003
				3 × 400	ON	12.22.2003
				2 × 300	r'	12.22.2003
Abell 539	SouthWest	5:15:33.8	+6:01:23.4	9 × 300	ON	12.21.2003
				2 × 300	r'	12.21.2003
				3 × 400	ON	12.22.2003
				3 × 300	r'	12.22.2003
				6 × 400	ON	12.22.2003
Abell 634	NorthWest	8:13:22.3	+58:28:46.8	1 ×1200	OFF	02.19.1999
				1 ×1200	ON	02.20.1999
				2 ×1200	ON	02.25.2003
				2 ×1200	OFF	02.25.2003
Abell 634	NorthEast	8:09:47.0	+58:23:15.8	1 ×1200	OFF	02.19.1999
				1 ×1200	ON	02.20.1999
				3 ×1200	ON	02.25.2003
				2 ×1200	OFF	02.25.2003
Abell 634	SouthWest	8:12:37.6	+58:00:39.9	1 ×1200	OFF	02.20.1999
				1 ×1200	ON	02.20.1999
				2 ×1200	ON	02.26.2003
				2 ×1200	OFF	02.26.2003
Abell 634	SouthEast	8:09:05.1	+57:55:04.2	1 ×1200	OFF	02.20.1999
				1 ×1200	ON	02.20.1999
				2 ×1200	ON	02.26.2003
				2 ×1200	OFF	02.26.2003
Abell 634	Out NW	8:07:40.9	+58:37:53.1	1 × 500	ON	02.26.2003
				2 × 550	OFF	02.26.2003
				3 × 400	ON	12.01.2002
				2 × 300	OFF	12.01.2002
				1 × 400	OFF	12.01.2002
				3 × 500	ON	12.02.2002
				2 × 500	OFF	12.02.2002
				1 × 500	OFF	12.03.2002
				1 × 500	ON	12.03.2002
Abell 634	Out N	8:10:30.0	+58:59:59.9	3 × 500	ON	12.01.2002
				3 × 500	OFF	12.01.2002
				3 × 500	ON	12.02.2002
				3 × 500	OFF	12.02.2002
				1 × 500	OFF	12.03.2002
				1 × 500	ON	12.03.2002
Abell 779	Centre	9:19:48.0	+33:45:32.0	3 ×1200	ON	02.27.2003
				3 ×1200	OFF	02.27.2003
				3 × 300	r'	02.28.2003
Abell 779	NorthWest	9:19:14.3	+34:15:31.9	6 × 600	OFF	02.27.2003
				4 × 600	ON	02.27.2003
				1 ×1200	ON	02.27.2003

Continued on next page.

Table 3.3 – continued from previous page

Name of Cluster	**(Pointing)**	**R.A.** hh:mm:ss.s	**Dec** ^{o} ' "	**N$_{exp}$ × T (s)**	**Filter**	**Date** MM.DD.YYYY
				1 × 600	ON	12.18.2003
				1 × 400	ON	12.18.2003
				2 × 300	r'	12.18.2003
Abell 779	SouthEast	9:20:21.7	+33:15:32.0	1 ×1200	ON	02.27.2003
				1 ×1200	OFF	02.27.2003
				4 × 600	ON	02.28.2003
				4 × 600	OFF	02.28.2003
				3 × 300	r'	12.18.2003
Abell 2666	Centre	23:50:56.2	+27:08:40.9	3 ×1200	ON	12.01.2002
				3 ×1200	OFF	12.01.2002
				3 × 300	r'	12.01.2002
				3 × 400	ON	12.02.2002
				4 × 400	OFF	12.02.2002
				1 × 200	ON	12.03.2002
				3 × 800	ON	12.03.2002
				4 × 100	r'	12.03.2002
				4 × 800	ON	12.04.2002
				3 × 800	OFF	12.04.2002
				1 × 100	r'	12.04.2002
				2 × 300	r'	12.04.2002
Abell 2666	East	23:52:21.4	+27:21:25.7	9 × 400	ON	12.22.2003
				3 × 300	r'	12.22.2003
				2 × 300	ON	12.18.2003
Abell 2666	North	23:50:56.2	+27:38:41.1	1 × 200	ON	12.04.2002
				3 × 300	OFF	12.04.2002
				1 × 1200	ON	12.18.2003
				2 × 300	r'	12.18.2003

CHAPTER

4

DATA REDUCTION

Here it will be defined the baseline reduction, those fundamental steps to make useful and physical quantities measurable of a science image.

4.1 Bias and Flat Field correction

As is well known the BIAS is an artificial number of counts introduced to avoid statistical and physical problems with negative pixels. With this level we make sure of what we go to read from the device is a positive lecture. Therefore the first step on brand new science images is to subtract that BIAS level from every image, including Flat Field images.

By fitting a (dependent axis polynomical) surface on bias images we proved that bias image, on every chip separately, has no structure. Hence the BIAS will be determined as a scalar. On one hand, the best way to compute the BIAS is a good sampling along the chip(s) to have the maximum number of representative pixels and hence the best juncture to carry out statistics. This is the reason why an image with no-integration time would produce the best sample to estimate the BIAS level. But, due to its relation with the heating, it could vary along the night so a number of bias images should be taken during observing time. Unfortunately, time uses to be so limited (and the readout process usually takes an important amount of it), then, on the other hand,

the alternative procedure is to take into account the *o*verscan section. This section is a ccd-reading extension of the true physical image dimensions for few not-real columns/rows. Median or Mode on this extension would yield a count level by pixel without exposing at the moment of reading, in other words, an instantaneous "bias image" with smaller dimension than the mentioned ones. We have checked the statistic trend of the overscan section on every image and whether well behaved, we used the corresponding statistic on the bias images of the night[1] extracting the real figure (equivalent to a plane with no slopes) which were subtracted to every image of the corresponding night.

After this, the sensitivity differences pixel by pixel and non uniform global ilumination reponse were corrected using a normalized FLAT FIELD image. Attending to the non uniform reponse we have to claim for some effects. Here we go to check two of them. The first one, the pixel by pixel different reponses normally come from unequal sensitivities between pixels or reading effects. In few cases, a pixel region with less relative reponse (to the rest of the frame) appears on the CCD due to a repeated pointing on it. Whilst the second one, irregular ilumination effects uses to be produced by vignetting and reflections inside the telescope structure.

Sky flat field images were taken with sunset and sunrise sky light for producing an appropiate level of counts (within the linearity limits) on the device, for every employed filter band. By combining the set of flat field images from the same filter, scaled to the mode or the median, and normalizing to the combined final median, we obtain a normalized flat field image, that would help us to correct partially vignetting and sensitivity effects on science images. When neccessary, due to a low number of individual flat field images, a superflat was built by using all the flat field images in the campaign.

4.2 Cosmetics

Slight dithering was designed into the observational plan in order to avoid the characteristic WFC gap, and also the bad columns of pixel and invalids regions. When bad columns and regions persisted beyond the basic treatment (normally this occurs at frames with few pointings, less than 3 or when one of this pointings has a poor signal to noise), we applied a linear interpolation through the lower distance between the bad area dimensions.

For the individual cropped images of relevant sources a model subtraction was performed for those galaxies blended with a star or a projected compan-

[1] Usually 9 or more BIAS exposures were taken by night at the beginning and a similar number at the end

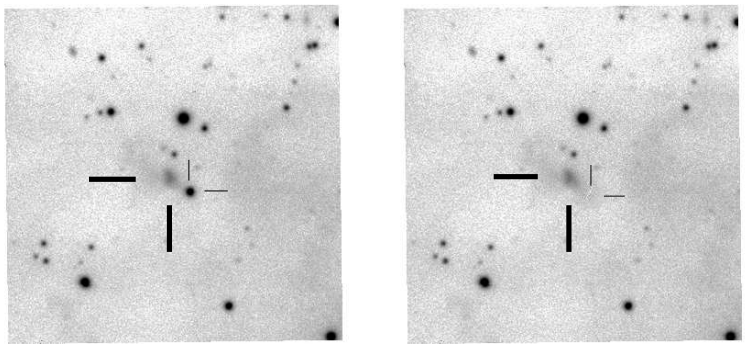

Figure 4.1:: Left diagram shows the image of a not catalogued galaxy in the sky region of Abell 539 cluster (pointed by thick lines) with a star (thin lines) embedded on its light profile. Right panel shows the same once the star model was subtracted.

ion. This procedure works in a simple way. First, a fit of the σ_{bg} isophote is computed then the center and shape are used to derive the profile of the contamining object; and, finally a model was built and subtracted. The look of resulting image depends on the seeing, the "degree" of blending, and relative intensities. It is worth noting that for very bad seeing, or total overlapping, or either saturate this procedure has not meanning. In fig. 4.1 "before" and "after" are displayed.

We tested whether this action only takes effect on the profile fitting and do not change dramatically the photometry within an integration limits[2] resulting in a good agreement.

4.3 Astrometry

The WFC has an extended list of known problems about the astrometric calibration. Some solutions are published on remarkable places, for exmaple the offered one at the WF survey page, based on their wide experience working with that camera at the INT. The theme is that this kind of solution is a system of equations with a free parameter. To fix this free parameter the telescope pointing coordinates should be used to link the polynomic transformation between X,Y to α,δ to a determined position on CCD X,Y space. This method would yield a typical indetermination of about $\sim$ 0.8" - 1". To improve these number a 2nd order correction would be needed in any case.

In this work, instead of a general solution, a particular astrometric solution for every image was computed. This way allow us to reach better precision and

[2]This integration limits exclude the star on both images, the original and masked one

reduce the rms error to $\sim$ 0.3" - 0.5" (0.6" in few worst cases).

Two scripts written in IDL and a original IRAF task allowed us to make use of more than 500 α,δ stars coordinates from USNO[3] by pointing (usually a 1000) crossing them with our X,Y positions. Then a general transformation of a RA-DEC tangencial+polynomic projection with a maximum of 5th order in the pure main terms (X and Y) and 4rd order in the cross-terms, has been applied. This considerations follow the previous works on WFC astrometry solution offered by the ING Wide Field Survey and the Cambridge Astronomical Survey Unit Wide Field Survey (CASU WFS). Their experience fixes the distorsion degree $\propto$ r^5 (r radius to center of the camera).

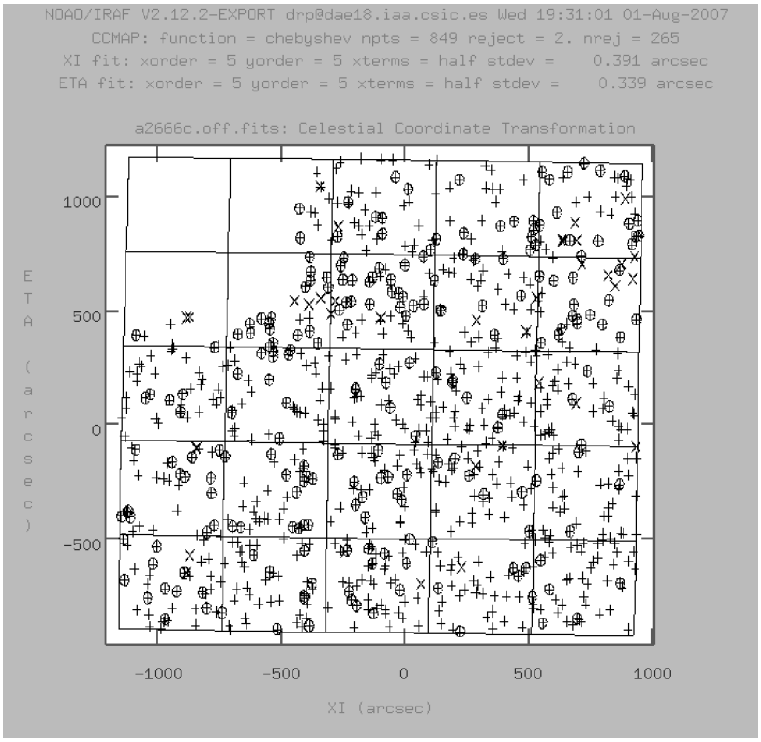

Figure 4.2:: Interactive graphical term were the *ccmap* fit could be checked. Please note the slight rotation for the whole frame.

The IRAF task that computes the polinomies and writes the astrometry coeficients into the image header is *CCMAP* (on imtools). CCMAP could be run interactively and reject those pairs of coordinates that prevents the general trend/fit (marked with circles on fig. 4.2). These objects could deviates up to

[3]This research has made use of the US Naval Observatory star catalog

30 arcsec the position predicted by the fit, and supposes less than the 20 % of the sample.

The most compelling interpretation is a fast propper motion for those objects that makes not valid the position provided by USNO. A rejection of 2 (or lower[4]) times the standard deviation were used to rule out the worst input coordinates.

Confronting the inferred coordinates from the solutions and "true" coordinates versus the position at the camera, distorsions effects can be checked out. Fig. 4.3 shows up the hard corrections on distorting trends for chip 1 versus X position and for chip 2 versus Y position.

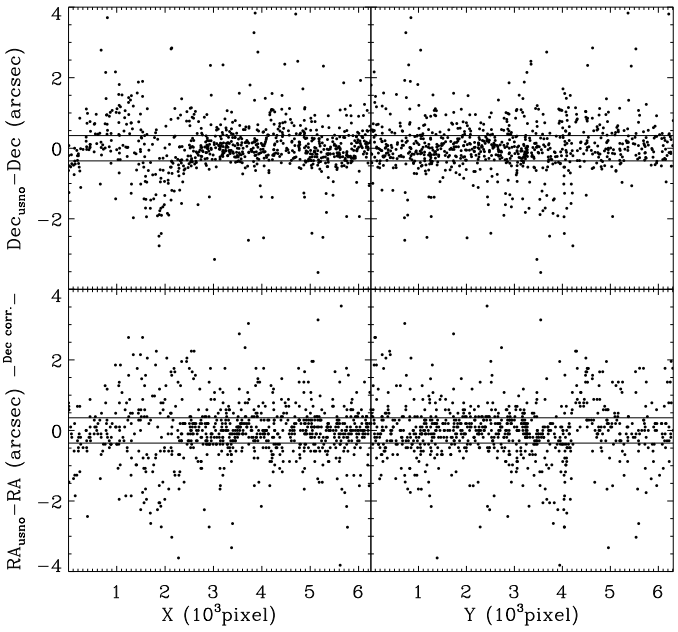

Figure 4.3:: Absolute differencies between USNO coordinates and those from our survey. Mode of square root deviations is 0.36" on that pointing for Abell 2666 central pointing, plotted as a solid line. Scatter is not totally random due to the special arrangement of the camera. Where the major length of a single chip is traced the fit reaches better solution grouping the points so a sensible change between chips can be showed up at $\sim$ 2000 in X, and 4000 in Y, taking into account the total size of a mosaiced image is about 6200 x 6200 pix.

[4]We applied a 1.7 σ rejection when a large amount of stars and objects coordinates were available.

4.4 Final images

After applying the scaling calibration factor (see § 5.2) the final mosaiced images were built. A new specific task for the WFC was developed to construct this kind of mosaic just employing the astrometric solution computed in the previous step of the work. *WFCMOSAIC*[5] task creates a plate that would contain the chips independently treated, unbiased, flatfielded, etc. Thus, just making a geodesical transformation following their astrometry solution all the chips could be put together. Nevertheless, in order to preserve morphological

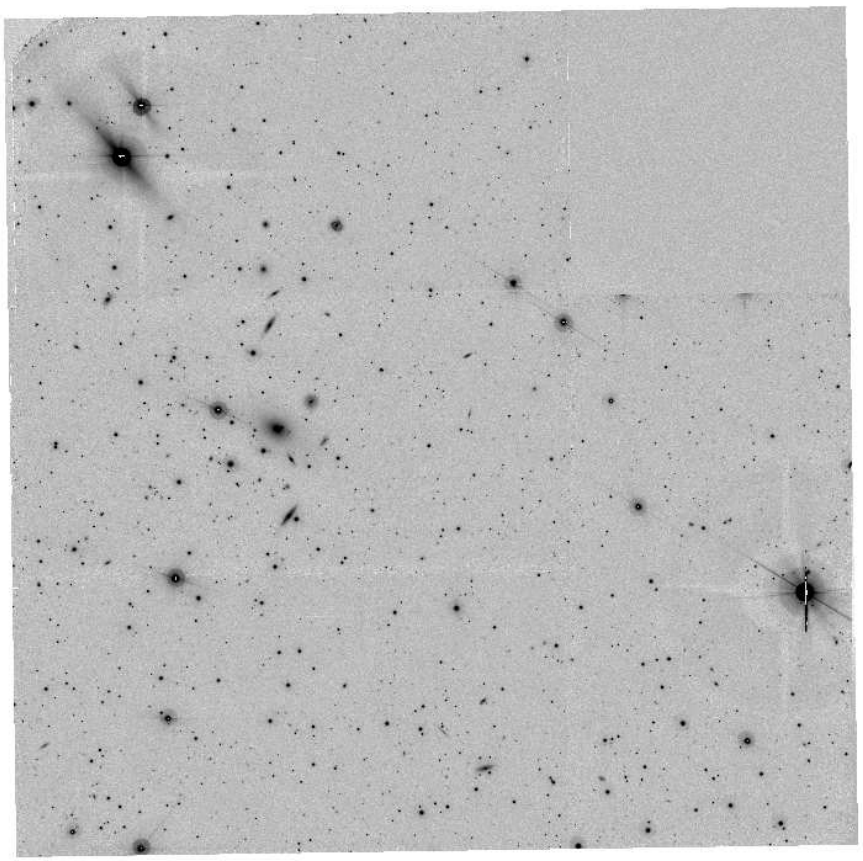

Figure 4.4:: Mosaiced combined image for the center of Abell 2666 cluster. Note that the northeast corner (top to the left) is affected by vignetting. In this particular image we also show the effect of a reflection due to a bright star (2 cases in this frame) in the field. Decreasing signal to noise could be noted on the gaps positions.

[5]Not an original task name, but so the implementation (see apendix A).

information which could be corrupted by the transformation (although we use *nearest* pixel parameter) few steps should be done before into the task process: e.g. create/preserve a minimum margin that allow us to combine with such a dithered pointing or an accurate allocation (even when a not uniform trimming were realized) of the chip on the final scheme.

On the final mosaic, the astrometry solution is recomputed improving the root mean square error down to the 0.3"-0.4" pointed above. Possible sky structure was looked for[6], and the 11' x 11' square to the NorthWest was filled with the same pixel-intensity background distribution as the whole frame[7]. Up to now the images were always treated in ADU but final images will be given in ADUs since we derived the campaign system zeropoints in ADUs/(erg $cm^{-2}s^{-1}$). Hence a normalization by exposure time (of the reference frame) is done.

After this we are ready to extract magnitudes, fluxes and other properties from our survey. Up to date, there is not much works which could be provide a spatial resolution of the Star Forming regions based on Hα emission line in a vast extension of the sky as shown in fig. 4.4.

On figs. 4.5, 4.6, 4.7, 4.8 and 4.9 the final mosaics for the continuum is shown.

[6]Most cases, background has no structure or it is neglectable to the final measurements of the individual objects

[7]This step was done for some reasons in the detection process with sextractor (see5.4)

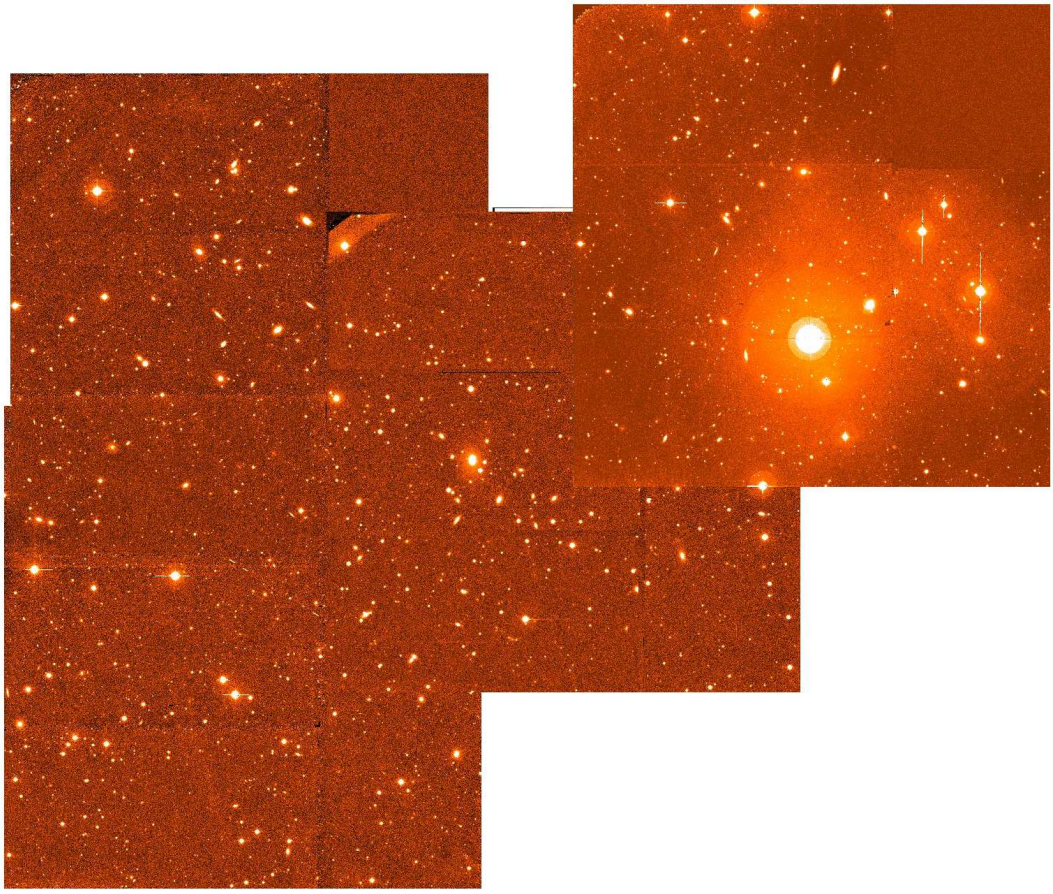

Figure 4.5:: Super mosaic of pointings in the Abell 400 sky region. North is to the top and East to the left. Each box represent the field of view covered by the Wide Field Camera ($\simeq$ 34'x34'). Few minutes overlaping is wanted in order to derive a relative calibration between pointings.

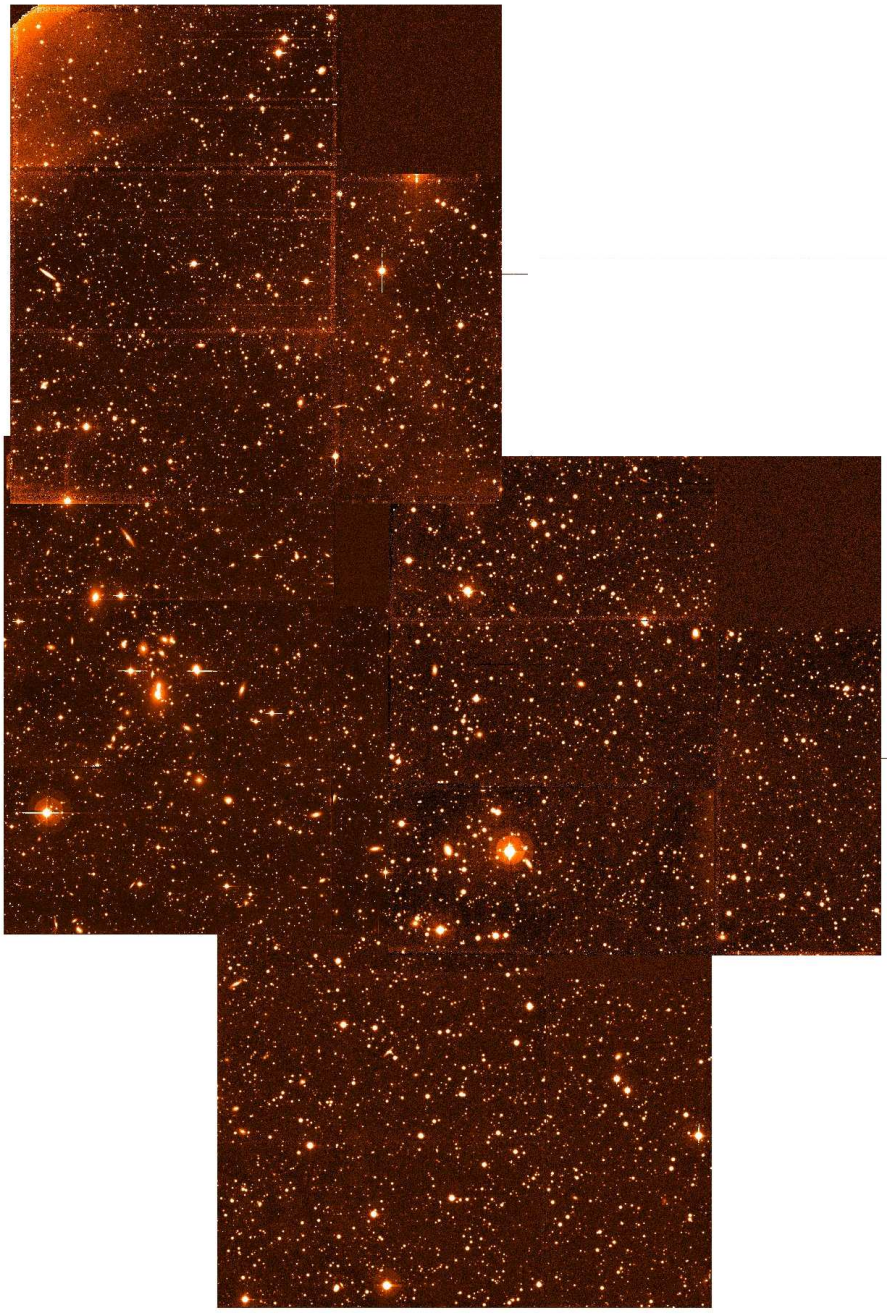

Figure 4.6:: Same of figure 4.5 for Abell 539.

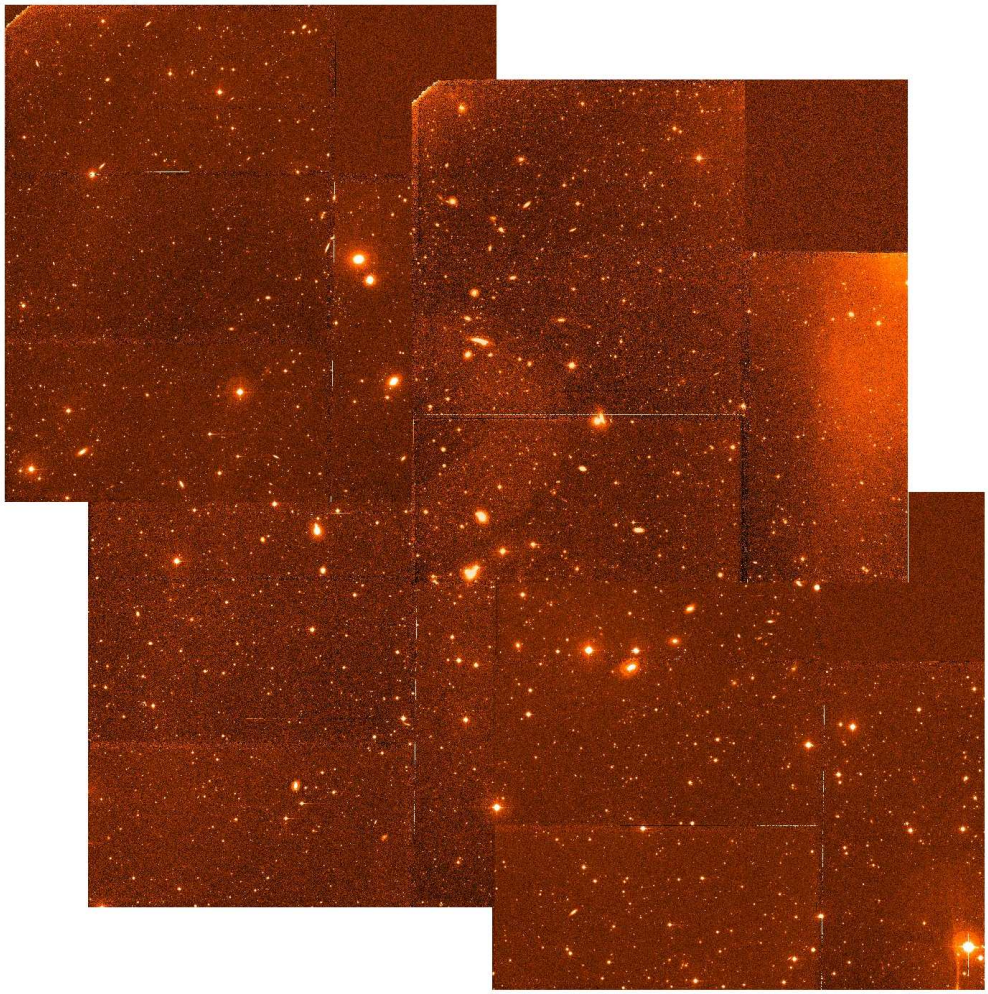

Figure 4.7:: Super mosaic of pointings in the Abell 634 sky region.

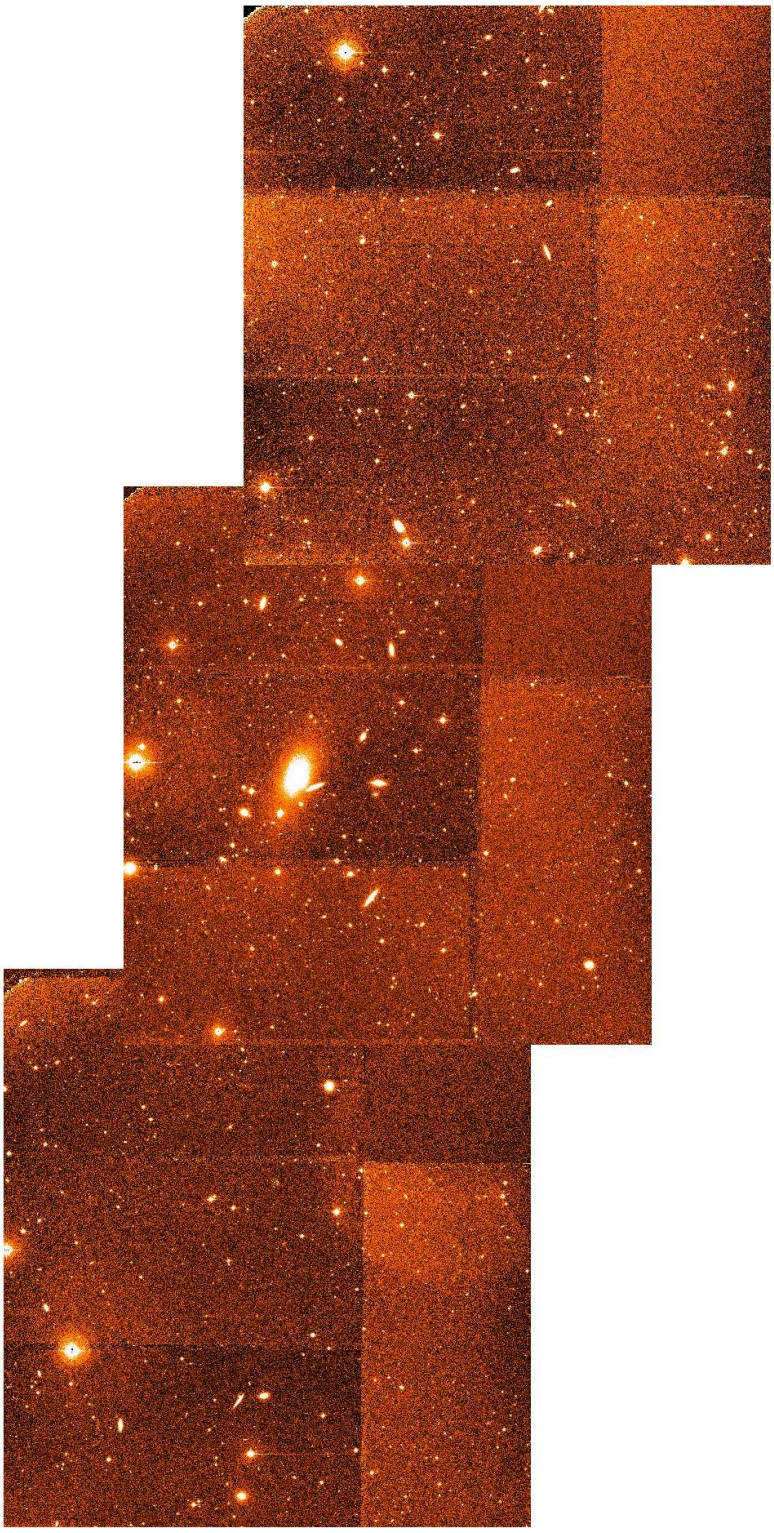

Figure 4.8:: Super mosaic of pointings in the Abell 779 sky region.

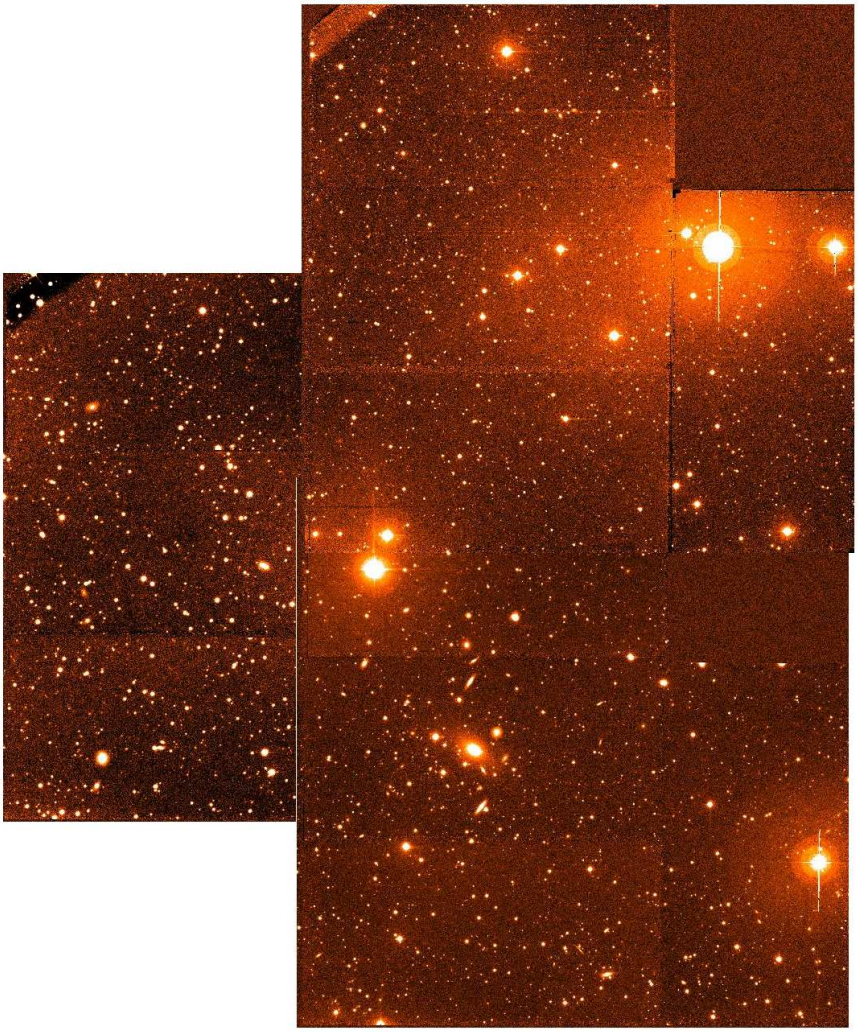

Figure 4.9:: Super mosaic of pointings in the Abell 2666 sky region.

CHAPTER

5

PHOTOMETRY. METHODOLOGY

5.1 Photometric system

The spectrophotometric technique born with the capability of construct specific filters at a high throughput consists in isolating narrow emission channels from a spectrum, enabling the study of the morphology and spatial distribution of the existing absorption/emission lines. This technique usually uses a set of, at least, two filters, one of them being a narrow filter, centered at the wavelength of the emission to study, while the other, possibly narrow or broad, is aimed to sample the continuum near the emission-line. In order to be able to sample the Hα emission within a "shell" of the Universe at redshifts between 0.02 and 0.03, two main narrow filters were selected among the availables. The [SII] filter at the INT, that would collect the wavelength of 6563 Å for every object with radial velocity between $\sim$ 6000 and 9000 km/s with an efficiency greater than the half maximum of the filter transmittance; while the local Hα and the Sloan r' filters would register the nearest continuum (see fig.5.1). We prefered to use the broad band filter Sloan r' for 3 of the clusters, instead of the corresponding narrow filter, for various reasons. The treatment is practically the same in most of the considerations. When a diferent processing was needed to be applied, it

will be commented. Here in after, the filter that gathers the Hα emission will be referred to as ON, while the filter sampling the adjacent continuum will be referred to as OFF band.

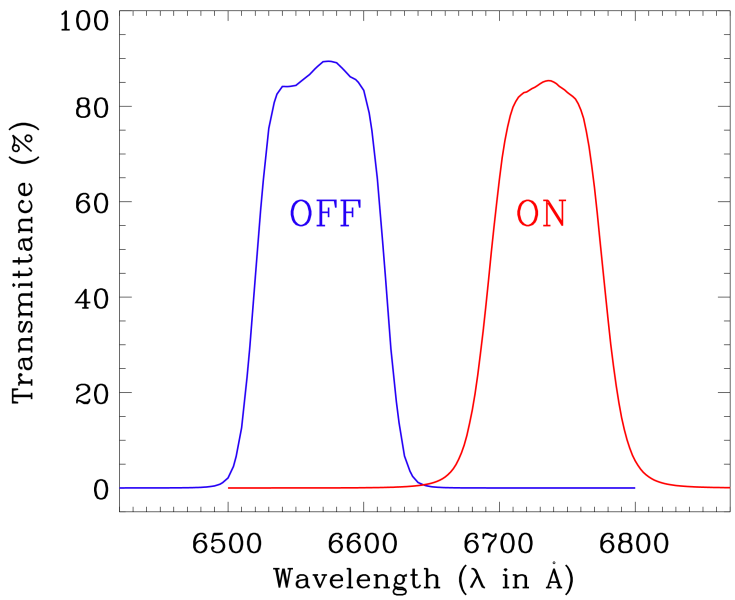

Figure 5.1:: Filter transmittance profiles. Both of them show a high transmittance efficiency at their central wavelength and a steeped drop at the two margin sides.

It must be mentioned that "the system" does not only consist of the filters but also the telescope, ccd's, atmosphere (wheather conditions, transparency, seeing...); and all of these components will play a role, therefore more plausible consequences and effects from all these parameters will be discussed below.

5.2 Zero points. Spectrophotometric calibration

The observatory of Roque de los Muchachos, in La Palma, enjoys one of the clearest skys in the world. Due to neccesity to calibrate the data coming from these telescopes, deep studies on transparency and extinction have been done. There exist even two relevant telescopes, measuring the averaged extinction for the whole night in the V band (MERCATOR) and for interval of time in the R band (CALSBERG). Under the asumption of no colour correction for those calibrated nights we applied the known atmospheric extinction curve, fig. 5.2.

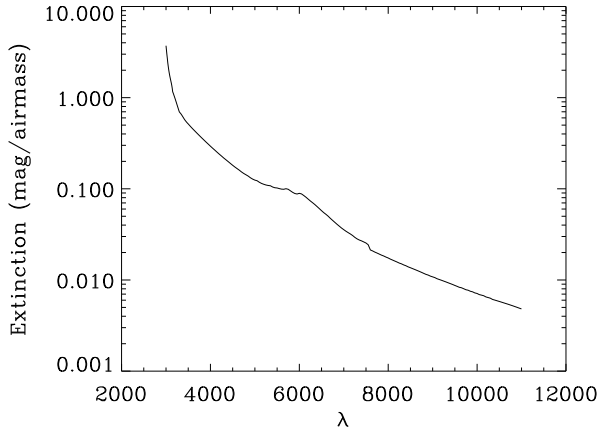

Figure 5.2:: Extinction curve for La Palma observatory. Note that ordinates are represented on a logarithm scale. Thus, it is easy to see that just a bit before 4000 Å atmosphere becomes practically opaque. Then UltraViolet and shorter wavelengths emissions are shielded (screened) at a high efficiency.

The assumption adopted here is to supposse there are no variations in the shape of the extinction curve, is to say, knowing the extinction in a given band, for instance the bands observed by MERCATOR (V) and CALSBERG(R) telescopes, we are able to compute the extinction at any other band, since it can be derived from an absolute shift of the extinction curve 5.2. Extinction coeficient for the ON band was computed then by interpolating the shifted curve at the central wavelength of the cluster of galaxies we were looking at. The atmospheric extinction derived from the ON band is found in table 5.2.

In order to calibrate the ON filter observations, a set of spectrophotometric standard stars from the Isaac Newton Group (ING) catalog[1] was included in the observational plan, covering a wide range of airmasses.

The *QPHOT* IRAF task was used to measure the flux (ADU) on the standard star image for a set of apertures. Then, under IDL was extracted the optimal aperture[2] and was derived the flux in ADUs (ADU per second). Following these steps, were computed instrumental magnitudes for every star on calibrable nights.

On the other hand, spectral energy distributions (SED) in the optical range

[1] Available at *http://www.ing.iac.es/ds/landscape/tn065-100/workflux.php*

[2] A simple instruction that takes the interpolated point where the light growth curve reaches the convergency.

Standard \ Date	2002.12.03	2003.02.25	2003.02.26	2003.02.27	2003.02.28
ING name	A.M. (airmass)	(A.M.)	(A.M.)	(A.M.)	(A.M.)
SP0501+527	1.20, 1.11, 1.10	–	1.09, 1.10, 1.31	1.10	1.11, 1.52, 1.55
SP0823+546	–	–	1.10, 1.11, 1.48	–	–
SP0934+554	–	–	–	1.12, 1.35, 1.37	1.12, 1.38, 1.39
SP1036+433	1.04, 1.10	1.11, 1.12, 1.37, 1.39	–	–	–
SP1204+119	–	1.72, 1.74	1.06, 1.07, 1.67	1.14, 1.15, 1.44, 1.45	–
SP1239+178	–	–	–	–	1.42, 1.43
SP1550+330	–	1.01, 1.00	–	1.01	–
SP2323+157	1.40	–	–	–	–

Table 5.1:: Spectrophotometric Standard Stars observed indicating the airmass.

of this set of standard stars are well known through prior public studies at the ING webpage. Thus we can estimate the unextinguished flux collected by our ON filter by convolving the absolute calibrated spectrum of the star with the filter transmittance profile. Fig. 5.3 shows the filter width superposed over a star spectrum. An intermediate step in the convolution process is to adequate the resolution for both, filter and star spectrum, until they have a common bin. Thus, by adding the product of the star spectrum height (usually converted from mJy or μJy to **erg s^{-1} cm^{-2} Å^{-1}**) by the throughput on the transmittance on every resolution-bin of wavelength, we get the theoretical (expected) flux for a star in physical units as well as their magnitude.

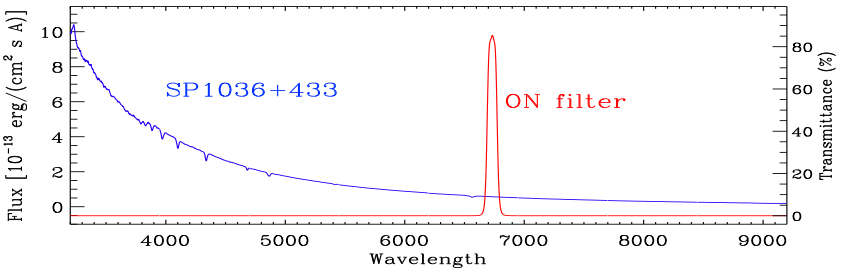

Figure 5.3:: The ON Filter transmittance profile superimposed over the spectrum of the spectrophotometric standard star SP1036+433.

From instrumental magnitudes together with expected magnitudes a least-square regression is performed. As it can be seen in fig. 5.4, the fitting does not reveal any changes depending on variation of airmass[3], showing that the uncertainty of our photometric calibration depends primarily on the nature of the stars than on the airmass variations.

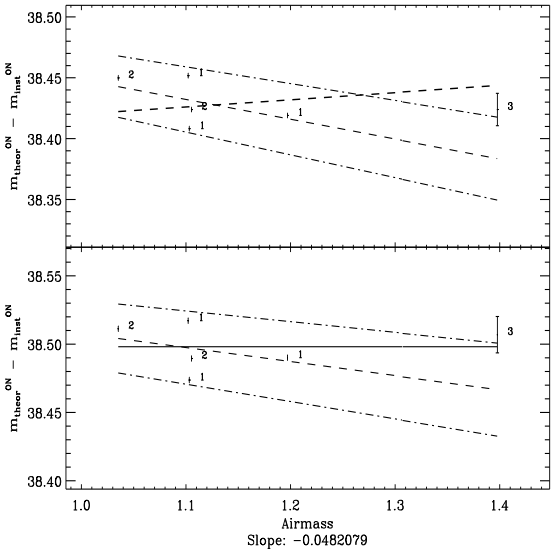

Figure 5.4:: **Top**: Airmass uncorrected measurements for the subtraction of theoretical and instrumental magnitude for the stars on 3rd December 2002. **Bottom**: Same difference with airmass correction. 1.- SP0501+527; 2.- SP1036+433; and 3.- SP2323+157.

Under these conditions a weighted average was be taken as the best way to infer the calibration constant for a single night. Those Zero points are presented below in table 5.2.

5.2.1 Filter transmittance profile

Every selected Hα source needs to be precisely inferred taking in acount the transmission efficiency of the filter profile. Hence we need to know the radial velocity, in order to place the source under the filter profile. However, the goal of our survey is to unveil a kind of sources that, in general, have not been known up to now. Hence, for all of these sources without a catalogued radial velocity (v_r) a spectroscopical follow-up is planned. Meanwhile, in the scope of this

[3]Fittings for the others calibrable nights show similar tendency.

Night	$\mathbb{C}_{\mathbb{F}}$ $(10^{-16}$ erg s^{-1}cm^{-2}/(ADU s^{-1}))	$\mathbb{C}_m$ **(mag)**	$\mathbb{K}_{\mathbb{ON}}$ **(mag)**
2002.12.03	**3.99±0.08**	**38.50±0.03**	**0.059±0.022**
2003.02.25	**4.01±0.15**	**38.49±0.04**	**0.068±0.008**
2003.02.26	**3.86±0.20**	**38.53±0.06**	**0.070±0.004**
2003.02.27	**3.76±0.14**	**38.56±0.04**	**0.071±0.004**
2003.02.28	**3.98±0.32**	**38.50±0.09**	**0.066±0.004**

Table 5.2:: Zero points from spectrophotometric calibration in flux units ($\mathbb{C}_{\mathbb{F}}$) and in magnitudes ($\mathbb{C}_m$) as well as ON band extinction coeficients ($\mathbb{K}_{\mathbb{ON}}$) for each night.

work, cluster velocity will be assumed for every source without determined v_r. In fig. 5.5 assuming a gaussian profile for the velocity ditribution, the position of each cluster is overplotted under the filter profil,e versus the wavelength.

As explained in detail in chapter 6, a two fold strategy was followed in order to deal with extended sources. In the first place, we assured that there has been performed a correct measurement of the extended galaxies and those other with radial velocity catalogued, by measuring them with an own developed set of scripts-running under IDL.

For these galaxies, and knowing that a slight variation in the v_r (radial velocity) could represent a strong change in the throughput given by filter, an appropiate correction factor derived from a catalogued v_r was applied.

For those objects without a known v_r in the actual public databases, it has been assumed the velocity of the host cluster .

5.3 Corrections to the Hα flux measurements

Hα fluxes directly measured on images are then converted to physical units performing the corresponding zeropoint correction for each night of the reference image. But further corrections as the filter transmittance or [NII] contamination should be tackled.

5.3.1 Filter Throughput Variations due to Converging Beam and changes in the Temperature

The Wide Field Camera (WFC) is attached to the Isaac Newton Telescope prime focus. As a consequance of this setting the focal ratio (f/3.29) results in a conical converging beam (maximum angle: 8.64^o) that affects directly the transmittance of the interferencial filters (Narrow filters ON and OFF - excluded the broad OFF: Sloan r'). As declared at the apendix D of the La

Palma ING (Isaac Newton Group) Observer's Guide, among others effects the most relevant is that wavelengths suffer a shift toward the blue; secondly, the peak of transmission decreases and the profile broadens making bigger the FWHM. The description at the apendix of those secondary effects is qualitative and in order to account for aproppiate corrections on every galaxy with known v_r given the high weight they could have on a delta-like emisison-line galaxy, further tests have been necesary. A. Zurita (private communication) checked numerically the broadenning and the transmission peak decrement of the filter for objects on and off the optical axis. **?**) fixes in 8.5 Å the shift to the blue of the filter central wavelength. There are no significative differences between objects on and off the optical axis ($\sim$ 0.1 Å) regarding the shift to the blue effect, neither they are for the peak transmission reponse nor for the FWHM of the filter which are always within the 1% of the original values. Now, accounting for this effects quantitatively a figure representing the clusters' velocity distributions under the filter profile is shown (fig. 5.5).

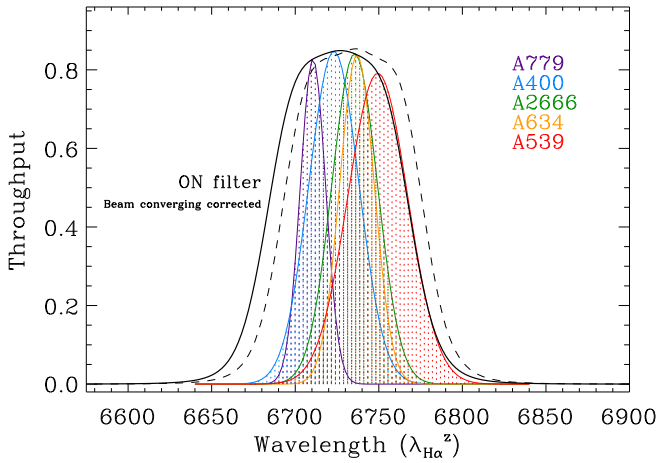

Figure 5.5:: Dashed line represents the original On filter transmission profile (public access at the ING web page). Solid line shows the computed throughput accounting for a converging beam (WFC@INT) (A. Zurita private communication). Velocity distributions for the clusters in the sample are plotted in colours assuming gaussian profiles, over the filter transmission efficiency. Every distribution curve has been normalized to the transmission at the peak of velocities of cluster. Note that the most shielded by the ON filter throughput is the right wing on Abell 539 cluster of galaxies. The rest of cluster galaxies verifying these velocity distributions will suffer a minor correction factor by a relative filter throughput effect.

According to the Observer's guide apendix D, temperature changes affect filter's performance due to thermal expansion and contraction of the materi-

als used for them. The interference filters are specified to work at 10 ^{0}C, so temperatures significantly different from this will affect the effective central wavelength of the filters. Thus, deviations from this value will produce peak wavelength shifts approximately linear with temperature about, typically, 0.3 Å per ^{0}C for our filter set. Since our working temperature has been alaways above 4-5 ^{0}C and below 12 ^{0}C, and given the small dependence on it, no temperature correction has been assumed.

5.3.2 Galactic extinction

The interstellar medium, the dust as well as the halo of our Galaxy reddens and/or absorbs the light coming from the considered clusters of galaxies, exitinguing the Hα absolute flux. In order to address this problem, we supposed a uniform Galactic extinction in the observed sky region for each cluster imaged. This is an acceptable supposition for clusters with high galactic latitude.

The values of Hα flux on table **??** are corrected for Galactic extinction following[4] Schlegel et al. 1998.

The applied galactic extinction coeficient are summarized in table 5.3.

Cluster	$\mathbf{A}_{H\alpha}$ (mag)
Abell 400	0.483
Abell 539	0.450
Abell 634	0.147
Abell 779	0.045
Abell 2666	0.104

Table 5.3:: $A_{H\alpha}$ extincition coeficient used for the clusters sample.

5.3.3 [NII] decontamination

Although ON is a narrow band filter, its full width ($\sim$ 100 Å) would contain at the same time the wanted single line of Hα, and, in addition the Nitrogen emission lines ([N II]$\lambda\lambda$6548,6584).

In order to infer Hα luminosities and the subsequent physical properties like star formation rates, the fluxes calculated by an image should be decontaminated from [NII].

[4]The proximity between Hα and R wavelengths convinced us to reject a further linear interpolation. Therefore we make the simple assumption that A_R is in the same footing as $A_{H\alpha}$, supported by the small standard deviation of the differences between interpolated $A_{H\alpha}$ and A_R (about 0.009 mag).

There are a few empirical corrections derived from more or less extended spectroscopic surveys. Once relative [NII]/Hα is quantified, a classification based either on galaxy/morphology or on a emission-line/galaxy type can be attempted (Kennicutt 1992). The Universidad Complutense de Madrid (UCM) Objective-prism survey (Gallego et al. 1997) was used to construct such a relation distinguishing among seven ELG types. The corrections range from 0.05 for Blue Compact Dwarfs (BCD) to 1.50 for Seyfert 2.

On the other hand one can look for a relation between the total emission flux (Hα, r-Band,...) and the relative [NII]/Hα to each luminosity bin (fig 9 on Gallego et al. 1997; Iglesias-Páramo et al. 2002), obtaining good aproximations.

Drift-scanning spectroscopy permitted to establish the weights for the final corrections due to the galaxy-integrated line-emissions (Jansen et al. 2000). Helmboldt et al. (2004) have made use of Jansen et al. (2000) data to infer a correction based on **r** absolute magnitud.

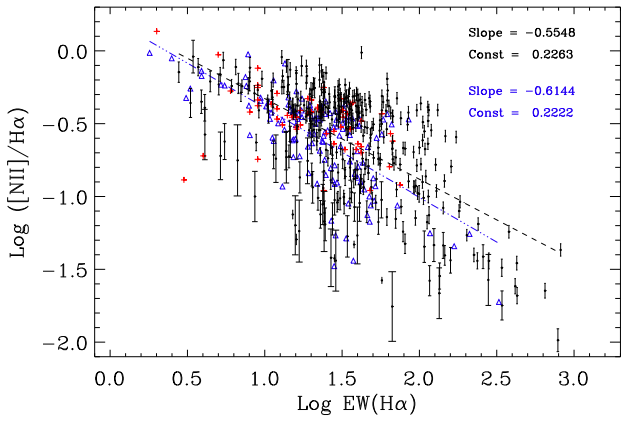

Figure 5.6:: Logarithmic relation between Hα equivalent width versus [NII] over Hα for: black dots with error bar, a four hundred nearby emission line galaxy survey (Moustakas & Kennicutt 2006). Red crosses are galaxies [NII] and Hα data from goldmine (Gavazzi et al. 2003a) in Virgo cluster; and blue triangle represent a major fraction of Jansen et al. (2000) data. Slopes and constants for the two main clouds of points are quoted.

Using recent data from Moustakas & Kennicutt (2006) we traced the trend of [NII]/Hα versus the equivalent width of the Hα line (see fig 5.6) for this extension of the Jansen survey of nearby emitting galaxies, and over points from Virgo goldmine database (red crosses) as well as points from the Nearby Field Galaxies Survey (NFGS) (Jansen et al. 2000).

This scattered-correlation let us actually see the first order of a [NII] decontamination we are looking for. Since some points from Moustakas & Kennicutt 2006 has been corrected forcing [NII]/H$\alpha \simeq 0.5$, for next analysis and further assumptions only data from (Jansen et al. 2000) have been used.

In this work, a linear fit using the emission lines equivalent widths from integrated galaxy measurements in table 4 in Jansen et al. 2000 was derived (fig. 5.7). The inferred correlation 5.1 is thus adopted to correct for [NII] contamination.

$$\text{Log EW}(\text{H}\alpha) \quad = \quad (-0.34 \pm 0.03) + (1.13 \pm 0.02) \cdot \text{Log EW}(\text{H}\alpha + [\text{NII}]) \quad (5.1)$$

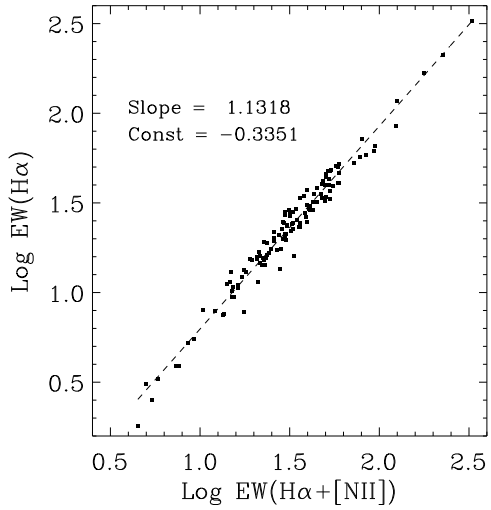

Figure 5.7:: Tight correlation between the Hα+[NII]$\lambda\lambda$6548,6584 ensemble equivalent width and Hα alone equivalent width. From the Nearby Field Galaxies Survey (Jansen et al. 2000) one hundred and twenty six points, for which have measured all involved lines and the Hα is related to Hβ=1, have been used to plot this figure.

5.3.4 Absorption by underlying population

Old stellar population belonging to an Hα emitting host galaxy present a complex spectra usually with high optical continuum and stressed absorption Balmer lines. This absorption competes directly with HII emission lines, since, while the gas and stellar continuum are added in the resultant spectrum, equivalent widths of lines are usually of different nature and then subtracting one each other. Estimate and correct this effect is a difficult task even if low resolution spectra are available.

In principle, at least a pair of Balmer lines, for instance Hγ and Hβ, observed equivalent widths are needed to determine the equivalent width of the underlying absorption. Then, according to models of stellar atmospheres, it is reasonable to assume that the absorption equivalent widths of Hα, Hβ and Hγ are equal (McCall et al. 1985). If, in addition, the emission equivalent width is suppossed to be much greater than the absorption, all weighted measurements predict a small absorption ($\sim$ 1-2 Å) (McCall et al. 1985).

Fig. 5.8 goes over the achievements of Starburst 99 model (Leitherer et al. 1999), Bruzual and Charlot spectral libraries (Bruzual & Charlot 2003), and Delgado et al. (2005) evolutionary synthesis models. Starburst 99 provides a tool to estimate the age of the burst through the EW(Hα) while Bruzual and Charlot spectra libraries, as well as Delgado et al. (2005) would be used as a guide for the estimation of the underlying population absorption through time. When host galaxy is younger than 1 Myr, synthesis models infer an absorption of about 1-2 Å and when it is between 1 and 10 Myr, they agree on a bit higher absorption ($\sim$ 3-4 Å) (Bruzual & Charlot 2003; Delgado et al. 2005).

In order to correct properly for the absorption equivalent width originated by underlying population, our catalogue was divided in two main classes: young and old emission-line galaxies. A high EW(Hα) is directly associated to a very young burst (with a low stellar continuum), this permiting us to take the burst age as the galaxy age, and therefore applying a small correction for underlying populations. The class of young emission galaxies is thus defined by fixing Log EW(Hα) $\geq$ 1.3 ($\simeq$ EW(Hα) $\geq$ 20 Å). This limit is marked on fig. 5.8 with an orange dashed line.

On the other side, a low EW(Hα) could be associated either to an old emission line galaxy, or small young burst/s in a (normal) star forming quiescent galaxy, so to go further we need more assumptions to help us. Given that Hα and continuum morphologies can be studied in detail along our sample, we go to distinguish between those objects dominated by the emission and those others where emission occupies a small portion of the continuum (central, arms...). If the emission dominates the galaxy, we can conjecture that it must be a young

evolved ELG, then its age is coupled to the hosted HII region and a suitable absorption could be derived and corrected by. If Hα emission does not dominate the continuum a lower constrain to the absorption equivalent width based on the continuum flux height can be inferred.

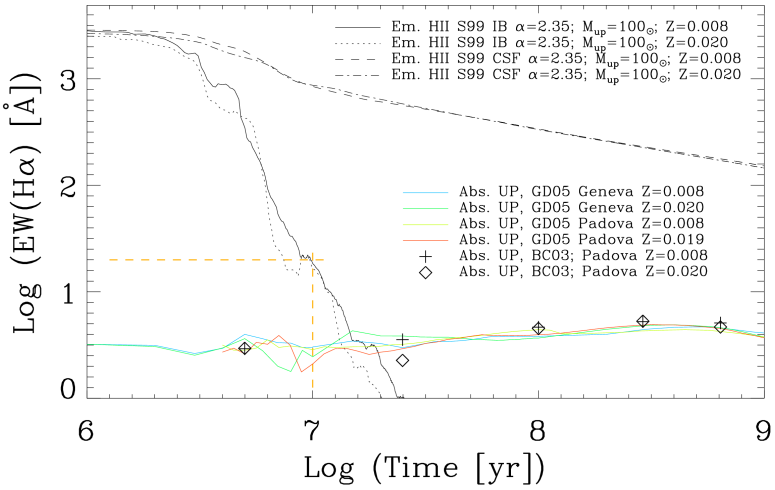

Figure 5.8:: Models for the EW(Hα) emission and absorption along the time.

5.4 SExtractor. A detection machine

Source Extractor, *SExtractor*, code has been used to detect and to derive the photometry properties of the sources in our sample images, except for the extended Hα emitters and catalogued sources for which a detailed study has been performed.

SExtractor abilities are described in Bertin & Arnouts 1996, but we want to make some of them explicit here. SExtractor has the capability of extracting sources automatically from big science images, associating a great number of measured parameters (Flux, Magnitude, Ellipticity, FWHM, ...etc). The advantages provided by SExtractor, quickness, depth, configuration, output params, evidently favour its use. "But not everything is simple" (please, let me quote this kind of obvious sentences to continue the flow of this discourse). Among these pros there are few points that can be considered as cons, for instance: configuration. It is obvious that this point must be carefully dealt, since if configuration is bad, any furher output will be useless. The number of

output params could also become a cons, because of the difficulty to manage such big tables. First it is neccesary to understand the significance of every parameter. "Not any information (and amount of it) is always useful".

Configuring SExtractor input params involve an effort in the way of being well adapted to the images and scopes. Several parameters play an important role in the detection process. To make affordable and tunable an extended search, the governement of the detection under SExtractor was specially subordinated to the DETECTION_THRESH param. In §6.1 the reader will find a detailed description of the strategy followed with SExtractor machine.

5.5 Detection efficiency and limiting magnitude

The limiting magnitude has been derived empirically for each field separately by taking the class of the last interval of magnitudes, corresponding to the faintest objects, over the total histogram of detected sources. It should be noted the agreement in defining the magnitude bin while building the detection histogram for every science frame, being thinner in that frames with a well sampled (bright to faint) collection of objects, and thus more poorly defined in near void frames. Therefore an uncertainty equal to the binwidth is adopted for this limit.

This limiting magnitude is intimately related to the detection efficiency which informs us about the objects recovered at each magnitude bin. To study the detection efficiency an artificial cluster image with similar characteristics of relative proportion of background objects and foreground stars and galaxies has been created with the help of *artdata* package under IRAF. Once the artificial image, where every object position and magnitude is known, had been created, SExtractor was executed on. Obviously, efficiency, considered just as recovered sources per magnitude bin, decreases when the threshold of detection (DETECT_THRESH) increases (see fig. 5.9). But, if we add to our consideration the count of spurious, we should reach a compromise that permits us to recover the maximum number of sources without creating a great amount of spurious detections. Within the returned catalogue a matching looking for true sources has been attempted. By tuning the DETECT_THRESH parameter at the initial conditions for SExtractor we explored the dependence on that param over the final account for recovered versus true sources ratio, as well as spurious versus true sources ratio. Full test can be consulted at Apendix B.

A count of the sources could be done following the simple procedure described in Cristóbal-Hornillos et al. (2003). Taking two half time exposure images we distinguished spurious from real images and made the histogram of the variation in counts with signal to noise constrain, evaluating the relative

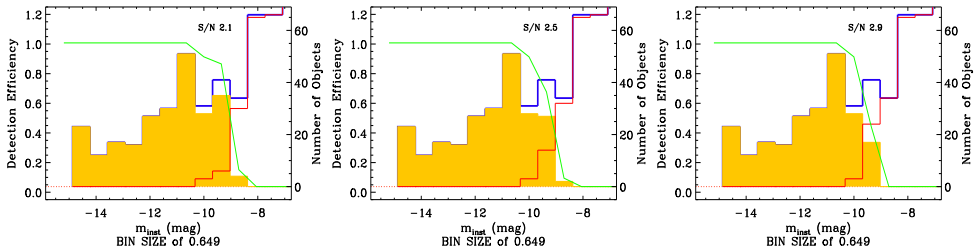

Figure 5.9:: From left to right: detection efficiency for 2.1, 2.5 and 2.9 DETECT_THRESH on an artificial image. On every plot: left Y-axis represents the efficiency; right Y-axis the number of sources; abcisse shows the instrumental magnitude bins; blue line represents the histogram of magnitudes for the original set of sources; red line represents the unrecovered sources; yellow body shows the distribution of magnitudes recovered; and green line traces the efficiency by bin of magnitude. Note how efficiency drops earlier at a higher constrain in the S/N ratio (= DETECT_THRESH).

weight of spurious to real detections (see fig. 5.10 - please, also check Apendix B), and reaching a final value to the DETECT_THRESH of 2.5, common in literature and guaranteed by the previous experience of our group (Iglesias-Páramo et al. 2003a).

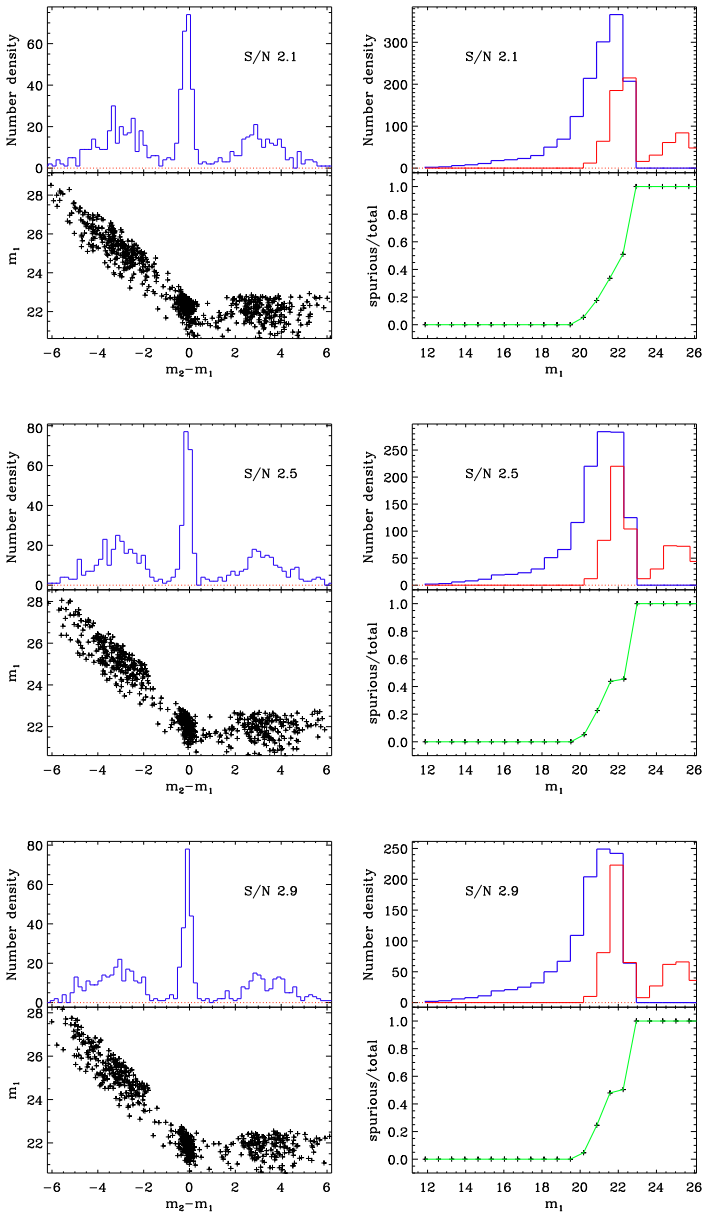

Figure 5.10:: Top to bottom: DETECT_THRESH 2.1, 2.5 and 2.9. For every box, histogram of magnitude difference (left up) over a pseudo magnitude colour diagram (left down), histogram of magnitudes for true (blue) and spurious (red) sources (right up) and the ratio spurious to total for each magnitude bin (green) (right down). Note that relative spurious to total shows a bump indicating the change of tendency. Until this point we can increase the DETECT_THRESH thus discarding most of spurious sources in higher proportional way than true sources. Over this point we would loose too much true sources, due to an unefficient way of detection.

5.6 Scaling the continuum. Extraction procedure

Basically, at this point, the goal being to obtain a good consistent zero point calibration for the filter set, a scale between ON and OFF band has been performed.

The hypothesis on which rely this part of the work is that the ratio between the stellar continuum heights of the two filters of the field stars at our frames is statistically the same. This ratio was a distribution where median is constant and can be forced to be equal to 1, so the calibration for the OFF band is then referred to that of the ON band.

With SExtractor FLUX_BEST output recovered on both bands and on every frame, the $\frac{F_{OFF}}{F_{ON}}$ ratio was easily computed for every overlapping section among chips. Given the arrangement of the camera, we looked for overlap between chip 1 or 2 from one pointing (e.g Abell 779 Centre) and chip 3 from another pointing (e.g. South). This would give us the chance to check the agreement between independent overlapped calibrated pointings, as well as to calibrate relatively those others pointings from non-calibrable nights.

There was one marginal case of superabundance of late-M type stars, where this assumption should not be made and where the needed considerations to avoid this effect had to be taken into account. The largest galactic latitude from our clusters corresponds to the Abell 400 and Abell 779 ($\|\text{GLAT}\| \sim 45^o$). The more distant to the galactic plane we get, the more likely is to observe a greater number of K and M type stars. Abell 779 stars magnitudes up to $r' \leq 17.8$ are completely covered by Sloan Digital Sky Survey[5].

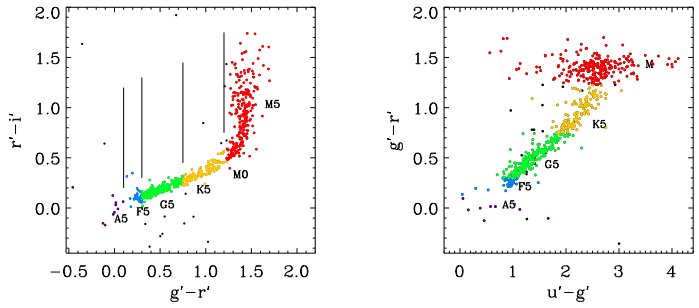

Figure 5.11:: Colour-colour diagrams for field stars on the Abell 779 frames. Stars spectral types classification was adopted from Fukugita et al. 1996 as detailed in text.

[5]This research has made use of the SDSS (Sloan Digital Sky Survey) database. *http://www.sdss.org*

In fig. 5.11 the locus of the different type of stars recovered from our survey by assuming the colours from SDSS are showed in a colour-colour diagram. We distinguished few spectral types of stars by following Fukugita et al. 1996 and Finlator et al. 2000 (A type and hotter: $g' - r' < 0.10$ and $r' - i' < 0.30$; F and G types ocuppies $0.10 < g' - r' < 0.75$; K is on $0.75 < g' - r' < 1.23$; and problematics M stars begin at $g' - r' \geq 1.23$) on the colour-colour (r'-i' versus g'-r') diagram to study how to they fill the ON OFF fluxes ratio in a histogram. Stars with spectral M type show a non uniform continuum across our filter set and, hence, could distort the scaling factor between frames if present at higher relative proportion respect to hotter spectral types. Abell 779 is probably the most unfavourable case to check this hypothesis. In fact it can be seen in fig. 5.12 how M types deviates from the normalization already applied and spreading a wide range in flux ratios, but due to its relatively poor relevance among the whole set of spectral types seen, the reliability of the scaling procedure is ensured.

The full width at half maximum of the distribution that peaks at the described scaling factor is used as an estimator of the uncertainty for this computational skill. Thus, when constructing colour-magnitud diagram in §6.1.4 this value will take a relevant place for the objects selection procedure.

SExtractor were run on every image from every campaing producing the catalogs among the overlapping through common objects is looked for. Whether overlap exists, the ratio between the flux of the stars (selected using S/G param) matched by celestial coordinates is computed and saved in a bigger file. This file is unique for cluster and it contains any possible cross identification among run numbers as well as their scaling factor (MEAN, MEDIAN, STDDEV and the [MEAN,SIGMA] from a gaussian fitted on a histogram distribution of flux ratios, are derived). If the field does not collect M or cooler stars all stats coincide (MEAN = MEDIAN = MEAN$_g$). If not the gauss mean is taken.

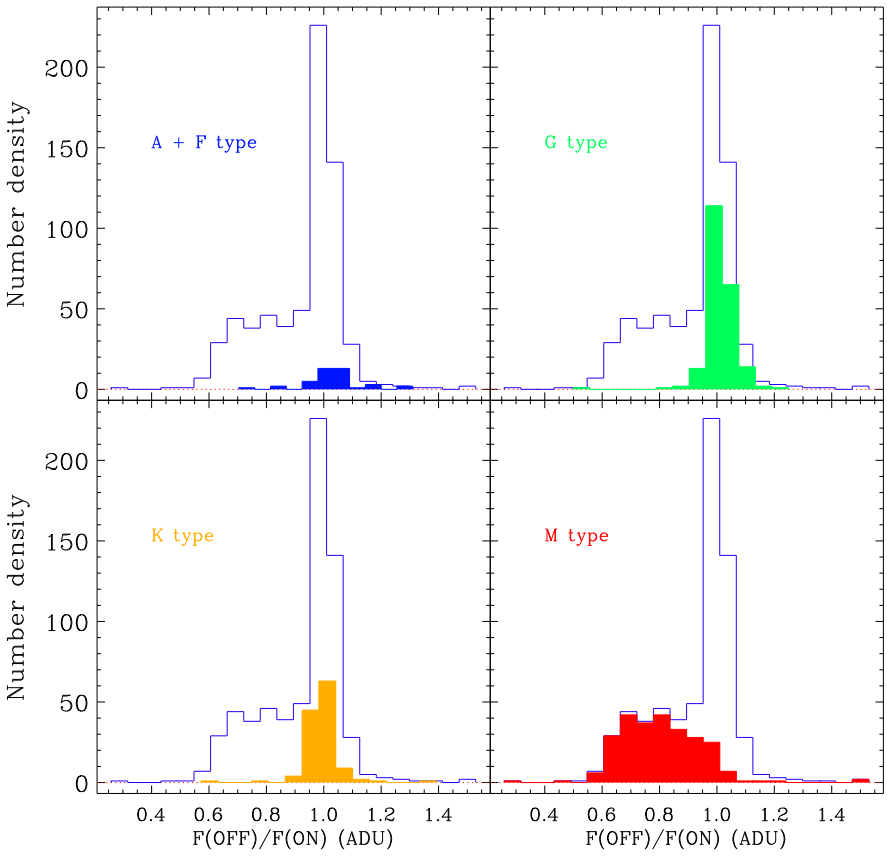

Figure 5.12:: Histograms distribution of $\frac{F_{OFF}}{F_{ON}}$ separated into stellar spectral types. The solid blue line (on every box) describes the histogram distribution for flux ratio from all spectral types ensemble; filled coloured body histograms follow the distribution for the different types. Note that the weight of the scaling factor relies practically on G type stars.

5.7 Reliability of the photometry

Some checking proofs were performed over the resulting photometry data, in order to infer whether it is in agreement with the published catalogs. Main trouble we found to carry out this test is the shortage of catalogs in the r-Band, and the absence in Hα for the sky region covered. Nevertheless, Abell 779 cluster was observed by the Sloan Digital Sky Survey (SDSS) and Abell 634 was partially covered by this survey. From the United States Naval Observatory (USNO) stars catalogs were extracted, bearing in mind its limitations.

Photometry on the continuum filter OFF has been referred to its central (effective) wavelength and converted[6] from $F(\lambda)$ to $F(\nu)$, extracting then a pseudo-m_R assuming

$$m_R = -2.5\ log\,[F(\nu)] + \mathbb{C}_{Johnson} \tag{5.2}$$

And then we compared our photometry with that of SDSS for the cluster Abell 779 by matching the celestial coordinates and by making a correction for the differences between the photometric constants assuming $\mathbb{C}_{Johnson} = 48.83$ and $\mathbb{C}_{AB} = 48.6$ ($\Longrightarrow \Delta C = 0.23$), and we obtained a mean (made iteratively) of 0.05 (see fig. 5.13).

A similar checking had been performed to Abell 539 with much less objects and the condition of existing in the USNO catalog. The constants for the corrections respect to USNO photometric system was assumed to be equal to those from the past example although according to the Sloan Data Release (URL *http://www.sdss.org/dr6/algorithms/jeg_photometric_eq_dr1.html*)

$$\begin{aligned} r_{sdss} &= r_{usno} - b25(r) * ((r' - i') - (r' - i')_{zp}) + zpOffset25(r) \\ &= r_{usno} - (-0.035) * ([-0.06, 0.38] - 0.21) + 0.000 \end{aligned} \tag{5.3}$$

which, depending on galaxy type[7], can vary from -0.009 to 0.006. Given the sensitivity of the test and for the scope of the work, we do not take a correction distint constant. The result is shown in figure 5.14.

Exploration for clusters Abell 400 and Abell 2666 yielded a poor results given by the clear limitations of USNO photometry (sensitivity of 0.1). However, we can declare here that the photometry is in agreement we prior published catalogs.

[6] Through $F(\lambda)d\lambda = F(\nu)d\nu \longrightarrow F(\nu) = \frac{\lambda^2}{c}F(\lambda)$

[7] Galaxy colours interval [-0.06, 0.38] taken from Fukugita et al. (1995) at z=0 and z=0.2 (table 5 and 6)

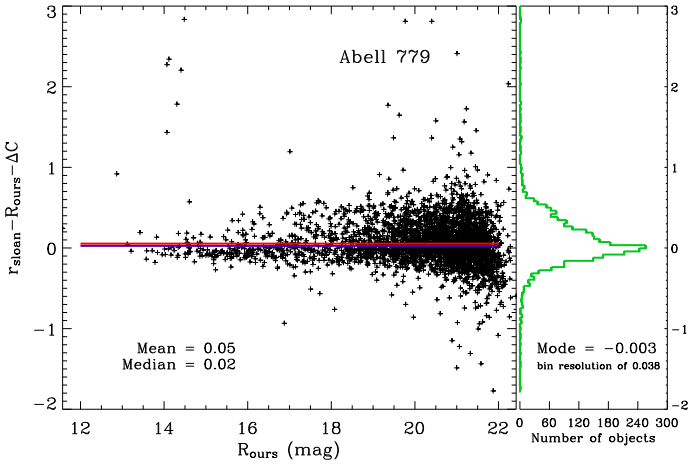

Figure 5.13:: On Y-axis is represented the subtraction of our R magnitude to the r magnitude from SDSS. X-axis is showing that subtraction along the R magnitude. To the right a histogram is used to describe the MODE. Red line is marking the *mean* and blue line is marking the *median*.

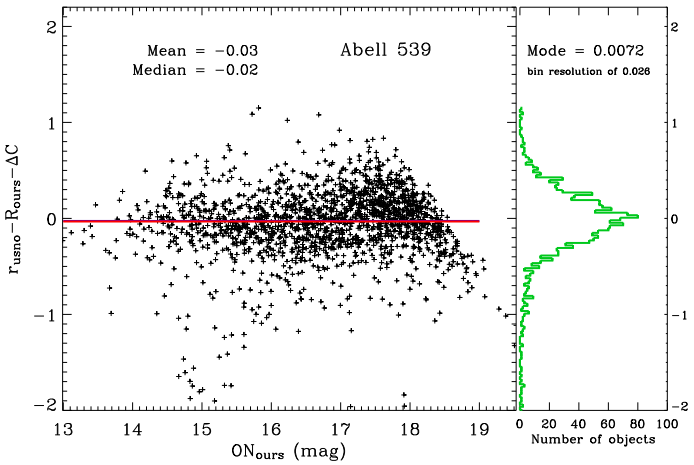

Figure 5.14:: On Y-axis is represented the subtraction of our R magnitude to the r magnitude from USNO. X-axis is showing that subtraction along the ON magnitude. To the right a histogram is used to describe the MODE. Red line is marking the *mean* and blue line is marking the *median*.

CHAPTER

6

Hα EMITTING CANDIDATES.

6.1 Configuring Parameters for SExtractor

Finding sources, determining their sizes and measuring fluxes and other scientific computation in astronomical images entails several strict considerations that should permit further empirical astrophysics working out.

SExtractor (Source Extractor) is a powerful code for extracting characterizing and measuring sources on science images, very extended in the astronomical community. To know more about SExtractor please see Bertin & Arnouts 1996. Here, we want to detach some of the main properties of the code or at least the most interesting for our purposes.

Basically, SExtractor delimits the position and extension of the objects by applying a convolution kernel[1] to the whole image yielding a smoothed image. After this, on the smoothed image, area and shape of objects over the THRESHOLD fixed are identified and fitted in a handful of ways: isophotal, auto, and isophotal corrected (elliptical). Among these fits the most suitable will be called BEST by SExtractor. Then flux inside the fit is measured on the original image. While, if LOCAL mode is enabled, sky/background is estimated using a median-mode approach on corone around the object circumscribed on

[1] This kernel should be similar to the stellar fwhm in order to enhance the "true" shape of the source and being efficient in delimiting the integration area.

a box (=BACK_SIZE which size is given by the user) in the original image. In addition to the flux, background and shape parameters, the SExtractor output catalogue can contain as many columns as rows are uncommented in the "default.param"[2] file. These explanations ought to be taken as a sketchy description of what SExtractor really do.

Next I want to move on a brief description of few parameters applied that SExtractor needs as an input through the "default.sex" file. The strategy here described were designed to be effective on images normalized to the integration time, is to say, with counts per second.

Our survey was planned to be deep, hence a deep extracting machine is needed. However we considered to run SExtractor THRESHOLD up to 1.5 (in background standard deviation units) too much spurious detection is produced. Then after few tests (see §5.5), we used the value 2.5. We fixed the ANALYSIS and DETECTION threshold to this number and MINIMUM AREA was adequated to the minimum disc ocupied by a star which is $(\pi \cdot (r^*_{FWHM})^2)$ [3]. Thus a stellar FWHM of ~ 1.0" (3 pixels diameter) would imply a MIN_AREA of ~ 7.1 pixels, but at this extreme case we did prefer to fix a bigger minimum area limit such as 10 pixels.

```
#-------------------------------- Extraction ----------------------------------
DETECT_TYPE      CCD             # CCD or PHOTO
FLAG_IMAGE       flag.fits       # filename for an input FLAG-image
DETECT_MINAREA   10              # minimum number of pixels above threshold
DETECT_THRESH    2.5             # <sigmas> or <threshold>,<ZP> in mag.arcsec-2
ANALYSIS_THRESH  2.5             # <sigmas> or <threshold>,<ZP> in mag.arcsec-2

FILTER           Y               # apply filter for detection (Y or N)?
FILTER_NAME      gauss_1.5_3x3.conv # name of the file containing the filter

DEBLEND_NTHRESH  6               # Number of deblending sub-thresholds
DEBLEND_MINCONT  0.01            # Minimum contrast parameter for deblending
```

The filtering carried out by SExtractor would help to enhance the signal to noise ratio for small and for low surface brightness objects, since the convolution of the image with a gaussian core with the exact dimensions of the stellar profile will blur the fake sources as well as will show up the good ones. Note that there is no available gaussian filter for seeing below 1.5" among the originals offered with the code. Nonetheless for the field of application in our images it would be enough. On one hand, DEBLENDING tools are of a relative importance in a survey at low redshift. We expect to observe galaxies with optical size ranging from few hundred parsecs to few tens of kiloparsec which put in arcsec at z

[2]File containing the output parameter column to appear in the SExtractor catalogue.

[3]Where r^*_{FWHM} is the half width at half maximum of a star profile.

~ 0.025 will cover from a pair of pixels to a hundred of pixels. Consequently, and given the crowd of cluster central parts, it is usual to have few galaxies profiles overlapping. On the other hand, Hα emission in galaxies could appear in a fragmented layout. This fact under a fine tuning of DEBLENDING tools would be interpreted as multiple detection that divides the galaxy. A serial of tests have brought us to final compromise of using a MINIMUM CONTRAST of 0.01 (in ADUs) (not much higher) and a maximum of 6 for the NTHRESH.

```
#------------------------------- Photometry -----------------------------------
PHOT_APERTURES          13.268,19.903,33.172,66.344 # MAG_APER aperture diameter(s) in pixels
PHOT_AUTOPARAMS         2.5,3.5                     # MAG_AUTO parameters: <Kron_fact>,<min_radius>

SATUR_LEVEL             40.                         # level (in ADUs) at which arises saturation

GAIN                    10434.577                   # detector gain in e-/ADU
PIXEL_SCALE             0.332                       # size of pixel in arcsec (0=use FITS WCS info)
```

Aperture photometry was intended to tabulate the magnitudes and fluxes at 2, 3, 5 and 10 Kpc diameter aperture. SATURATION level has determined for each particular frame, while GAIN is the product of the total EXPOSURE TIME by the gain of the 4th chip[4] (i.e. 3600 s x 2.9 $\sim$ 10440. e^- s/ADU).

```
#------------------------------- Star/Galaxy Separation ------------------------
SEEING_FWHM             0.82            # stellar FWHM in arcsec
STARNNW_NAME            default.nnw     # Neural-Network_Weight table filename
```

The Star/Galaxy separation output parameter is not crucial for the main scope of this work but it would be very useful for latter considerations and discrimination. This is the reason for a good determination of the SEEING_FWHM. One simple script running under IRAF was written by making use of task from *apphot* package. With this easy script (developed for working like a task with "eparam" editing page in a *cl* environment) stars in the frame are found (DAO algorithm -*daofind*) and a profile is fitted on every of them. The normalized profiles are then averaged and a <FWHM> is derived. The Neural-Network applied is the provided with the code.

```
#------------------------------- Background -----------------------------------
BACK_SIZE               256     # Background mesh: <size> or <width>,<height>
BACK_FILTERSIZE         3       # Background filter: <size> or <width>,<height>

BACKPHOTO_TYPE          LOCAL # can be GLOBAL or LOCAL

BACK_TYPE               AUTO  #
```

[4]Scaling procedure leads the ADU statistics and sensitivity relative to the central chip number 4.

Bakcground estimation could fill several pages of concerning considerations but it is not the intention of the writer annoying the reader so let say that our selection is a LOCAL background computed automatically within a box around the source which size (BACK_SIZE is fixed for the whole image) needs to be balanced between the size of the biggest not-spurious source and the fact that when reaching a threshold the effect of this operation is to smooth the image spreading out light of the source and contamining the estimation of the local background with light coming from the closest sources.

```
#-------------------------- Memory (change with caution!) --------------------------
MEMORY_OBJSTACK    65000    # number of objects in stack
MEMORY_PIXSTACK    1700000  # number of pixels in stack
MEMORY_BUFSIZE     8192     # number of lines in buffer
```

Given the amount of objects retrieved ($\sim$ 5000) by SExtractor on 1 WFC frame ($\sim$ 6200x6200 pix^2) the memory needs to be adjusted with certain, let say, surplus space.

6.1.1 Unresolved sources

We pointed out the chance of loosing compact galaxies that being unresolved in our frames would be misclassified by the S/G parameter in SExtractor and consequently rejected as stars in the process. This was first suggested by Andreon & Cuillandre 2002. In order not to miss possible candidates we accounted for stars together with the galaxies and no classified objects (those with a $0.2 < S/G < 0.8$) preserving the S/G information about it.

This conservative consideration did result in the production of very large catalogues. Saturated or trunked objects, and also those too near the edge of the image were dropped out the catalogue. After some needed characterizing conditions, for instance a magnitude limit, to preserve the quality of the results the sizes of catalogues become easier to deal with.

Probably this kind of sources, the unresolved ones, represents the main arguments to make use of SExtractor given the simplicity in extracting point-like objects deeply just by adjusting appropiately the set of params.

6.1.2 Systematic effects

Next I would like to comment a foible in the photometry measurement feature the Bertin's code. SExtractor could measure the flux enclosed by a number of object size definition: ISOPHOTAL, ISOPHOTAL CORRECTED, APERTURE and AUTO. ISOPHOTAL photometry define the object limits by using

the background and the input threshold, while ISOCOR (ISOPHOTAL CORRECTED) corrects the isophotal definition for a loss of flux/area suppossing a gaussian profile. APERTURE mode uses a radius to fix a circular region around the object where the integration of counts takes place. Last mode, AUTO, defines a kron-like elliptical aperture for the object. Usually, ISO or AUTO fluxes and magnitudes are saved as BEST, except when the influence of nearby sources exceed the 10%, then ISOCOR is saved as BEST[5]. The aim of commenting this capabilities of SExtractor is to remark that at low surface brightness the kron definition according to this code loses an important amount of light (up to the 40-50%). This foible for faint objects (galaxy-type) is already declared by Bernstein, Freedman, & Madore (2002) and e. g. by large surveys as the *Faint Galaxies in Deep Advanced Camera for Surveys Observations* by Benítez et al. (2004) where a light leak of the 50% for fainter galaxies is pointed out.

Hence, we should claim for a careful consideration of faintest magnitudes stated in this work. Nonetheless, given the constrains and considerations prior to execution, we make extensive use of the Source Extractor machine and we can rely on the results here presented.

6.1.3 Colour-Magnitude Diagram

The colour-magnitude diagram would suppose a very useful tool for selecting candidates to be Hα emitters in our frames. But, CMD would need a supporing criterium that makes of the selection a complete list of candidates to the fixed appropiate limits. Based on our filter set (ON and OFF bands) The emission colected through the ON filter is

$$F_{ON} \;=\; C_s \int [F_{cont}(\lambda) + F_{H\alpha}(\lambda)\ \delta(\lambda - \lambda_{H\alpha})]\ T_{ON}(\lambda)\ d\lambda \qquad (6.1)$$

Whilst for the OFF filter

$$F_{OFF} \;=\; C_s \int F_{cont}(\lambda)\ T_{OFF}(\lambda)\ d\lambda \qquad (6.2)$$

Where

[5]from the guide: *DON'T PANIC. Source Extractor for dummies.* B. W. Holwerda

$\mathbf{C}_s$ is the inverse of calibration constant for the system ($erg\ (cm^{-2}\ s^{-1}) \rightarrow ADU/s$)

$\mathbf{F}_{cont}(\lambda)$ is the flux density ($erg\ cm^{-2}\ s^{-1}\ \text{Å}^{-1}$) and can be taken as the continuum height throughout the spectral range considered.

$\mathbf{F}_{H\alpha}(\lambda)$ is the flux density on the Hα line ($erg\ cm^{-2}\ s^{-1}\ \text{Å}^{-1}$). In this rationale, this line is assumed to be infinitely thin ($\delta(\lambda - \lambda_{H\alpha})$).

$\mathbf{T}_{ON}(\lambda)$ accounts for the ON filter transmittance as function of wavelength (s.u.).

$\mathbf{T}_{OFF}(\lambda)$ same for the OFF filter.

Resulting fluxes[6], F_{ON} and F_{OFF}, are shown in ADU/s.

Working in magnitudes,

$$m_{OFF} = -2.5\ log\,(F_{OFF}) + \mathbb{C} \tag{6.3}$$
$$m_{ON} = -2.5\ log\,(F_{ON}) + \mathbb{C} \tag{6.4}$$

And now, building the colour

$$m_{OFF} - m_{ON} = -2.5\ log\left(\frac{F_{ON}}{F_{OFF}}\right) \tag{6.5}$$

For computing the errors we must work in electrons (photoelectrons), then, noting that the OFF filter calibration is scaled to the ON filter by the mean ratio of the stars fluxes in the field (see §5.6);

$$< \int F_{cont}(\lambda) T_{ON}(\lambda) d\lambda > \simeq < \int F_{cont}(\lambda) T_{OFF}(\lambda) d\lambda > \tag{6.6}$$

and assuming then a constant height of the continuum flux throughout the filters width ($\rightarrow F_{cont} \neq F_{cont}(\lambda)$), this F_{cont} can exit of the integral, and it

[6]From convolution between SED and filter transmittance profile which area is $A_F(ON) = \int_{ON} T_{ON}(\lambda)\ d\lambda$

would be a good approach to write,

$$\begin{aligned} m_{OFF} - m_{ON} &= -2.5\ log\left(\frac{\int [F_{cont}(\lambda) + F_{H\alpha}(\lambda)\ \delta(\lambda - \lambda_{H\alpha})]\ T_{ON}(\lambda)d\lambda}{\int F_{cont}(\lambda)\ T_{OFF}(\lambda)d\lambda}\right) \\ &= -2.5\ log\left(\frac{\int F_{cont} T_{ON}(\lambda)d\lambda}{\int F_{cont}\ T_{OFF}(\lambda)d\lambda} + \frac{\int F_{H\alpha}(\lambda)\ \delta(\lambda - \lambda_{H\alpha})\ T_{ON}(\lambda)d\lambda}{\int F_{cont}\ T_{OFF}(\lambda)d\lambda}\right) \\ &\simeq^{(6.6)} -2.5\ log\left(1 + \frac{\int F_{H\alpha}(\lambda)\delta(\lambda - \lambda_{H\alpha})\ T_{ON}(\lambda)d\lambda}{F_{cont}\int T_{ON}(\lambda)d\lambda}\right) \end{aligned} \tag{6.7}$$

and therefore, directly,

$$m_{OFF} - m_{ON} = -2.5\ log\left(1 + \frac{F_{H\alpha} T_{ON}(\lambda_{H\alpha})}{F_{cont}\ A_F(ON)}\right) \tag{6.8}$$

Moving on the first expression for the colour and extracting the fraction, we can compute the appropiate errors,

$$\Delta\frac{F_{ON}}{F_{OFF}} = \left|\frac{\partial\ \frac{F_{ON}}{F_{OFF}}}{\partial\ F_{ON}}\right|\ \Delta F_{ON} + \left|\frac{\partial\ \frac{F_{ON}}{F_{OFF}}}{\partial\ F_{OFF}}\right|\ \Delta F_{OFF} \tag{6.9}$$

$$\Delta\frac{F_{ON}}{F_{OFF}} = \frac{\sigma\left[F_{ON}\right]}{F_{OFF}} + \frac{F_{ON}\ \sigma[F_{OFF}]}{{F_{OFF}}^2} \tag{6.10}$$

Knowing that,

$$\Delta F_X = \sigma\left[F_X\right] = \sqrt{(F_X^{obj} + F_X^{sky}\ S)\ G\ T + S\ N^2} \tag{6.11}$$

Where

F_X^{obj} Flux in ADU/s coming from object on filter X (ON or OFF).

F_X^{sky} Flux in ADU/s coming from sky on filter X.

S Integration surface in pixels.

G Gain of the system in e^-/ADU.

T Integration time (s).

N Readout noise in e^-.

Arriving to

$$\sigma\left[\frac{F_{ON}}{F_{OFF}}\right] = \frac{\sigma\left[F_{ON}\right]}{F_{OFF}} + \frac{F_{ON}\ \sigma[F_{OFF}]}{F_{OFF}^2} \tag{6.12}$$

hence

$$(m_{OFF} - m_{ON})_{\pm n\sigma} = -2.5\ log\left[\frac{F_{ON}}{F_{OFF}} \mp \mathbf{n}\left(\frac{\sigma\left[F_{ON}\right]}{F_{OFF}} + \frac{F_{ON}\ \sigma[F_{OFF}]}{F_{OFF}^2}\right)\right] \tag{6.13}$$

If we do not limit the minimum observable equivalent width[7] we will have

$$\frac{F_{ON}}{F_{OFF}} = 1 + \frac{F_{H\alpha}T(\lambda_{H\alpha})}{F_{cont}\ A_F(ON)} \tag{6.14}$$

From $EW(H\alpha) = \frac{F_{H\alpha}}{F_{cont}}$ if $EW(H\alpha) \longrightarrow 0$ [8] then detection, on the colour-magnitud diagram, would be restricted by

$$(m_{OFF} - m_{ON})_{\pm n\sigma} = -2.5\ log\left[1 \mp \mathbf{n}\left(\frac{\sigma\left[F_{ON}\right]}{F_{OFF}} + \frac{F_{ON}\ \sigma[F_{OFF}]}{F_{OFF}^2}\right)\right] \tag{6.15}$$

Which could be rewritten as follows

$$\begin{aligned}(m_{OFF} - m_{ON})_{\pm n\sigma} = -2.5\ log\Bigg[1 \mp \frac{\mathbf{n}}{G\ T}\Bigg(&\frac{1}{F_{OFF}}\sqrt{(F_{ON}+F_{ON}^{sky}\ S)GT+SN^2} + \\ &+ \frac{F_{ON}}{F_{OFF}^2}\sqrt{(F_{OFF}+F_{OFF}^{sky}\ S)GT+SN^2}\Bigg)\Bigg]\end{aligned} \tag{6.16}$$

Let see an application to our particular case: the Wide Field Camera at the INT with the ON-band (Hα redshifted) filter. This set shows the following characteristics,

Leaning on real data from our observables, we did model the approach be-

[7] Definition in order to it would be the method and the system what put lower limits on the detectable equivalent width that, obviously, it never will be zero.

[8] This is a reasonable supposition for the most sources since the term $\frac{F_{H\alpha}T(\lambda_{H\alpha})}{F_{cont}\ A_F(ON)}$ is lower than 1 for equivalent widths inferior to 100. This value corresponds aproximately to the ratio $\frac{T(\lambda_{H\alpha})}{A_F(ON)}$ at the redshifts for the sample.

GAIN	$2.9^{\dagger}$	e^{-}/ADU
Readout NOISE	$6.9^{\dagger}$	e^{-}/ADU
λ_{eff}	6725.96	Å
Filter Area	74.7029	–

Table 6.1:: † Values for central chip (CCD4) of WFC@INT, and ON filter.

haviour for the sources integration area according to the flux variation (in counts) and we found a simple relation $Log_{10}\ area\ \propto\ Log_{10}\ F$ that follows the general trend area-flux(sources) in counts. Taking those values from table 6.1, together with zero point calibration constant, and with extinction (see §5.2), we derived magnitudes in the Johnson-Cousins photometric system by adding $\mathbb{C} = 48.83$. Using a family of common integration times from our survey [300, 800, 1200, 3600] (s), and, finally fixing **n** at 5 we obtain figure 6.1.

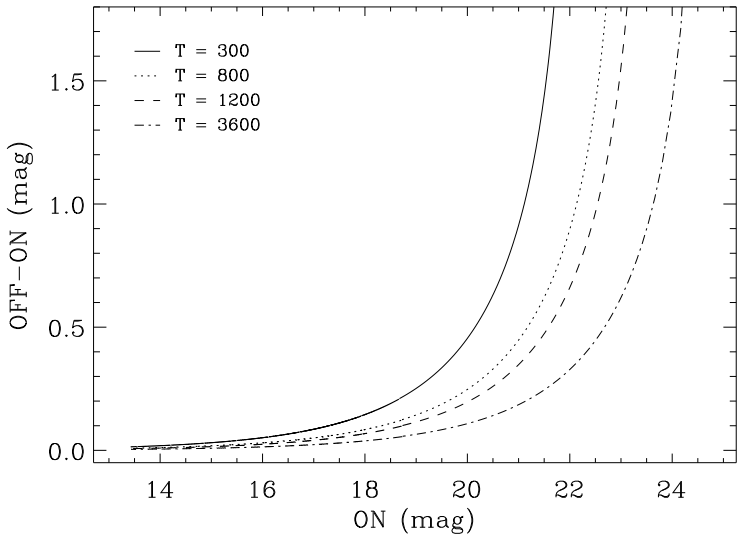

Figure 6.1:: On Y-AXIS the built colour ON-OFF; on X-AXIS the ON magnitude. Lines are representing the 5σ (of the figure ON-OFF) curve from theoretical derivation (this Section). These emitters-selecting branches have diferent asymptothic vertical reaching point. Those points (on the base -abcise- of the asymptote) are the theoretically limiting magnitudes. Note that the larger exposure time is, the higher appears the limiting magnitude.

This formalism follows the same philosophy of that from Pascual et al. 2007

but in a bit different and simplified way. According to the branchs on figure 6.1 every object lying in ordinates over the path traced by the plotted curve would be preselected as an Hα emitting candidate.

6.1.4 Preselection of candidates

This section was called "PRE"-selection of candidates because there is two cluster (Abell 634 and 779) with partial Sloan Digital Sky Survey covering that will permit a refinement in the Hα sources selection procedure. For all of those others clusters (Abell 400, 539 and 2666), this procedure would suppose the final selection step until the spectroscopic follow up will be completed.

I want to remark the complexity of detection and selection of sources in large survey frames. In our case the detection in ON and OFF band should be carefully designed to be balanced in reponse between different images. Due to few reasons, the dual mode of SExtractor were ruled out. Among these reasons the most importants are: the images do not match in X,Y positions so further measurements should not be representative; and, even though, when an approximate matching could be got, which is a very hard thing, a difference in the seeing radius (a common situation in our frames) between ON and OFF will may end in an underestimation of one of the flux (usually the OFF one). Hence SExtrator were run on ON and OFF images independently with the same configuration (given by the "default.sex" file detailed in § 6.1), we took the X, Y positions and interpreted under IRAF (with the set of task that computed the astrometry solution) we produced a celestial coordinate for every object on each band, and then we matched by (RA, Dec) the outputs resulting the final table. Nonetheless, by dodgin the bug of fluxes bad derived, another handicap appears. It could happen that a source reaches the flux threshold ($2.5\ \sigma_{bg} = 2.5$ background standard deviation) only in one of the frames. This would be concerning if the no detection take place on the OFF band. Two main cases ought to be declared here. First, when the source has been rejected by SExtractor machine during the catalogue building. This could occur if the object is blended or coincide spatially with (or it is enough near of) a cosmic ray. That type of situation would be rectified when remeasuring under IDL. Second, when the source really do not reach the flux threshold imposed. In this interesting second case, what we could be seeing is an emission-line dominated source. A procedure to confirm the nature of these important objects was performed. We recovered the X, Y info for all of them and forced to measured inside the area extracted from the recognised ON source. If the detection is lower than $2.5\ \sigma_{bg}$ then an upper limit value[9] is assumed. This kind of objects

[9] $2.5\ \sigma_{bg}\ \mathrm{A}_{sd}$, where σ_{bg} is the standard deviation of the background; and, A_{sd} is the area

will appear in the CMD with an arrow, thus stating their condition of great uncertainty in the OFF flux.

Once described the tools for selecting candidates we go to move on the data. Here we present the CMD for the pointings of Abell 2666. Table 6.2 collect the relevant figures from the selection on Abell 2666 cluster. Those numbers correspond to the points over the selection curve in figure 6.2

As depicted in §5.6 the continuum OFF band was scaled to the ON band by using the stars in the field. The width of the distribution profile of the flux ratio between OFF and ON would help us to limit spurious detection near the selecting upper "branch" in the colour-magnitude diagram. This criterium (univoque for each cluster frame field) is added to $m_{OFF} - m_{ON})_{-\mathbf{n}\sigma}$ curve like a vertical shift into the colour-magnitude diagram. This number is tabulated on column (3) of table 6.2 for this example cluster Abell 2666.

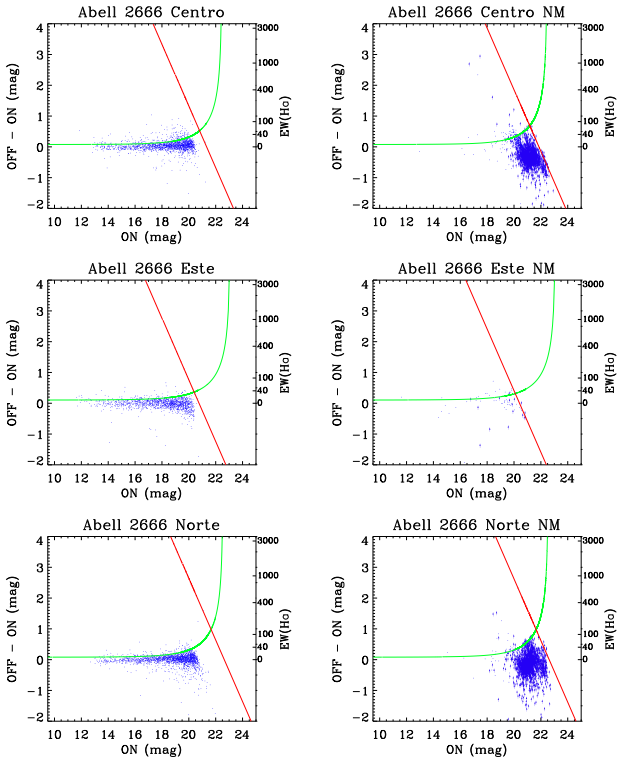

Figure 6.2:: From top to bottom pointings of Abelll 2666 Center, East and North. Right column shows the CMD for objects remeasured with IDL.

of the Seeing Disc (sd)

Pointing Name (1)	**T** (2)	**S** (3)	$\mathbf{N}_{gal}$ (4)	$\mathbf{m}_L$ (5)	$\mathbf{ON}_L$ (6)	$\mathbf{C}_{ON}\mathbf{95}$ (7)	$\mathbf{C}_{ON}\mathbf{50}$ (8)	$\mathbf{OFF}_L$ (9)
Abell 2666 C	5.0	0.0766	216	22.41	21.28	19.97	20.29	21.32
Abell 2666 C NM	5.0	0.0766	58	22.40	23.41	20.99	21.15	21.85
Abell 2666 E	5.0	0.1042	88	23.03	20.65	18.80	19.99	20.76
Abell 2666 E NM	5.0	0.1042	14	23.02	20.78	19.98	20.54	20.41
Abell 2666 N	5.0	0.0804	124	22.49	21.91	20.21	20.51	22.64
Abell 2666 N NM	5.0	0.0804	22	22.48	27.03	21.21	21.40	22.62

Table 6.2:: (1) Name of the Pointing in the Cluster. NM indicates the CMD based on the Not Matched objects in first SExtractor step; (2) Threshold **n** on the CMD selecting curve { -2.5 Log_{10}(1-**n** $\sigma'[F]$)}; (3) Shift in magnitudes to the $(m_{OFF}-m_{ON})_{-\mathbf{n}\sigma}$ [detailed explanation on § 5.6 final part]; (4) Number of objects selected till $m_R = 20.0$; (5) Theoretical limiting magnitude. The derivation of this theoretical magnitude limit does not account for seeing efects; (6) m_{ON} limit empirical; (7) Completeness in the ON band at 95%; (8) Completeness in the ON band at 50%; (9) m_{OFF} limit empirical.

6.2 Photometry of extended galaxies.

An accurate method for measuring the extended sources photometry was developed running under *Interactive Data Language* (IDL). This few scripts allowed us to solve problems related to the complex morphology of Hα emitting sources. With this programme we measured all galaxies with known velocity and those others showing emission that are optically resolved.

A basic description of the procedure is given in the appendix C.

Correlation with IRAF photometry has been checked and we ascertained that is equivalent for objects with no companions and only a slightly different when a near source is present (see fig. 6.3).

First, we cropped the galaxies with know radial velocity in the Nasa Extragalactic Database (NED)[10] with a sky region around the object of about 2x2 arcmin. In addition, by visual inspection on NET images (result from subtracting the ON band minus OFF band astrometrically) we created a second group with all of those galaxies with traces of emission in our frames. This list of galaxies were also cropped in the same way.

Since this, the treatment has been indentical for both groups. The photometry IDL-scripts used/wrote for this purpose, first aligned the cropped images (ON and OFF); derived the center, semiaxes and ellipticity for the isophote at 3 σ_{bg} (≡ standard deviation of the background); computed the growth of

[10]This research has made use of the NASA/IPAC Extragalactic Database (NED) which is operated by the Jet Propulsion Laboratory, California Institute of Technology, under contract with the National Aeronautics and Space Administration

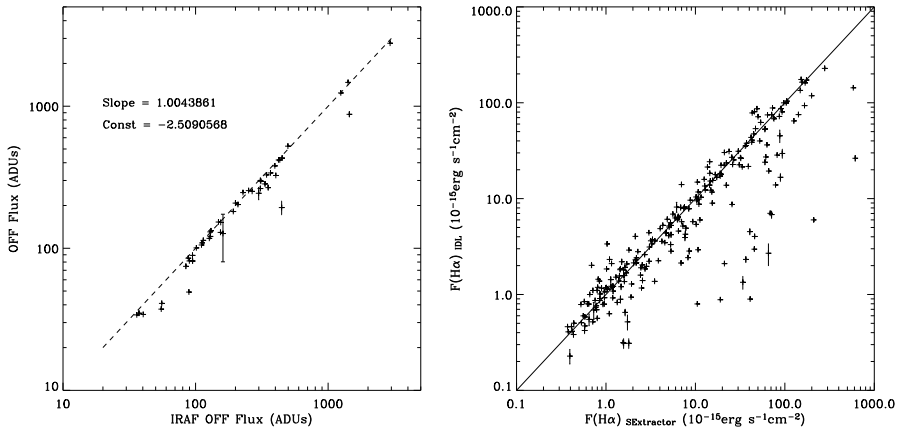

Figure 6.3:: Left: Comparison of photometry under IRAF versus our IDL-script programme. QPHOT circular apertures were used under IRAF until the convergency of the growth curve to derive the fluxes for this set of objects belonging to Abell 539. Y-axis show the obtained flux under IDL. Note that only few objects show greater fluxes on IRAF than according to the IDL-script. These few objects are affected by light contamination by close companion. Right: Comparison of photometry under SExtractor versus the IDL-script used for extended sources. SExtractor has a more power tool for deblending and it can be seen that measures with IDL - which avoids companions - leak flux in objects with a close projected companion.

light curves for OFF and Hα (= ON minus OFF) fixing the integration radius where the convergency is achieved; integrated the counts within this ellipse on both images; derived a natural source of undetermination by introducing small variations in the centering process and the definition of the ispohote; extracted a radial (elliptical) profile and the petrosian radius for a Fp = 0.2; saved all values (including sky determinations in both filters).

Galaxies with V_r known

This set of objects presents a wide range of types and properties. Choosing the galaxies with radial velocity in a determined sky region ought not imply a bias in the selection but it already means we are adopting the previous bias when the spectroscopy was done on those galaxies. Then it is worth noting that the fact of whether a galaxy has assigned a radial velocity, indicates that this galaxy has been interesting for someone in someway. Thus if unbiassed, this selection would yield an heterogeneous group of galaxies showing different optical properties, but in practice we are usually choosing the biggest or brightest (or others "est") galaxies in the cluster.

We launched a searching in the NASA Extragalactic Database (NED) with

an enclosed radius enough to contain the area covered of cluster, and velocity within $v_{cluster} \pm 1500$ km s^{-1}. The output lists were called NED lists. Taking these NED lists of objects, classified as galaxies, within 120 arcmin search radius we are retrieving near the 30 percent of the objects with know recesional velocity of the clusters.

From this part of the work we expect a small fraction of the number of "NED" galaxies in our frames, for being Hα emitting candidates. Next chart (table 6.3) summarizes our findings.

Cluster	**NED Number (IOF†)**		**Hα fraction††**
Abell 400	122	(30)	15
Abell 539	164	(48)	31
Abell 634	111	(23)	21
Abell 779	177	(55)	36
Abell 2666	90	(30)	20

Table 6.3:: First column: cluster name; second column: number of galaxies in NED with $0.015 < z < 0.035$ and search radius 120 arcmin from cluster center; third column (parenthesis): † IOF = In Our Frames; fourth column: fraction of galaxy retrieved (column 3) that is candidate to be Hα emitting (†† the condition to be Hα emitting object imposed upon the previous column is to verify that the F(Hα) were 3 times greater than its uncertainty).

What can be seen from table 6.3 is that the fraction of Hα emitters[11] is over the 50 % except for Abell 400 where we do not look for Hα emitters by visual inspection. A priori this percentage could suggest that the NED catalogues coulb be biassed to Hα emitting objects.

Others emitting sources

From the final mosaiced images ON and OFF, through a simple task developed for this purpose *WCSNET*, we get the Hα NET images by substracting attending at the WCS. In this Hα+[NII] image (decontamination is described in §5.3.3 then for simplicity hereinafter it will be referred as Hα) emitting sources are easily showed up by a visual inspection. Marking and saving the positions, a catalog of emitting sources was created. When a match with the NED list occurs, the object dropped from this list. Hence, this list could be called the NO_V ("no velocity") list.

The individual objects were cropped and treated in the same way like described in 6.2, although in some cases the object considered could appear compact or not resolved.

[11] Here, be "emitter" simply means that those objects show $F(H\alpha) > 3\in_{F(H\alpha)}$.

A graphic example of a NO_V emitting galaxy in the region of Abell 539 (catalog name 2MASX J05152893+0700188) is shown in figure 6.4.

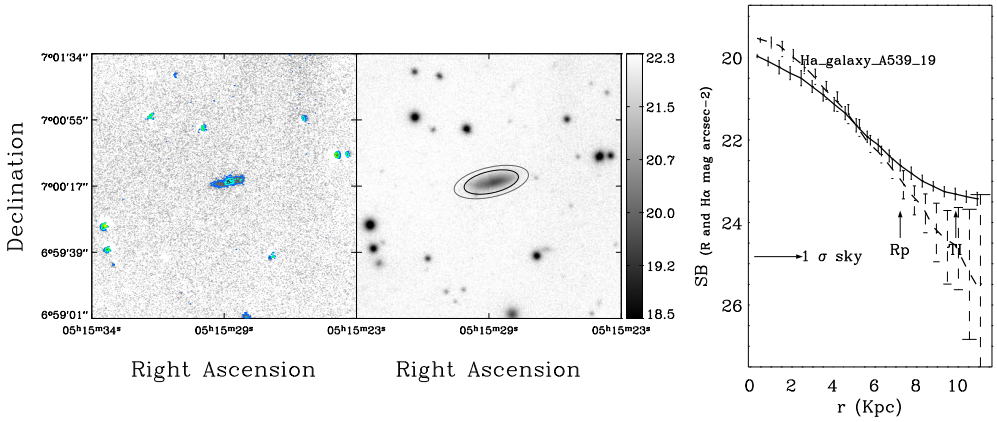

Figure 6.4:: This galaxy known in the archives as 2MASX J05152893+0700188 has no a catalogued radial velocity and presents an interesting structure in its Hα emission. Left pannel represents the pure Hα+[NII] emission, where lightblue contours follow the peaks of the possible Hα knots; central pannel shows the continuum emission; right pannel shows the light curve profile for the continuum (solid line) and continuum+Hα (dashed line). The sky bright is marked as well as the total integrations radius (Ti) and the Petrosian radius (rp).

The catalogs are "alive", everyday a change can happens, then at the moment of starting of these studies only a handful of velocities for galaxies in the Abell 634 area were known, but, nowadays, many redshifts have been published since the Sloan Digital Sky Survey has covered the South part of the cluster. Something similar would described what happened to clusters like Abell 539 to which belongs the galaxy of the figure 6.4. Here, some figures and values of the considered NO_V objects at the moment of the beginning of this study are presented on table 6.4.

Cluster	$\mathbf{N}^t_{NOV}$	$\mathbf{N}^e_{NOV}$	**Log EW(Hα)**
Abell 539	65	63	1.44
Abell 634	148	141	1.31
Abell 779	67	65	1.26
Abell 2666	32	29	1.16

Table 6.4:: First column: cluster name; second column: number of emitting galaxies in NOV (no velocity sample) collected in our frames; third column: median of the logarithm of the equivalent width of Hα; fourth column: standard deviation of the logarithm of the equivalent width of Hα. Here, again, the mathematic definition of being emitter is to show a flux over 3 times the uncertainty.

6.3 Morphological Parameters: Concentration and Asymmetry

One of the advantages of this Hα Imaging Survey is the capability to discern parts, structure and "taxonomy" of the emission. Star formation taking place in the normal arms of a late type galaxy distinguished from a single giant burst at the nucleus/core of a early disc-like galaxy information gains an extra value that complete the meaning of a equivalent width computed all over the object. Therefore concentration and asymmetry will be computed on every visual-selected galaxy. Next, few technical details on the computational requirements for deriving of the concentration and asymmetry will be explained.

6.3.1 Asymmetry

Computing the asymmetry of an extended sources has become a highlighted tool for classifying galaxies. Such others useful definitions, it needs a considerable amount of prior requisites. Among this requisites we go to remark two: centering and background contribution to the asymmetry. These two special figures should be determined precisely, because they are fundamental sources of error to the final asymmetry value. Center estimation is crucial in asymmetry derivation, cause a new whole rotated object defintion will be hold to it. Thus a change by just 1 pixel in the Frei et al. (1996) sample can vary the value of asymmetry by as much as 50% (Conselice et al. 2000).

Let me introduce the two definitions for the asymmetry computed upon our sample. Few authors have already published valid definitions for the asymmetry (Abraham et al. 1996; Conselice 1997; Conselice et al. 2000; Lauger et al. 2005; see Yagi et al. 2006 for a brief review on its Apendix). Then, why a new? in fact, these definitions actually, are not new definitions but an adoption[12] and adaptation[13] to our data for extracting a compatible universal procedure for deriving the asymmetry.

To infer a good asymmetry param is primarily needed to know the center of the object and to be able to shift it to the closest vertex of pixel. This is required by a correct matching between the original and the rotated image. Therefore a gaussian kernel with σ roughly equal to that of the point spread function (PSF) of the night was convolved to the original image. Then, if nucleated, an

[12]The first definition appears in Conselice et al. (2000); while the second one is taken from Lauger et al. (2005)

[13]The previous treatment of data is an adaptation of the Conselice et al. (2000) and of the Yagi et al. (2006)

isophotal ellipse is fitted to a high level of counts on the OFF (≡ continuum) image (usually 200 times the standard deviation of the background), and the center of the ellipse is assumed to be the center of the source. Otherwise (if not nucleated) the same fitting is performed at a lower isophotal level. Only if the shift to the closest vertex is greater than 0.1 pixel[14], the two dimensional shifting (by interpolation) will be done. Now, the center of the object is well known and it is where we wanted. The gaussian-smoothed image is also used to determine the pixels of the background that are disposable within the image limits. The same amount of pixels in the object area is taken among the nearest pixels to the object that are representative of the background (≡ below 2.5 times the σ_{bg}). This array is called the patched sky, and it will serve to compute the contribution of the background to the total asymmetry. Finally, to be able of proceeding we must assure there is no contamining objects within the rotation area. Patching blended objects is not a trivial operation, but for objects relatively outer the light profile of the concerning object a procedure were developed (see §4.2).

Implementation of all these features a more others serving to the purpose of the asymmetry calculation have been written in IDL language (see a more complete description in Apendix D).

First definition is

$$\mathbb{A}_s = \frac{\sum \left| I^\theta - I \right|}{2 \sum |I|} - \mathbb{A}^s_{bg} \tag{6.17}$$

where

$\mathbb{A}_s$ Desired asymmetry;

I is the pixel intensity for the original image;

I^θ is the pixel intensity of the rotated image;

θ is the rotation (180^0); and

$\mathbb{A}^s_{bg}$ Contribution of the background to the asymmetry which is equal to $\frac{\sum |N^\theta - N|}{2 \sum |I|}$ beign N the background intensity pixel by pixel in an area equivalent to the covered by the source.

[14]We considered unefficient make shiftings below this limits because a 2D interpolation of the image could produce uncontrollable sources of errors

The second definition of asymmetry computed is

$$\mathbb{A}_l \quad = \quad \frac{\sum^{I^\theta > n\sigma_{bg}} \left| I^\theta - I \right|}{2 \sum I} - \mathbb{A}^l_{bg} \tag{6.18}$$

where, there are common items with the first definition, and the rest are:

$\mathbb{A}_l$ Desired asymmetry;

σ_{bg} background standard deviation;

n is a threshold in σ_{bg} units, for masking the rotated image;

$\mathbb{A}^l_{bg}$ Asymmetry of the background $\frac{\sum |N^\theta - N|}{2 \sum I}$ beign N the background intensity in an area equivalent to the covered by the source.

Since our purpose is to make general as possible our results, our asymmetry definitions have been applied to the Frei et al. (1996) r-Band images of his sample as a control sample in order to compare with others authors. Figure 6.5 shows the result of this comparison with the definitions used by Conselice in 1997 and 2000, which are $\sqrt{(\frac{\sum (I^{180} - I)^2}{2 \sum I^2})}$ and $min(\frac{\sum |I^{180} - I|}{\sum I}) - min(\frac{\sum |N^{180} - N|}{\sum I})$ respectively. In Conselice (2003), the authors revisited the treatment following the same prior definition.

Definitions of the asymmetry in Conselice et al. (2000) ranges between 0 and 2, this is the reason why in figure 6.5 appear divided by two. Others comparisons were tested through the relationships given in Yagi et al. (2006) finding similar correlation and scatter. Once tested the self-consistency and the validity of the computational method for the derivation of the asymmetry, the same procedures were applied to "NED" and "NO_V" sample list for every cluster. Tables and results can be seen at §7.3.1.

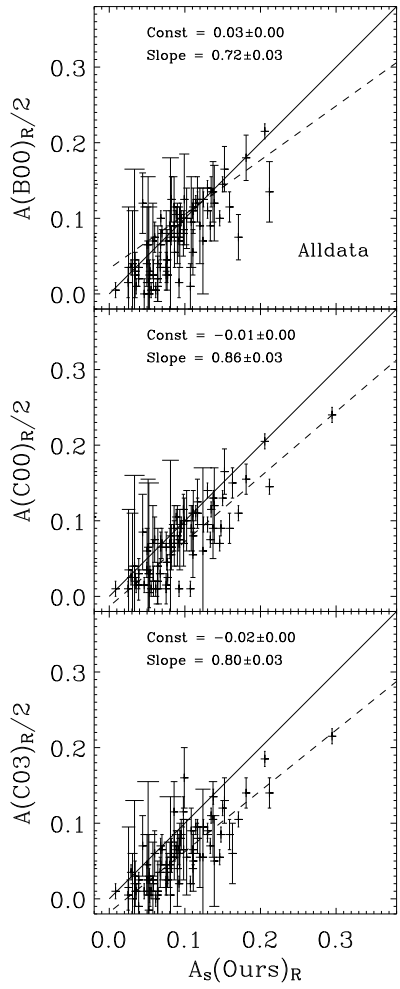

Figure 6.5:: A_s asymmetry param computed for this survey is on abscise. On Y-axis from top to bottom Bershady et al. (2000) asymmetry and Conselice's asymmetries 2000, and 2003 are plotted. Note that the $A(B00)_R$, $A(C00)_R$ and the $A(C03)_R$ are divided by two in order to be comparable with our calculations. Solid line represents the straight line of slope 1. Dashed line represents the best linear fit to the data.

6.3.2 Concentration

Concentration provides a partial measurement of the compactness of the light. Obviously, together with the total flux, it also bring information of the distribution of the light in a composite axial symmetry reference system of the 2D real object, is to say, a indirect way to know the light profile.

Concentration parameter, like asymmetry, needs some previous considerations, but with noticeable differences. First of requirements is to know the real total flux. Unlike the asymmetry, the concentration has to be referred to the total flux[15]. Nonetheless, assuming a "real total" flux is, at the moment, still harder than limiting the integration radius. Favoured by our measuring procedure, we planned the computation of the concentration till the radius defined in 6.2. Hence, despite of concentration should be easier implemented we advice that comparison will be subordinated to the "total" flux definition. Apart of the referring flux, a good center, the sky substraction, derive the concentration requires a good parametrization of the shape: the ellipticity. It is evident that if any of these inputs are wrongly introduced in the script the result will not be reliable. The output center and ellipticity from the asymmetry computation were used to infer the concentration.

Two concentration parameters were computed. According to Bershady et al. (2000) (also used by Conselice et al. (2000); Conselice (2003) and Lauger et al. (2005))

$$\mathbb{C}_S = 5 \cdot Log(\frac{r_{80}}{r_{20}}) \tag{6.19}$$

and to make our result useful as much as possible, we also computed another extended concetrantion index defined as

$$\mathbb{C}_L = \frac{r_{90}}{r_{50}} \tag{6.20}$$

This second definition for the concentration is an instrumental derivation that can be obtained automatically as an output from SExtractor. We only derived it for extended emitting galaxies.

Thus, as explained above, these definitions depends on the total flux what corresponds to an integration radius. Under the procedure established for this survey, the radius at which the integration gets meanning, is reached where the curve of the light profile converges. On the other part, the integration

[15] Asymmetry could be derived upto a partial radius (50% or 80% of the total flux) yielding a plenty of meanning figure which is used in Conselice et al. (2000) to compare with more distant objects derivation of the asymmetry, where the low surface brightness of the galaxy is lost

radius for the Bershady et al. (2000) and Conselice (2003) is fixed basing on the bright ratio $\eta = I(r)/ < I(r) >$. So taking into account this, we can expect some differences between both concetrations calculations according on the surface brightness profile of the galaxy problem. Figure 6.6 shows the resulting comparison bewteen procedures for the calculation of concentration over the r-Band images from Frei et al. (1996) sample.

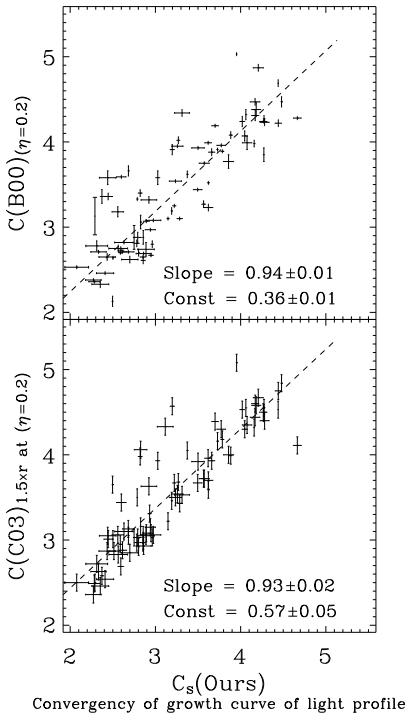

Figure 6.6:: Comparison between the two computational method on inferring the concentration based on the same definition. Please, note that the difference showed by the Y-cut and slope, are mainly due by the different integration radius.

The total agreement bewteen computations could be reached by redefining the integration radius where the "total flux" is achieved. Some authors think that the total flux recoverable from a source is reached at 2 or 3 petrosian radius.

Nonetheless other considerations, under the prescriptions described by this work we are in place of extending our results, since they seems comparable (precision and sensitivity) and consistent (tendency) with the studies in the literature.

CHAPTER

7

THE NEARBY CLUSTERS OF GALAXIES Hα IMAGING SURVEY.

PART I

7.1 Properties of Hα emission within the Clusters.

7.1.1 A census of sources. Distributions.

In the present section, we firstly checked the brightness depth of the survey on every clusters and general behaviour of some quantities as the Equivalent Width of Hα, and how it is distributed.

Figure 7.1 shows the different frequency distribution of the R Cousins magnitude for the Hα emitting sources encountered in each cluster, as well as the possible contamination by stellar population. These point-like sources have not been removed from the main catalogue in order not to lose cluster member sources not resolved. That kind of "decontamination" needs for spectroscopical follow-up.

As seen in the chapter 3 clusters Abell 634 and Abell 779 reach a deepest limiting magnitude thanks to the better point spread function (narrower) on their science images (See figure 7.1). Therefore, we find fainter sources in the R-band for Abell 634 and Abell 779 than for the others clusters.

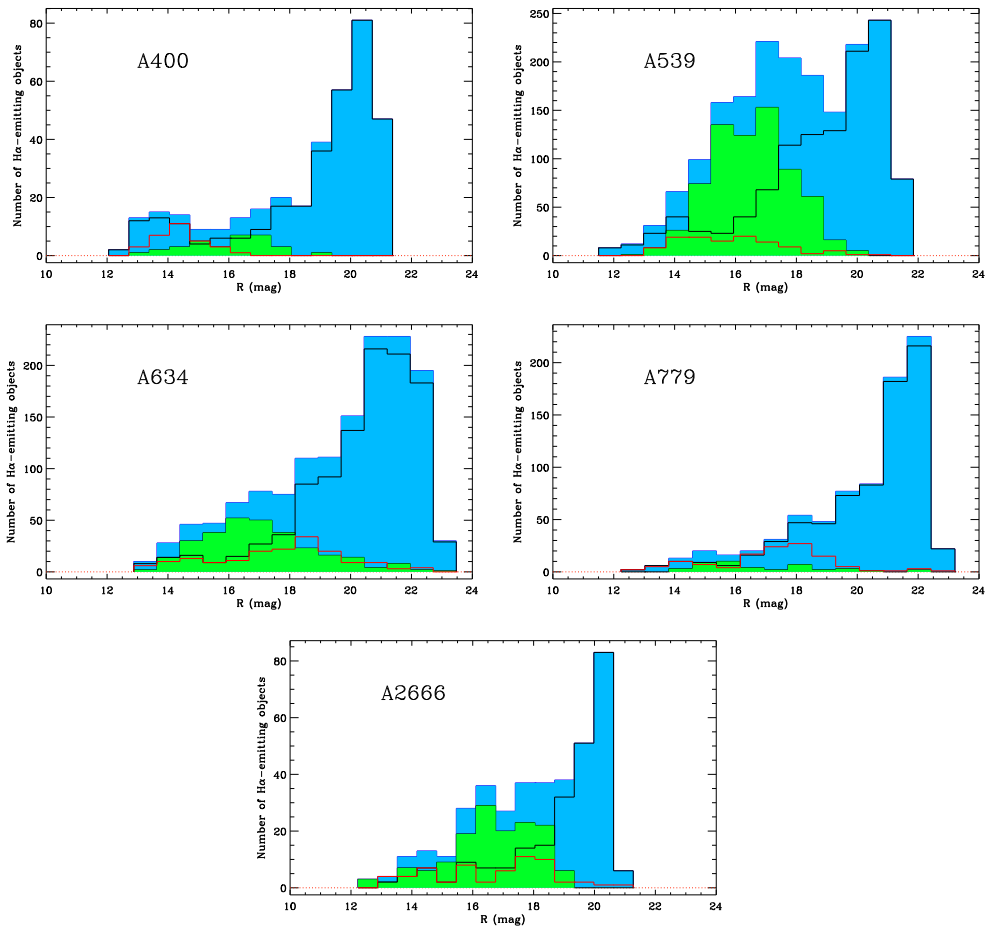

Figure 7.1:: Histograms for the distribution of the apparent Johnson R magnitude among the confirmed Hα emitting objects for every cluster separately.

Apart from this, all clusters show similar behaviour with an exponential increasing distribution with magnitude except Abell 539 cluster which presents a relative maximum peaking at 18 R mag. This apparent bimodal distribution is due to the high contamination, the greater one among our clusters, coming from field stars (light green body distribution on fig. 7.1), since this cluster is on the galactic plane.

The expected amount of stars contamining the catalogue of emitting objects is proportional to the number of sources detected and classified as stars by SExtractor (S/G separation). In turn, distribution of stars given by TRILEGAL[1](Girardi et al. 2005) is in agreement with the amount of point-like objects encountered in our R-catalogues for each cluster according to their Galactic latitud and covered area. Here in after, in this section, in order to avoid confusing results, the point-like objects classified by SExtractor will not be included in the analysis (graphs) although that concerned Hα positive sources have been fully considered as candidate for a spectroscopic follow-up and have been added to the final catalogue with an appropiate internal flag.

The limiting magnitude reaches R $\sim$ 21 mag in any case, and it can be considered complete up to R = 20, but for simplicity and some reasons explained in §7.1.3 and, overall, in order to be able to compare quantities among the clusters in the sample, further analysis in this section will only consider bright sources up to R = 19 mag. This assures us to have a complete and well defined sample of galaxies in every cluster, as well as to keep the total sample of clusters in the same way, complete, homegeneus and consistent. Nonetheless the catalogue will keep all recovered detections.

Histogram distribution of EW(Hα) for detected sources are presented in figure 7.2. In that figure what can be seen is the distribution of the equivalent width of Hα for the emitters found in our sample of clusters excluding the point-like detections, up to R $\simeq$ 19 mag, and normalized to the maximum. Overplotted with dashed-line the scaled (to the height of the figure) distribution for 334 galaxies in the field (James et al. 2004) presents an EW at their peak, greater than for most the clusters in our sample. However, we also see two clusters, Abell 539 and 400, presenting a very similar statistic *mode* and full width at half maximum than the field within the range of compatibility permitted by the binwidth. In this way we can distinguish two families (or three) among the selected clusters, according to the mode of its equivalent

[1]A model of spatial distribution and magnitudes for stars in the Galaxy. URL *http://trilegal.ster.kuleuven.be*

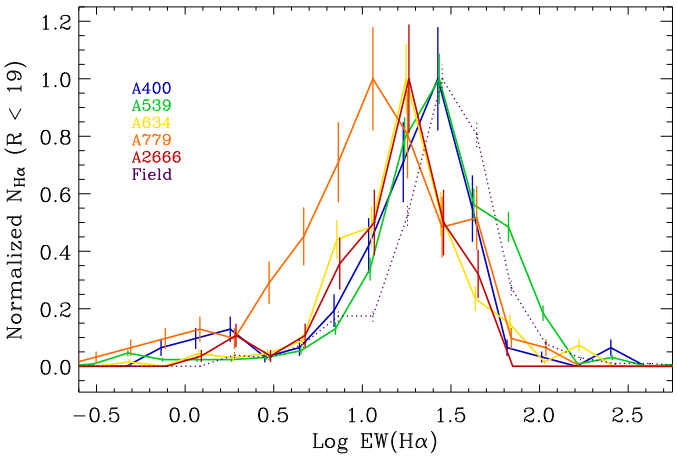

Figure 7.2:: Frequency distribution of the Logarithm of the EW(Hα) (BIN $\sim$ 0.17) for galaxies in the cluster sample covered up to R = 19 mag. Abell 400 is represent by the blue solid line; Abell 539 is on green; Abell 634 is on yellow; Abell 779 is on orange; Abell 2666 distribution is burgundy colored; and, the dashed purple line describes the frequency for field galaxies according James et al. (2004). Error bar per bin are significatively bigger in those clusters with lower number of 2MASS detections

width distribution. One, those showing an EW at their peak (Abell 634, 2666 and 779 which could lead to a third family) lower than the field, and, two, those other with an EW at the peak comparable to that of the field (Abell 539 and 400). It should be noted as an indication, this division separates the clusters in X-Ray rich and poor in a natural way.

For checking the perception of two families within the sample among the equivalent width distributions plus an additional including luminosities, a set of Kolmogorov-Smirnov tests between clusters (cluster-cluster) and field (cluster-field) had been performed and the charts with KS-statistics and significances is given in tables 7.1 to 7.8. In an apparent natural way we unveiled a marginal similarities linking the distributions of EW(Hα) of dwarfs in clusters with X-ray defined potentials to that of the field, and the absolute deviation of the distributions of EW(Hα) of dwarf in X-Ray poor clusters respect to the field galaxies and the rest of clusters. Moreover, a separated trend for the distribution of EW(Hα) and L(Hα) of brights in any clusters respect to the field is revealed here. Oppositely, Tanaka et al. (2004); Rines et al. (2005); Haines et al. (2007) have found for their samples that there is not differences among the EW distribution respect to that of galaxies in the field. Such different findings could be due to: 1) the nature of considered clusters (Abell 400 and

539 have really a medium rich in X-ray luminosities); 2) the cluster area covered (Tanaka et al. (2004) goes down to $\Sigma_{5th} \simeq 0.4$ - a value well beyond the virial radius covered by us; Rines et al. (2005) covers some virial radius before reaching infall region), since a number of projected and just accreted (and non pre-processed) galaxies could be changing the shape of the distribution; 3) unfair EW(Hα) and F(Hα) values because of the slit/fibers limitations compared to the "true" Hα integrated flux and total equivalent width presented in this work; and 4) all of those works do integrate a collection of environment and densities (from isolation to very crowded clusters core through infall regions) which does smooth the variation in the Flux and EW figures, bluring a cluster's effect in & out.

Cluster	N_{gal}	**A400**		**A539**		**A634**		**A779**		**A2666**	
A400	49	0.0204	1.00	0.115	0.678	0.177	0.514	0.395	0.00683	0.336	0.0327
A539	158	0.115	0.678	0.00633	1.000	0.216	0.129	0.442	0.000194	0.410	0.000694
A634	34	0.177	0.514	0.216	0.129	0.0294	1.00	0.326	0.0685	0.267	0.207
A779	26	0.395	0.00683	0.442	0.000194	0.326	0.0685	0.0385	1.000	0.269	0.258
A2666	26	0.336	0.0327	0.410	0.000694	0.267	0.207	0.269	0.258	0.0385	1.000

Table 7.1:: Table of KS-test results on Luminosity distribution for the Giant SF galaxies in the clusters sample.

Cluster	N_{gal}	**Field**	
A400	49	0.226	0.0442
A539	158	0.186	0.0116
A634	34	0.238	0.0781
A779	26	0.450	0.000175
A2666	26	0.369	0.00374

Table 7.2:: Table of KS-test results on Luminosity distribution for the Giant SF galaxies on the clusters sample and field (from James et al. 2004).

Cluster	N_{gal}	**A400**		**A539**		**A634**		**A779**		**A2666**	
A400	60	0.0167	1.000	0.329	2.10e-05	0.267	0.0161	0.368	0.000472	0.259	0.0325
A539	334	0.329	2.10e-05	0.00299	1.00	0.543	8.81e-16	0.463	7.26e-10	0.516	3.93e-12
A634	70	0.267	0.0161	0.543	8.81e-16	0.0143	1.00	0.284	0.00976	0.105	0.864
A779	57	0.368	0.000472	0.463	7.26e-10	0.284	0.00976	0.0175	1.00	0.281	0.0176
A2666	57	0.259	0.0325	0.516	3.93e-12	0.105	0.864	0.281	0.0176	0.0175	1.00

Table 7.3:: Table of KS-test results on Luminosity distribution for the dwarf SF galaxies in the clusters sample.

Cluster	N_{gal}	**Field**	
A400	60	0.323	8.59e-05
A539	334	0.348	6.03e-14
A634	70	0.292	0.000206
A779	57	0.214	0.0284
A2666	57	0.255	0.00500

Table 7.4:: Table of KS-test results on Luminosity distribution for dwarf SF galaxies int the clusters sample and field (from James et al. 2004).

Cluster	N_{gal}	**A400**		**A539**		**A634**		**A779**		**A2666**	
A400	49	0.0204	1.00	0.153	0.320	0.200	0.356	0.445	0.00147	0.236	0.261
A539	158	0.153	0.320	0.0127	1.000	0.316	0.00552	0.510	8.96e-06	0.281	0.0475
A634	34	0.200	0.356	0.316	0.00552	0.0294	1.00	0.342	0.0489	0.190	0.614
A779	26	0.445	0.00147	0.510	8.96e-06	0.342	0.0489	0.0385	1.000	0.423	0.0128
A2666	26	0.236	0.261	0.281	0.0475	0.190	0.614	0.423	0.0128	0.0385	1.000

Table 7.5:: Table of KS-test results on Hα Equivalent Width distribution for giants SF galaxies in the clusters sample.

Cluster	N_{gal}	**Field**	
A400	49	0.354	0.000169
A539	158	0.287	9.75e-06
A634	34	0.436	3.94e-05
A779	26	0.696	3.94e-10
A2666	26	0.505	1.57e-05

Table 7.6:: Table of KS-test results on Hα Equivalent Width distribution for giants SF galaxies in the clusters sample and field (from James et al. (2004)).

Cluster	N_{gal}	**A400**		**A539**		**A634**		**A779**		**A2666**	
A400	60	0.0167	1.000	0.221	0.0116	0.357	0.000350	0.461	4.30e-06	0.368	0.000472
A539	334	0.221	0.0116	0.00299	1.00	0.434	3.20e-10	0.508	9.15e-12	0.432	1.27e-08
A634	70	0.357	0.000350	0.434	3.20e-10	0.0143	1.00	0.394	6.92e-05	0.0694	0.997
A779	57	0.461	4.30e-06	0.508	9.15e-12	0.394	6.92e-05	0.0351	1.000	0.421	4.77e-05
A2666	57	0.368	0.000472	0.432	1.27e-08	0.0694	0.997	0.421	4.77e-05	0.0175	1.00

Table 7.7:: Table of KS-test results on Hα Equivalent Width distribution for dwarfs SF galaxies in the clusters sample.

Cluster	N_{gal}	**Field**	
A400	60	0.188	0.0679
A539	334	0.0943	0.203
A634	70	0.455	4.17e-10
A779	57	0.452	1.28e-08
A2666	57	0.441	3.10e-08

Table 7.8:: Table of KS-test results on Hα Equivalent Width distribution for dwarfs SF galaxies in the clusters sample and field (from James et al. (2004)).

7.1.2 Spatial distribution

Clustercentric Radial trends

In addition, some results related to the spatial distribution of the Hα emitters within the cluster and possible links with the structure of the cluster will be visited.

For this purpose two definitions of cluster radius will be used. So, here, the expressions taken for computing those figures are offered.

The most used parameters in which the radius of a cluster are expressed are the r_{200} and the virial radius (r_{vir}). In the recent literature we found definitions for both of them, considering a Universe with $\Omega_\Lambda = 0.70$ and $\Omega_M = 0.3$ and $H_0 = 70$ Km·s^{-1}·Mpc^{-1}.

$$r_{200} = \frac{\sqrt{3}\sigma_v}{1000(km\ s^{-1})} \cdot \frac{1}{h_0\sqrt{\Omega_\Lambda + \Omega_M\ (1+z)^3}} \tag{7.1}$$

The virial radius has an aproximation for nearby clusters that can be expressed as

$$r_{vir} = \frac{3.5\sigma_v}{1000(km\ s^{-1})}(1+z)^{-\frac{3}{2}} \tag{7.2}$$

Looking for a trend with clustercentric (projected-)distance for bright and faint galaxies we plotted the averaged Hα flux and the equivalent width separately, for some bin radius as can be seeing in fig. 7.3. The blue and red solid lines represents the mean value for faints and brights respectively, while the colored region represents the snapped up values dispersion area. Abell clusters 400, 539, and 634 show a trend in the EW for their bright Hα emitting galaxies as expected from recent papers (Lewis et al. 2002; Haines et al. 2006, 2007). While, for Abell clusters 779 and 2666 the apparent trend for bright Hα sources is anticorrelated with the distance to center of clusters. First of all it has to be noted that both Abell 779 and Abell 2666 has not a significative number of luminous Hα galaxies for tracing such a tendency. Moreover the presence of bright galaxies in Abell 2666 does not exceed the central $0.4\times$ r_{200} of radius of cluster.

Balogh et al. (1998) founds that the increasing profile in Hα brightness is not completely justified by the Morphology-Density (T-Σ) relation, also confirmed by later works as Lewis et al. (2002), opening the possibility to a second effect acting on clusters of galaxies which accounts for the different trends between the morphological type and the mean Hα surface brightness.

On this profiles, fig. 7.3, we must first state the different behaviour seen between the bright and faint population, relative to the typical values of flux and EW for them. Also it is noticeable the differences among the clusters respect to bright population, where "rich" X-Ray clusters, Abell 400 and 539, present a radial trend for their bright Hα emitting population which avoids the central parts of the cluster. This is not reproduced among the X-Ray poor clusters. The radial trend for Abell 634, 779 and 2666 is consistent with a constant flux and equivalent width, homogeneus distribution of bright Hα galaxies. Respect to the faint population, we found evidences of a permanent presence of star forming faint galaxies on every cluster uniformly spatially distributed. Haines et al. (2007) founds that the fraction of star forming faint sources starts increasing as local density decreases reaching the 1000% at the point where density decreases to 1 Mpc^{-1} (on approach, virial radius is between 1-4 Mpc^{-1} for their sample). However, it still remain unclear whether the median flux also experiments such increasing. According to our findings the median flux for the SF faint population keep stable along the cluster radius up to the virial radius, even in the X-Ray luminous clusters, Abell 400 and 539, on where a correlation between clustercentric distance and local density is expected. Furthermore, those authors find no correlation between the EW(Hα) in brights and the local density for which, under the supposition of a direct relation of clustercentric distance with local density, this two clusters, Abell 400 and 539, are describing a clear monotonic tendency when travelling out the cluster radius. This is in agreement with previous results over a wider range of densities, sky extension and clusters properties (Lewis et al. 2002; Tanaka et al. 2004).

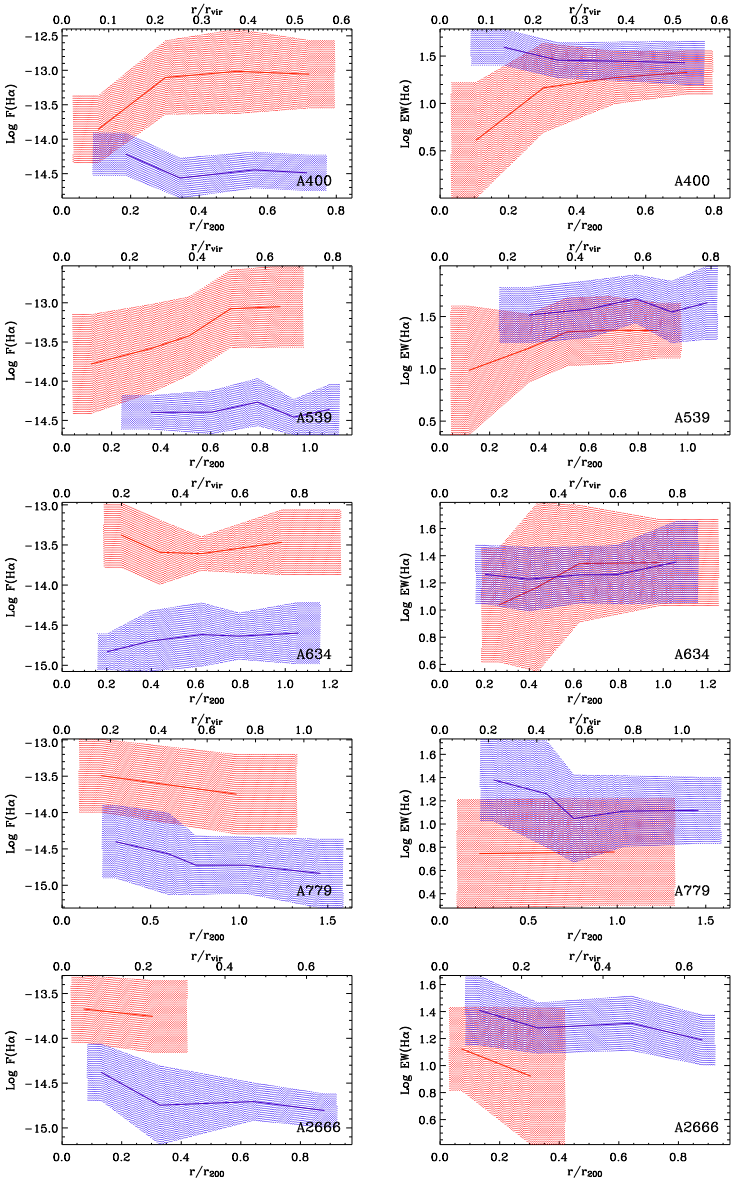

Figure 7.3:: Left: for each cluster the averaged (simple sigma clipped mean) profile of the Hα flux in logarithm (solid lines), embedded on a colour shadowed region which represents the standard deviation of points, through 4 or 7 radial points along the distance to the center of cluster; within this graph we can distinguish the trend followed by bright galaxies in red from the trend of faints in blue. Right: the same for the EW. Again, the amplitude of the colored area covers the deviation of the mean in both brights (red) and faints (blue).

Location within the cluster

The classical relation between the morphological type and the SF (Kennicutt 1998), together with the widely proven morphology-density relation (Dressler 1980; Dressler et al. 1997) have open the path to a SF-density relation (Lewis et al. 2002; Balogh et al. 2004; Tanaka et al. 2004). In that way a very illustrative graphical exercise have been performed and presented here.

A developed technique for drawing densities will serve us to introduce important new two-dimensional maps entailing new information about the spatial distribution of galaxies with ongoing star formation activity. The information highlighted by this new figures will be confronted with the existing information about massive galaxies (2MASS). This, first of all, will provide us with robust diagnostic tool for linking the associations of Hα emitters to the cluster. In a second step but not less relevant, by distinguishing on bright and faint galaxies among the SF measured, we can produce, in addition, density maps of those kinds of galaxy; and, then, being able to discern internal structure associated to a particular range of galaxy masses. The information contained in the next figures (figs. 7.4, 7.5,7.6,7.7 and 7.8) has similar information to a computation of a projected-density except for the background contamination. The background object contamination in the density-maps is almost null when broad continuum is used and lower than the 20% if narrow continuum is used. At this respect, to have null background contamination for a broad band (optical) survey a complete spectroscopy redshift catalogue is needed. In this sense, the density computed used typical projected distance and constrained velocities to the Nth neighbour (Σ_{Nth}) is more adequate to point out a "true" local density. Nevertheless, the definition used here is meaningful and useful to describe sources positions and associations. Thus, in one sight the reader can assimilate the shape and location of two component: the massive (2MASS) and the active star forming galaxies (This survey).

By building a rack of pixels with significative content of information of Hα emitters (block average), a 2D mapping distribution could be drawn, figs 7.4, 7.5,7.6,7.7 and 7.8. For these maps of clusters the individual astrometry solution has been built-in and the 2MASS galaxies spatial distribution has been accounted for through their object density[2]. Light blue squares represent the WFC pointing limits. Colour scale, from white to darkblue[3], traces the density, from low to high, of sources which type (bright, faint or total = bright+faint) is indicated in the top left corner. Thus, we represented three figures per cluster:

[2]black contours

[3]white-red-yellow-green-blue

one for spatial distribution of density of bright galaxies ($M_R \leq$ -19); a second one for spatial distribution of density of faint galaxies ($M_R >$ -19); and a third one for the spatial distribution the total (bright and faint ensemble) galaxy density. The last one is shown larger (twice) than the other representations in the following pages for every cluster.

Firstly, we must note that an absolute density scale had not been used, and a relative (to the maximum on each plot) colour scale had been used to draw the maps, which is structure descriptive of the situation throughout the cluster. Secondly, it should be precised that, because of the dithering around the initial pointings as well as a smoothing (gauss) on the density maps, the extension of the distribution of galaxies exceeds those limits fixed by the physical size of the detector. For all figures, the reader also must bear in mind the projected dimension of the WFC (blue frame), which is 34x34 arcmin, to consider the real sky extension observed.

Going into the figures, it can be noted for all of them in the total galaxy map, that the density profiles of SF galaxies are well confined into the 2MASS contours, except for the case of Abell 539 in which the majority of the emitting-sources are shifted off the center of cluster.

The contribution to the total density of SF galaxies can be divided in 2 classes. On one hand, the bright star-forming population is clearly linked to the 2MASS density distribution. On the other hand, the star forming dwarf (SFD) population distribution shows a different behaviour if host cluster is massive or not. In Abell 400 and Abell 539 the SFD population, down right in the figs 7.4,7.5, differs slightly from the bright population, down left in the figs **??**, avoiding the high density areas of massive galaxies and allocating preferentially between relative maxima of 2MASS density. Early works on properties of dwarf population related to the environment have already pointed out a decreasing activity of star formation in a high density (global) environment, keeping similar spectroscopic properties to the field low luminosity population (Vilchez 1995, 1997).

More recently Haines et al. (2006, 2007) have showed up that active SF dwarf population is found in relative low local density places within the cluster growing from small fraction up to the 100% in the field, while passive dwarfs are preferentially placed at a higher local density or with a massive companion.

While Abell 400 and 539, X-ray luminous clusters, show a large population of SF galaxies, either bright or faint, with clear distinct location within the cluster, on the other side, Abell 634, 779 and 2666, figs 7.6,7.7 and 7.8 respectively, show no basic differences in the separated distribution of sources. For

these three cluster the SFD population extends the spatial distribution of the scant SF brights to the outer parts of the cluster.

In the case of using narrow band for registering the continuum (clusters Abell 634 and A779), we searched in NED for concentration of galaxies in the line of sight and into the field covered. According to Gal et al. (2003) there are 2 optical clusters without a known recesional velocity in our Abell 634 frames plus one which is out but close to a frame edge at $z > 0.1$[4], and only 1, with $z = 0.085$, in the field of view of Abell 779 plus two close to our frames at high z. The 2MASS contours are not affected by this set of clusters, and the contamination in terms of amount of positive emitting sources, as much as Abell 634 and 779 are concerned, is a maximum of 20% as declared in §7.1.3.

[4]Remind that we removed from these clusters, Abell 634 and 779 observed by SDSS, every object with PhotoZ > 0.1

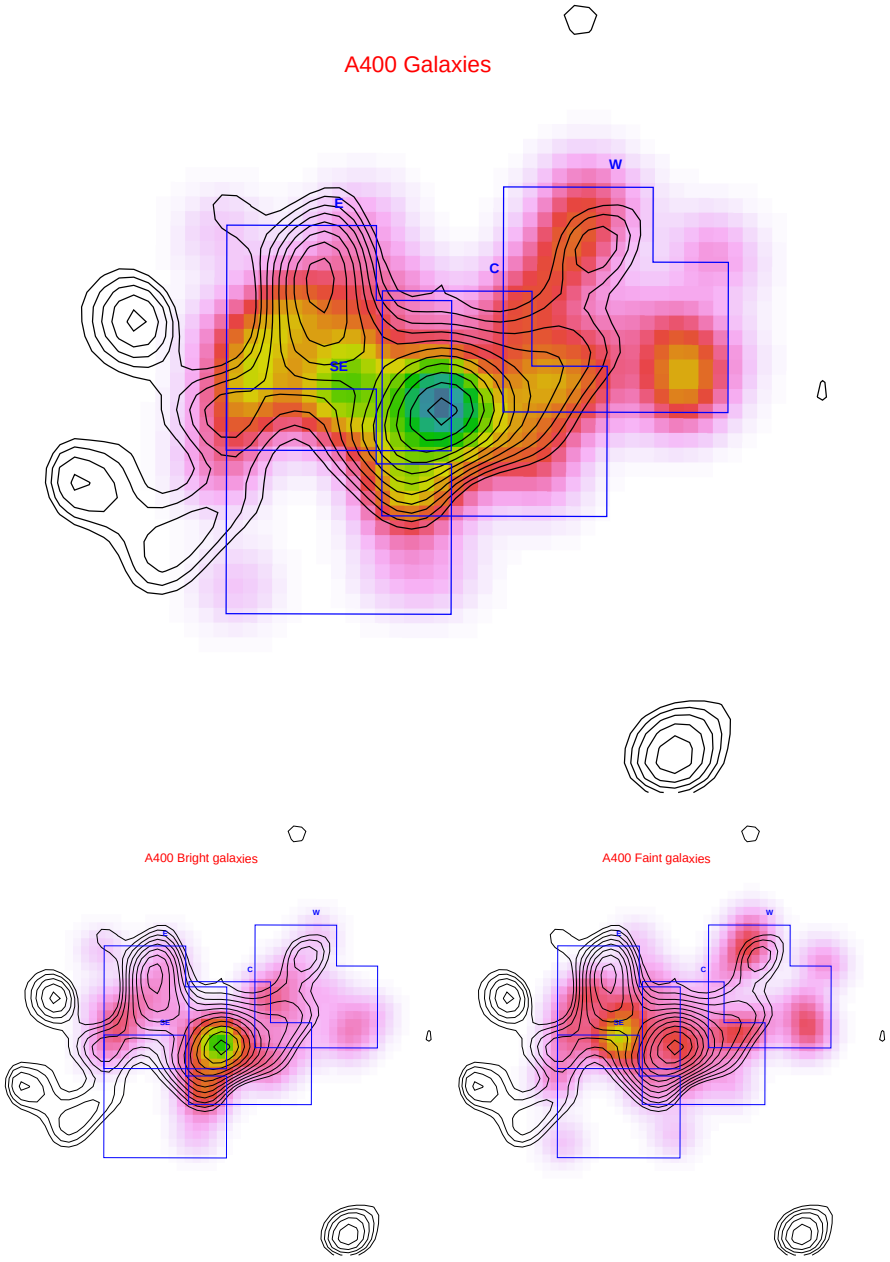

Figure 7.4:: Map of Hα-emitter density with 2MASS contours (in black), and WFC pointings (in light blue). The lowest density of Hα emitters in the map is on white. Low relative densities are traced by warm colours while high relative densities are traced by cool colours.

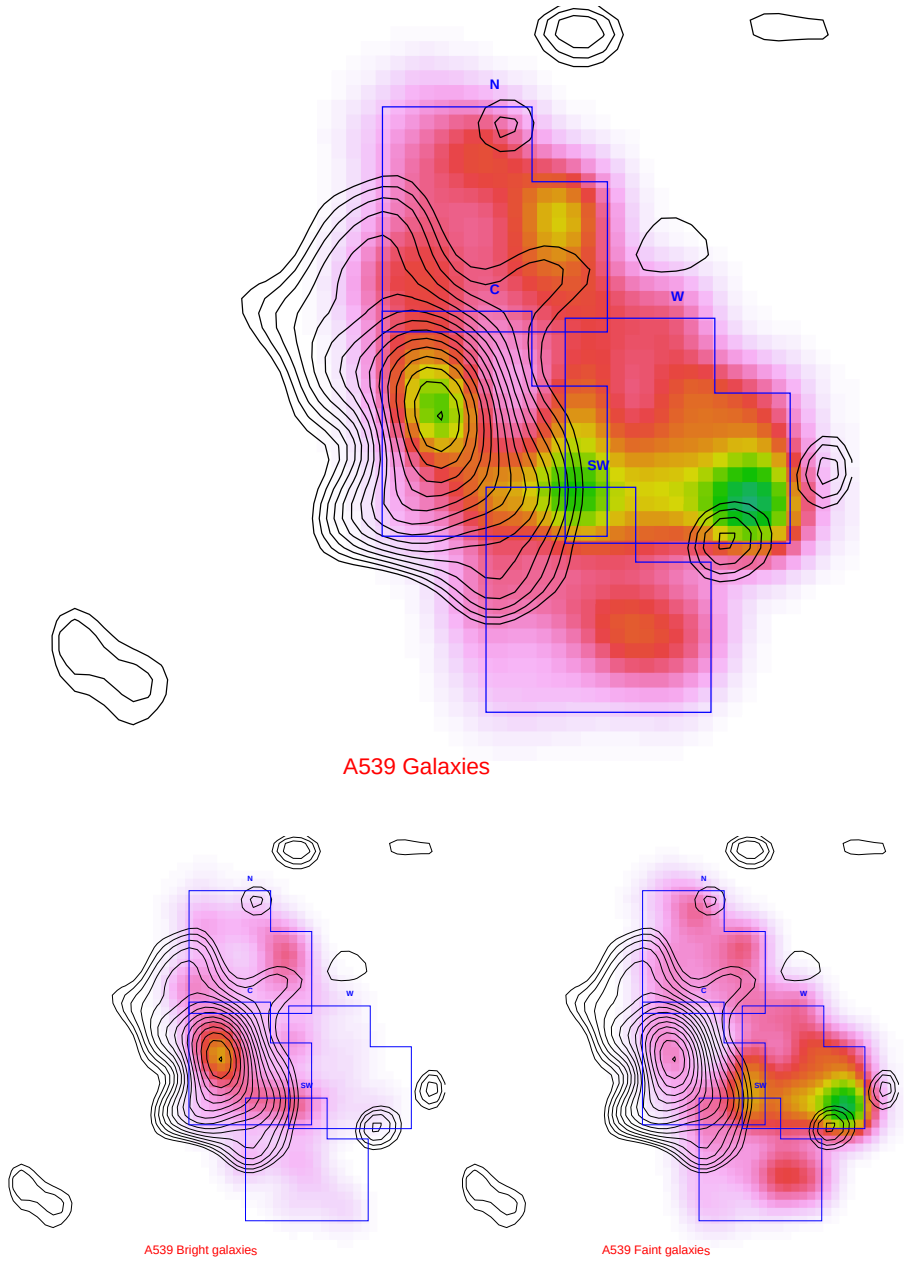
N
C
W
SW
A539 Galaxies
A539 Bright galaxies
A539 Faint galaxies

Figure 7.5::


A634 Galaxies
NE
NW
C
SE
SW
A634 Bright galaxies
A634 Faint galaxies

Figure 7.6::

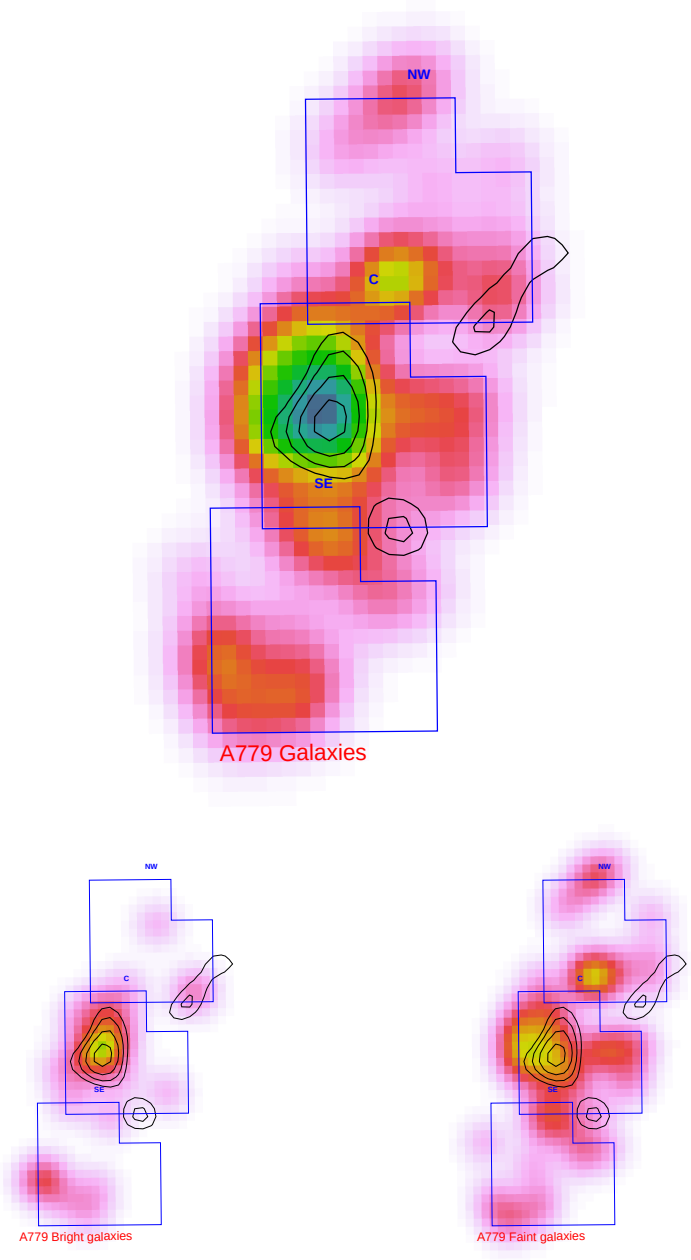
NW
C
SE
A779 Galaxies
NW
C
SE
A779 Bright galaxies
NW
C
SE
A779 Faint galaxies

Figure 7.7::

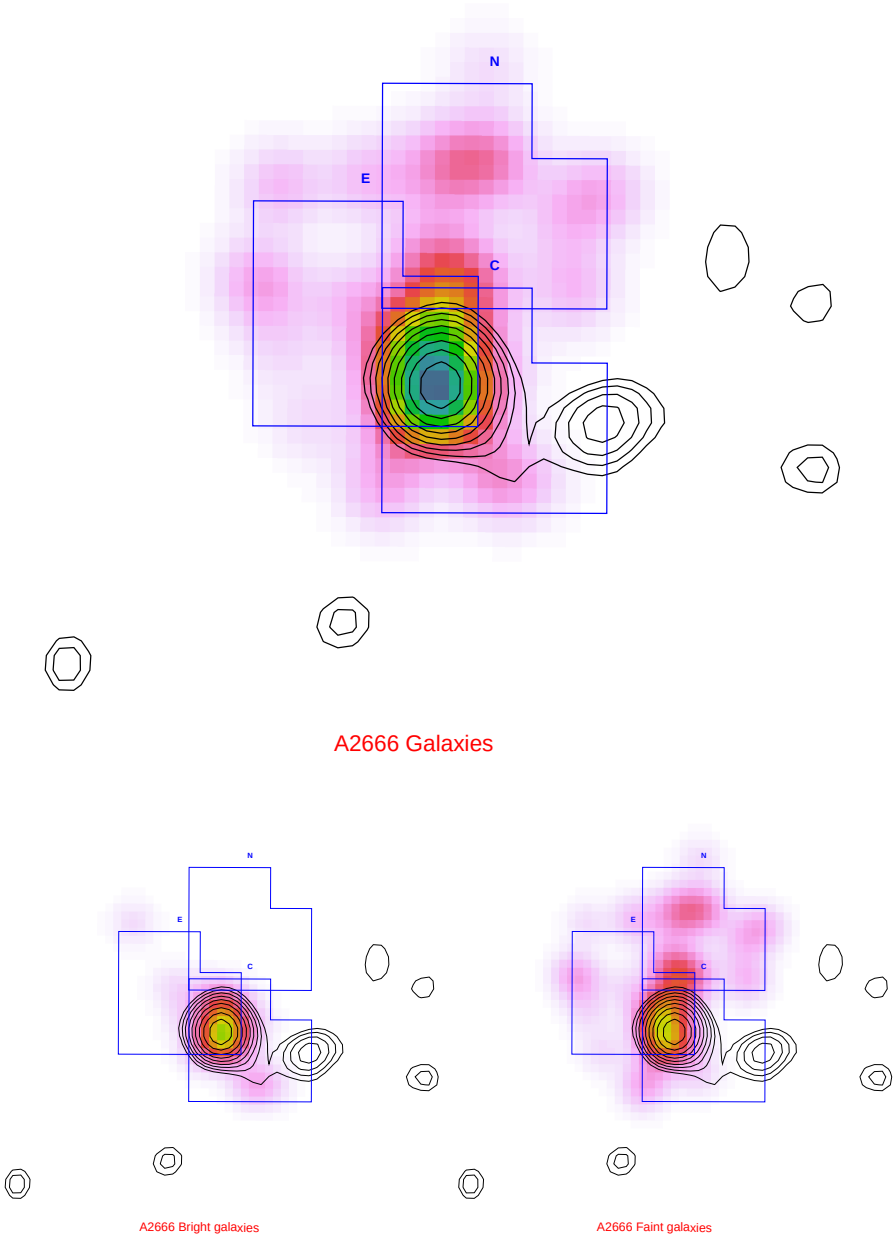
N
E
C
A2666 Galaxies
N
E
C
A2666 Bright galaxies
N
E
C
A2666 Faint galaxies

Figure 7.8::

7.1.3 Estimation of the contamination due to AGN's, background objects

Cores of no obscured Active Galactic Nuclei (AGN) could present a high excitation spectral pattern where a great Hα or [NII] doublet emission-lines would be noticeable, appearing among our objects as a Star forming sources. The fraction of AGN (f_{AGN}) in literature ranges over a wide interval of values from 2.8% (Rines et al. 2005), or 5% (Martini et al. 2006), up to a 40% (Martinez et al. 2007) depending on the AGN separation criterium and on the environment of application. But, while first ratio from Rines et al. 2005 is derived for clusters up to their $5r_{200}$ using Kewley et al. (2001) criterium, the last one is computed with a different criterium on the BPT diagram[5], respect to the total number of galaxies on groups,. For our interestings, a more adequate f_{AGN} value could be taken among Popesso & Biviano (2006) or Martini et al. (2006), since both works have been realized at the cluster environment and at the same absolute limiting magnitude. On one hand, Popesso & Biviano (2006) establishes an anticorrelation between the σ_v (velocity dispersion of the cluster) and f_{AGN}, allocating the latter within 15-25% for cluster of galaxies with velocity dispersion in [300,1000] km s^{-1}. On the other hand, Martini et al. (2006) confirms their AGNs through X-Ray observations finding a f_{AGN} is at least $\sim 5\%$ of cluster galaxies. A combination of the findings from the literature plus the information we gathered with the imaging (2D structure info about emission is available) will be used by assuming:

- Central compact sources in Hα imaging over a more extended continuum are susceptible of beign AGN[6].
- Due to our integration field area, an upper limit of a 10% of the galaxies in the cluster would be expected as AGN candidate.

Also there are few combinations of spectral bands in absorption/emission at the considered cluster redshift that would produce a determined number of fake positive detections if OFF-Band narrow is used. From a sample of normal spiral+elliptical library of spectra, the convolution with the ON-Band and OFF-Band profiles, both narrow, has been carried out and the equivalent width, which is directly linked with the pseudo-colour $m_{OFF} - m_{ON}$, has been derived. Then, by redshifting the spectra using $\lambda F_\lambda(z) = \frac{1}{1+z}\lambda_0 F_{0\ \lambda_0}$ we itered

[5] which distinguishes and accounts for "pure" AGN, and "hybrid" objects (thought to be a composition of SF in the very core together with an active nucleus)

[6] It should be noted that by following only this criterium, nuclear starburst could be misclassified as AGN

the operation yielding a pattern of where that sample galaxies could appears as a detection by our system (see fig. 7.9). In fact this test shows a minimum equivalent width around 0 below of which it is not possible to discern neither the nature of the emission (it could be even an absorption) nor the distance to the source if we only have the narrow photometry info. Luckily the 2 clusters observed with narrow OFF-Band (Abell 779 and 634) have been pointed by the SDSS survey given us, through its photometric redshift estimation (PhotoZ) and the spectroscopic redshift, tools to derive the contamination from background objects. In such conditions, and knowing the strong dependence on magnitude errors for the PhotoZ validity, we fixed a maximum magnitude R = 19. Even in that case, the median error bar and therefore the discrimination range from PhotoZ for objects below 0.1[7] is about 0.02 in redshift. This is not enough to discern whether an objects is within the cluster velocity range ($\sim 7500 \simeq 0.025$) or it is twice. Thus, the spectroscopic redshift ought to be used to estimate the relative proportion of sources found in the clusters sky region with redshift consistent with the cluster redshift and velocity dispersion. For the particular case of Abell 779 it has been found that an 80 % of the Hα-emitting objects are in the mentioned conditions against a 20 % which do belong to other two background clusters (at z$\sim$ 0.48 and 0.56) in its line of sight (LOS). Same experiment on Abell 634 has reproduced these proportions between background and cluster objects, although, there is not declared any cluster contamination behind Abell 634. So we can conjecture that this could be a general effect independent of background overdensities.

Apart from these cases, a relative, but not very likely, background objects contamination raises, given the wavelength covering range of the filters. As deduced from fig. 7.10 four clear statements could be declared here: [OIII]$\lambda\lambda$4959,5007 at z $\sim$ 0.34; [Hβ]λ4861 at z $\sim$ 0.38; [OII]$\lambda\lambda$3726,3729 at z $\sim$ 0.80; or Lyα λ1217 at z $\sim$ 4.53. All of them have a window in redshift of about $\pm$ 0.006, except for Lyα which is $\pm$ 0.03. This kind of detections would have a low continuum which results in a large ON excess in the colour-magnitude diagram (§6.1.4) and therefore making it candidate of a particular spectroscopic follow up. Indeed, if the source emits in [OII] (the nearest one) as much as it is detectable in our frames, it is expected that this (suitable of being a background object) will statistically occupy a special locus on the CM diagram, because of the high equivalent width associated to that kind of object.

[7]For this calculation we ruled out objects above photoZ $\simeq$ 0.1, we are not interested in, as well as those objects with error 1. -since we interpreted although they represent near the 17% of the objects with PhotoZ $\leq$ 0.1, median error bar could be no representative-. Then we applied median computation to the collection of errors for the rest by obtaining 0.022.

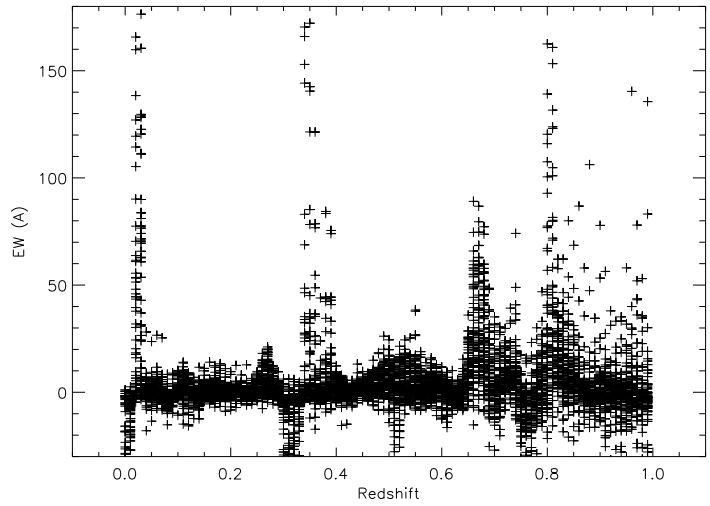

Figure 7.9:: On Y-Axis the EW

Iglesias-Páramo (private communication) found that, for our field, a contamination of about 0.5 to 3 [OII] emission line sources from background are expected in each cluster covered field. For this calculation it has been used the Luminosity function of [OII] emitters at z $\simeq$ 0.88 (aprox. at the same redshift where there are placed our contaminating background [OII] objects) from Hippelein et al. (2003). There has been also used an aproached luminosity limit expected for our sample of L $\sim 10^{39}$ ergs s^{-1} cm^{-2}; and, finally a 3x3 space simulation of background volume, taking into account every cosmological correction. In the same way, number of [OIII]$\lambda\lambda$4959,5007 emitters at z $\sim$ 0.35 contamining our fields ($\in$ [0.75,1.00] degree square) with luminosities around or greater than 10^{39} erg s^{-1} ranges from 1 to 4 in our clusters. This kind of contamination affects equally the ON-OFF$_{narrow}$ and the ON-OFF$_{broad}$ filters tandem. We confirmed through the Sloan spectroscopic z at Abell 779 the numbers declared here, finding that there are no [OII] emitters and only 2 [OIII] emitters, but since we rejected every object with *PhotoZ* greater than or equal to 0.1 for ON-OFF$_{narrow}$ we forced to be null the likelihood of find [OII], [OIII], Hβ or Lyα background objects in Abell 634 and 779 clusters.

Unfortunately, for the rest of the clusters, with the solely information provided by the ON and OFF filter set this kind of "spurious" detection cannot be fully discarded. Furthermore, even though there had been available spectroscopy, aperture effects declared by Kewley et al. (2005) could induce false

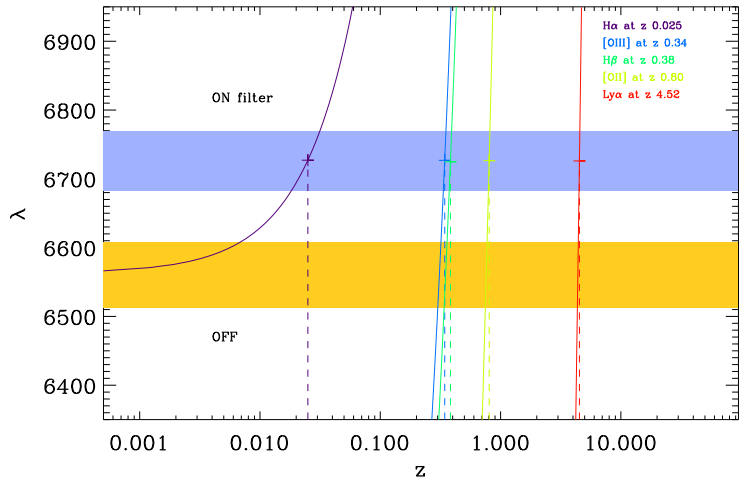

Figure 7.10:: Locus of red shiftings for the most important emission lines perceived by the ON filter. Filters area (central wavelength +/- filter_width/2) are plotted in colours (light blue for ON-band, and Yellow-egg for OFF-band) covering the wavelength of detection. On Y axis, wavelength in Å; on X axis: redshift.

AGNs or LINERs classification, or even when some optical broad band data were available and hence a redshift estimation (through photometric estimators), as in the case of Abell 634 and 779, we would not have been able to discern contamination coming from a near ($z \leq 0.1$) background objects.

7.2 The catalogue.

Considering the current electronic facilities only the first few rows of the corresponding table for each cluster are presented here. Total catalogue for each cluster could be found on the attached compact disc[8]. Column description of tables 7.9, 7.10, 7.11, 7.12, and 7.13 is (1) name for the present catalogue without the prefix **HαIGS** (Hα Image Galaxy Survey); (2) Right Ascension (J2000) in hours, minutes and seconds; (3) Declination (J2000) in degrees, minutes and seconds; (4) Integrated Flux of Hα+[NII] and uncertainty (10^{-15} $erg\ s^{-1}\ cm^{-2}$); (5) Integrated Equivalent Width of the Hα+[NII] and uncertainty (Å); (6) Integrated Flux of Hα (10^{-15} $erg\ s^{-1}\ cm^{-2}$); (7) Integrated Equivalent Width of

[8]If your retrieved this thesis without the CD, the total catalogue of Hα sources can be claimed to the author via email *drp@iaa.es*

the Hα; (8) $R_{Cousins}$ magnitude with uncertainty from continuum image; (9) Integrated Luminosity of Hα (10^{39} $erg\ s^{-1}$); and, (10) Radial velocity (km s^{-1} the mean cluster velocity is assumed if there is no a catalogued velocity).

Name (1)	RA (2)	Dec (3)	$F^N_{H\alpha}$ (4)	$EW^N_{H\alpha}$ (5)	$F_{H\alpha}$ (6)	$EW_{H\alpha}$ (7)	R (8)	$L_{H\alpha}$ (9)	cz (11)
025726+060850	$02^h\ 57^m\ 25.95^s$	06°08'50.34"	3.31 ±0.07	5.0 ±0.3	1.86	2.8	16.159±0.023	2.52 ±0.10	7495
025618+055754	$02^h\ 56^m\ 17.70^s$	05°57'54.41"	48.0 ±1.1	16.2 ±0.7	31.5	10.6	14.54 ±0.01	42.8 ±1.4	6283
025640+055448	$02^h\ 56^m\ 40.46^s$	05°54'48.03"	19.2 ±0.4	2.99±0.14	10.1	1.58	13.704±0.010	13.7 ±0.5	7114
025646+060316	$02^h\ 56^m\ 45.80^s$	06°03'16.20"	172 ±3	86 ±3	141	70	14.96 ±0.01	192 ±4	7815
025702+061336	$02^h\ 57^m\ 02.19^s$	06°13'36.02"	4.1 ±0.3	1.03±0.10	1.9	0.47	14.23 ±0.01	2.5 ±0.4	6766
025705+055508	$02^h\ 57^m\ 05.35^s$	05°55'07.81"	10.0 ±1.6	9.8 ±1.8	6.2	6.0	15.70 ±0.01	8.4 ±2.2	5791
025718+055847	$02^h\ 57^m\ 17.76^s$	05°58'47.35"	12.8 ±0.3	2.20±0.09	6.5	1.11	13.82 ±0.01	8.8 ±0.4	7612
025743+055158	$02^h\ 57^m\ 43.46^s$	05°51'57.68"	0.8 ±1.0	0.2 ±0.3	0.3	0.2	14.22 ±0.01	0.4 ±1.4	8089
025751+060308	$02^h\ 57^m\ 50.56^s$	06°03'08.35"	5.85 ±0.11	1.12±0.04	2.71	0.52	13.92 ±0.01	3.68 ±0.15	6745
025815+055501	$02^h\ 58^m\ 15.03^s$	05°55'01.07"	0.1 ±1.0	0.1 ±0.3	0.0	0.1	14.516±0.012	0.1 ±1.4	6441
025734+055838	$02^h\ 57^m\ 33.63^s$	05°58'37.69"	7.4 ±0.7	0.66±0.07	3.2	0.29	13.10 ±0.01	4.4 ±0.9	6861
025746+055707	$02^h\ 57^m\ 45.85^s$	05°57'06.52"	67.5 ±2.0	17.8 ±1.0	44.9	11.9	14.28 ±0.01	61 ±3	7200
025821+060544	$02^h\ 58^m\ 21.11^s$	06°05'44.01"	2.5 ±0.8	0.24±0.08	1.0	0.24	13.15 ±0.01	1.3 ±1.1	6829
025814+055819	$02^h\ 58^m\ 14.21^s$	05°58'19.08"	13.43 ±0.24	2.23±0.09	6.82	1.13	13.77 ±0.01	9.2 ±0.3	6757
025812+055011	$02^h\ 58^m\ 11.76^s$	05°50'10.95"	5.8 ±2.2	0.9 ±0.4	2.6	0.4	13.675±0.024	4 ±3	7347
025742+060121	$02^h\ 57^m\ 41.59^s$	06°01'21.12"	11.9 ±0.5	1.94±0.20	5.9	0.97	13.75 ±0.05	8.1 ±0.6	7141
025742+060137	$02^h\ 57^m\ 41.51^s$	06°01'37.06"	17.9 ±0.6	1.77±0.14	8.8	0.87	13.21 ±0.03	12.0 ±0.9	6641
025747+060140	$02^h\ 57^m\ 47.34^s$	06°01'39.79"	19.7 ±0.5	4.15±0.19	10.8	2.28	14.03 ±0.01	14.7 ±0.7	7346
025737+060250	$02^h\ 57^m\ 37.41^s$	06°02'49.68"	3.3 ±1.8	1.0 ±0.6	1.5	0.5	14.43 ±0.01	2.1 ±2.5	7466
025618+060414	$02^h\ 56^m\ 17.95^s$	06°04'13.80"	2.783±0.009	16.9 ±0.6	1.837	11.1	17.68 ±0.03	2.493±0.012	7314
025617+055334	$02^h\ 56^m\ 17.29^s$	05°53'34.16"	1.030±0.003	38 ±3	0.754	28	19.63 ±0.07	1.024±0.004	7314
025613+060651	$02^h\ 56^m\ 12.62^s$	06°06'51.05"	47.49 ±0.06	28.8 ±0.7	33.60	20.4	15.178±0.024	45.60 ±0.09	7314
025648+055454	$02^h\ 56^m\ 48.15^s$	05°54'53.57"	10.758±0.012	49.6 ±1.8	8.169	37.7	17.38 ±0.03	11.086±0.016	7314
025653+055221	$02^h\ 56^m\ 53.38^s$	05°52'20.78"	116.24 ±0.14	29.0 ±0.7	82.33	20.6	14.215±0.022	111.73 ±0.19	7314
025657+061222	$02^h\ 56^m\ 56.67^s$	06°12'21.77"	261.42 ±0.22	45.3 ±1.0	196.18	34.0	13.818±0.022	266.2 ±0.3	7314
025658+061702	$02^h\ 56^m\ 58.26^s$	06°17'01.90"	1.456±0.004	26.5 ±1.5	1.019	18.5	18.87 ±0.05	1.383±0.006	7314
025658+060356	$02^h\ 56^m\ 58.17^s$	06°03'56.40"	10.063±0.010	118 ±7	8.563	101	18.40 ±0.06	11.621±0.013	7314
025657+054625	$02^h\ 56^m\ 57.04^s$	05°46'24.51"	1.656±0.003	55 ±4	1.275	43	19.53 ±0.07	1.731±0.005	7314
025716+061337	$02^h\ 57^m\ 16.15^s$	06°13'36.63"	1.637±0.004	43 ±3	1.220	32	19.27 ±0.07	1.655±0.005	7314
025724+055803	$02^h\ 57^m\ 24.47^s$	05°58'03.02"	7.777±0.012	30.3 ±0.9	5.539	21.6	17.20 ±0.03	7.516±0.016	7314

Table 7.9:: Catalogue of objects for cluster A400.

Name (1)	RA (2)	Dec (3)	$F^N_{H\alpha}$ (4)	$EW^N_{H\alpha}$ (5)	$F_{H\alpha}$ (6)	$EW_{H\alpha}$ (7)	R (8)	$L_{H\alpha}$ (9)	cz (11)
051439+062737	$05^h\ 14^m\ 38.87^s$	06°27'36.75"	38.4 ±2.5	6.5 ±0.6	22.4	3.8	13.79 ±0.01	41 ± 5	8960
051507+062360	$05^h\ 15^m\ 07.15^s$	06°23'59.55"	19.4 ±1.6	4.8 ±0.5	10.9	2.7	14.201±0.011	20 ± 3	8708
051535+065002	$05^h\ 15^m\ 34.77^s$	06°50'02.16"	0.29 ±0.10	0.21 ±0.09	0.11	0.21	15.38 ±0.04	0.20± 0.19	8286
051551+061340	$05^h\ 15^m\ 50.51^s$	06°13'40.12"	88.2 ±2.2	35.7 ±1.5	64.2	26.0	14.74 ±0.01	118 ± 4	9325
051551+061237	$05^h\ 15^m\ 50.64^s$	06°12'36.71"	8.75 ±0.20	15.9 ±0.7	5.73	10.4	16.37 ±0.01	10.6 ± 0.4	8256
051553+061814	$05^h\ 15^m\ 52.55^s$	06°18'14.05"	13.89 ±0.24	2.06 ±0.07	6.97	1.03	13.65 ±0.01	12.9 ± 0.4	8574
051558+064656	$05^h\ 15^m\ 58.31^s$	06°46'56.12"	16.6 ±1.2	4.6 ±0.5	9.3	2.5	14.316±0.014	17.1 ± 2.2	8196
051560+062520	$05^h\ 15^m\ 59.98^s$	06°25'20.01"	3.92 ±0.16	1.83 ±0.14	1.94	0.90	14.894±0.022	3.6 ± 0.3	8837
051618+061736	$05^h\ 16^m\ 18.20^s$	06°17'35.79"	9.5 ±0.8	7.2 ±0.8	5.6	4.3	15.42 ±0.01	10.4 ± 1.5	9698
051625+062031	$05^h\ 16^m\ 25.39^s$	06°20'30.83"	0.7 ±0.5	0.16 ±0.11	0.3	0.16	14.02 ±0.01	0.5 ± 0.9	8738
051632+061428	$05^h\ 16^m\ 32.35^s$	06°14'27.88"	0.80 ±0.03	0.55 ±0.03	0.34	0.23	15.33 ±0.01	0.62± 0.06	8529
051634+062658	$05^h\ 16^m\ 33.90^s$	06°26'58.10"	1.3 ±0.4	0.69 ±0.23	0.6	0.30	14.99 ±0.01	1.1 ± 0.8	8133
051638+063358	$05^h\ 16^m\ 38.46^s$	06°33'58.27"	67.0 ±1.7	36.5 ±1.7	48.9	26.7	15.06 ±0.01	90 ± 3	7737
051639+062751	$05^h\ 16^m\ 38.85^s$	06°27'51.35"	3.5 ±0.3	0.89 ±0.19	1.6	0.40	14.23 ±0.10	2.9 ± 0.6	9373
051639+061835	$05^h\ 16^m\ 39.24^s$	06°18'35.06"	0.88 ±0.05	0.47 ±0.04	0.37	0.19	15.027±0.016	0.68± 0.09	8381
051644+061309	$05^h\ 16^m\ 43.67^s$	06°13'08.64"	0.79 ±0.23	0.49 ±0.15	0.33	0.20	15.20 ±0.01	0.6 ± 0.4	9215
051646+062243	$05^h\ 16^m\ 45.79^s$	06°22'42.68"	2.10 ±0.13	1.01 ±0.10	0.96	0.46	14.923±0.018	1.78± 0.25	8410
051647+062954	$05^h\ 16^m\ 47.00^s$	06°29'53.55"	1.2 ±0.3	0.27 ±0.07	0.5	0.27	14.07 ±0.04	0.9 ± 0.5	7210
051650+062319	$05^h\ 16^m\ 49.51^s$	06°23'19.18"	0.90 ±0.03	0.220±0.010	0.34	0.220	14.19 ±0.01	0.62± 0.05	8714
051651+062246	$05^h\ 16^m\ 50.54^s$	06°22'46.49"	0.05 ±0.10	0.02 ±0.03	0.01	0.02	14.555±0.017	0.03± 0.18	8184
051718+064643	$05^h\ 17^m\ 18.11^s$	06°46'42.72"	51.0 ±2.0	26.4 ±1.6	35.6	18.5	15.01 ±0.01	66 ± 4	7425
051559+063613	$05^h\ 15^m\ 58.79^s$	06°36'13.31"	75.2 ±1.2	22.4 ±0.8	51.5	15.4	14.41 ±0.01	95.3 ± 2.3	8027
051453+061506	$05^h\ 14^m\ 53.08^s$	06°15'06.39"	171 ±7	34 ±3	123	25	13.974±0.019	229 ±12	8953
051636+063017	$05^h\ 16^m\ 35.52^s$	06°30'16.61"	2.8 ±1.1	0.41 ±0.17	1.2	0.17	13.615±0.010	2.1 ± 2.1	7135
051550+063618	$05^h\ 15^m\ 50.21^s$	06°36'18.45"	0.11 ±0.25	0.04 ±0.09	0.03	0.04	14.66 ±0.01	0.1 ± 0.5	9353
051634+063015	$05^h\ 16^m\ 33.71^s$	06°30'14.85"	2.7 ±1.4	0.8 ±0.5	1.2	0.4	14.43 ±0.03	2 ± 3	8649
051636+062920	$05^h\ 16^m\ 36.30^s$	06°29'19.82"	7.02 ±0.23	1.28 ±0.07	3.32	0.60	13.88 ±0.01	6.1 ± 0.4	9334
051639+063041	$05^h\ 16^m\ 38.71^s$	06°30'40.84"	0.903±0.016	0.530±0.020	0.380	0.223	15.14 ±0.01	0.70± 0.03	7930
051559+061820	$05^h\ 15^m\ 58.62^s$	06°18'20.37"	2.04 ±0.16	3.7 ±0.3	1.11	2.0	16.37 ±0.01	2.1 ± 0.3	9287
051654+063359	$05^h\ 16^m\ 53.66^s$	06°33'58.57"	45.9 ±0.9	82 ±6	37.2	66	16.35 ±0.04	68.8 ± 1.7	7615

Table 7.10:: Catalogue of objects for cluster A539.

Name (1)	RA (2)	Dec (3)	$F^N_{H\alpha}$ (4)	$EW^N_{H\alpha}$ (5)	$F_{H\alpha}$ (6)	$EW_{H\alpha}$ (7)	R (8)	$L_{H\alpha}$ (9)	cz (11)
081421+575232	$08^h\ 14^m\ 20.53^s$	57°52'31.56"	4.0± 0.4	1.8 ± 0.3	2.0	0.9	14.830±0.012	3.2± 0.6	8077
081615+583524	$08^h\ 16^m\ 15.06^s$	58°35'24.13"	8.3± 0.7	5.1 ± 0.9	4.7	2.9	15.19 ±0.01	7.5± 1.1	7924
081317+580039	$08^h\ 13^m\ 17.24^s$	58°00'38.80"	98 ± 8	30 ± 5	71	22	14.43 ±0.01	113 ±12	7820
081526+581045	$08^h\ 15^m\ 25.82^s$	58°10'44.66"	37 ± 4	3.3 ± 0.6	20	1.8	13.10 ±0.01	32 ± 6	8184
081539+581748	$08^h\ 15^m\ 38.71^s$	58°17'48.17"	17 ± 3	2.8 ± 0.9	9	1.5	13.78 ±0.03	14 ± 5	7895
081606+580021	$08^h\ 16^m\ 05.54^s$	58°00'20.76"	6.0± 0.5	1.02± 0.19	2.7	0.47	13.798±0.014	4.4± 0.8	7826
081208+575429	$08^h\ 12^m\ 08.39^s$	57°54'28.66"	103 ± 9	59 ±10	81	46	15.11 ±0.01	130 ±15	7794
081154+575708	$08^h\ 11^m\ 53.61^s$	57°57'07.55"	100 ± 9	37 ± 6	73	27	14.63 ±0.01	117 ±15	8364
081157+584204	$08^h\ 11^m\ 57.34^s$	58°42'03.69"	144 ±12	30 ± 5	102	20	14.01 ±0.01	164 ±20	8482
081251+575516	$08^h\ 12^m\ 50.54^s$	57°55'16.48"	53 ± 4	8.3 ± 1.4	32	5.0	13.72 ±0.01	51 ± 7	8004
081349+573401	$08^h\ 13^m\ 49.02^s$	57°34'00.91"	36 ± 3	19 ± 3	24	12	15.04 ±0.01	39 ± 5	7877
081347+580450	$08^h\ 13^m\ 46.86^s$	58°04'49.68"	87 ± 7	28 ± 5	61	20	14.51 ±0.01	98 ±11	8232
081439+580124	$08^h\ 14^m\ 38.89^s$	58°01'24.36"	164 ±15	22 ± 4	112	15	13.53 ±0.01	179 ±24	7885
081415+581159	$08^h\ 14^m\ 15.37^s$	58°11'58.98"	75 ± 6	53 ± 9	56	40	15.34 ±0.01	92 ±10	7785
081418+582256	$08^h\ 14^m\ 18.08^s$	58°22'56.17"	17.7± 1.7	8.0 ± 1.5	10.6	4.8	14.86 ±0.01	17 ± 3	7996
081542+581046	$08^h\ 15^m\ 42.47^s$	58°10'45.85"	27.0± 2.2	44 ± 8	20.2	33	16.26 ±0.01	32 ± 4	8304
081653+583020	$08^h\ 16^m\ 52.94^s$	58°30'20.10"	6.9± 0.6	25 ± 4	4.8	17	17.106±0.015	7.7± 0.9	7704
081804+580558	$08^h\ 18^m\ 04.32^s$	58°05'58.00"	2.9± 0.3	4.2 ± 0.8	1.6	2.3	16.11 ±0.01	2.6± 0.5	8034
081810+580534	$08^h\ 18^m\ 09.58^s$	58°05'33.73"	26.1± 2.5	5.7 ± 1.1	15.0	3.3	14.07 ±0.01	24 ± 4	7495
081545+581915	$08^h\ 15^m\ 44.85^s$	58°19'14.80"	93 ± 9	6.8 ± 1.3	55	4.0	12.88 ±0.01	88 ±14	8151
081227+575010	$08^h\ 12^m\ 26.97^s$	57°50'09.77"	24.3± 2.5	41 ± 8	18.0	30	16.303±0.019	29 ± 4	7944
081246+574751	$08^h\ 12^m\ 45.86^s$	57°47'51.31"	4.4± 0.6	20 ± 5	3.0	12	17.351±0.020	4.7± 1.0	7944
081425+581753	$08^h\ 14^m\ 24.85^s$	58°17'53.13"	4.6± 0.4	2.1 ± 0.4	2.3	1.0	14.86 ±0.01	3.7± 0.6	7944
081448+581232	$08^h\ 14^m\ 47.54^s$	58°12'31.78"	3.0± 0.3	1.10± 0.20	1.4	0.51	14.648±0.014	2.2± 0.4	7944
081460+580559	$08^h\ 14^m\ 59.58^s$	58°05'58.51"	10.4± 0.9	7.4 ± 1.3	6.2	4.4	15.35 ±0.01	9.9± 1.4	7944
081520+580523	$08^h\ 15^m\ 20.35^s$	58°05'23.30"	13.8± 1.5	6.5 ± 1.4	8.0	3.8	14.900±0.020	12.9± 2.4	7944
081533+574006	$08^h\ 15^m\ 33.01^s$	57°40'05.88"	8.2± 0.7	20 ± 3	5.5	12	16.69 ±0.01	8.8± 1.1	7944
081634+575940	$08^h\ 16^m\ 34.00^s$	57°59'40.37"	44 ± 4	44 ± 7	33	33	15.74 ±0.01	51 ± 6	7944
081717+580325	$08^h\ 17^m\ 17.15^s$	58°03'24.74"	22.5± 1.9	6.5 ± 1.1	13.1	3.8	14.37 ±0.01	20 ± 3	7944
081837+583234	$08^h\ 18^m\ 37.42^s$	58°32'33.78"	23.6± 1.9	24 ± 4	16.2	16	15.72 ±0.01	25 ± 3	7944

Table 7.11:: Catalogue of objects for cluster A634.

Name (1)	RA (2)	Dec (3)	$F^N_{H\alpha}$ (4)	$EW^N_{H\alpha}$ (5)	$F_{H\alpha}$ (6)	$EW_{H\alpha}$ (7)	R (8)	$L_{H\alpha}$ (9)	cz (11)
091859+340802	$09^h\ 18^m\ 58.60^s$	34°08'01.62"	0.214 ± 0.011	0.35 ± 0.03	0.085	0.35	16.26 ±0.01	0.098 ± 0.013	6671
091927+334728	$09^h\ 19^m\ 27.31^s$	33°47'27.61"	81 ± 3	30 ± 3	58	23	14.70 ±0.01	66 ± 4	5781
092002+332755	$09^h\ 20^m\ 02.13^s$	33°27'55.20"	0.87 ± 0.10	1.57 ± 0.25	0.42	0.76	16.36 ±0.01	0.48 ± 0.12	7415
092026+333057	$09^h\ 20^m\ 26.38^s$	33°30'57.08"	0.50 ± 0.04	0.44 ± 0.06	0.20	0.18	15.58 ±0.01	0.23 ± 0.05	7009
092059+331143	$09^h\ 20^m\ 59.42^s$	33°11'42.63"	5.91 ± 0.24	2.52 ± 0.21	3.05	1.30	14.80 ±0.01	3.5 ± 0.3	6389
092101+330737	$09^h\ 21^m\ 01.18^s$	33°07'36.56"	6.1 ± 0.4	3.5 ± 0.3	3.3	1.9	15.10 ±0.01	3.8 ± 0.4	6942
091947+334459	$09^h\ 19^m\ 46.79^s$	33°44'58.68"	25 ± 4	1.07 ± 0.22	12	0.49	12.240±0.019	14 ± 5	6871
091819+333326	$09^h\ 18^m\ 19.05^s$	33°33'25.74"	38.8 ± 2.1	7.9 ± 0.7	23.2	4.7	0.00 ±0.01	26.6 ± 2.4	7176
091834+341739	$09^h\ 18^m\ 33.98^s$	34°17'38.51"	6.7 ± 0.3	1.75 ± 0.15	3.3	0.86	14.26 ±0.01	3.8 ± 0.3	6525
091936+332543	$09^h\ 19^m\ 36.10^s$	33°25'43.44"	15.6 ± 2.0	2.7 ± 0.5	8.1	1.4	13.83 ±0.01	9.3 ± 2.4	7066
092037+330430	$09^h\ 20^m\ 36.92^s$	33°04'29.59"	87 ± 4	19.3 ± 1.7	58	13.0	14.09 ±0.01	67 ± 5	6481
091955+330626	$09^h\ 19^m\ 54.51^s$	33°06'26.33"	13.1 ± 0.7	4.6 ± 0.5	7.3	2.6	14.60 ±0.01	8.4 ± 0.8	7427
091917+340029	$09^h\ 19^m\ 17.39^s$	34°00'29.07"	6.8 ± 1.3	1.3 ± 0.3	3.2	0.6	13.89 ±0.01	3.7 ± 1.5	7126
091924+333727	$09^h\ 19^m\ 24.20^s$	33°37'26.80"	5.5 ± 1.6	0.55 ± 0.19	2.3	0.23	13.210±0.012	2.7 ± 1.9	6383
091919+335252	$09^h\ 19^m\ 19.10^s$	33°52'52.01"	26.3 ± 1.3	6.3 ± 0.6	15.3	3.7	14.17 ±0.01	17.6 ± 1.5	7040
091935+335317	$09^h\ 19^m\ 34.86^s$	33°53'17.43"	5.5 ± 0.6	1.7 ± 0.3	2.7	0.8	14.45 ±0.01	3.1 ± 0.7	6398
091931+333852	$09^h\ 19^m\ 31.10^s$	33°38'51.82"	54 ± 3	127 ±19	46	108	16.66 ±0.06	53 ± 3	7106
091941+334417	$09^h\ 19^m\ 41.41^s$	33°44'16.74"	118 ± 8	18.6 ± 2.0	79	12.5	13.72 ±0.01	91 ± 9	6110
091945+334442	$09^h\ 19^m\ 45.48^s$	33°44'42.32"	45 ±12	7.2 ± 2.5	27	4.2	13.721±0.017	30 ±15	5183
091947+334459	$09^h\ 19^m\ 46.84^s$	33°44'58.69"	28 ± 4	1.16 ± 0.25	12	0.54	12.267±0.017	15 ± 5	6952
091745+340925	$09^h\ 17^m\ 44.99^s$	34°09'25.28"	0.295 ± 0.012	0.87 ± 0.09	0.133	0.39	16.89 ±0.03	0.152 ± 0.014	6678
091811+333956	$09^h\ 18^m\ 11.10^s$	33°39'55.98"	9.9 ± 0.4	48 ± 4	7.5	36	17.44 ±0.01	8.6 ± 0.5	7467
091827+340754	$09^h\ 18^m\ 26.51^s$	34°07'54.10"	0.160 ± 0.016	0.91 ± 0.13	0.072	0.41	17.61 ±0.01	0.083 ± 0.018	6858
091827+340209	$09^h\ 18^m\ 26.81^s$	34°02'09.39"	0.0012± 0.0016	0.000± 0.010	0.0000	0.000	17.21 ±0.04	0.0000± 0.0018	6929
091844+334352	$09^h\ 18^m\ 44.49^s$	33°43'51.98"	0.00 ± 0.03	0.00 ± 0.09	0.00	0.00	16.813±0.018	0.00 ± 0.04	6992
091853+343056	$09^h\ 18^m\ 52.53^s$	34°30'56.19"	9.9 ± 0.6	18.2 ± 2.0	6.6	12.1	16.38 ±0.01	7.6 ± 0.7	6552
091855+340206	$09^h\ 18^m\ 55.26^s$	34°02'05.54"	0.316 ± 0.014	1.06 ± 0.11	0.145	0.49	17.037±0.018	0.167 ± 0.016	6674
091911+342709	$09^h\ 19^m\ 11.35^s$	34°27'09.40"	0.231 ± 0.015	0.90 ± 0.10	0.104	0.41	17.20 ±0.01	0.120 ± 0.017	6341
091913+331856	$09^h\ 19^m\ 13.02^s$	33°18'55.82"	3.98 ± 0.19	13.4 ± 1.4	2.55	8.6	17.039±0.020	2.93 ± 0.22	6742
091931+332605	$09^h\ 19^m\ 31.29^s$	33°26'05.30"	15.9 ± 0.8	50 ± 4	12.1	38	16.96 ±0.01	13.9 ± 0.9	6806

Table 7.12:: Catalogue of objects for cluster A779.

Name (1)	RA (2)	Dec (3)	$F^N_{H\alpha}$ (4)	$EW^N_{H\alpha}$ (5)	$F_{H\alpha}$ (6)	$EW_{H\alpha}$ (7)	R (8)	$L_{H\alpha}$ (9)	cz (11)
235020+265446	$23^h\ 50^m\ 19.83^s$	26°54'46.43"	35.8 ±1.8	10.2 ± 0.8	22.1	6.3	14.36 ±0.01	36 ±3	8291
235023+271152	$23^h\ 50^m\ 22.98^s$	27°11'52.29"	9.6 ±0.3	8.7 ± 0.4	5.8	5.3	15.61 ±0.01	9.6 ±0.4	7975
235049+271336	$23^h\ 50^m\ 49.15^s$	27°13'36.11"	5.99±0.11	10.2 ± 0.4	3.70	6.3	16.30 ±0.01	6.10±0.18	8559
235136+271217	$23^h\ 51^m\ 35.96^s$	27°12'16.50"	2.34±0.21	1.60± 0.17	1.14	0.78	15.31 ±0.01	1.9 ±0.3	8049
235050+270821	$23^h\ 50^m\ 49.78^s$	27°08'20.88"	30.5 ±0.6	28.1 ± 1.3	21.5	19.8	15.633±0.012	35.4 ±1.0	7964
235117+271213	$23^h\ 51^m\ 17.47^s$	27°12'12.80"	2.31±0.05	7.5 ± 0.3	1.37	4.5	17.01 ±0.01	2.26±0.08	8973
235118+271438	$23^h\ 51^m\ 17.59^s$	27°14'38.35"	5.63±0.12	37.1 ± 1.6	4.11	27.1	17.77 ±0.01	6.77±0.20	8368
235060+271308	$23^h\ 50^m\ 59.98^s$	27°13'08.17"	28.4 ±0.8	6.8 ± 0.3	16.7	4.0	14.16 ±0.01	27.4 ±1.4	8312
235118+271737	$23^h\ 51^m\ 18.43^s$	27°17'36.95"	21.7 ±0.5	5.66± 0.23	12.4	3.24	14.27 ±0.01	20.4 ±0.9	7875
235101+271528	$23^h\ 51^m\ 01.05^s$	27°15'27.87"	4.5 ±0.7	1.4 ± 0.3	2.2	0.6	14.418±0.013	3.5 ±1.2	8511
235059+271428	$23^h\ 50^m\ 59.08^s$	27°14'27.93"	21.4 ±0.7	11.0 ± 0.6	13.4	6.9	15.00 ±0.01	22.0 ±1.2	8356
235047+271717	$23^h\ 50^m\ 47.48^s$	27°17'17.44"	175 ±4	32.2 ± 1.2	126	23.1	13.88 ±0.01	207 ±6	7999
235101+271720	$23^h\ 51^m\ 00.68^s$	27°17'19.60"	8.7 ±0.7	3.5 ± 0.3	4.7	1.9	14.74 ±0.01	7.7 ±1.1	9051
235159+272014	$23^h\ 51^m\ 58.97^s$	27°20'14.40"	25.9 ±0.5	5.76± 0.21	14.9	3.31	14.09 ±0.01	24.5 ±0.8	8130
235052+270958	$23^h\ 50^m\ 52.21^s$	27°09'58.33"	62.3 ±1.3	12.4 ± 0.5	39.5	7.9	13.97 ±0.01	65.1 ±2.1	7648
235056+270736	$23^h\ 50^m\ 55.89^s$	27°07'36.39"	6.7 ±0.6	2.08± 0.23	3.4	1.05	14.45 ±0.01	5.6 ±1.1	8142
235056+270516	$23^h\ 50^m\ 56.36^s$	27°05'16.06"	80 ±4	9.1 ± 0.6	49	5.5	13.35 ±0.01	80 ±6	8012
235059+270852	$23^h\ 50^m\ 58.60^s$	27°08'51.51"	23.9 ±1.0	1.84± 0.16	11.8	0.91	12.93 ±0.03	19.5 ±1.7	8190
235117+271438	$23^h\ 51^m\ 17.47^s$	27°14'37.86"	5.17±0.16	35.7 ± 2.2	3.76	26.0	17.818±0.016	6.2 ±0.3	8368
235130+270318	$23^h\ 51^m\ 30.00^s$	27°03'17.73"	4.84±0.09	5.08± 0.20	2.73	2.87	15.78 ±0.01	4.50±0.15	8426
234958+265420	$23^h\ 49^m\ 58.13^s$	26°54'20.41"	6.01±0.24	8.3 ± 0.5	3.62	5.0	16.07 ±0.01	6.0 ±0.4	8041
235027+274300	$23^h\ 50^m\ 27.05^s$	27°43'00.36"	2.14±0.04	8.2 ± 0.3	1.29	4.9	17.18 ±0.01	2.12±0.07	8041
235111+270736	$23^h\ 51^m\ 10.79^s$	27°07'36.38"	5.7 ±0.3	8.0 ± 0.6	3.4	4.8	16.08 ±0.01	5.7 ±0.5	8041
235106+270629	$23^h\ 51^m\ 05.63^s$	27°06'29.03"	6.21±0.19	44 ± 4	4.64	33	17.85 ±0.04	7.6 ±0.3	8041
235117+271438	$23^h\ 51^m\ 17.46^s$	27°14'37.82"	6.83±0.21	45 ± 3	5.13	34	17.779±0.015	8.4 ±0.3	8041
235247+273755	$23^h\ 52^m\ 47.22^s$	27°37'55.43"	40.0 ±1.1	37.1 ± 1.8	29.2	27.1	15.64 ±0.01	48.1 ±1.8	8041
234917+273704	$23^h\ 49^m\ 16.99^s$	27°37'04.33"	6.74±0.12	22.8 ± 0.8	4.62	15.7	0.00 ±0.01	7.61±0.19	8041
234920+272544	$23^h\ 49^m\ 20.29^s$	27°25'44.23"	22.3 ±0.4	60.9 ± 2.3	17.4	47.5	16.81 ±0.01	28.6 ±0.6	8041
234928+272251	$23^h\ 49^m\ 28.44^s$	27°22'50.70"	1.35±0.11	11.1 ± 2.1	0.85	7.0	18.01 ±0.09	1.39±0.19	8041
234928+272301	$23^h\ 49^m\ 28.25^s$	27°23'00.89"	1.7 ±0.6	19 ±12	1.1	12	18.3 ±0.3	1.9 ±1.0	8041

Table 7.13:: Catalogue of objects for cluster A2666.

PART II

Her, we move on the individual object that form the gallery of SF galaxies and first a operational definition will be adopted to construct a Working Subsample, then we go to analyse for this subsample the structure of the Hα emission, deriving and tabulating concentration, asymmetry and petrosian radii from the computed surface brightness profiles for the continuum and Hα. Finally we go to check the cluster effects, if any, and compare with the fields and literature data.

7.3 The *Working Subsample* of cluster galaxies: definition and construction

A higher quality selection of the whole sample have been designed according to the successful criteria adopted by Iglesias-Páramo et al. (2002) in the past for the same survey . Making extensive use of the NASA Extragalactic Database (NED) I searched the known galaxies with radial velocity consistent with being member of the corresponding cluster, in the surveyed area. In addition, visual inspection of the net Hα[9] frames allowed us to identify a population of SF objects which have been added to this *Working Subsample*. In order to reduce the spurious detections we considered only those objects with emission above five times their uncertainty ($F(\mathrm{H}\alpha) > 5\ \sigma_F$). The resulting *Subsample* is expected to have a high success-rate of selecting SF members in clusters as declared by Cortese et al. (2003).

A careful treatment has been taken with this set of images. As mentioned in §6.2 and explained in Appendix C, the measurements carried out on these images ensure a better adapted fitting of the shape, and derivation of the flux and equivalent width. Furthermore, profiles for the Hα+continuum, ON, and the red-continuum, OFF, asymetries and concentration of the Continuum and net Hα image were computed independently and presented in tables **??**.

The range of Hα fluxes, although it expands those from Iglesias-Páramo et al. (2002) at his larger fluxes, already remains low (-15.80 < Log F(Hα) < -12.64), while the equivalent widths are between 3 and 1010 Å.

On this reduced sample of galaxies we studied the 2D structure of the Hα emission. Definitions of compactness and asymmetry from §6.3 have been applied and tabulated. Radial profiles of individual SF sources have been examined in §7.3.2.

[9] Remind that this nomenclature in the image corresponds to the Hα + [NII] lines ensemble.

Table 7.14:: Catalogue of A400 *Working Subsample*.

Name (1)	**RA** (2)	**Dec** (3)	$\mathbf{F}_{H\alpha}$ (4)	$\mathbf{EW}_{H\alpha}$ (5)	$\mathbb{C}_s$ (6)	$\mathbb{A}_s$ (7)	$\mathbf{R}_p$ (8)	**SFR** (9)
025726+060850	$02^h\ 57^m\ 25.95^s$	06°08'50.34"	10.8	2.28	3.132±0.022	0.095	2.8	0.156 ±0.008
025618+055754	$02^h\ 56^m\ 17.70^s$	05°57'54.41"	8.8	0.87	2.93 ±0.04	0.061	8.5	0.127 ±0.009
025640+055448	$02^h\ 56^m\ 40.46^s$	05°54'48.03"	5.9	0.97	2.47 ±0.04	0.007	15.0	0.086 ±0.007
025646+060316	$02^h\ 56^m\ 45.80^s$	06°03'16.20"	6.82	1.13	3.18 ±0.07	0.030	5.0	0.098 ±0.003
025702+061336	$02^h\ 57^m\ 02.19^s$	06°13'36.02"	44.9	11.9	2.11 ±0.07	0.134	12.8	0.65 ±0.03
025705+055508	$02^h\ 57^m\ 05.35^s$	05°55'07.81"	3.2	0.29	3.498±0.012	0.069	6.2	0.046 ±0.010
025718+055847	$02^h\ 57^m\ 17.76^s$	05°58'47.35"	2.71	0.52	3.295±0.011	0.037	6.1	0.0392±0.0016
025751+060308	$02^h\ 57^m\ 50.56^s$	06°03'08.35"	6.5	1.11	2.88 ±0.06	0.043	5.9	0.093 ±0.004
025734+055838	$02^h\ 57^m\ 33.63^s$	05°58'37.69"	6.2	6.0	2.69 ±0.04	0.087	4.1	0.089 ±0.023
025746+055707	$02^h\ 57^m\ 45.85^s$	05°57'06.52"	1.9	0.47	2.758±0.012	0.023	5.4	0.027 ±0.004
025814+055819	$02^h\ 58^m\ 14.21^s$	05°58'19.08"	141	70	2.30 ±0.08	0.127	9.3	2.04 ±0.04
025742+060121	$02^h\ 57^m\ 41.59^s$	06°01'21.12"	10.1	1.58	3.398±0.004	0.086	11.1	0.146 ±0.006
025742+060137	$02^h\ 57^m\ 41.51^s$	06°01'37.06"	31.5	10.6	2.24 ±0.07	0.055	9.0	0.455 ±0.015
025747+060140	$02^h\ 57^m\ 47.34^s$	06°01'39.79"	1.86	2.8	2.60 ±0.09	0.128	4.0	0.0269±0.0010

The Working Subsample for Abell 400 is not as complete as the other clusters because the visual search for Hα emitting galaxies did not take place.

A spectroscopic follow up using WYFFOS at the William Herschel Telescope was performed and carried out for Abell 400, giving us the chance of constructing a subsample for this cluster to study in a deepest way than the rest of cluster in the sample. However, this grand spectroscopic survey project is ongoing and the time requested to reduce, treat and analysis exceeded the deadline for this thesis work, needing to be presented forward. Nevertheless, galaxies in the covered field of Abell 400 with a known velocity consistent to be member of the cluster and a measurable Hα emsission have been studied and offered here, and the corresponding complete subsample for this cluster will be constructed, using the data from WYFFOS, in a next future.

In every table 7.14, 7.15, 7.16, 7.17, and 7.18, columns are: (1) HαIGS Catalogue name; (2) Right Ascension equinox J2000; (3) Declination equinox J2000; (4) Integrated Flux of Hα emission nitrogen corrected in 10^{-15} erg s^{-1} cm^{-2}; (5) Equivalent width of Hα (nitrogen corrected) in Å; (6) Compactness and derived uncertainty according to expression 6.19; (7) Asymmetry (following the formulae 6.17); (8) Petrosian radius ($\eta = 0.20$) in kiloparsec; and (9) Star-formation rate according L(Hα)=$9.4{\cdot}10^{40}\frac{SFR}{M_\odot yr^{-1}} erg\ s^{-1}$ from **??** in order to be consistent with our previous study.

Values lower than 0 for asymmetry are the result of a computational limitation or application. Symmetric structures in a noisy images could deviates the asymmetry calculation to negative values. Uncertainty in the asymmetry is around 0.2.

Table 7.15:: Catalogue of A539 *Working Subsample*.

Name (1)	**RA** (2)	**Dec** (3)	$\mathbf{F}_{H\alpha}$ (4)	$\mathbf{EW}_{H\alpha}$ (5)	$\mathbb{C}_s$ (6)	$\mathbb{A}_s$ (7)	$\mathbf{R}_p$ (8)	**SFR** (9)
051439+062737	$05^h\ 14^m\ 38.87^s$	06°27'36.75"	1.8	3.0	2.27 ±0.09	-0.130	14.2	0.035 ±0.010
051507+062360	$05^h\ 15^m\ 07.15^s$	06°23'59.55"	4.4	14	2.19 ±0.10	-0.121	3.7	0.086 ±0.020
051551+061340	$05^h\ 15^m\ 50.51^s$	06°13'40.12"	9.7	9.5	2.37 ±0.09	0.163	7.2	0.191 ±0.006
051551+061237	$05^h\ 15^m\ 50.64^s$	06°12'36.71"	11.9	20.9	2.80 ±0.09	0.035	3.1	0.234 ±0.008
051553+061814	$05^h\ 15^m\ 52.55^s$	06°18'14.05"	5.17	5.3	2.46 ±0.04	0.057	7.2	0.102 ±0.004
051558+064656	$05^h\ 15^m\ 58.31^s$	06°46'56.12"	3.20	27	2.07 ±0.12	0.008	2.5	0.063 ±0.005
051560+062520	$05^h\ 15^m\ 59.98^s$	06°25'20.01"	4.0	1.6	2.446±0.011	0.050	8.7	0.079 ±0.014
051618+061736	$05^h\ 16^m\ 18.20^s$	06°17'35.79"	51.1	10.0	3.123±0.003	0.023	6.2	1.00 ±0.03
051632+061428	$05^h\ 16^m\ 32.35^s$	06°14'27.88"	3.59	6.9	2.54 ±0.07	0.002	4.6	0.071 ±0.003
051638+063358	$05^h\ 16^m\ 38.46^s$	06°33'58.27"	15.0	2.4	3.30 ±0.05	0.041	11.6	0.30 ±0.03
051639+062751	$05^h\ 16^m\ 38.85^s$	06°27'51.35"	13.1	22.1	2.192±0.025	-0.199	7.8	0.257 ±0.019
051639+061835	$05^h\ 16^m\ 39.24^s$	06°18'35.06"	2.01	121	2.74 ±0.09	0.111	2.7	0.0396±0.0022
051646+062243	$05^h\ 16^m\ 45.79^s$	06°22'42.68"	4.0	6.5	2.32 ±0.10	0.091	9.0	0.079 ±0.012
051650+062319	$05^h\ 16^m\ 49.51^s$	06°23'19.18"	4.3	14	2.56 ±0.03	0.001	6.5	0.084 ±0.014
051718+064643	$05^h\ 17^m\ 18.11^s$	06°46'42.72"	5.39	12.4	2.82 ±0.09	-0.531	4.0	0.106 ±0.003
051559+063613	$05^h\ 15^m\ 58.79^s$	06°36'13.31"	8.2	6.4	2.531±0.011	0.032	4.7	0.16 ±0.03
051453+061506	$05^h\ 14^m\ 53.08^s$	06°15'06.39"	5.4	13.6	2.70 ±0.03	0.024	2.3	0.107 ±0.006
051636+062920	$05^h\ 16^m\ 36.30^s$	06°29'19.82"	1.21	8.4	2.82 ±0.07	0.094	1.8	0.024 ±0.003
051654+063359	$05^h\ 16^m\ 53.66^s$	06°33'58.57"	17.6	41	1.95 ±0.10	-0.264	14.4	0.346 ±0.012
051520+062825	$05^h\ 15^m\ 19.90^s$	06°28'25.32"	14.8	11.8	2.70 ±0.06	0.006	2.1	0.291 ±0.013
051637+062706	$05^h\ 16^m\ 37.01^s$	06°27'06.49"	3.8	11.1	2.38 ±0.06	0.013	2.5	0.075 ±0.010
051637+062653	$05^h\ 16^m\ 37.09^s$	06°26'53.11"	1.92	16.0	2.53 ±0.14	-0.438	2.4	0.0378±0.0010
051646+063723	$05^h\ 16^m\ 46.31^s$	06°37'22.84"	1.64	25	2.1 ±0.3	0.003	1.6	0.0323±0.0025
051710+065539	$05^h\ 17^m\ 09.80^s$	06°55'38.84"	4.38	24.7	2.08 ±0.03	0.114	6.4	0.086 ±0.003
051527+060655	$05^h\ 15^m\ 27.13^s$	06°06'55.43"	51	27	2.33 ±0.10	0.057	6.2	0.99 ±0.05
051532+060150	$05^h\ 15^m\ 31.53^s$	06°01'49.81"	3.60	72	2.505±0.024	0.193	8.6	0.0709±0.0022
051533+063219	$05^h\ 15^m\ 32.79^s$	06°32'19.25"	92	15.1	2.42 ±0.07	0.056	10.6	1.81 ±0.06
051521+062013	$05^h\ 15^m\ 20.79^s$	06°20'12.82"	6.1	7.9	2.27 ±0.06	0.086	5.8	0.120 ±0.007
051532+062941	$05^h\ 15^m\ 32.32^s$	06°29'41.40"	158	197	2.19 ±0.06	-0.096	3.9	3.12 ±0.06
051646+061720	$05^h\ 16^m\ 46.03^s$	06°17'20.41"	1.5	25	2.04 ±0.19	0.075	1.2	0.030 ±0.006
051652+061932	$05^h\ 16^m\ 51.66^s$	06°19'32.07"	6.5	34	2.19 ±0.08	0.087	3.5	0.127 ±0.015
051559+062702	$05^h\ 15^m\ 58.85^s$	06°27'02.27"	11.2	36	2.59 ±0.09	0.101	2.6	0.221 ±0.011
051631+064404	$05^h\ 16^m\ 31.43^s$	06°44'03.93"	37.8	19.4	2.61 ±0.07	0.025	10.1	0.743 ±0.022
051641+062420	$05^h\ 16^m\ 40.79^s$	06°24'19.91"	23	15	1.98 ±0.03	0.202	12.3	0.45 ±0.05
051638+063357	$05^h\ 16^m\ 38.14^s$	06°33'57.38"	12.7	20.2	2.22 ±0.12	0.167	5.4	0.250 ±0.009
051507+065734	$05^h\ 15^m\ 07.26^s$	06°57'34.12"	5.48	18.4	2.46 ±0.09	0.027	3.6	0.108 ±0.004
051512+064927	$05^h\ 15^m\ 11.65^s$	06°49'27.23"	8.0	15.9	2.81 ±0.08	0.290	13.1	0.158 ±0.008
051520+065514	$05^h\ 15^m\ 20.04^s$	06°55'14.34"	2.71	19.5	2.19 ±0.05	0.073	4.2	0.053 ±0.003
051518+064654	$05^h\ 15^m\ 18.39^s$	06°46'54.47"	0.8	2.0	2.83 ±0.06	0.055	6.3	0.015 ±0.005
051529+070019	$05^h\ 15^m\ 28.96^s$	07°00'19.24"	1.4	4.2	2.411±0.005	0.032	9.2	0.028 ±0.005
051528+065919	$05^h\ 15^m\ 28.34^s$	06°59'18.97"	2.62	20	2.14 ±0.08	0.062	4.0	0.052 ±0.003
051607+064515	$05^h\ 16^m\ 06.71^s$	06°45'15.16"	10.9	20	2.71 ±0.03	0.133	7.9	0.214 ±0.007
051631+064404	$05^h\ 16^m\ 31.42^s$	06°44'04.00"	9.75	23.7	2.27 ±0.08	0.081	5.1	0.192 ±0.005
051636+064448	$05^h\ 16^m\ 35.61^s$	06°44'47.72"	3.46	10.8	2.38 ±0.05	-0.445	2.5	0.068 ±0.003
051634+064211	$05^h\ 16^m\ 34.06^s$	06°42'10.80"	25.1	21.4	2.29 ±0.06	0.089	7.2	0.494 ±0.019
051639+064222	$05^h\ 16^m\ 39.02^s$	06°42'21.70"	8.5	25	2.15 ±0.03	-1.944	6.5	0.166 ±0.017
051636+064448	$05^h\ 16^m\ 35.61^s$	06°44'47.72"	28.9	20.8	2.51 ±0.03	0.067	8.0	0.569 ±0.019
051640+064743	$05^h\ 16^m\ 39.78^s$	06°47'42.81"	8.73	21.8	2.451±0.012	0.030	5.8	0.172 ±0.004
051702+064830	$05^h\ 17^m\ 02.15^s$	06°48'29.78"	11.3	70	2.00 ±0.05	0.321	5.0	0.222 ±0.005
051701+064613	$05^h\ 17^m\ 00.73^s$	06°46'12.55"	53.2	29.6	2.88 ±0.07	0.114	7.2	1.05 ±0.05
051710+064759	$05^h\ 17^m\ 10.21^s$	06°47'58.50"	3.2	17.3	2.46 ±0.06	-0.059	4.4	0.063 ±0.007
051718+064643	$05^h\ 17^m\ 18.03^s$	06°46'42.79"	10.6	20.2	2.64 ±0.06	0.030	7.8	0.209 ±0.007
051550+065334	$05^h\ 15^m\ 50.49^s$	06°53'33.71"	19.1	22.4	2.87 ±0.03	0.118	3.2	0.376 ±0.013
051608+065451	$05^h\ 16^m\ 07.72^s$	06°54'50.82"	11.73	272	1.8 ±0.6	-0.870	1.4	0.231 ±0.005
051633+070719	$05^h\ 16^m\ 33.08^s$	07°07'19.40"	5.1	17.6	2.18 ±0.06	-0.484	7.2	0.101 ±0.005
051635+065616	$05^h\ 16^m\ 34.56^s$	06°56'16.26"	12.2	20.4	2.71 ±0.04	0.020	3.0	0.239 ±0.010
051651+065338	$05^h\ 16^m\ 51.43^s$	06°53'37.61"	2.27	10.3	2.71 ±0.03	-1.022	3.5	0.0446±0.0021
051554+071010	$05^h\ 15^m\ 53.66^s$	07°10'10.41"	4.30	103	2.47 ±0.11	-0.165	7.1	0.085 ±0.004
051603+070726	$05^h\ 16^m\ 03.18^s$	07°07'25.83"	42.0	6.3	2.86 ±0.03	0.529	10.1	0.83 ±0.04
051610+070729	$05^h\ 16^m\ 10.13^s$	07°07'28.60"	6.3	5.5	2.84 ±0.05	-0.447	5.4	0.124 ±0.007
051622+070636	$05^h\ 16^m\ 22.09^s$	07°06'35.70"	91	8.1	2.776±0.025	0.049	22.6	1.79 ±0.08

Continued on next page.

Table 7.15 – continued from previous page

Name	RA	Dec	$F_{H\alpha}$	$EW_{H\alpha}$	$\mathbb{C}_s$	$\mathbb{A}_s$	R_p	SFR
051633+070719	$05^h\ 16^m\ 33.08^s$	07°07'19.39"	46	8.9	3.52 ±0.03	0.073	26.6	0.92 ±0.08
051649+071153	$05^h\ 16^m\ 49.15^s$	07°11'53.43"	5.4	1.3	2.86 ±0.05	0.000	19.0	0.107 ±0.021
051402+055555	$05^h\ 14^m\ 01.85^s$	05°55'54.95"	2.65	0.63	3.22 ±0.09	0.019	4.4	0.052 ±0.005
051402+054613	$05^h\ 14^m\ 01.94^s$	05°46'13.43"	116	24.0	2.80 ±0.07	0.071	12.8	2.29 ±0.13
051414+055143	$05^h\ 14^m\ 13.94^s$	05°51'43.31"	37.2	66	2.27 ±0.07	-1.510	7.8	0.731 ±0.018
051414+055208	$05^h\ 14^m\ 13.78^s$	05°52'08.45"	3.32	0.60	3.35 ±0.06	0.139	6.8	0.065 ±0.004
051527+055529	$05^h\ 15^m\ 27.17^s$	05°55'28.82"	123	25	2.346±0.018	0.027	15.3	2.44 ±0.14
051533+054638	$05^h\ 15^m\ 32.78^s$	05°46'38.11"	51.5	15.4	2.39 ±0.07	0.333	10.6	1.013 ±0.024
051606+060421	$05^h\ 16^m\ 05.97^s$	06°04'21.27"	35.6	18.5	2.40 ±0.06	0.039	9.5	0.70 ±0.04
051605+060128	$05^h\ 16^m\ 05.33^s$	06°01'27.82"	0.34	0.220	3.419±0.007	0.049	6.5	0.0066±0.0005
051606+060121	$05^h\ 16^m\ 06.08^s$	06°01'20.81"	0.96	0.46	3.07 ±0.05	0.023	6.9	0.019 ±0.003
051602+055657	$05^h\ 16^m\ 02.40^s$	05°56'56.64"	0.37	0.19	3.138±0.024	0.066	5.3	0.0072±0.0009
051617+060109	$05^h\ 16^m\ 16.71^s$	06°01'08.80"	1.6	0.40	3.148±0.004	0.020	7.0	0.031 ±0.007
051536+061556	$05^h\ 15^m\ 35.81^s$	06°15'55.74"	48.9	26.7	2.98 ±0.03	0.070	7.4	0.96 ±0.03
051551+061236	$05^h\ 15^m\ 50.60^s$	06°12'36.38"	0.34	0.23	3.48 ±0.06	-3.202	4.7	0.0066±0.0007
051359+061006	$05^h\ 13^m\ 58.50^s$	06°10'06.02"	5.6	4.3	3.398±0.011	-0.104	4.4	0.110 ±0.016
051453+061506	$05^h\ 14^m\ 53.05^s$	06°15'06.01"	1.94	0.90	3.70 ±0.04	-0.047	1.5	0.038 ±0.003
051516+063328	$05^h\ 15^m\ 15.85^s$	06°33'28.31"	9.3	2.5	3.745±0.016	0.056	7.6	0.182 ±0.023
051515+063311	$05^h\ 15^m\ 14.55^s$	06°33'11.44"	6.97	1.03	3.42 ±0.06	0.059	11.8	0.137 ±0.005
051508+063547	$05^h\ 15^m\ 07.80^s$	06°35'47.36"	5.73	10.4	2.755±0.007	0.055	4.1	0.113 ±0.004
051532+062941	$05^h\ 15^m\ 32.32^s$	06°29'41.39"	64.2	26.0	2.38 ±0.09	0.063	7.8	1.26 ±0.04
051502+064103	$05^h\ 15^m\ 01.84^s$	06°41'02.71"	10.9	2.7	3.54 ±0.06	0.082	6.9	0.21 ±0.03
051453+063402	$05^h\ 14^m\ 53.12^s$	06°34'01.66"	22.4	3.8	3.94 ±0.05	0.054	6.9	0.44 ±0.05

Table 7.16:: Catalogue of A634 *Working Subsample*.

Name (1)	**RA** (2)	**Dec** (3)	$\mathbf{F}_{H\alpha}$ (4)	$\mathbf{EW}_{H\alpha}$ (5)	$\mathbb{C}_s$ (6)	$\mathbb{A}_s$ (7)	$\mathbf{R}_p$ (8)	**SFR** (9)
081421+575232	$08^h\ 14^m\ 20.53^s$	57°52'31.56"	157	16	3.63 ±0.05	0.154	26.2	2.7 ±0.4
081526+581045	$08^h\ 15^m\ 25.75^s$	58°10'44.91"	2.6	5	3.02 ±0.07	0.045	8.6	0.044 ±0.013
081154+575708	$08^h\ 11^m\ 53.61^s$	57°57'07.55"	30	49	2.71 ±0.05	0.218	2.6	0.51 ±0.05
081251+575516	$08^h\ 12^m\ 50.54^s$	57°55'16.48"	24	41	3.012 ±0.016	0.103	4.4	0.41 ±0.04
081349+573401	$08^h\ 13^m\ 49.02^s$	57°34'00.91"	3.6	14	2.80 ±0.10	0.008	3.3	0.062 ±0.008
081347+580450	$08^h\ 13^m\ 46.86^s$	58°04'49.68"	5.5	5.8	2.37 ±0.05	-0.073	5.6	0.094 ±0.013
081439+580124	$08^h\ 14^m\ 38.89^s$	58°01'24.36"	12.7	20	2.50 ±0.04	0.084	4.4	0.22 ±0.03
081415+581159	$08^h\ 14^m\ 15.37^s$	58°11'58.98"	1.31	12	2.74 ±0.07	-0.200	3.3	0.022 ±0.004
081418+582256	$08^h\ 14^m\ 18.08^s$	58°22'56.17"	0.146	3.6	1.69 ±0.19	0.040	1.8	0.0025±0.0004
081542+581046	$08^h\ 15^m\ 42.47^s$	58°10'45.85"	0.75	70	2.50 ±0.10	0.195	2.1	0.0129±0.0017
081653+583020	$08^h\ 16^m\ 52.94^s$	58°30'20.10"	0.61	6.4	2.87 ±0.03	0.121	7.4	0.0104±0.0016
081810+580534	$08^h\ 18^m\ 09.58^s$	58°05'33.73"	12.4	3.6	4.921 ±0.017	0.164	3.5	0.21 ±0.03
081545+581915	$08^h\ 15^m\ 44.85^s$	58°19'14.80"	18.6	1010	2.28 ±0.20	0.034	4.3	0.253 ±0.025
081246+574751	$08^h\ 12^m\ 45.86^s$	57°47'51.31"	0.72	11	2.83 ±0.14	0.163	1.7	0.0123±0.0025
081448+581232	$08^h\ 14^m\ 47.54^s$	58°12'31.78"	0.94	17	2.71 ±0.05	0.188	2.1	0.0161±0.0020
081837+583234	$08^h\ 18^m\ 37.42^s$	58°32'33.78"	1.4	10	2.50 ±0.04	0.127	4.1	0.024 ±0.005
081337+580818	$08^h\ 13^m\ 37.27^s$	58°08'18.23"	3.9	17	2.18 ±0.10	0.076	3.5	0.067 ±0.008
081204+575502	$08^h\ 12^m\ 04.47^s$	57°55'01.50"	0.58	7.6	3.40 ±0.08	0.216	6.8	0.0099±0.0013
081214+575318	$08^h\ 12^m\ 13.91^s$	57°53'17.94"	4.3	15	2.49 ±0.03	0.161	8.4	0.073 ±0.009
081201+574454	$08^h\ 12^m\ 00.88^s$	57°44'53.50"	1.38	17	2.45 ±0.05	-1.887	3.3	0.024 ±0.003
081259+573049	$08^h\ 12^m\ 58.92^s$	57°30'48.53"	2.4	46	2.44 ±0.16	0.077	1.5	0.042 ±0.005
081249+574750	$08^h\ 12^m\ 48.80^s$	57°47'50.04"	1.80	12	3.04 ±0.08	0.097	3.8	0.031 ±0.004
081307+574859	$08^h\ 13^m\ 07.06^s$	57°48'59.00"	37	3.2	3.94 ±0.04	0.055	10.7	0.63 ±0.13
081322+574759	$08^h\ 13^m\ 22.02^s$	57°47'59.17"	1.6	2.3	2.49 ±0.10	0.081	4.0	0.027 ±0.008
081352+580055	$08^h\ 13^m\ 52.47^s$	58°00'55.31"	0.78	8.4	3.09 ±0.07	0.083	1.8	0.0133±0.0017
081218+574621	$08^h\ 12^m\ 18.26^s$	57°46'20.55"	0.34	12	2.53 ±0.21	0.211	1.4	0.0058±0.0009
081356+575320	$08^h\ 13^m\ 55.89^s$	57°53'19.64"	1.05	12	2.80 ±0.07	0.159	1.8	0.018 ±0.003
081435+575525	$08^h\ 14^m\ 34.64^s$	57°55'25.10"	0.33	20	2.54 ±0.07	0.132	1.6	0.0057±0.0008
081438+574210	$08^h\ 14^m\ 37.66^s$	57°42'09.73"	0.51	29	2.5 ±0.4	0.065	0.9	0.0087±0.0013
081457+574845	$08^h\ 14^m\ 56.88^s$	57°48'45.32"	0.78	12	3.23 ±0.06	0.175	1.9	0.0134±0.0021
081456+575506	$08^h\ 14^m\ 55.52^s$	57°55'06.43"	1.18	46	2.54 ±0.11	0.081	2.3	0.0201±0.0022
081503+575033	$08^h\ 15^m\ 03.38^s$	57°50'33.32"	1.32	51	2.59 ±0.09	0.111	1.8	0.0225±0.0024
081639+575858	$08^h\ 16^m\ 39.03^s$	57°58'58.40"	1.18	10	3.12 ±0.09	0.012	2.1	0.020 ±0.003
081658+575600	$08^h\ 16^m\ 58.39^s$	57°56'00.40"	0.71	76	2.26 ±0.07	0.166	1.0	0.0122±0.0013
081657+575558	$08^h\ 16^m\ 56.56^s$	57°55'58.41"	2.4	25	2.41 ±0.05	0.284	4.7	0.042 ±0.005
081708+575602	$08^h\ 17^m\ 08.13^s$	57°56'01.92"	0.74	10	2.95 ±0.08	0.124	3.3	0.0127±0.0020
081459+580451	$08^h\ 14^m\ 58.84^s$	58°04'51.26"	0.70	16	2.71 ±0.16	0.156	1.9	0.0119±0.0016
081526+581045	$08^h\ 15^m\ 25.75^s$	58°10'44.91"	4.2	29	2.54 ±0.13	0.070	3.0	0.072 ±0.009
081727+580325	$08^h\ 17^m\ 27.05^s$	58°03'25.41"	1.00	25	2.73 ±0.15	0.140	7.2	0.0171±0.0021
081842+580244	$08^h\ 18^m\ 41.75^s$	58°02'43.65"	3.9	15	2.38 ±0.03	-0.082	4.0	0.067 ±0.008
081238+581129	$08^h\ 12^m\ 37.63^s$	58°11'29.43"	1.6	6	1.96 ±0.06	0.068	6.9	0.027 ±0.005
081248+581542	$08^h\ 12^m\ 47.72^s$	58°15'42.09"	2.8	11	2.478 ±0.020	0.067	4.7	0.047 ±0.010
081317+582142	$08^h\ 13^m\ 17.30^s$	58°21'41.83"	14	3.9	2.30 ±0.03	0.255	15.7	0.24 ±0.05
081345+581436	$08^h\ 13^m\ 44.54^s$	58°14'36.02"	16.2	16	2.672 ±0.021	0.131	6.9	0.28 ±0.03
081331+582024	$08^h\ 13^m\ 30.51^s$	58°20'24.46"	1.4	0.51	3.83 ±0.05	0.113	7.2	0.023 ±0.005
081409+581410	$08^h\ 14^m\ 09.30^s$	58°14'10.35"	3.0	12	3.18 ±0.08	0.181	2.7	0.050 ±0.011
081355+580234	$08^h\ 13^m\ 55.46^s$	58°02'33.52"	55	4.0	3.533 ±0.008	0.036	14.6	0.94 ±0.15
081445+581647	$08^h\ 14^m\ 44.78^s$	58°16'47.28"	15.0	3.3	3.7650±0.0003	0.093	8.0	0.26 ±0.04
081460+581420	$08^h\ 14^m\ 59.97^s$	58°14'20.28"	4.8	17	2.58 ±0.07	0.072	4.0	0.082 ±0.010
081036+574601	$08^h\ 10^m\ 36.11^s$	57°46'01.19"	20.2	33	2.98 ±0.07	-0.211	3.6	0.34 ±0.04
081150+575035	$08^h\ 11^m\ 50.21^s$	57°50'35.37"	10.6	4.8	3.19 ±0.05	0.060	8.5	0.18 ±0.03
081747+574427	$08^h\ 17^m\ 46.62^s$	57°44'26.90"	56	40	3.44 ±0.03	0.163	2.3	0.98 ±0.11
081217+575831	$08^h\ 12^m\ 16.60^s$	57°58'31.38"	112	15	3.05 ±0.07	0.114	15.7	1.91 ±0.25
081235+575738	$08^h\ 12^m\ 34.60^s$	57°57'37.87"	61	20	2.843 ±0.019	0.108	7.8	1.05 ±0.12
081433+580853	$08^h\ 14^m\ 33.42^s$	58°08'53.24"	24	12	2.898 ±0.022	0.055	10.2	0.42 ±0.05
081505+582126	$08^h\ 15^m\ 05.10^s$	58°21'26.34"	32	5.0	4.11 ±0.05	0.102	5.6	0.54 ±0.07
081604+580416	$08^h\ 16^m\ 04.26^s$	58°04'16.02"	73	27	3.17 ±0.05	0.090	6.8	1.24 ±0.15
081156+575111	$08^h\ 11^m\ 55.74^s$	57°51'10.92"	37	3.2	3.94 ±0.04	0.055	10.7	0.63 ±0.13
081450+575553	$08^h\ 14^m\ 49.98^s$	57°55'53.17"	4.7	2.9	3.54 ±0.03	0.037	4.1	0.080 ±0.012
081321+575109	$08^h\ 13^m\ 21.31^s$	57°51'09.27"	2.0	0.9	3.71 ±0.03	0.166	4.8	0.034 ±0.007

Table 7.17:: Catalogue of A779 *Working Subsample*.

Name (1)	**RA** (2)	**Dec** (3)	$\mathbf{F}_{H\alpha}$ (4)	$\mathbf{EW}_{H\alpha}$ (5)	$\mathbb{C}_s$ (6)	$\mathbb{A}_s$ (7)	$\mathbf{R}_p$ (8)	**SFR** (9)
092002+332755	$09^h\ 20^m\ 02.13^s$	33°27'55.20"	5.7	25	2.51 ±0.06	0.092	2.4	0.070 ±0.004
092101+330737	$09^h\ 21^m\ 01.18^s$	33°07'36.56"	5.7	25	2.51 ±0.06	0.092	2.4	0.070 ±0.004
091947+334459	$09^h\ 19^m\ 46.79^s$	33°44'58.68"	5.7	25	2.51 ±0.06	0.092	2.4	0.070 ±0.004
091819+333326	$09^h\ 18^m\ 19.05^s$	33°33'25.74"	5.7	25	2.51 ±0.06	0.092	2.4	0.070 ±0.004
091834+341739	$09^h\ 18^m\ 33.98^s$	34°17'38.51"	5.7	25	2.51 ±0.06	0.092	2.4	0.070 ±0.004
091955+330626	$09^h\ 19^m\ 54.51^s$	33°06'26.33"	5.7	25	2.51 ±0.06	0.092	2.4	0.070 ±0.004
091917+340029	$09^h\ 19^m\ 17.39^s$	34°00'29.07"	1.46	64	2.26 ±0.12	0.338	1.9	0.0178±0.0023
091919+335252	$09^h\ 19^m\ 19.10^s$	33°52'52.01"	1.43	20	3.32 ±0.09	0.159	2.7	0.0174±0.0023
091931+333852	$09^h\ 19^m\ 31.10^s$	33°38'51.82"	3.19	10.6	3.648±0.014	0.132	3.5	0.039 ±0.003
091941+334417	$09^h\ 19^m\ 41.41^s$	33°44'16.74"	0.37	5.9	2.49 ±0.07	0.182	1.4	0.0045±0.0003
091947+334459	$09^h\ 19^m\ 46.84^s$	33°44'58.69"	2.2	36	2.43 ±0.05	0.197	5.2	0.027 ±0.003
091811+333956	$09^h\ 18^m\ 11.10^s$	33°39'55.98"	2.88	142	2.24 ±0.08	-0.219	9.0	0.035 ±0.003
091931+332605	$09^h\ 19^m\ 31.29^s$	33°26'05.30"	0.77	12.3	2.60 ±0.04	0.108	1.8	0.0095±0.0006
091946+332359	$09^h\ 19^m\ 45.53^s$	33°23'58.65"	11.6	39	3.59 ±0.04	0.543	5.6	0.142 ±0.009
092006+332307	$09^h\ 20^m\ 05.53^s$	33°23'06.83"	0.47	4.7	2.41 ±0.11	0.002	3.4	0.0057±0.0005
092037+334222	$09^h\ 20^m\ 37.16^s$	33°42'22.22"	1.60	83	2.25 ±0.07	0.173	2.8	0.0195±0.0011
092002+330608	$09^h\ 20^m\ 01.84^s$	33°06'08.23"	0.38	3.3	2.68 ±0.05	0.214	2.3	0.0046±0.0005
091849+341407	$09^h\ 18^m\ 48.58^s$	34°14'07.16"	1.71	32	2.529±0.022	0.059	2.7	0.0209±0.0013
091855+341348	$09^h\ 18^m\ 54.99^s$	34°13'47.79"	0.63	3.7	2.56 ±0.06	0.152	1.8	0.0077±0.0007
091913+325919	$09^h\ 19^m\ 13.16^s$	32°59'18.51"	1.78	9.8	2.958±0.018	0.125	2.3	0.0217±0.0022
091918+331925	$09^h\ 19^m\ 18.03^s$	33°19'25.18"	0.63	6.4	2.43 ±0.06	0.164	2.7	0.0077±0.0005
091929+332741	$09^h\ 19^m\ 28.84^s$	33°27'41.36"	1.36	10.3	3.548±0.019	0.157	2.4	0.0167±0.0014
091939+335404	$09^h\ 19^m\ 39.49^s$	33°54'04.20"	0.50	7.7	2.95 ±0.08	0.182	1.7	0.0061±0.0004
092018+332346	$09^h\ 20^m\ 18.20^s$	33°23'45.54"	51	22	2.936±0.010	0.146	13.2	0.62 ±0.05
092021+331629	$09^h\ 20^m\ 20.51^s$	33°16'29.34"	0.53	1.4	2.476±0.016	0.049	4.2	0.0065±0.0006
092021+332656	$09^h\ 20^m\ 21.18^s$	33°26'56.04"	1.8	4.9	3.21 ±0.06	0.131	7.6	0.022 ±0.004
092029+334302	$09^h\ 20^m\ 28.69^s$	33°43'02.03"	4.42	25	2.44 ±0.07	0.092	2.0	0.054 ±0.003
092038+325925	$09^h\ 20^m\ 37.74^s$	32°59'24.70"	12.1	38	2.96 ±0.04	-1.853	3.2	0.147 ±0.009
092041+334331	$09^h\ 20^m\ 41.00^s$	33°43'31.32"	7.5	36	3.09 ±0.04	0.090	6.1	0.091 ±0.005
092051+325910	$09^h\ 20^m\ 50.68^s$	32°59'09.94"	12	0.54	3.36 ±0.05	0.030	15.8	0.16 ±0.05
092101+332245	$09^h\ 21^m\ 01.39^s$	33°22'44.79"	79	12.5	2.583±0.024	-0.100	13.5	0.97 ±0.10
092001+341741	$09^h\ 20^m\ 00.58^s$	34°17'41.29"	46	108	2.65 ±0.15	0.189	2.9	0.56 ±0.04
091857+341509	$09^h\ 18^m\ 56.69^s$	34°15'08.66"	15.3	3.7	2.86 ±0.03	0.059	9.8	0.187 ±0.016
091742+341219	$09^h\ 17^m\ 42.32^s$	34°12'19.43"	3.2	0.6	3.628±0.010	0.033	12.5	0.039 ±0.016
091906+340030	$09^h\ 19^m\ 05.51^s$	34°00'30.29"	7.3	2.6	3.28 ±0.03	0.078	9.4	0.089 ±0.008
091857+335554	$09^h\ 18^m\ 57.12^s$	33°55'54.38"	3.3	0.86	2.962±0.024	0.058	8.5	0.040 ±0.004
091928+333909	$09^h\ 19^m\ 28.09^s$	33°39'09.46"	23.2	4.7	3.69 ±0.04	0.078	7.7	0.28 ±0.03
091928+333909	$09^h\ 19^m\ 28.09^s$	33°39'09.46"	12	0.49	3.42 ±0.05	0.037	13.4	0.15 ±0.05
091928+333909	$09^h\ 19^m\ 28.09^s$	33°39'09.46"	3.3	1.9	3.25 ±0.03	0.120	3.7	0.040 ±0.004
091928+333909	$09^h\ 19^m\ 28.09^s$	33°39'09.46"	0.42	0.76	2.88 ±0.08	0.082	3.5	0.0052±0.0013

Table 7.18:: Catalogue of A2666 *Working Subsample*.

Name (1)	**RA** (2)	**Dec** (3)	$\mathbf{F}_{H\alpha}$ (4)	$\mathbf{EW}_{H\alpha}$ (5)	$\mathbb{C}_s$ (6)	$\mathbb{A}_s$ (7)	$\mathbf{R}_p$ (8)	**SFR** (9)
235020+265446	$23^h\ 50^m\ 19.83^s$	26°54'46.43"	1.16	10.2	2.37 ±0.03	0.057	2.5	0.0203±0.0010
235023+271152	$23^h\ 50^m\ 22.98^s$	27°11'52.29"	0.99	14.8	2.338±0.025	0.088	2.8	0.0174±0.0015
235049+271336	$23^h\ 50^m\ 49.15^s$	27°13'36.11"	5.0	37	1.98 ±0.07	0.197	3.7	0.087 ±0.007
235136+271217	$23^h\ 51^m\ 35.96^s$	27°12'16.50"	22.0	21.0	2.67 ±0.07	0.004	13.1	0.386 ±0.010
235050+270821	$23^h\ 50^m\ 49.78^s$	27°08'20.88"	20.6	5.8	3.28 ±0.03	0.073	12.8	0.361 ±0.015
235117+271213	$23^h\ 51^m\ 17.47^s$	27°12'12.80"	0.86	19	2.33 ±0.10	0.144	3.3	0.0150±0.0017
235118+271438	$23^h\ 51^m\ 17.59^s$	27°14'38.35"	0.79	8.2	2.442±0.006	-0.363	2.8	0.0138±0.0018
235060+271308	$23^h\ 50^m\ 59.98^s$	27°13'08.17"	1.13	9.4	2.66 ±0.12	-0.332	2.9	0.0198±0.0017
235118+271737	$23^h\ 51^m\ 18.43^s$	27°17'36.95"	0.64	7.0	2.63 ±0.15	0.083	2.0	0.0112±0.0009
235101+271528	$23^h\ 51^m\ 01.05^s$	27°15'27.87"	1.13	10.8	2.85 ±0.03	0.102	2.8	0.0197±0.0006
235059+271428	$23^h\ 50^m\ 59.08^s$	27°14'27.93"	1.41	7.2	2.16 ±0.05	0.145	5.1	0.0247±0.0011
235047+271717	$23^h\ 50^m\ 47.48^s$	27°17'17.44"	0.97	5.3	1.86 ±0.06	0.397	4.5	0.0169±0.0011
235101+271720	$23^h\ 51^m\ 00.68^s$	27°17'19.60"	0.43	4.9	2.66 ±0.03	0.119	2.0	0.0075±0.0012
235159+272014	$23^h\ 51^m\ 58.97^s$	27°20'14.40"	0.72	4.3	2.50 ±0.09	0.002	2.8	0.0125±0.0005
235052+270958	$23^h\ 50^m\ 52.21^s$	27°09'58.33"	0.571	16.7	2.73 ±0.04	0.108	2.7	0.0100±0.0004
235056+270736	$23^h\ 50^m\ 55.89^s$	27°07'36.39"	0.54	3.2	2.38 ±0.08	0.088	3.5	0.0094±0.0010
235056+270516	$23^h\ 50^m\ 56.36^s$	27°05'16.06"	0.85	7.0	2.11 ±0.06	0.031	6.6	0.0148±0.0020
235059+270852	$23^h\ 50^m\ 58.60^s$	27°08'51.51"	17.4	47.5	3.00 ±0.07	0.112	3.0	0.305 ±0.007
235130+270318	$23^h\ 51^m\ 30.00^s$	27°03'17.73"	4.62	15.7	2.42 ±0.04	0.169	5.8	0.0810±0.0020
234958+265420	$23^h\ 49^m\ 58.13^s$	26°54'20.41"	29.2	27.1	2.51 ±0.08	0.074	7.4	0.512 ±0.019
235027+274300	$23^h\ 50^m\ 27.05^s$	27°43'00.36"	5.13	34	2.094±0.025	0.028	6.2	0.090 ±0.004
235111+270736	$23^h\ 51^m\ 10.79^s$	27°07'36.38"	4.64	33	2.04 ±0.12	0.230	3.0	0.081 ±0.003
235106+270629	$23^h\ 51^m\ 05.63^s$	27°06'29.03"	3.4	4.8	2.64 ±0.05	0.090	4.1	0.060 ±0.006
235117+271438	$23^h\ 51^m\ 17.46^s$	27°14'37.82"	1.29	4.9	3.03 ±0.08	0.109	3.3	0.0226±0.0007
235247+273755	$23^h\ 52^m\ 47.22^s$	27°37'55.43"	3.62	5.0	2.422±0.010	0.057	5.7	0.063 ±0.004
234917+273704	$23^h\ 49^m\ 16.99^s$	27°37'04.33"	2.73	2.87	2.57 ±0.03	0.077	5.2	0.0478±0.0016
234920+272544	$23^h\ 49^m\ 20.29^s$	27°25'44.23"	11.8	0.91	2.98 ±0.06	0.031	17.0	0.207 ±0.018
234928+272251	$23^h\ 49^m\ 28.44^s$	27°22'50.70"	49	5.5	3.376±0.012	0.082	13.9	0.86 ±0.06
234925+272844	$23^h\ 49^m\ 25.06^s$	27°28'44.00"	3.4	1.05	3.08 ±0.05	0.053	5.3	0.059 ±0.011
234947+273750	$23^h\ 49^m\ 47.30^s$	27°37'50.48"	39.5	7.9	3.40 ±0.06	0.132	11.9	0.693 ±0.023
235017+274003	$23^h\ 50^m\ 16.92^s$	27°40'02.53"	14.9	3.31	2.89 ±0.05	0.045	12.1	0.260 ±0.008
235022+274241	$23^h\ 50^m\ 21.81^s$	27°42'41.17"	4.7	1.9	3.50 ±0.03	0.079	5.3	0.082 ±0.011
235040+274303	$23^h\ 50^m\ 40.43^s$	27°43'03.30"	126	23.1	2.92 ±0.03	0.170	9.8	2.20 ±0.07
235105+272614	$23^h\ 51^m\ 05.33^s$	27°26'14.04"	13.4	6.9	2.68 ±0.05	0.007	8.6	0.234 ±0.012
235051+274136	$23^h\ 50^m\ 51.41^s$	27°41'35.71"	2.2	0.6	3.94 ±0.05	-1.021	6.6	0.038 ±0.013
235057+274023	$23^h\ 50^m\ 57.18^s$	27°40'22.60"	12.4	3.24	3.32 ±0.04	0.064	4.0	0.217 ±0.009
235106+274227	$23^h\ 51^m\ 05.62^s$	27°42'26.91"	16.7	4.0	2.66 ±0.05	0.077	14.4	0.292 ±0.015
235146+274003	$23^h\ 51^m\ 45.90^s$	27°40'03.06"	4.11	27.1	2.212±0.020	0.074	7.0	0.0720±0.0021
235021+271742	$23^h\ 50^m\ 21.08^s$	27°17'42.09"	1.37	4.5	2.99 ±0.04	0.128	5.0	0.0240±0.0009
235020+265446	$23^h\ 50^m\ 19.89^s$	26°54'46.40"	21.5	19.8	2.89 ±0.07	0.067	13.2	0.377 ±0.011
235050+270820	$23^h\ 50^m\ 49.76^s$	27°08'19.99"	1.14	0.78	3.33 ±0.04	0.181	4.1	0.020 ±0.004
235106+270629	$23^h\ 51^m\ 05.63^s$	27°06'29.13"	3.70	6.3	2.46 ±0.03	0.092	5.2	0.0649±0.0019
235105+271825	$23^h\ 51^m\ 05.42^s$	27°18'25.05"	5.8	5.3	2.57 ±0.04	0.134	6.3	0.102 ±0.005
235040+274309	$23^h\ 50^m\ 40.25^s$	27°43'09.32"	22.1	6.3	3.69 ±0.04	0.102	12.1	0.39 ±0.03

7.3.1 Structural parameters of the individual Hα-sources: concentration and asymmetry.

Star formation (SF) activity in galaxies is a powerful scent of recent signature of interaction (or absence of), evolution and near environment. But there is as much information in the amount of SF as in the shape, location and concentration. Here we add a valuable information to the precedent sections.

Morphs: compactness and asymmetry.

It is known that the SF activity changes in discs along the Hubble sequence are produced by an increase in the number of SF regions and by an increase of the characteristic masses of individual regions (Kennicutt et al. 1989; Kennicutt 1998). All those variations can be recorded and expressed by the morphological parameters: compactness and asymmetry.

Many recent attempts of establishing a robust combination of this parameters, in order to define a firm basis to describe internal structure of galaxies have been carried out (Abraham et al. 1996; Conselice 1997; Conselice et al. 2000; Lauger et al. 2005; Yagi et al. 2006). This resulted in a favourable scenario, given the abundant means, to investigate current SF emission and its relation with the structure since it would settle a starting point for comparisons in the star formation area.

Since a correlation between the asymmetry/compactness and the morphological type is known a time ago (Kennicutt 1998), we looked for peculiar behaviours of these correlations in clusters. Figs. 7.11 and 7.12 show not only a general guideline of behaviour that avoids great values of EW for low asymmetries and for great values of compactness.

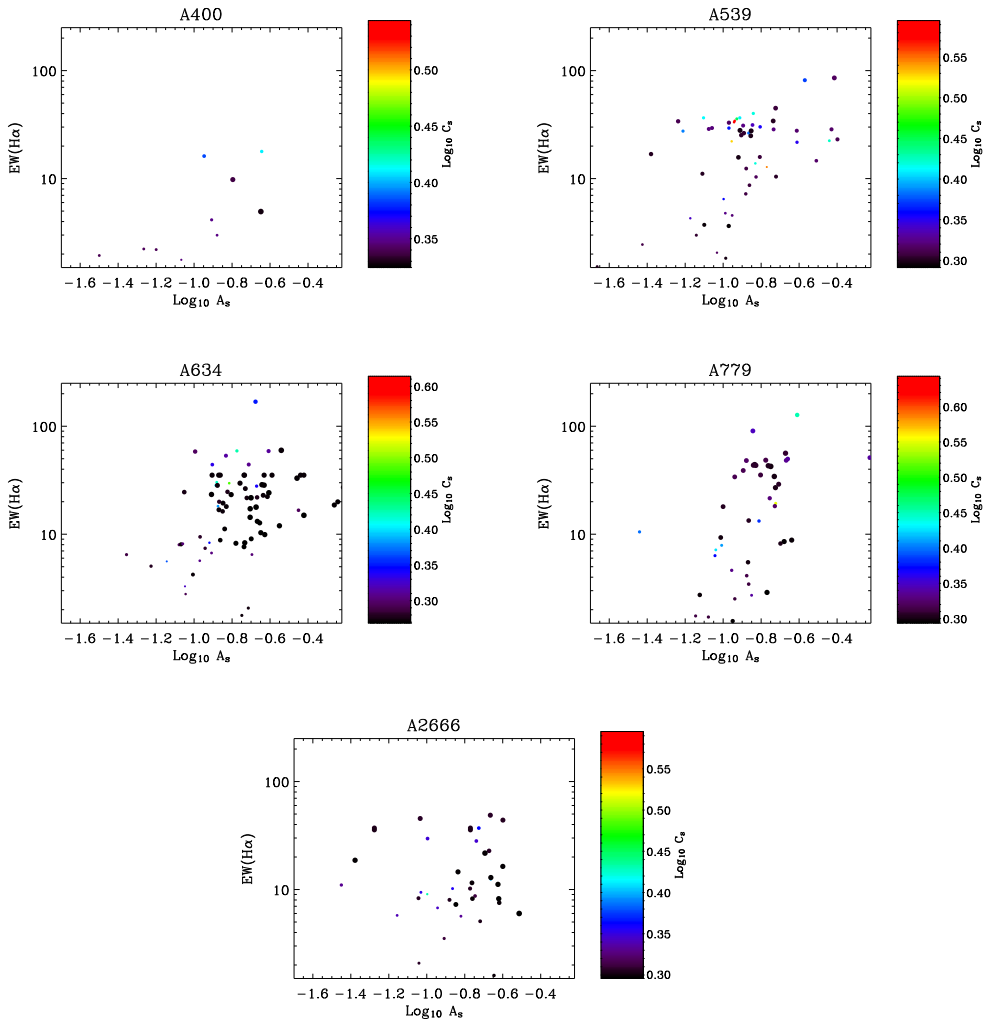

Figure 7.11:: EW(Hα) versus logarithm of Asymmetry. Colour-coded points follow the adjacent bar for values of compactness. Point size is inversely related to the brigth of the source throuhg the $R_{Cousins}$ mag. (The more bright source is the more small its point is.)

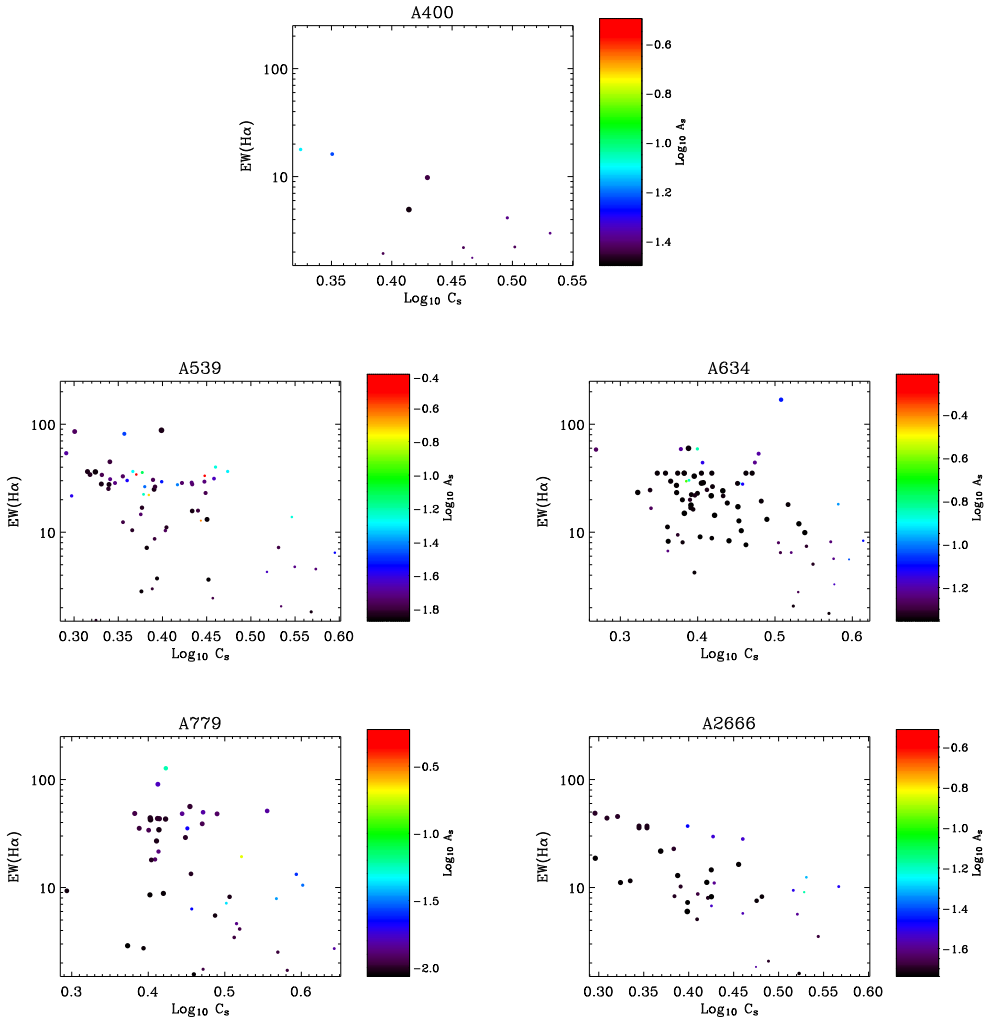

Figure 7.12:: EW(Hα) versus logarithm of Concentration. Colour-coded points follow the adjacent bar for values of asymmetry. Point size is inversely related to the brigth of the source throuhg the $R_{Cousins}$ mag. (The more bright source is the more small its point is.)

In fig. 7.13 we confronted the concentration $\mathbb{C}_S = 5 \cdot Log(\frac{r_{80}}{r_{20}})$ and the asymmetry $\mathbb{A}_s = \frac{\sum|I^\theta - I|}{2\ \sum|I|} - \mathbb{A}^s_{bg}$ derived for every single galaxy in the working subsample. Solid lines are the criteria from Bershady et al. (2000) to discriminate between main spectral types, and a collection of disjoint areas inferred from Lauger et al. (2005) drawing the probably loci for a number of circumstances and morphological classification have been overplotted with colour code as follows: mergers are on green, spirals+irregulars on blue, central starburst on yellow, compacts on orange, and ellipticals on red.

Moss & Whittle (2000) founds a trend to show compact SF if emission comes from variation of the local density. In fact, on fig. 7.13 where the compactness and asymmetry can be compared to the typical elliptical or great spiral with central starburst by means of the coloured areas, we see that, globally, SF sources in clusters tend to be compact, however the central starburst region is practically empty in every studied cluster supporting the idea that there is no affection to the whole mass of the galaxy, only external parts interact with the medium and other galaxies" (REFERENCIAS), on the discussion about the galaxy evolution in cluster, and making of ram-pressure stripping the major environment effect taking place within the virial radius of cluster[10]. Taking as true the merger loci in that diagram, fig. 7.13, I would like to point out that there is not a high rate of merger in cluster environment within the r_{200}, as expected by the . A typical SF galaxy in a cluster of galaxies is, then, a small late-type or compact source with asymmetry and compactness values similar to those of the BCD of Cairós PhD thesis.

The shortage of points in fig. 7.13 for Abell 400 is due to the reasons claimed in the second par. on $ 7.3.

[10] Apparently no matter about the richness of the cluster considered

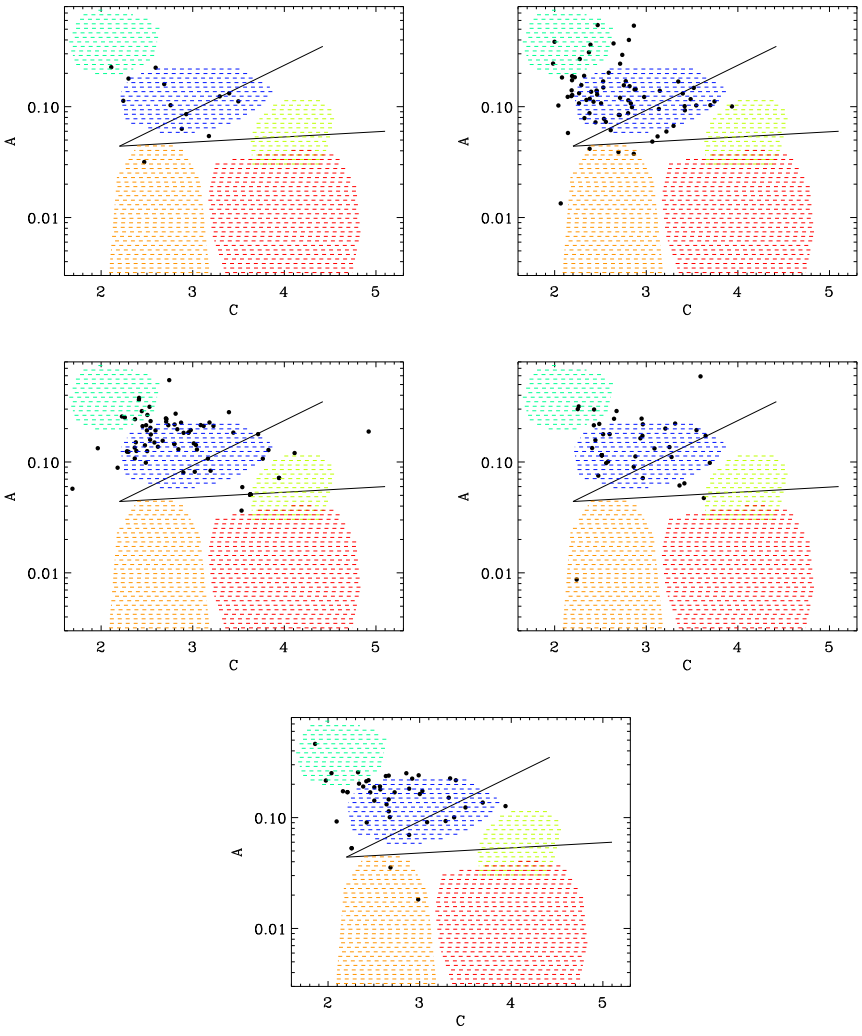

Figure 7.13:: These figures show the concentration for the continuum (in abcisses), against the asymmetry (in ordinates) for the SF galaxies studied in this work (*Working Subsample*). Coloured regions are marking the most probably loci for mergers (in green), spirals+irregulars (in blue), central starburst (in yellow), compacts (in orange), and ellipticals (in red) (according to Lauger et al. (2005))

7.3.2 Radial and Surface brightness profiles in SF galaxies.

Radial profiles for every single extended galaxy with ongoing activity of star formation have been computed using an own-developed IDL programme. Fitting were not carried out and only the surface brightness profiles for ON and OFF filters have been derived. These data would allow us to study if exists truncation and how the scale length is compared to the isolated and virgo cluster galaxies presented in Koopmann & Kenney (2004b).

Firstly, for anchoring the comparison framework with Virgo and Koopmann's isolated data we go to study how the extension of a galaxy is with regard to its integrated absolute magnitude at the isophote 24 (mag arcsec^{-2}). Koopmann (1997) have found that there is no significatively differences between the relation $M_R(r_{24})$-r_{24} for isolated and virgo members in a sample of selected bright galaxies. In fig 7.14, for bright galaxies (M_R <-19) the loci occupied by our sample of galaxies do coincide fairly[11] with Koopmann points. Nevertheless, the extrapolation to the faint population of the fitting suggested by the authoress does not trace in any case the trend presented by the points for the faint galaxy population. In fact, the relative weight of faint galaxy points in Abell 779 (fitted by the blue solid line) appears as the most deviated from the general tendency for the whole sample points fitting (blue dashed line), and ask us for a test for checking the SF truncation radius in every cluster.

A more than likely understimation of the slope for the fit between the $M_R(r_{24})$ versus the r_{24} just with the virgo and isolated points is showed up in fig. 7.14. Nevertheless, apart of this effect, and apart of that mild transition between clusters following an order sorted by the dense/warm intracluster medium suggested by the change of slope, it could be pointed out firmly that the stellar scale length does not suffer apparently differential variation between field and environment within the virial radius in our defined sample of cluster.

[11] Abell 539 shows more scattering at brighter magnitudes

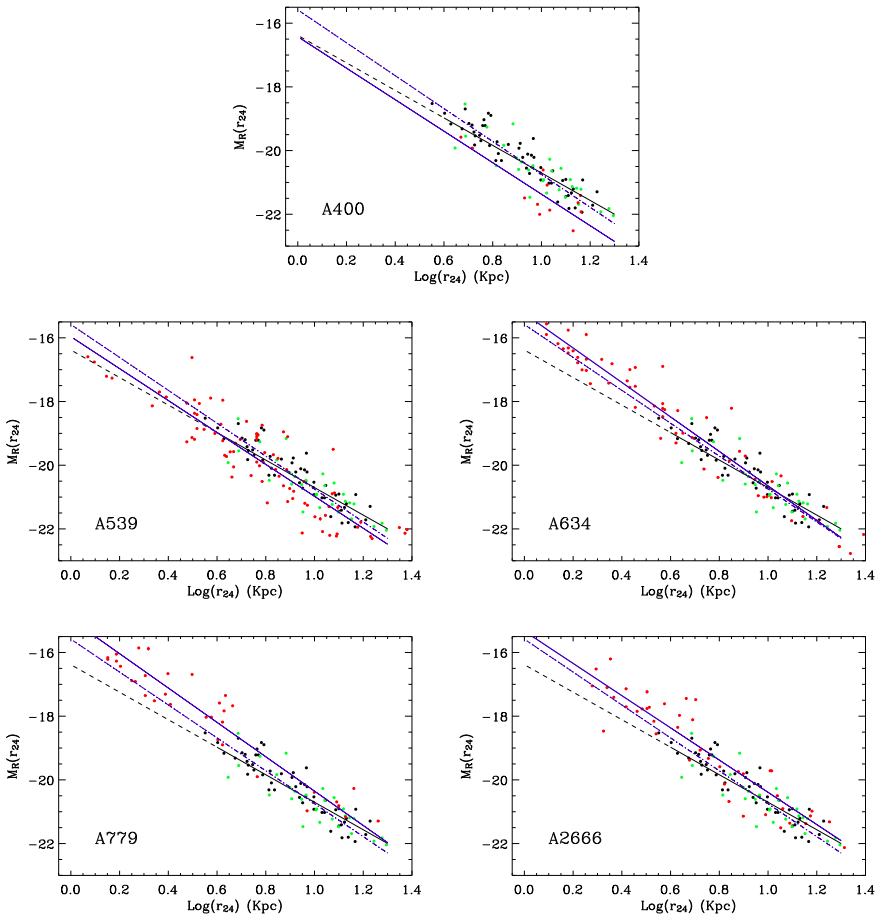

Figure 7.14:: M_R at r_24 versus the logarithm of the r_24. On every plot solid black line with the extension dashed follows the fit presented in the Koopmann's PhD thesis. The point-dashed thin blue line represents the fit for the whole (4 cluster Abell 539, 634, 779 and 2666 dataset). Solid blue line traces the fit for the cluster represented considered individually. Red points are from the considered cluster. Green points are the isolated and black points are the virgo values from Koopmann & Kenney (2004b).

On fig. 7.15 we found overplotted the median of the radial Surface Brightness profile for the SF galaxies ($SB_{H\alpha}$) in our sample of clusters on points for field and Virgo galaxies (Koopmann & Kenney 2004b). The requesting for deriving the profile in our galaxies is to verify[12] that the absolute magnitude is brighter than -19.5 and the petrosian radius is greater than or equal to 3 arcsec. Nuclear emission in isolated and Virgo galaxies stands out above the Hα galaxy profiles in our cluster sample. But looking only at the disc emission it could be appreciated such a tendency as an increasing slope that can be seen qualitatively related to an increasing of X-ray bolometric cluster luminosity, suggesting a there is a mild trend of the known relation between the ICM and the ram-pressure stripping, and the two of them together with the discs truncation which shortens the scale length for spirals in cluster.

Abell 539 cluster shows an abrupt drop of the SB(Hα) profile compared to the rest of cluster pointing the ram pressure stripping as the main effect taking place in a medium rich X-ray luminous cluster for shortenning the SF radius. According to Boselli & Gavazzi (2006), the effect of the ram pressure, taking into account that the stellar lengths are preserved at long wavelengths ($\lambda_R \simeq 6000$Å), can be dated, being younger than a hundred of Myr. The high efficiency in sweeping up the external parts of the gas from discs.

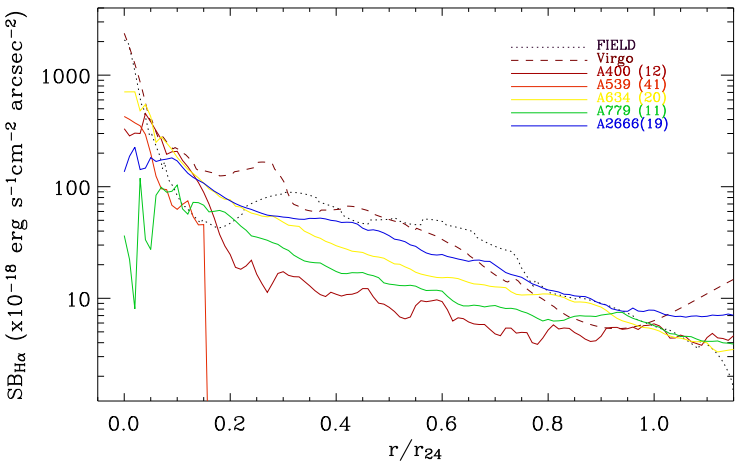

Figure 7.15::

[12]in order to ensure we are observing an extended and uniform set of bright galaxies

7.4 Discussion. Correlation with fundamental properties of the clusters.

It can easily checked that there is no relationship among the clusters properties, considered globally, which drive us to think they are similar at all. However, we already presented in §7.1.1 a test and significances pointing a moderate high probability of having similar parental distributions in the EW and L(Hα) for galaxies of some "poor clusters" and field galaxies, and rejecting the similarity among the original distribution of EW and L(Hα) for galaxies in x-ray luminous clusters and field galaxies. During the same discourse, two of the low velocity dispersion/x-ray poor clusters show a high likelihood of having a common origin for the EW and Fluxes of Hα line in their galaxies. Thus, the frame we could drawn is to start separating in rich and in poor clusters. Nonetheless the properties phase-space between them is not empty. In fact we found that for some properties (EW or Hα distribution) for the Abell 634 approach to a, let say, poor-cluster behaviour, while other properties approach to the rich-cluster (defined here by Abell 400 and 539) behaviour. Then, does it exist a property which could link the two "families" of environment for SF galaxies? If we use a figure[13] for each cluster related in some to the virial status, for instance σ_v (velocity dispersion) - see fig. 7.16, it can be seen that all of the clusters in the sample, richs and poors, follow the same tight correlation. This diagram 7.16 represents the fraction of spectroscopically confirmed bright (M_R ¡ -20) galaxy members f_{SF}^{G} versus the velocity dispersion of the host cluster.

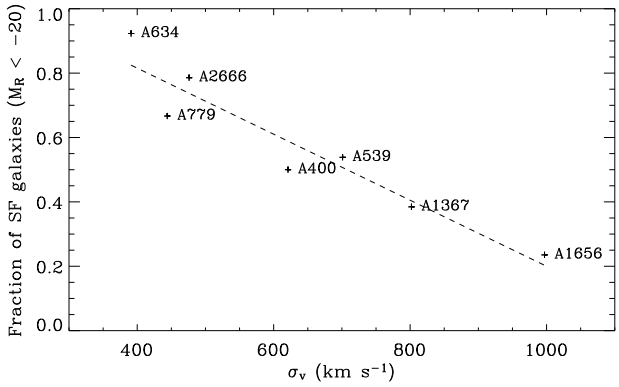

Figure 7.16::

[13]related to the X-Rays or to the amount of cluster members

Although the σ_v have been proven to be correlated with the X-ray luminosity and hence with an evolutionary stage of the host cluster, it can be argued that this velocity dispersion could be deviated/unrelated to the true virialization phase for a determined number of members (a fixed total mass) of a cluster, since some substructures can contribute significatively to the σ_v: a fact what change the connection to the expected system relaxation.

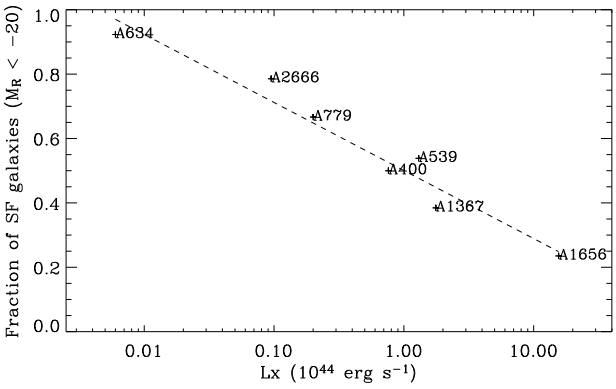

Figure 7.17::

On fig. 7.17 we found a similar tight correlation between f_{SF}^{G} and the X-ray bolometric luminosity[14] for every cluster.

[14]Taken from the literature (White et al. 1997).

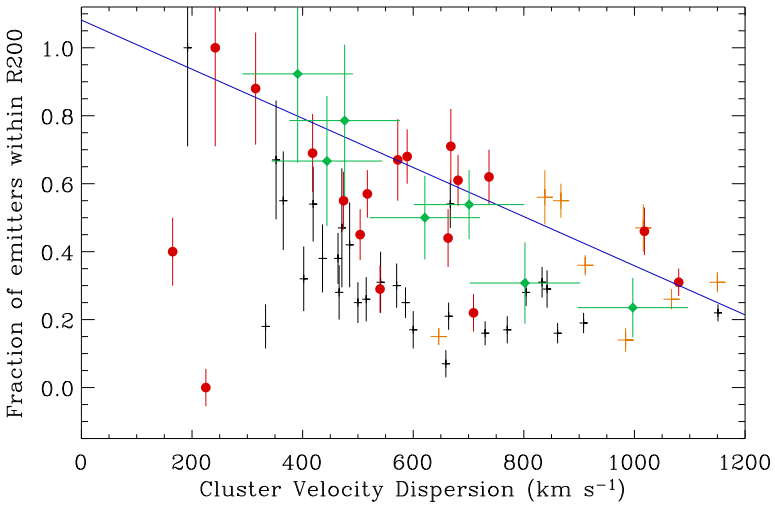
Fraction of emitters within R200
1.0
0.8
0.6
0.4
0.2
0.0
0
200
400
600
800
1000
1200
Cluster Velocity Dispersion (km s^{-1})

Figure 7.18::

CHAPTER

8

SPECTROSCOPIC FOLLOW UP

8.1 Photometry for peculiar objets: DRP A634a and DRP A539a

From the catalogues (chap. 7), we selected to extreme objects in order to carry a spectroscopic follow up. In this section a summary of the photometric properties, table 8.1, as well as a trimmed sky section around the sources is shown (figs. 8.1 and 8.2).

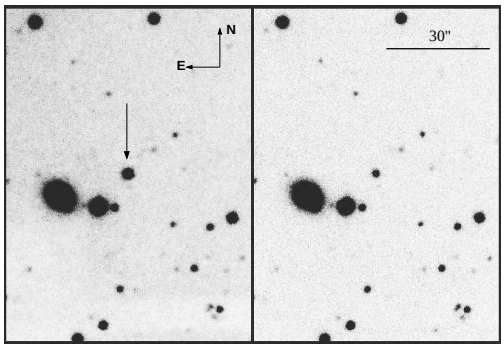

Figure 8.1:: ON-band (Hα - left) and OFF-band (red continuum - right) images of DRP-A539a region. The arrow indicates the position of the object.

Both objects, DRP-A539a and DRP-A634a, appear very compact and much brighter in ON-band than in OFF-band, as shown in figs 8.1 and 8.2. While DRP-A539a appears to be an isolated source, a diffuse low surface brightness structure has been detected extending North East from DRP-A634a. Hereinafter, the compact source will be referred to as DRP-A634a, whereas the diffuse low surface brightness structure will be named LSB-A634a. Some knotty faint Hα emission can be seen at the northern tip of LSB-A634a, which will be referred to as LSB-A634a_knot. Table 8.1 shows the relevant photometric properties of these objects, as measured from our Hα and continuum frames. The luminosities have been corrected for Galactic extinction following Schlegel et al. (1998), and the Cardelli et al. (1989) extinction curve. The Hα+[NII] luminosity of LSB-A634a_knot has been estimated assuming that it is located at the same distance as DRP-A634a[1].

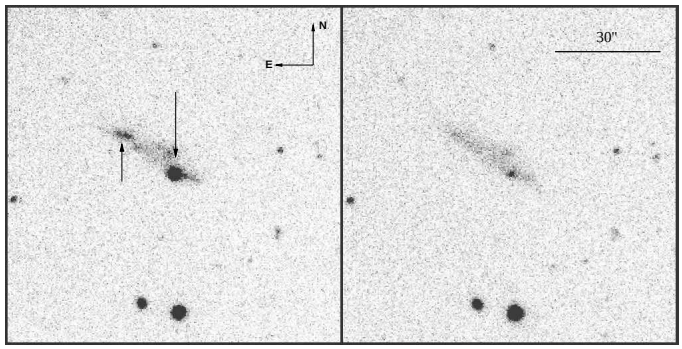

Figure 8.2:: ON-band (Hα - left) and OFF-band (red continuum - right) images of DRP-A634a region. The downward arrow indicates the position of DRP-A634a. The upward arrow points to LSB-A634a_knot . The low surface brightness structure apparent in the right panel is LSB-A634a.

Object	**R.A. (J2000)**	**Dec. (J2000)**	L(**H**α+[**N**II]) (**10**^{40} **erg s**$^{-1}$)	**EW**(**H**α+[**N**II]) (**Å**)	r' **(mag)**
DRP-A539a	$05^h\ 16^m\ 51.7^s$	$+06^o$ 19' 32.1"	1.66 ± 0.05	410 ± 50	19.82
DRP-A634a	$08^h\ 13^m\ 55.6^s$	$+58^o$ 02' 32.4"	4.4 ± 0.4	1010 ± 230	20.75†

Table 8.1:: Basic photometric properties of DRP-A539a and DRP-A634a: (1) Object; (2) R.A.; (3) Dec.; (4) Luminosity of the Hα+[NII] (extinction corrected, see body text); (5) Hα+[NII] equivalent width; (6) Synthetic absolute B magnitude; and (7) *Sloan r'* magnitude. †synthetic r'.- see the text for details

[1]The possible origins of these objects and their environment will be discussed in §8.2.

8.1.1 Spectroscopy observations

Long slit spectroscopy of DRP-A539a, DRP-A634a and LSB-A634a was obtained with the Alhambra Faint Object Spectrograph and Camera (ALFOSC) attached to the 2.5m Nordic Optical Telescope (NOT) at the ORM on 19th November 2004 and 9th December 2004. Grisms #8 and #14 were used, giving useful spectral ranges of λ5825–8350Å and λ3275–6125Å respectively. The spatial resolution across the slit was 0.19" pix^{-1}. During the first night, the slit width was set to 1.2" resulting in an effective spectral resolution of 7.1 Å and a 1800 s exposure for each spectral range was obtained for DRP-A634a. The second night was devoted to DRP-A539a and LSB-A634a. Due to an improvement in the weather conditions the slit width was set to 0.4", yielding a spectral resolution of 2.8 Å. A total of 3×1800 s exposures for each spectral range of DRP-A539a were taken with the slit oriented along the parallactic angle. Finally, a 600 s exposure using grism #8 was performed in order to observe the extended emission of LSB-A634a; in this case, the slit was centered on DRP-A634a and was carefully oriented at an angle of 54^o (from North to East). Due to an increase in the humidity, this exposure was stopped after 600 s. Table 8.1.1 shows the log of spectroscopic observations.

Object	**Date**	**Spect. Range (Å)**	**Exp. Time (s)**	**Slit width (arcsec)**	**Position angle (deg)**
DRP-A634a	2004-11-19	3700-6100	1×1800	1.2	PA†
DRP-A634a	2004-11-19	6000-8000	1×1800	1.2	PA
DRP-A539a	2004-12-09	3700-6100	3×1800	0.4	PA
DRP-A539a	2004-12-09	6000-8000	3×1800	0.4	PA
DRP-A634a	2004-12-09	6000-8000	1×600	0.4	54

Table 8.2:: Spectroscopy Observations log. † PA = Paralactic Angle

Data reduction was performed using IRAF, following the standard procedure of bias correction, flat-fielding and wavelength and flux calibration. 1-D spectra of DRP-A539a and DRP-A634a were extracted by adding the flux in the spatial sections along the slit which maximize their signal to noise ratios. A total of 10 and 7 pixels were added for DRP-A539a and DRP-A634a respectively. The same procedure was followed to extract a 1-D spectrum for LSB-A634a. As a consequence of its low surface brightness only a faint emission line, spatially corresponding to LSB-A634a_knot, was obtained after adding a total of 21 pixels. As indicated below, this emission line was identified as Hα.

Both nights were only partially photometric, so an absolute spectrophotometric flux calibration was not attempted. However, the spectrophotometric standard star Hiltner 600 was observed before and after each object with each grism, thus a relative calibration of the spectra in physical units was performed.

The spectra corresponding to the red grism were scaled to the blue ones by using the continuum level and the flux of the [HeI]λ5876Å line, present in the blue and red spectra. The scaling factors were found to be ~ 1 within an error bar of $\sim 20\%$. Beyond 7600Å fringing effects begin to be noticeable and data at longer wavelengths is ineffective. Figures 8.3 and 8.4 show the combined (red grism + blue grism) spectra of DRP-A539a and DRP-A634a respectively. Both spectra are dominated by narrow emission lines and show a very faint underlying continuum.

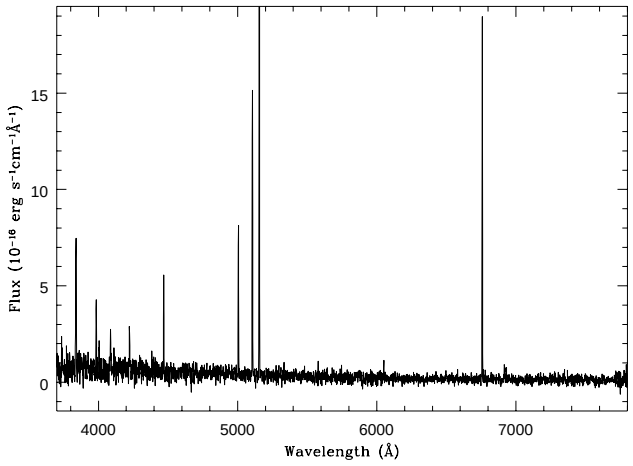

Figure 8.3:: Combined spectrum of DRP-A539a scaled to [OIII]λ 4959 Å.

The emission lines were measured with the IRAF task splot. The errors of the line fluxes are estimated from the standard deviation of a series of independent repeated measurements, sampling the adjacent continuum for each line. In order to calculate the extinction, the Balmer decrement was computed using the Hα, Hβ, Hγ and Hδ line fluxes and compared to their theoretical values (Hummer & Storey 1987).

Given the low continuum shown by both objects, no correction for underlying absorption was performed.

Radial velocities were computed from a sigma-weighted average of the red-

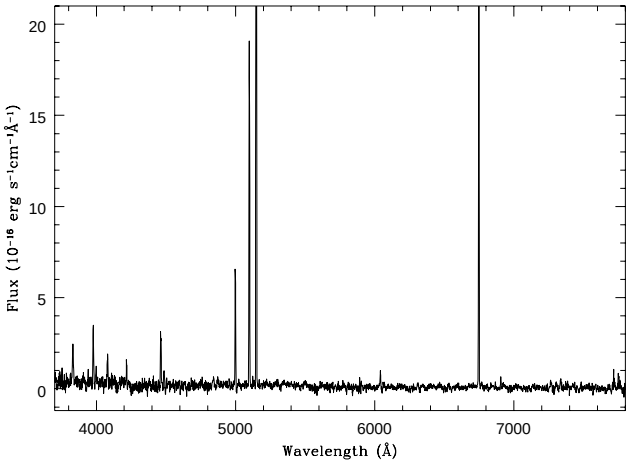

Figure 8.4:: Same as Figure 8.3 for DRP-A634a.

shifts corresponding to the individual emission lines. After applying the heliocentric corrections, values of $v_{rad} = 8940 \pm 40$ km s^{-1} and 8470 ± 30 km s^{-1} were found for DRP-A539a and DRP-A634a respectively. The quoted errors correspond to the standard deviations of the velocities derived from individual lines. The measured velocities are offset by about 500 km s^{-1} from the mean heliocentric velocities adopted for the parent clusters. As will be discussed in Sections 4.1 and 4.2, the projected positions of our two objects with respect to the center of the clusters, together with their redshifts, are consistent with their corresponding cluster memberships.

In the spectrum of LSB-A634a_knot, shown in fig. 8.5, despite the low signal to noise ratio, an emission line was detected at the 3.5 σ level. This line, centered at $\lambda = 6747$Å is almost coincident with the wavelength of the Hα line of DRP-A634a. Assuming that this line effectively corresponds to Hα, a radial velocity of 8390 km s^{-1} is inferred for LSB-A634a_knot, after correcting for heliocentric relative motions.

In table 8.3 we present the spectroscopic properties of DRP-A539a and DRP-A634a: reddening corrected line fluxes, reddening coefficient $C(H\beta)$, equivalent widths of Hβ, Hα and [OII], Hβ flux, as well as the fluxes of the

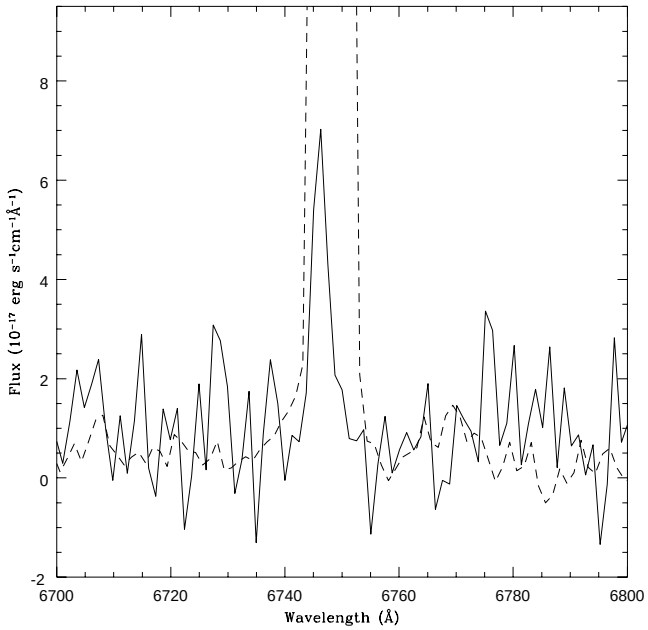

Figure 8.5:: The solid line shows the spectrum of LSB-A634a_knot, spatially binned to increase the signal to noise ratio. The dashed line shows the spectrum of DRP-A634a around the Hα line. The scale of the flux axis has been set to show the Hα line of the knot component.

most prominent emission lines relative to Hβ. As can be seen, the values reported for the Hα equivalent width, though slightly larger than the ones derived from Hα imaging are consistent within the errors.

Table 8.3 also shows the electron temperatures and oxygen abundances derived using *temden* and *ionic* tasks in the IRAF *nebular* package in STSDAS. Oxygen abundances were derived directly from spectral lines of [OII]λ3727, [OIII]$\lambda\lambda$4959,5007 and using their electron temperatures from the measurements of [OIII]λ4363.

Table 8.3 also shows the electron temperatures and oxygen abundances derived using *temden* and *ionic* tasks in the IRAF *nebular* package in STSDAS. Oxygen abundances were derived directly from spectral lines of [OII]λ3727, [OIII]$\lambda\lambda$4959,5007 and using their electron temperatures from the measurements of [OIII]λ4363.

Line	λ **(Å)**	f_λ	**DRP-A539a**	**DRP-A634a**
[OII]	3727	0.28	1058 ± 7	375 ± 17
[NeIII]	3868	0.24	522 ± 14	419 ± 80
HI	3889	0.24	210 ± 19	112 ± 15
HI	3970	0.22	320 ± 30	258 ± 17
[SII]	4068	0.20	77 ± 15	——
Hδ	4101	0.19	268 ± 15	171 ± 22
Hγ	4340	0.13	513 ± 10	473 ± 21
[OIII]	4363	0.13	70 ± 20	202 ± 16
HeI	4471	0.10	——	53 ± 13
[ArIV]	4711	0.04	——	59 ± 14
Hβ	4861	0.00	1000 ± 16	1000 ± 10
[OIII]	4959	-0.04	1869 ± 7	2740 ± 14
[OIII]	5007	-0.05	5280 ± 40	8272 ± 10
HeI	5876	-0.26	73 ± 8	105 ± 10
Hα	6563	-0.37	2827 ± 5	2789 ± 5
[NII]	6584	-0.37	47 ± 5	27 ± 5
HeI	6678	-0.38	——	29 ± 5
[SII]	6717	-0.39	112 ± 10	46 ± 5
[SII]	6731	-0.39	130:	29 ± 5
HeI	7065	-0.43	——	58 ± 7
[ArIII]	7135	-0.44	——	85 ± 9
C(Hβ)			0.27	0.47
T_e([OIII])	(K)		12800 ± 1500	16800 ± 700
T_e([OII])	(K)		11900 ± 1000	14800 ± 500
12+log(O^+/H^+)			7.65 ± 0.14	6.75 ± 0.06
12+log(O^{++}/H^+)			7.93 ± 0.14	7.83 ± 0.05
12+log(O/H)			8.12 ± 0.14	7.87 ± 0.06
F(Hβ)	(10^{-15} erg cm^{-2} s^{-1})		4.21 ± 0.09	8.75 ± 0.08
EW(Hβ)	(Å)		77 ± 17	280 ± 90
EW(Hα)	(Å)		510 ± 90	1290 ± 120
EW([OII])	(Å)		70 ± 15	110 ± 40

Table 8.3:: Reddening corrected line intensities of the Objects DRP-A539a and DRP-A634a relative to Hβ=1000. The reddening coefficient C(Hβ), electron temperatures, oxygen abundances, as well as the Hβ flux and the equivalent width and for Hβ, Hα and [OII] are quoted. Hβ flux has been corrected for Galactic and intrinsic extinction using the extinction law $R = 3.1$ and their C(Hβ)

8.1.2 Results

Figure 8.6 shows the radial profiles[2] of DRP-A539a and DRP-A634a, derived from our sharpest images. The first is marginally different from the typical stellar profile, showing a radius at half maximum $r_{FWHM} \simeq 0.44''$ ($\langle r^{star}_{FWHM} \rangle \simeq 0.39''$). The second is almost indistinguishable from the stellar profile, with $r_{FWHM} \simeq 0.39''$ ($\langle r^{star}_{FWHM} \rangle \simeq 0.38''$). After correcting these profiles for the effect of seeing under the assumption of gaussian PSF[3], effective (half light) radii of 0.14" and 0.09" are derived, which correspond to 84 and 32 pc for DRP-A539a and DRP-A634a respectively. These effective radii are lower than most values presented for misclassified compact galaxies in the Millennium Galaxy Catalogue (Liske et al. 2006) and resemble the values typically shown by UCDGs in nearby clusters (Drinkwater et al. 2004).

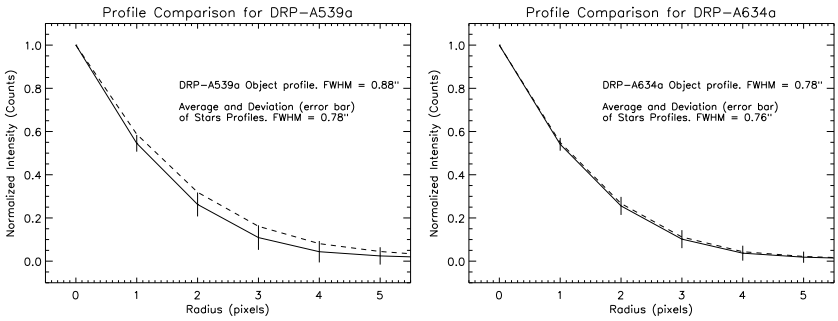

Figure 8.6:: Radial profiles of DRP-A539a (left panel) and DRP-A634a (right panel) indicated by the dashed lines. The solid lines correspond to the stellar profiles averaged over a large number of stars for each frame.

As concerns LSB-A634a, the length of its major axis from our continuum image was estimated to be $\approx 28''$. At the distance of DRP-A634a this length corresponds to 16 kpc. This value is in good agreement with the dimensions of edge-on disc galaxies. The angular size of the system argues against it being a high redshift object. If, for example, the emission line reported in Section 2.2 was one of the [OIII] lines, the redshift would be $z \approx 0.35$, and the corresponding diameter of the system at such a distance would be 138 kpc, which is highly unlikely for an edge-on galaxy. For the same reason, we can

[2]We derived the radial profiles using the IRAF task *radprof*. This task fits a point spread function on each star and selected objects in the field through an input coordinate file, deriving a Full Width at Half Maximum of the fitted profile.

[3]Driver et al. 2005 have reported a slight deviation of a gaussian behaviour when correcting effective radii of galaxies for the effect of seeing in the Millennium Galaxy Catalogue (MGC). For the scope of this work gaussianity behaviour of the PSF is assumed.

discard the possibility of this system being located at larger distances.

Broad band magnitudes can be derived for DRP-A634a since SDSS frames are available. Aperture photometry corrected for Galactic extinction of DRP-A634a yields $M_{g'} = -15.81$ mag and $M_{r'} = -14.50$ mag. The broad band magnitudes of the composite system LSB-A634a+DRP-A634a were also derived, obtaining $M_{g'} = -17.38$ mag and $M_{r'} = -17.30$ mag. Since DRP-A539a was observed with the *Gunn r'* filter, a value of $M_{r'} \approx -16.07$ mag was estimated for this galaxy. By applying the average $g' - r' = -0.02$ mag of the sample of Ultracompact Blue Dwarf Galaxies of Corbin et al. (2006), a value of $M_{g'} \approx -16.09$ is obtained for DRP-A539a. The magnitudes derived for DRP-A539a and DRP-A634a are brighter than those typical of early-type UCDGs in clusters (Mieske et al. 2006). Nevertheless, the Starburst99 model (Leitherer et al. 1999) predicts that the optical magnitudes of an instantaneous burst of star formation can fade by more than 3 magnitudes in about 10^8 yr. These results together with the limits to the sizes of DRP-A539a and DRP-A634a, open the possibility of them being the progenitors of early-type UCDGs recently found in nearby clusters.

The equivalent widths of the most conspicuous Balmer emission lines of our two objects are relatively high: EW(Hβ) (77 and 280Å for DRP-A539a and DRP-A634a respectively) are in fact above the median value ($\sim$ 40Å) reported for the sample of HII galaxies of Terlevich et al. (1991) and also for the sample of HI-rich dwarf galaxies in the Hydra cluster of Duc et al. (2001). In addition, EW(Hα+[NII]) (510 and 1290 Å respectively) are several times larger than the corresponding values of star forming dwarf galaxies reported in other clusters such as Fornax (Drinkwater et al. 2001), Virgo (Boselli & Gavazzi 2002,?), Coma (Iglesias-Páramo et al. 2002) and A1367 (Iglesias-Páramo et al. 2002; Cortese et al. 2006). When comparing with the UCBDs of Corbin et al. (2006) we find that the equivalent width of DRP-A539a is among the typical values of this sample, but DRP-A634a remains an extreme case. The high equivalent widths shown by our two galaxies reveal very strong and young star formation activity. The ages and stellar mass of the recent star formation episodes can be estimated from the luminosities and equivalent widths of the Balmer lines. By assuming an instantaneous burst of star formation, and using Starburst99 (Leitherer et al. 1999) for a Kroupa IMF with $M_{up} = 100$ M$_\odot$ and $M_{low} = 0.5, 0.1$ M$_\odot$ and the Padova AGB tracks, we find that the ages predicted are 5.8 and 4.5 Myr (5 and 4 Myr using Geneva High tracks) for DRP-A539a and DRP-A634a respectively. The corresponding masses which are being converted into stars are 2.0 and 2.2 10^6M$_\odot$ respectively, with an

uncertainty of 15%[4]. This computation assumes the approximation that all Lyman continuum photons are absorbed by the gas.

Figure 8.7 shows the luminosity-metallicity relation for dwarf galaxies (after Pilyugin et al. 2004), including the points for DRP-A539a and DRP-A634a, with $M_B = -15.60$ mag and -15.89 mag respectively. B absolute magnitudes have been obtained from $M_{g'}$ after applying the correction term $g' - B = -0.21$, as reported by Fukugita et al. (1995) for late-type dwarf galaxies. The two points follow the mean relation reported for nearby dwarf galaxies and remain far from the locus occupied by typical tidal dwarf galaxies (TDG) (see review by Kunth & Östlin 2000 and references therein). In figure 8.7, the point corresponding to the integrated system LSB-A634a+DRP-A634a appears to separate from the luminosity-metallicity relation by more than 1 mag, being too luminous for the metallicity derived for DRP-A634a (table 8.3).

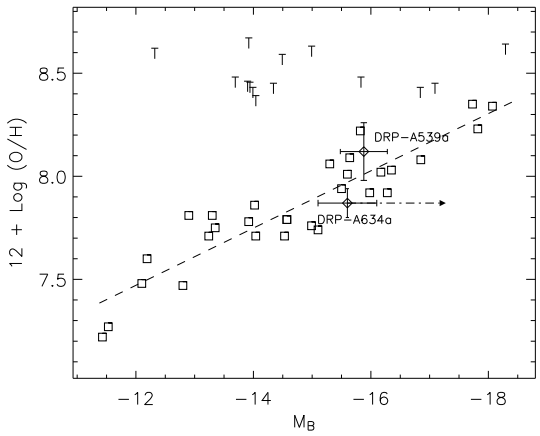

Figure 8.7:: Luminosity-Metallicity relation for nearby dwarfs galaxies (open squares) adapted from Pilyugin et al. (2004). "T" symbols represent Tidal dwarfs (e.g. Kunth & Östlin 2000 and references therein). Our objects are overplotted as open diamonds with their error bars. The position of the luminosity M_B of the ensemble system LSB-A634a+DRP-A634a, is pointed out by the arrow.

[4]The derived values for the age and stellar mass of the burst are the nominal values obtained from the measured imaging Hα flux and corresponding error (derreddening error is included).

8.2 Discussion

8.2.1 DRP-A539a

Figure 8.8 shows the optical DSS (Palomar Digitalized Sky Survey) frame of the inner region of the cluster A539. Contours corresponding to the X-ray emission[5] and to the surface density of galaxies (from 2MASS) of A539 are overlaid. It can be seen that the maxima of surface density of galaxies and X-ray are coincident. The X-ray luminosity of A539 is 6.7 10^{44} erg s^{-1} (White et al. 1997). Its velocity dispersion was estimated to be 629 km s^{-1}, thus giving a total dynamical mass for the cluster of 32×10^{13} M$_{\odot}$ (Struble & Rood 1999). The projected distance of DRP-A539a from the center of A539 is 300 kpc, which corresponds to $0.2 \times r_{200}$. This short distance together with the measured radial velocity of DRP-A539a, ensures that this object is well within the region defined by the caustic of the cluster (see Figure 2 of Rines et al. 2003[6]).

The existence of such an active star forming object at such a short distance from the center of a cluster is unusual and opens several questions about its nature and origin. One possibility is that this object could be a tidal dwarf galaxy, resulting from a galaxy-galaxy interaction. These kinds of objects have been previously reported in different environments such as clusters (Duc et al. 1999, 2000; Iglesias-Páramo et al. 2003b), groups (Iglesias-Páramo & Vílchez 2001; Mendes de Oliveira et al. 2004) or just pairs of interacting galaxies (Mirabel et al. 1992; Duc et al. 2000). TDGs originate out of the tidal features resulting during the interaction, and under certain conditions they can escape the potential well of the parent galaxy and evolve independently (Elmegreen et al. 1993). A visual inspection of the ON-band and OFF-band frames shows no signatures of galaxy-galaxy interactions around DRP-A539a. The closest galaxy is 2MASX J05165377+0619216, an S0 galaxy whose radial velocity is $v = 8063$ km s^{-1}, located at a projected distance of 32 arcsec (about 18 kpc). We analyzed the isophotes of this galaxy and did not find any distortion or abnormal twist of the isophotes that could be taken as a signature of interaction. Moreover, no diffuse emission was detected around this galaxy in the direction of DRP-A539a. In addition, as shown in Figure 8.7, DRP-A539a follows the mean luminosity-metallicity relation derived for a large sample of dwarf galaxies. Based on these arguments, we can discard DRP-A539a as being a TDG.

[5] From 0.4-2.4 Kev ROSAT map.

[6] In the particular case of A539, the caustic appears well defined and any possible contamination is low. However, these authors remark that although the caustic separates cluster members from foreground and background galaxies in a more efficient way than the velocity sigma clipping, still some interloppers may lie within the caustics.

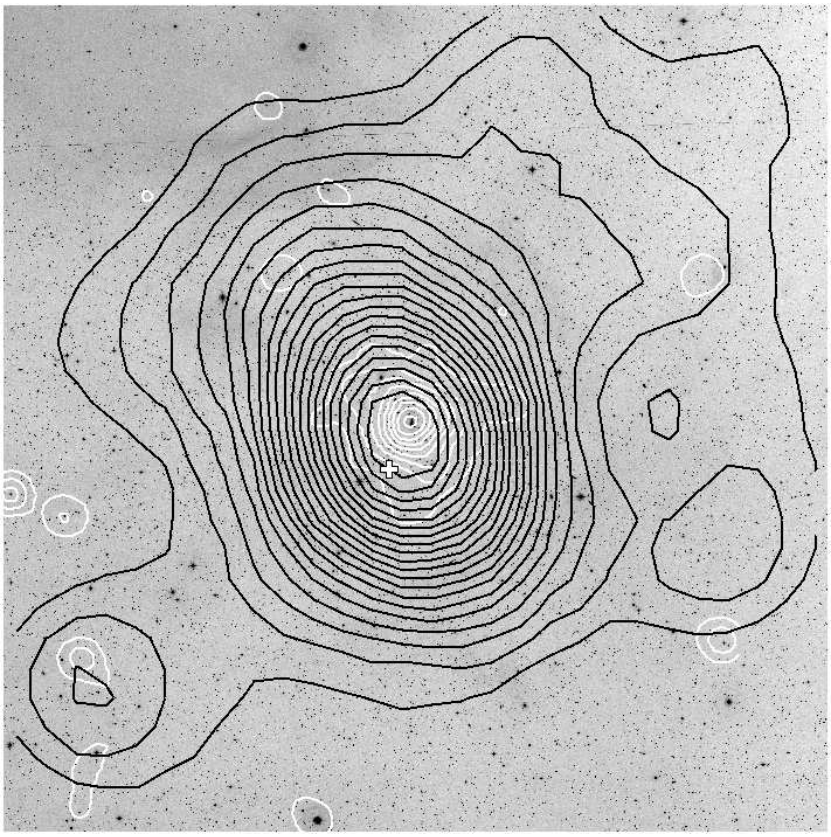

Figure 8.8:: Abell 539 cluster DSS image with X-Ray ROSAT detection (white) and 2MASS galaxy spatial-density contours (black) overplotted (2x2 degrees) (relative units have been used for both contours parameters). Cross marks the position of the compact starburst galaxy relative to the cluster center. (North is to the top and East is to the left.)

Another possibility is that DRP-A539a is the product of ICM-induced efficient star formation in gas clouds drifting into the cluster (Bekki & Couch 2003). In this scenario the star formation activity results from the compression of molecular clouds stripped from spiral galaxies through galaxy-galaxy or galaxy-tidal field interactions. Isolated intra-cluster HII regions have already been reported in the Virgo cluster (Gerhard et al. 2002; Cortese et al. 2004). However, these HII regions are more than one order of magnitude less luminous than DRP-A539a. It should be noted that the objects studied in Cortese et al. (2004) are located close to the two bright spirals VCC 836 and VCC 873, which are probably their progenitors. Nonetheless, DRP-A539a does not appear to be associated to any gas-rich bright galaxy, suggesting that either the parent molecular cloud is the result of an ancient episode of gas stripping, where the stripped galaxy is already far away, or rather we are facing a star forming dwarf galaxy (SFDG) falling for the first time into the cluster core. Theoretical models predict that SFDGs lose their external gas very rapidly when they enter the cluster potential well, due to the ram pressure exerted by the ICM (Mori & Burkert 2000) and also, according to Bekki & Couch (2003),the timescale for transformation of gas into stars due to ICM pressure is of the order of 10 Myr; for this reason we argue that DRP-A539a is in the very early stages of the infall process.

8.2.2 DRP-A634a

Figure 8.9 shows the optical DSS frame of the cluster A634 with the overlaid contours corresponding to the surface density of galaxies derived from 2MASS. This cluster is not detected in X rays by the ROSAT mission, so an upper limit of $6{\cdot}10^{41}$ erg s^{-1} is adopted for its X-ray luminosity. The non detection of X-ray emission means that this cluster is probably in the process of formation and therefore a virialized core is not yet in place. Nevertheless, the smoothed surface density contours from 2MASS show a dense central aggregate of galaxies showing the galaxy cluster location and shape. We must note that the cluster center as indicated by the 2MASS-contours, α = 08:15:08, δ = +58:14:58, is about 12 arcmin away from the center quoted in Struble & Rood (1999). Hereafter, for our dynamical considerations and being conservative, we have adopted the center of the cluster inferred by the 2MASS contours. The heliocentric velocity measured for DRP-A634a differs from the cluster heliocentric velocity by $1.34 \times \sigma_{A634}$ km s^{-1}, and this object is located at a projected distance of 398 kpc from the cluster center. Both values, heliocentric velocity and projected distance, would place DRP-A634a within the caustic of every galaxy

cluster presented in Rines et al. (2003), at the 2 σ confidence level[7]; Especially in the case of A194, a cluster presenting velocity dispersion and extension in the sky very similar to those of A634. The non detection in X-ray of A634 together with the substantial distance of DRP-A634a to the cluster center, may weaken the hypothesis that the strong star formation activity shown by this object could be the result of compression of molecular clouds due to the pressure exerted by the ICM. Nonetheless, we must bear in mind that the lack of detection of X-Ray emission in A634 does not necessarily mean it is devoid of a significant ICM.

The comparable radial velocities measured for DRP-A634a and LSB-A634a, and their close position in the sky could be indicative of both objects being physically related. The optical morphology of the LSB-A634a+DRP-A634a system may suggest an edge-on, late-type, low surface brightness galaxy, with an off-center very bright knot accounting for most of the optical light. In this scenario, would this system be anywhere close to the Tully-Fisher (TF) relation? To answer this question, first we have assumed that the difference between the radial velocities of DRP-A634a and LSB-A634a_knot provides an estimation of the internal velocity of the system, giving 2 $V_{max} \approx 80$ km s^{-1}. Secondly, we have applied the results of Pierini & Tuffs (1999), who derived the TF relation for a sample including dwarf star-forming galaxies from the Virgo Cluster Catalogue in the K' band. The $M_{K'}$ magnitude of the system was derived from the M_B magnitude (see sect. 3) making use of: 1) the average $(B-K)$ colour for the Virgo sample of 57 (*Sdm-Sd/Sm* to *Im/BCD*) galaxies[8]: $(B-K) \simeq 2.85$; and 2) the mean colour, $(B-K_s) \simeq 2.20$, obtained for the sample of BCDs from Noeske et al. (2003). Taking the average value of both results, $< (B-K) >= 2.53 \pm 0.33$, we found $M_{K'} = -19.70 \pm 0.35$ mag for the system LSB-A634a+DRP-A634a. Applying the fit of Pierini & Tuffs (1999) (see their figure 6) to our value of V_{max}, their TF relation predicts $M_{K'} = -16.89$ mag, nearly 3 mag fainter than the value of $M_{K'}$ estimated above for the whole system. In the optical, several papers on the TF relation for low luminosity galaxies have appeared recently. The TF relation for local discs and irregular galaxies from Ziegler et al. (2002) would predict a value of $M_B \sim -15$ mag for our $V_{max} \approx 40$ km s^{-1}, about 2 mag fainter than the value measured for our system. According to Swaters (1999) (figure 13, page 117), galaxies with absolute magnitudes fainter than $M_{r'} \simeq -18$ systematically fall

[7] In the case the cluster center quoted by Struble & Rood (1999) is adopted, the corresponding projected distance would amount to 16 kpc and DRP-A634a will be a cluster member at a higher confidence level.

[8] The GOLDmine database (Gavazzi et al. 2003b) was used to derive these data - http://goldmine.mib.infn.it/

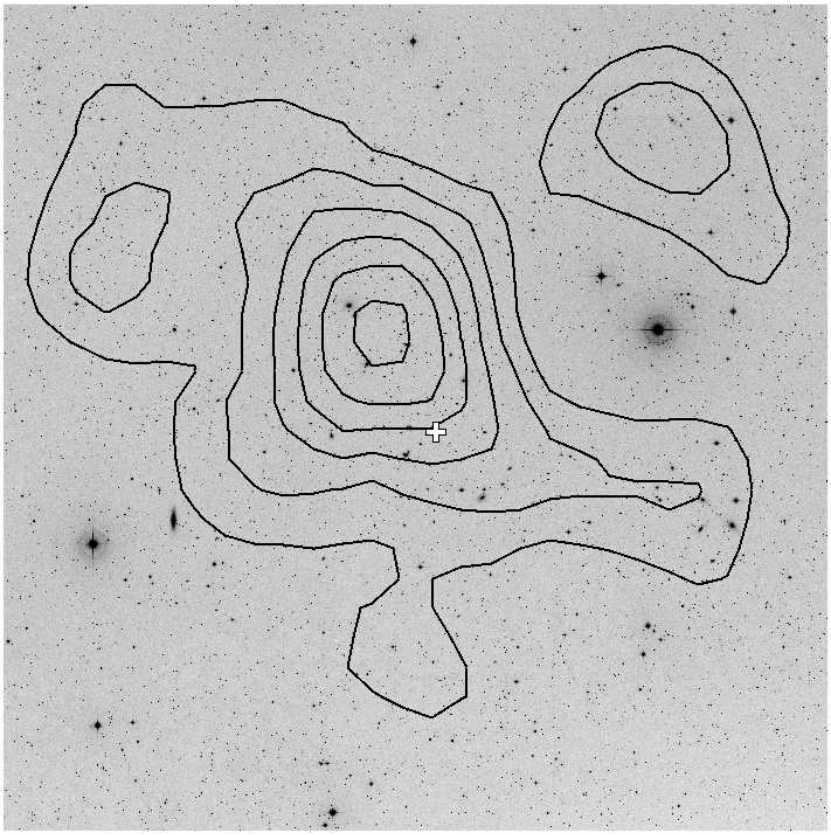

Figure 8.9:: Abell 634 overview (2x2 degrees) with the 2MASS galaxy spatial-density contours (relative units, black). Cross marks the position of the compact dwarf galaxy detected (North is to the top and East is to the left). Because of the extreme low X Ray emission detected by ROSAT for this cluster, no X-Ray contours can be overplotted.

below a straight line TF relation. This fact has been highlighted by McGaugh (2000) pointing out the different evolutionary stage of gas-rich dwarfs with respect to spiral discs. More recently Schombert (2006) concluded that dwarf galaxies form a distinct sequence, being more diffuse than disc galaxies. To summarize, the predictions of the TF relation for galaxies with internal velocity of order $V_{max} \approx 40$ km s^{-1} yield luminosity values much fainter than that determined here for this system. On the other side, as mentioned in sect. 3 this integrated system separates from the luminosity-metallicity relation being too luminous for its metallicity. According to these findings, the object formed by LSB-A634a+DRP-A634a is not proven to be a single galaxy.

Even though the LSB-A634a+DRP-A634a system is not likely to be a single

galaxy, still both objects could be physically related. Under this assumption, we propose that the strong star formation activity shown by DRP-A634a is the result of the encounter between these objects. In fact, examples of recent star formation bursts associated to small groups of galaxies which are falling into a cluster have already been reported in the literature (Sakai et al. 2002; Gavazzi et al. 2003b; Cortese et al. 2006), and are thought to be associated to the so-called preprocessing of galaxies before entering the cluster environment. This mechanism could account for a non negligible fraction of the evolution of galaxies in dense environments. Further observations of this intriguing system are needed in order to fully understand its nature and evolutionary state.

8.3 Conclusions

We have reported two examples of extreme star forming objects in nearby clusters with different properties and at different evolutionary phases. The observations show that albeit they do not share the same origin, both compact and young starbursts show a very intense star formation activity, even when compared to similar objects in other nearby clusters or in less dense environments.

The origin of the two starbursts reported in this paper are probably associated to different physical mechanisms: DRP-A539a is directly associated to the dense and hot ICM which compresses intergalactic clouds and induces star formation episodes in a short timescale, before ram pressure is able to sweep the external gas. The case of DRP-A634a can be related to the so-called "preprocessing" of galaxies before they enter the cluster environment. In this case, the aggregates of galaxies whose final fate is to fall into the cluster inner regions, are the environments where secondary evolution is taking place.

Two questions arise from these considerations: what is the relative importance of such compact and extreme starbursts with respect to the global SFR of nearby clusters? and, is there any evolutionary link between them and the early-type ultracompact dwarf galaxies already reported in the literature? (Drinkwater et al. 2004) To answer the first question, a detailed search based on Hα surveys is required. We note that an extensive spectroscopic survey of Abell 539 devoted to studying the star formation in cluster galaxies has been carried out by Rines et al. (2005), but DRP-A539a was not selected there because their sample of galaxies was NIR-magnitude limited. The same would have happened with DRP-A634a if the cluster A634 had been surveyed under the same conditions. These non detections are naturally explained by the fact that these objects are dwarfs and very young. However, they show up very easily in wide field Hα imaging surveys despite their size and small stellar content.

These kinds of surveys are required to carry out a detailed census of compact starbursts in clusters of galaxies. In this way, their relative contribution to the total SFR budget of nearby clusters will definitely be determined. As concerns the second question, several explanations have already been proposed for the origin of UCDGs (see Jones et al. 2006 for an interesting review), although the discussion remains open. We propose that compact and strong starbursts like the ones presented in this paper could evolve to early-type dwarf galaxies after cessation of star formation and, if stripping is efficient as the galaxy approaches the innermost regions of the cluster, become UCDGs like the ones reported in Virgo and Fornax clusters. A complete census of compact starbursts in clusters, with accurate projected positions and surface densities will also help to answer this question.

CHAPTER

9

CONCLUSIONS AND FUTURE WORK

In this thesis a deep survey for star forming galaxies have been carried out. The Hα imaging has been deep enough to largely include the lower luminosity galaxy population, as well as, providing the appropiate spatial resolution to study both, the structure of the emission for individual galaxies and the distribution of star forming galaxies throughout the clusters. This observational design has provided bidimensional information, hence avoiding well known slit and fiber aperture effects - present in aperture limited surveys - in the derivation of the SFR, Hα luminosity and EW.

In what follows we summarize the main conclusions of this work.

- A total 4.2 square degrees over the 5 Abell clusters of galaxies # 400, 539, 634, 779 and 2666 have been mapped within the present Deep Hα Imaging Survey, reaching, on average, for each cluster up to the r_{200}. New catalogues of star forming candidate sources selected in this survey have been produced for the cluster sample, including over four thousands new entries.
- The Hα luminosity and EW distributions for the sample of clusters have

been built. The shapes of these distributions appear clearly diffenciated from the corresponding distributions for the field galaxies sample, taken from the literature; these distributions for clusters favouring the presence of galaxies with low Hα luminosity and EW values which appear rare in the field sample.

· A significant population of star-forming low luminosity galaxies has been unveiled on every cluster in this sample. For this population of SF dwarf galaxies, on every cluster, a two-dimensional spatial distribution has been derived at.

Given the wealth of new information obtained, we go to remark among others the following specific conclusions.

· Under a Kolmogorov-Smirnov (KS) test, the hipothesis that distributions of Hα luminosity of SF bright galaxies (M_R < -19) from Abell clusters 400, 539, 634, 779 and 2666 on one side and from the field on the other side do come from the same parental distribution can be rejected at a high ($\geq$ 0.93) confidence level.

· Under a Kolmogorov-Smirnov (KS) test, the hipothesis that distributions of Hα luminosity of SF dwarf galaxies (-19 < M_R < -16) from Abell clusters 400, 539, 634, 779 and 2666 on one side and from the field on the other side do come from the same parental distribution can be rejected at a high ($\geq$ 0.97) confidence level.

· KS test on distributions of Hα luminosity of SF bright galaxies (M_R < -19) from Abell 400, and from Abell 539 shows that can not be rejected the hipothesis that they do come from the same parental distribution.

· The hipothesis that the distributions of Hα luminosity of SF bright galaxies (M_R < -19) from Abell 634, 779 and 2666 do come from the same parental distribution using a KS test can not be rejected.

· The hipothesis that the distributions of Hα luminosity of SF faint galaxies (-19 < M_R < -16) from Abell 400, 539 and 634 do come from the same parental distribution using a KS test can be rejected at a high ($\geq$ 0.98) confidence level.

· KS test on distribution of Hα luminosity of SF faint galaxies (-19 < M_R < -16) from Abell 400, 539 and 779 on one side and from Abell 634 or 2666 on the other side do come from the same parental distribution can be rejected at a high ($\geq$ 0.93) confidence level.

- Hα fluxes of SF bright galaxies for Abell 400 and Abell 539 clusters seems to be radial dependent within the r_{200} with the clustercentric projected distance. The median flux of sources increases when moving further away the cluster center. Something identical happens to the Equivalent Widths of Hα for which, in Abell 400, 539, even in Abell 634, increasing along the projected distance to the cluster center.

- No radial dependence is observed for the Hα flux of SF bright galaxies in Abell 634, 779, and 2666. For the EW of SF bright galaxies we found no radial dependence in Abell clusters 779 and 2666 within the r_{200}.

- For SF dwarf galaxies neither the Hα flux nor the EW, show a clustercentric radial variation at all.

- Spatial (-projected) distribution of number density of SF bright galaxies in every cluster follows systematically the 2MASS density contours for the corresponding cluster; placing the highest number densities of SF bright galaxies at the higher 2MASS densities.

- For Abell 400 the spatial distribution of number density of SF dwarf galaxies is confined within the 2MASS contours but its overdensity of SF dwarfs avoids the highest densities of 2MASS contours. While, in Abell 539 the spatial distribution of SF dwarfs does not follow the 2MASS density contours.

- For the Abell clusters 634, 779 and 2666 the spatial distribution of SF dwarf population is well described by the density contours of 2MASS, except the spread.

- Surface brightness profile, asymmetry and concentration have been computed for every galaxy in a Working Subsample, selected independently on every cluster. No clear tendency has been shown between the asymmetry nor the concentration and the EW(Hα).

- From the concentration-asymmetry diagram with regions marking the expected places for a general classification of morphological type, the majority of galaxies in this Working Subsample can be settled in the group of late-type (spirals+irregulars), and just few cases in others.

- Radius of the stellar component at the isophote 24 mag arcsec^{-2} (r_{24}) at the continuum wavelength do coincide for the range of absolute magnitudes M_R integrated up to the r_{24} with the loci occupied by field and

virgo galaxies from the literature, showing that the stellar component did not suffer environmental effects on our cluster sample.

· Points for SF dwarf galaxies in the diagram $M_R(r_{24})$ vs. Log r_{24}, do change (decreases) the slope respect to that extrapolated from the points of Virgo and of field galaxies.

· Hα surface brightness ($SB_{H\alpha}$) profile scaled to the r_{24}, averaged among the cluster galaxy profiles, shows a severe truncation for Abell 539 cluster respect to the field, to the Virgo and to the other cluster galaxies considered; while Abell 634 and 2666 show a similar trend to that of the Virgo and field galaxies.

· For this set of five clusters plus the catalogues of Abell 1367 and Coma cluster from our group, tight correlations between the fraction of bright galaxies (M_R < -19) with ongoing star formation f_{SF}^G and the velocity dispersion, and between f_{SF}^G and the X-Ray bolometric luminosity of the cluster, are stated and derived.

· A complete and operative working pipeline (including original software) for treating, calibrating, detecting, measuring, cataloguing, and managing imaging data has been developped.

· The mean accuracy of the astrometry solution computed for every cluster in our sample is better than 0.5 arcsec, reaching down to 0.3 arcsec for some pointings.

· An average (among clusters in the sample) limiting detection of 10^{-16} ergs s^{-1} cm^{-2} in the flux Hα is achivied for the sample.

· The detection procedure permits to extract sources as faint as 21.5 mag in $R_{Cousins}$ with a completeness of 95% for almost all the pointings in every cluster, except for Abell 2666 which magnitude depth is 1 mag brighter.

A magnificent spectroscopic follow-up with a set of few instruments (e.g. ALBIREO: slit-spectrograph at the 1.5m telescope of the "Observatorio Sierra Nevada"; CAFOS: slit-spectrograph at the 2.2m telescope in the Calar Alto Observatory; and, WYFFOS: multi-fiber spectrograph at the William Herschel Telescope in the "Roque de los Muchachos", La Palma) has already started during this thesis work. It will form part of a new thesis work, in which I collaborate.

The "Environmental Effects on Chemodinamical Evolution of Galaxies in Clusters" is an ambitious ESO-GTC programme of observation where I am

involved, and for what the catalogues presented in this work will supposse a starting point of the proposed study.

I have an special interest on WINGS project, for the affinity it has with this work, now, we have already began observing the Hα emission for a subsample of the total clusters, for which a complete broad band deep database exists.

A last desideratum on an atractive project would be to carry out a similar (to this) study at high redshift dense structures that may be revealed by the ALHAMBRA survey. Given the observational design, both Hα and redshift could be extracted for the bright starburst population in groups and clusters, taking advantage over previous work.

This research has made use of the NASA/IPAC Extragalactic Database (NED) which is operated by the Jet Propulsion Laboratory, California Institute of Technology, under contract with the National Aeronautics and Space Administration.

This publication makes use of data products from the Two Micron All Sky Survey, which is a joint project of the University of Massachusetts and the Infrared Processing and Analysis Center, funded by the National Aeronautics and Space Administration and the National Science Foundation.

APPENDIX

A

IRAF TASKS

Some scripts were performed to run under IRAF in order to build up such a pipeline which help us in data management. Here, the most used tasks will be described through their param configuration and some basic instructions.

For individually measured galaxies (those with a known radial velocity and those others with apparent Hα emission) few steps were followed before measuring. The treatment consisted of cropping, aligning, scaling, sky subtraction, and finally combining.

A.1 GALFIND

This procedure looks for a list of celestial coordinates on a list of image with astrometry solution. *Galfind* makes use of *rd2xy* (toolbox.imgtools under STSDAS package) and of **gawk** language programme. Then, from "NED list" and from the hand-made list of objects with three column information (First: name; second: Right Ascension (in hours); and, third: Declination (in degrees)) *galfind* can explore within the directories specified searching for every fit that verifies it can contain the required pointing. Table A.1 shows the parameters for galfind.

Galfind assigns a name for the trimmed image which is a composite of the input name from list *coolist*, the filter, and a numbering according to the times

I R A F
Image Reduction and Analysis Facility

PACKAGE = user
TASK = galfind

coofile	=	A1367.galfind.cat	File of coordinates to be find.
destin	=	IMAGES/	Destiny directory.
(dirfile	=	directorios2.txt)	File containig the list of directories where the search has to be done.
(prefix	=	r3)	Prefix of images in directory.
(trimsiz	=	2.)	Section of images to be trimmed.
(trimtyp	=	arcmin)	Arcmin or pixels
(pixsiz	=	0.332)	Pixel size.
(filtkey	=	WFFBAND)	Keyword of the Image header for the filter used.
(verbos	=	no)	Print messages?
(coolist	=	)	
(dirlist	=	)	
(imlist	=	)	
(mode	=	ql)	

what the object is found.

A.2 NFO

Using together SExtractor and IDL, we computed the scale factor between every chip presenting an overlap with another one. In addition we know the scale between chips for the WFC through a flat series, thus we can derive the scale between any chip of any pointing and the central chip of the reference image. SExtractor measured and classified the objects while IDL read the output catalogue distinguished stars, matched by (RA, Dec) and computed some params: MEDIAN, MEAN and MODE of the ratios of flux (with their standard deviation) and through the histogram of those ratios, fitting a gaussian, the gaussian MEAN (and its variance), as well as the FWHM characteristic of the exposure. We make no distinction among filter resulting in a complete (long) table of scale factors. This operation consumed a great amount of computational time, but give us the chance of segregating quickly bad images (those with large scale factors, or those with a great ¡FWHM¿). This scaling factors have been used for the individual cropped images and for mosaicing.

The task *nfo* were thought to be an easy way to access the database of coeficients that scale every pointing frame and chip of every night to the others, in particular to the central chip of the reference run.

Before combining or mosaicing we must know the scale factors to the ref-

erence image, so making a list with image filenames this task search for them into the database.

I R A F
Image Reduction and Analysis Facility

PACKAGE = user
TASK = nfo

list	=	62_CGCG_415-043_NED01.SII.nfo	Images List to be reported.
cluster	=	A400	Cluster Name.
ref_run	=	329160	Reference RUN number for the whole cluster image sample.
(output	=	)	Output file (default = .ccomb). Will be used as input for ccomb
(report	=	/mnt/datos1/A400/FE_A400.dat)	File containing the calibration scales.
(seeing	=	/mnt/datos1/A400/A400_ccd4.rep)	File containing the seeing for the run (cf. ccd4).
(csfacto	=	0.83140275,0.91164526,0.96755238)	Chip Scales factor file for the reference image.F14,F24,F34
(rkeywrd	=	RUN)	RUN number Header Keyword.
(tkeywrd	=	EXPTIME)	Integration TIME Header Keyword.
(fkeywrd	=	WFFBAND)	FILTER name Header Keyword.
(chipnum	=	DASCHAN)	CHIP number Header Keyword
(date_ob	=	DATE-OBS)	DATE header info
(utime	=	UTSTART)	UT header info
(inlist	=	)	
(kfile	=	)	
(mode	=	ql)	

A.3 CCOMB

The output from *nfo* is used directly as input in *ccomb*. *Ccomb* is collection of tasks joined under a unique environment. The task is thought to: adjust the scale (following the scale factors computed with the stars); make equal the FWHM, if demanded; align the images (by using a simple shift and linear transformation; or if needed and possible, by making geodesical transformation using the celestial solution in the header) [needs the *immatch* package]; subtract the background (which correspond to the sky); and, finally, combining by median of the images and rejecting those points over 3 times the averaged-sigma (=avsigclip).

The resulting image from the use of *ccomb* has the level of counts prepared to be converted in physical units and according to the calibration factor which translate ADUs in ergs s^{-1} cm^{-2}, we get the F_{ON} and F_{OFF} from their respective parent images.

I R A F
Image Reduction and Analysis Facility

PACKAGE = user
TASK = ccomb

input	=	list.nfo	List of images and factors.
output	=	output.fits	Output image name.
(cmbtype	=	median)	Type of combine operation.
(reject	=	avsigclip)	Type of rejection.
(lthresh	=	INDEF)	Lower threshold.
(hthresh	=	INDEF)	Upper threshold.
(nlow	=	1)	minmax: Number of low pixels to reject.
(nhigh	=	1)	minmax: Number of high pixels to reject.
(nkeep	=	1)	Minimum to keep (pos) or maximum to reject (neg)
(mclip	=	yes)	Use median in sigma clipping algorithms?
(lsigma	=	2.5)	Lower sigma clipping factor.
(hsigma	=	2.5)	Upper sigma clipping factor.
(fwhmcv	=	no)	Convolve a gaussian kernel to balance the FWHM.
(gaussiz	=	35.)	Extent of Gaussian kernel in pixels.
(skysubs	=	yes)	Take the images to a common sky level.
(skyvalu	=	21.)	Common Sky value for the final images.
(mask_	=	yes)	Mask the images to compute the sky background?
(autog	=	yes)	Launch AUTOGEO?
(toleran	=	1.8)	In arcseconds. Upper limit searching radius to match coordinates.
(fthresh	=	20.)	Daofind threshold
(fitgeom	=	general)	Fitting geometry
(funct	=	polynomial)	Surface type
(xxorder	=	3)	Order of x fit in x
(xyorder	=	2)	Order of x fit in y
(xxterms	=	full)	X fit cross terms type
(yxorder	=	2)	Order of y fit in x
(yyorder	=	3)	Order of y fit in y
(yxterms	=	full)	Y fit cross terms type
(calctyp	=	real)	Computation type
(niter	=	3)	Maximum number of rejection iterations
(progres	=	yes)	Print messages about progress of task ?
(interac	=	yes)	Fit transformation interactively ?
(reject_	=	3.)	Rejection limit in sigma units.
(interpo	=	spline3)	Interpolant (nearest|linear|poly3|poly5|spline3|sinc).
(bound	=	constant)	Boundary extension
(const	=	0.)	Constant for constant boundary extension.
(fluxcon	=	yes)	Preserve image flux?
(time	=	EXPTIME)	Exposure TIME header keyword.
(verbos	=	yes)	Print messages in geomap and geotran?

more params.

Table A.1 – more params

(verbos_	=	yes)	Print messages in imcombine?
(aligni	=	yes)	Preserve aligned/sky/gauss/scaled images?
(coordf	=	no)	Preserve coordinates files?
(kfile	=	)	
(inlist	=	)	
(mode	=	ql)	

A.4 DITHERCAL

Dithercal is simple dithering calculator. Given the large number of images in our database, in order to produce the best final image,every intermediate step should be controlled and I needed to save a log of every operation made. *Dithercal* does derive the offset (ΔX,ΔY) [in pixels] between two images using the stars in common for both frames, and also does save a table which will be used as a database of shiftings between pointings.

I R A F
Image Reduction and Analysis Facility

PACKAGE = user
TASK = ccomb

infile	=	lista.txt	Input file with the images list.
referenc	=	refer_image.fits	Reference image or list with at least one chip of reference image (IMPORTANT header coordinates)
(foffset	=	default)	File containing the offset for the reference images. if "" or default then .refd
(outfile	=	default)	File containing the offset for the infile list images. if "" or default then .dit
(maxoffs	=	2.)	Maximum dithering to align the images
(oftype	=	arcsec)	Type of input maximum offset
(pixsiz	=	0.33)	Pixel size in case of type "pixel"
(key_ra	=	RA)	Right ascension header keyword
(key_dec	=	DEC)	Declination header keyword
(verbose	=	no)	Print progress
(ilist	=	)	
(mode	=	ql)	

Once the reference image is chosen, on every image in the input list a search for stars is made (makes uses of *daofind*), (X,Y) pairs are converted to (RA,Dec), and the matching returns a lists of four columns ($\rightarrow$ X$_{ref}$,Y$_{ref}$,X$_{dith}$,Y$_{dith}$) and if the mean difference between the coordinates distances verifies that it is within a fixed radius (maximum offset = *maxoffs*), then, the dithering is saved together with the image name.

A.5 WFCMOSAIC

WFCMOSAIC is an own developed task to build-up the mosaic of chips from the WFC (INT). This Camera is composed by 4 EEV of 2k by 4k pixels of 0.33" size; and the main bug to resolve in order to construct the mosaic is to

account for the different angle inclination a positions of the chips, including the 90^o rotated chip # 2.

The task read from the header the data related to the trimmed size and the number of the chip, as well as the astrometric solution. It creates a base plate astrometric image where chips will lie. This container is a bit bigger than needed to fit the camera puzzle in order to register the possible dithering offsets between the same pointing.

I R A F
Image Reduction and Analysis Facility

PACKAGE = user
TASK = wfcmosaic

inlist	=	l176.lst	List of images to be mosaiced
mosaic	=	prueba176.fits	Output image name
referenc	=	r329176_ccd4_b_f.fits	Single image to be used as reference for the list (preferably CCD4 for WFC@INT)
(databas	=	sol.db)	WCSMAP Database
(origin	=	2154,4200)	Original image dimension. (XXXX,YYYY).
(trimsec	=	TRIMSEC)	Trim section from original image dimension.([XXX1:XXX2,YYY1:YYY2]). Or header keyword.
(rdnoise	=	READNOIS)	Readnoise header keyword
(gain	=	GAIN)	Gain header keyword
(ditheri	=	no)	Does exist a set of dithered images for this pointing ?
(offset	=	0.)	If so, please insert the approx. offset for this pointing relative to the center image. (Dx,Dy).
(off_typ	=	arcsec)	Type of offset. (arcsec — pixel)
(pixsiz	=	0.332)	Pixel size in arcseconds.
(fi_str	=	)	
(mode	=	ql)	

APPENDIX

B

COMPLETENESS AND DETECTION LIMITS TESTS

B.1 Creating an artificial image

For this purpose we go to make use of the IRAF tasks contained in the *ART-DATA* package.

First, with *mknoise* the plate where synthetic galaxies will lie in, had been created by adjusting the "eparam" with a proper set of values. The parameters *ncols* and *nlines* have been set aproximately to the typical dimensions [X,Y = 2100,4100] of an individual chip of the WFC. The *background* has been put at the median of the level of counts for the 1200s integrated exposure ON images ($\sim$ 200 ADU). *Gain* has been set to the mean value of gain for the 4 chips of WFC (before the conversion to SDSU generation 3 in 2007 april) at 2.5 e^-/ADU, also *rdnoise* param that took the value of 6.5 e^-. No cosmic rays were added.

On this *noise.fits* images a collection of stars and galaxies must be spread. To generate these lists we used *starlist* and *gallist*. Both tasks allow to change the spatial and luminosity distribution of the source to be made. In addition, within the *gallist* param, it is possible to limit the angular size (in pixels), and to fix the starting redshift point. A set of 4 object lists have been written with

these tasks. One for the field stars ($\simeq$ 250) with a uniform spatial distribution and a salpeter luminosity function for the magnitude distribution, and three for galaxy distribution. The first of these galaxy distributions was intended to reflect the foreground galaxy distribution (5-10 galaxies; uniform; z=0; rest of params in their default values), the second one describes the background population (2000-5000 gals.; uniform; z=0.05; powlaw; 0.4 percentage of ellipticals), and the third one traces the cluster galaxies properties (30-100 gals.; hubble -150 core radius-; z=0.025; schecter; 0.5 % of E).

Finally with *mkobjects* task we applied those distributions to the noise created image by setting *background* to 0, *star* profile to moffat and a typical seeing radius of 2.4 pixels (about 1.6 arcsec of real seeing), and a poisson noise of 0 since it can be considered neglectable[1]. The result is an image as in the fig. B.1.

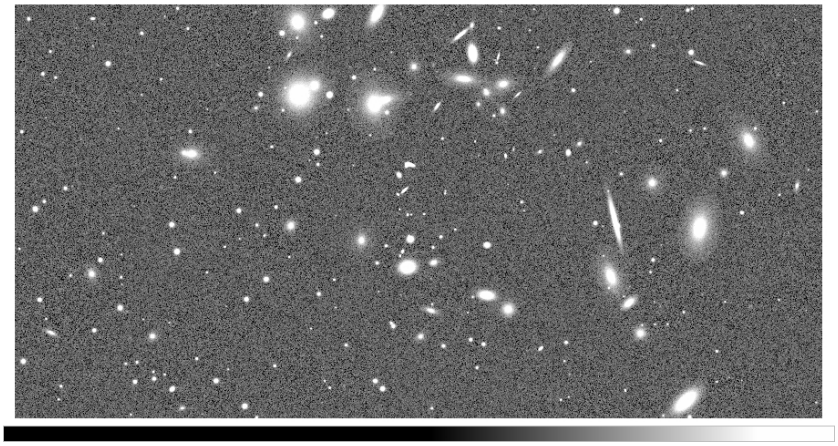

Figure B.1:: Artificial image of 2100x4100 pixels created with ARTDATA package tasks and following the instructions described in the text.

B.2 Detection efficiency

By knowing the true distribution of sources detectable in an image, a routine which testifies the goodness of our detection method can be performed.

SExtractor have been run over the artf_image repeteadly with increasing values for the DETECTION and ANALYSIS_THRESH params. Then, such a

[1] remind that we are producing here an image which is the result of a combination of, at least, three dithered images with high exposure time therefore the poisson noise is indeed overcome by the readout noise

programme has been written in IDL to compare the original files for creating the image with the files of the recovered sources by SExtractor. The result of this comparison can be visualized in fig. B.2

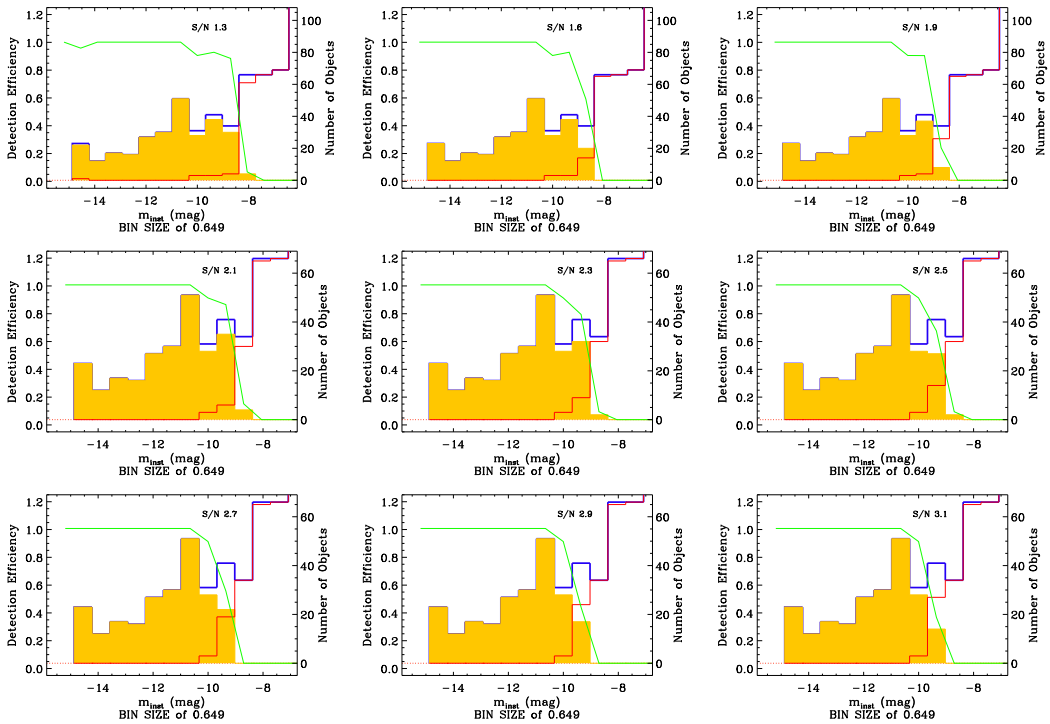

Figure B.2:: On every plot: left Y-axis represents the efficiency; right Y-axis the number of sources; abcisse shows the instrumental magnitude bins; blue line represents the histogram of magnitudes for the original set of sources; red line represents the unrecovered sources; yellow body shows the distribution of magnitudes recovered; and green line traces the efficiency by bin of magnitude.

From the figure is easy to infer that: the higher DETECTION_THRESH is set, the brighter the limiting magnitude is recovered. The efficiency drops from a maintained value of 1 to 0 in less than 2 magnitudes bin. Now we need account for the spurious sources to reach a compromise between the number of "false sources" recovered and the detection threshold (The lowest if no spurious were found).

B.3 Ruling out Spurious

Probing into the amount of spurious or the reliability of a detection on a science image involve to know the nature of the sources detected in order to be able for discriminating between real sources and those produced by the non-uniform and not random-white noise. For this purpose I have implemented a procedure based on the criteria used by Bershady et al. (1998) that uses exclusive images with half-exposure time. From this point the procedure we used differs basically in the philosophy of the method from that of Bershady et al. (1998) and of Cristóbal-Hornillos et al. (2003). Then by detecting and measuring on one image we can compare with the detected and measured on the other image with exactly the same configuration file for the SExtractor execution on. SExtractor's dual mode permits to detect on a image and measure on the other one with the fitted parameters X_IMAGE, Y_IMAGE, APERTURE, ELLIPTICITY, THETA (inclination), extracted from the first one. We first aligned and trimmed the images by using the WCS plate solution inferred for each one. After this a pre-reduction has been applied to half-exposure images separately[2], and on this images we executed SExtractor on image A yielding the A_A.cat and then on image B in dual mode first with image A as the reference yielding B_A.ca, and again now using B as reference yielding B_B.cat and A_B.cat, everything for a set of DETECT_THRESH. We checked and there is no distincts conclusions from compare A_A.cat with B_A.cat or compare B_B.cat with A_B.cat. So, crossing the catalogues thus produced, those objects with magnitudes differing by more than 5 times the σ_{noise} were considered to be spurious detections, and they are represented by the outer wings of the distribution in fig. B.3, B.4 and B.5.

On the right column of figs. B.3, B.4, and B.5, a histogram of the recovered real sources (blue line) and spurious sources (red line) is plotted showing (adjacent-down diagram) the steped increase of none-real detection (near the limiting magnitude). We selected the DETECTION_THRESH 2.5 because a bump appears as a consequence of the change of the behaviour in spurious detection. From this point increase the DETECTION_THRESH seems to be an unefficient way to rule out spurious since we could be loosing proportionally more real sources.

[2]But with the same BIAS and FF correction

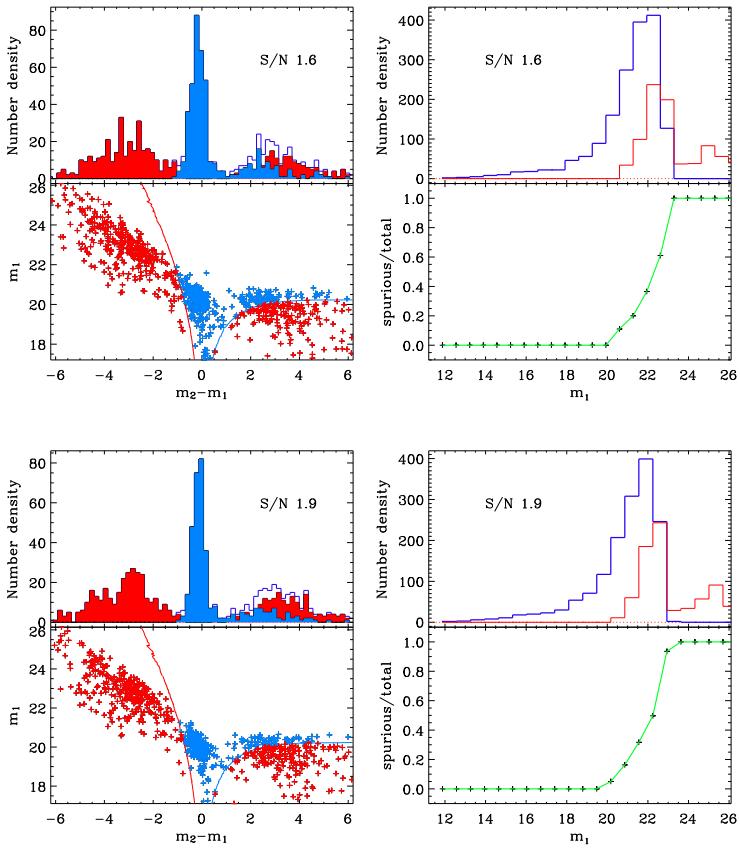

Figure B.3::

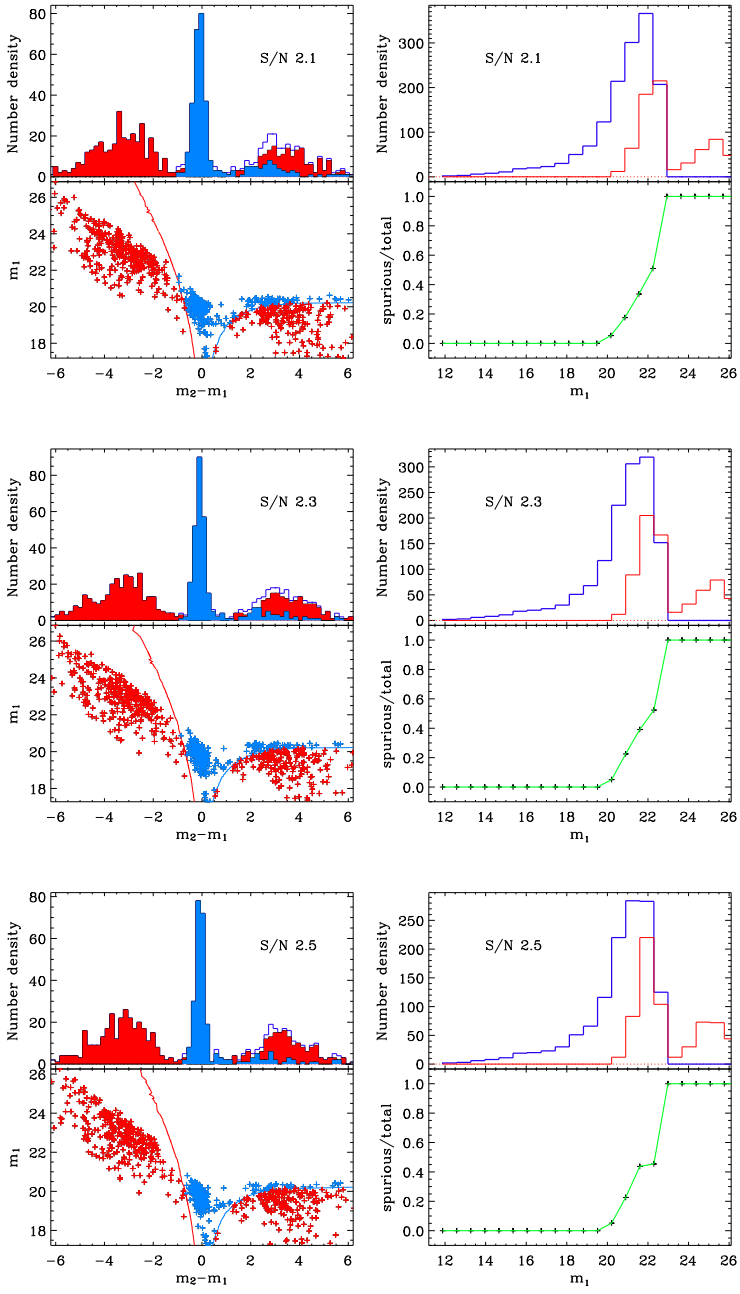

Figure B.4::

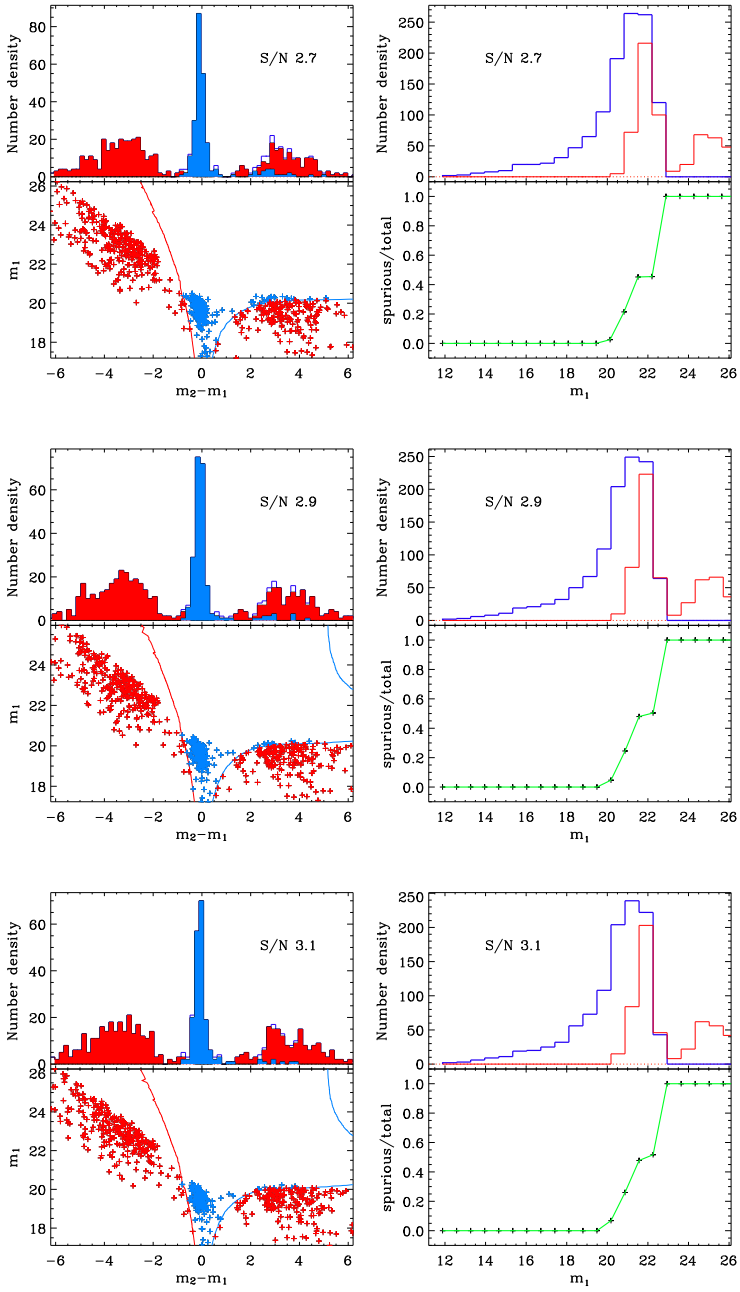

Figure B.5::

APPENDIX

C

ATLAS OF IMAGES AND PROFILES

In this pages, the reader will find the images and profiles for the first 9 objects of every cluster in the Working Subsample.

C.1 Abell 400

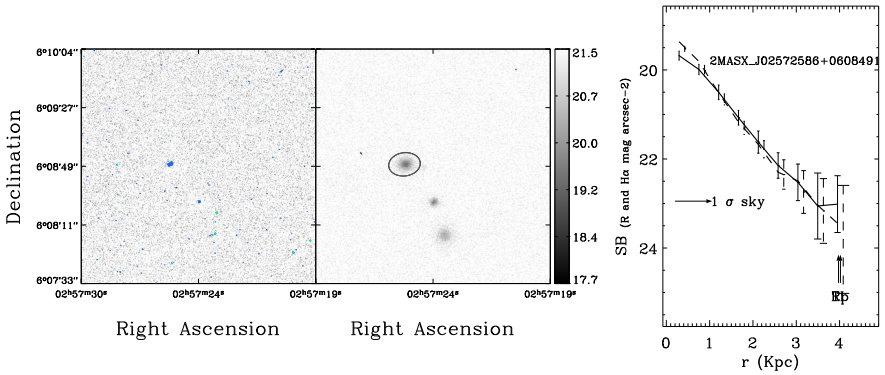
Declination
Right Ascension
Right Ascension
2MASX_J02572586+0608491
SB (R and Hα mag arcsec−2)
r (Kpc)
1 σ sky
Rp
Tl

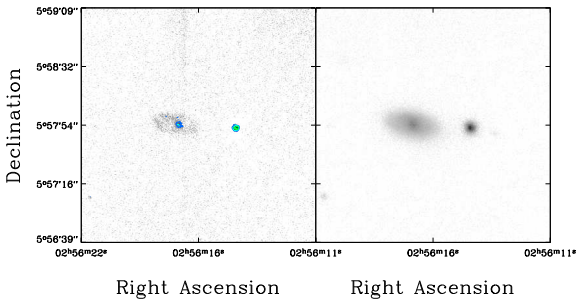
Declination
Right Ascension
Right Ascension

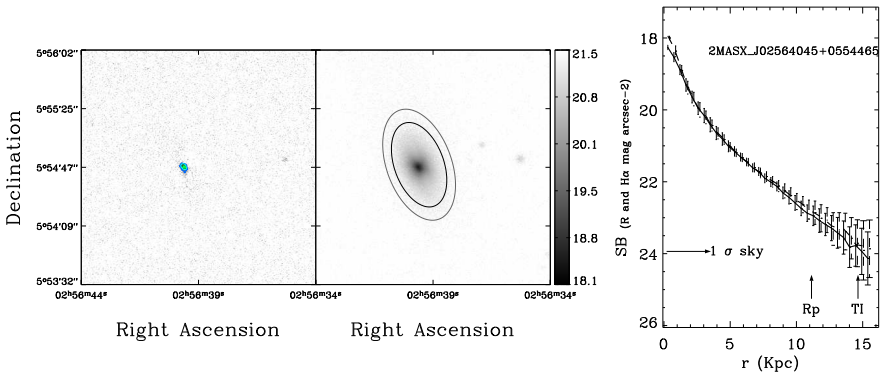
Declination
Right Ascension
Right Ascension
2MASX_J02564045+0554465
SB (R and Hα mag arcsec−2)
r (Kpc)
1 σ sky
Rp
Tl

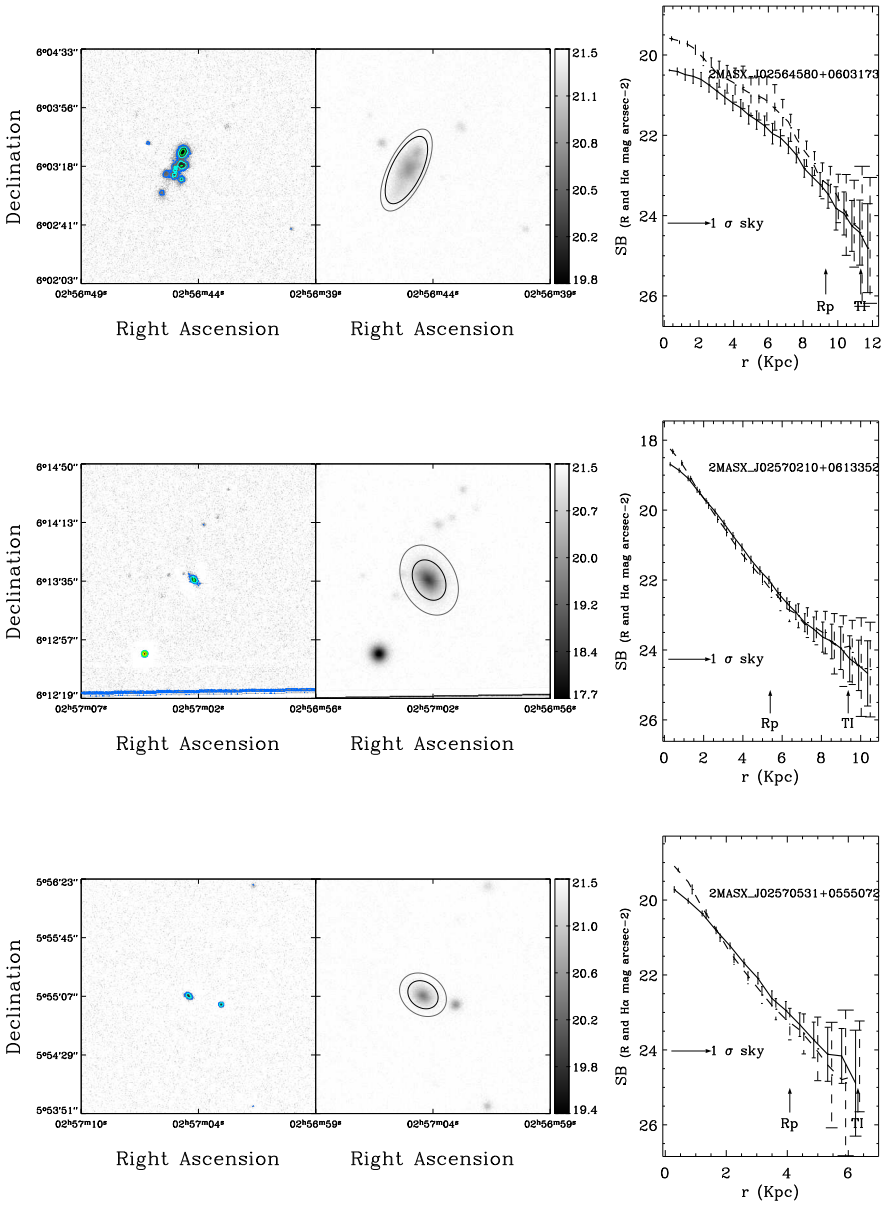
Declination
Right Ascension
Right Ascension
SB (R and Hα mag arcsec−2)
r (Kpc)
2MASX_J02564580+0603173
1 σ sky
Rp
Tl
2MASX_J02570210+0613352
2MASX_J02570531+0555072

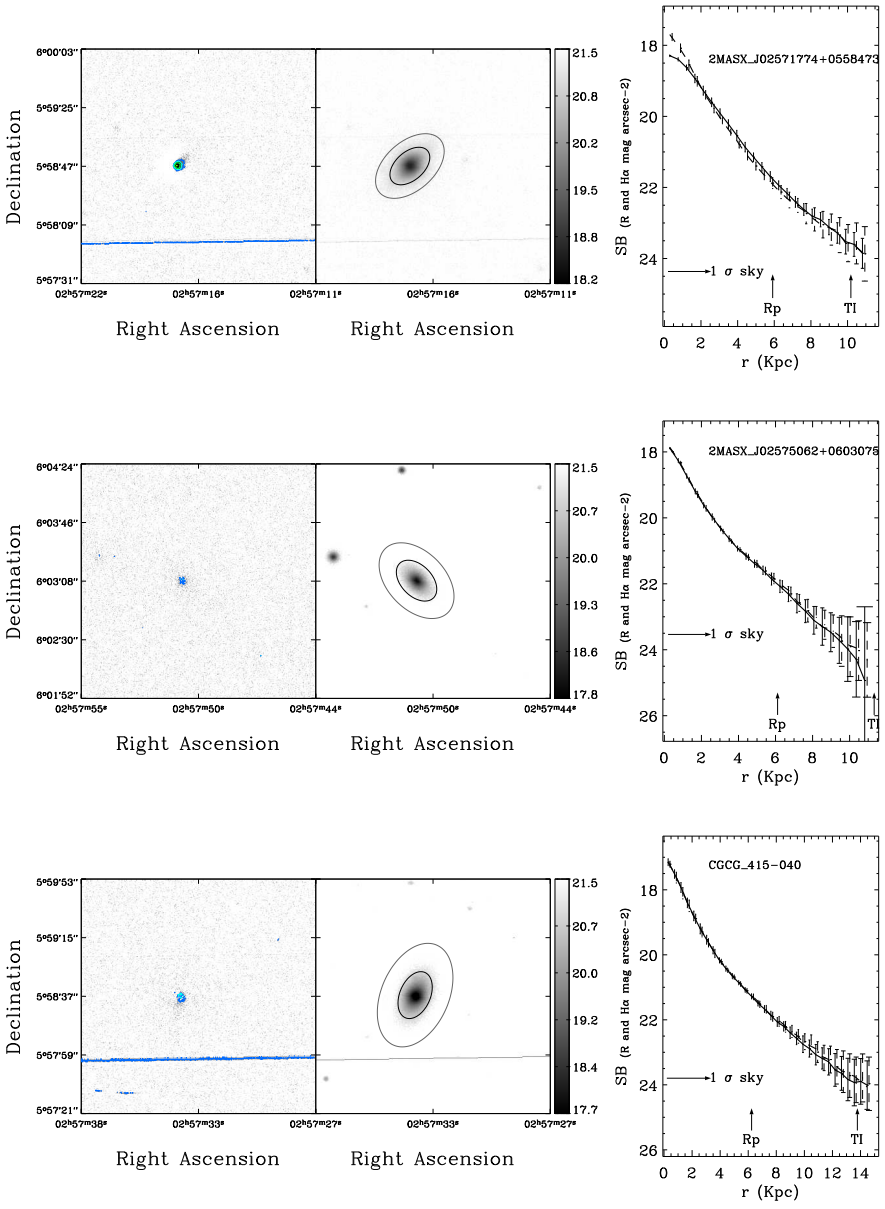
Declination
Right Ascension
Right Ascension
2MASX_J02571774+0558473
2MASX_J02575062+0603075
CGCG_415-040
SB (R and Hα mag arcsec−2)
r (Kpc)
1 σ sky
Rp
Tl

C.2 Abell 539

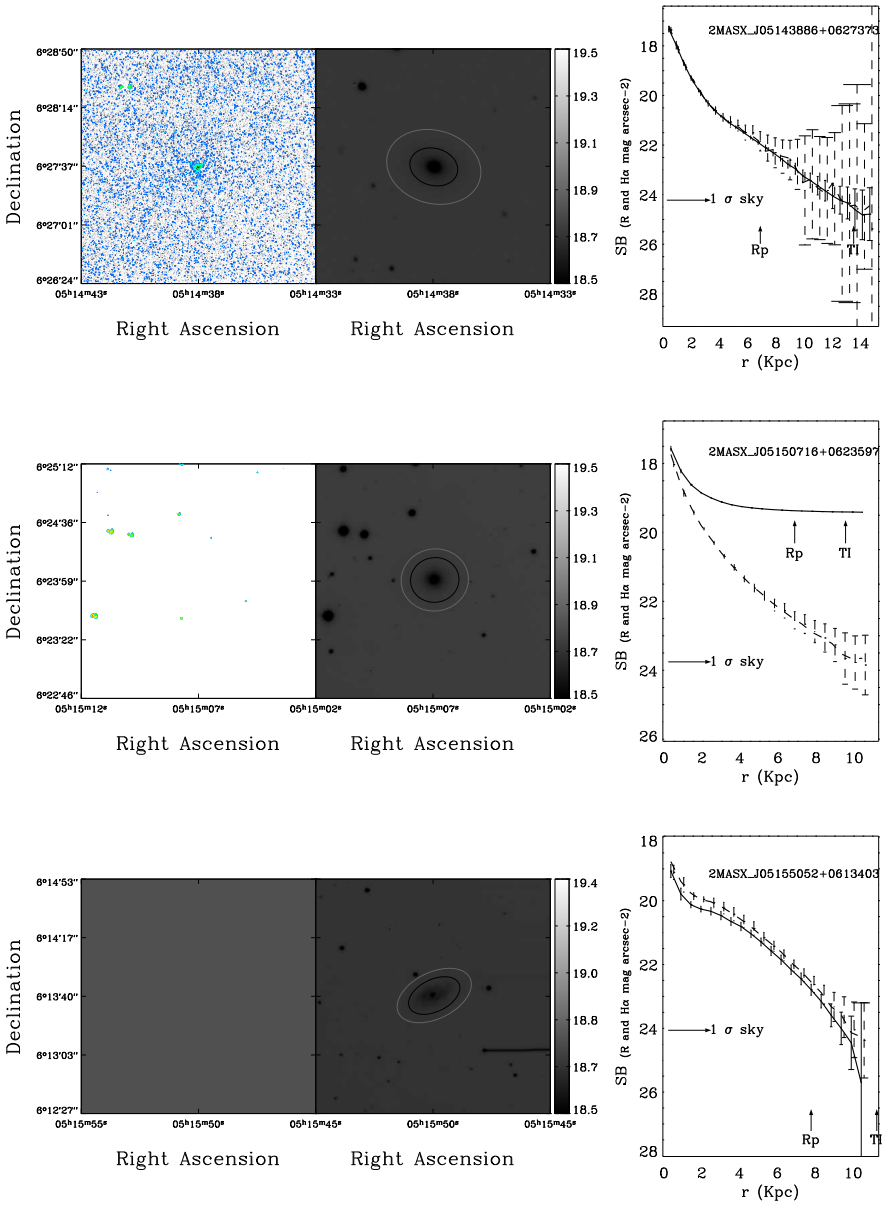
Declination
Right Ascension
Right Ascension
2MASX_J05143886+0627373
SB (R and Hα mag arcsec−2)
1 σ sky
Rp
Tl
r (Kpc)
2MASX_J05150716+0623597
2MASX_J05155052+0613403

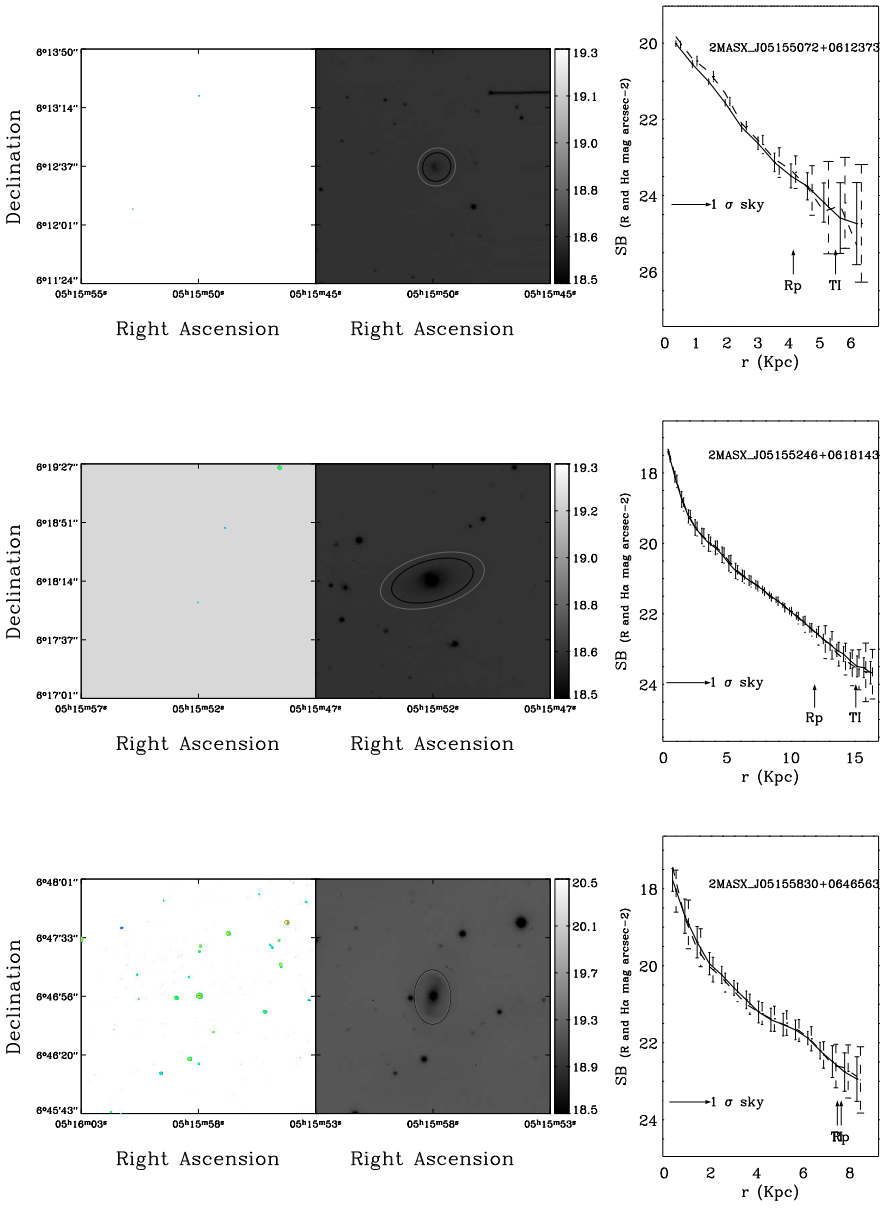
Declination
Right Ascension
Right Ascension
2MASX_J05155072+0612373
2MASX_J05155246+0618143
2MASX_J05155830+0646563
SB (R and Hα mag arcsec−2)
r (Kpc)
1 σ sky
Rp
Tl

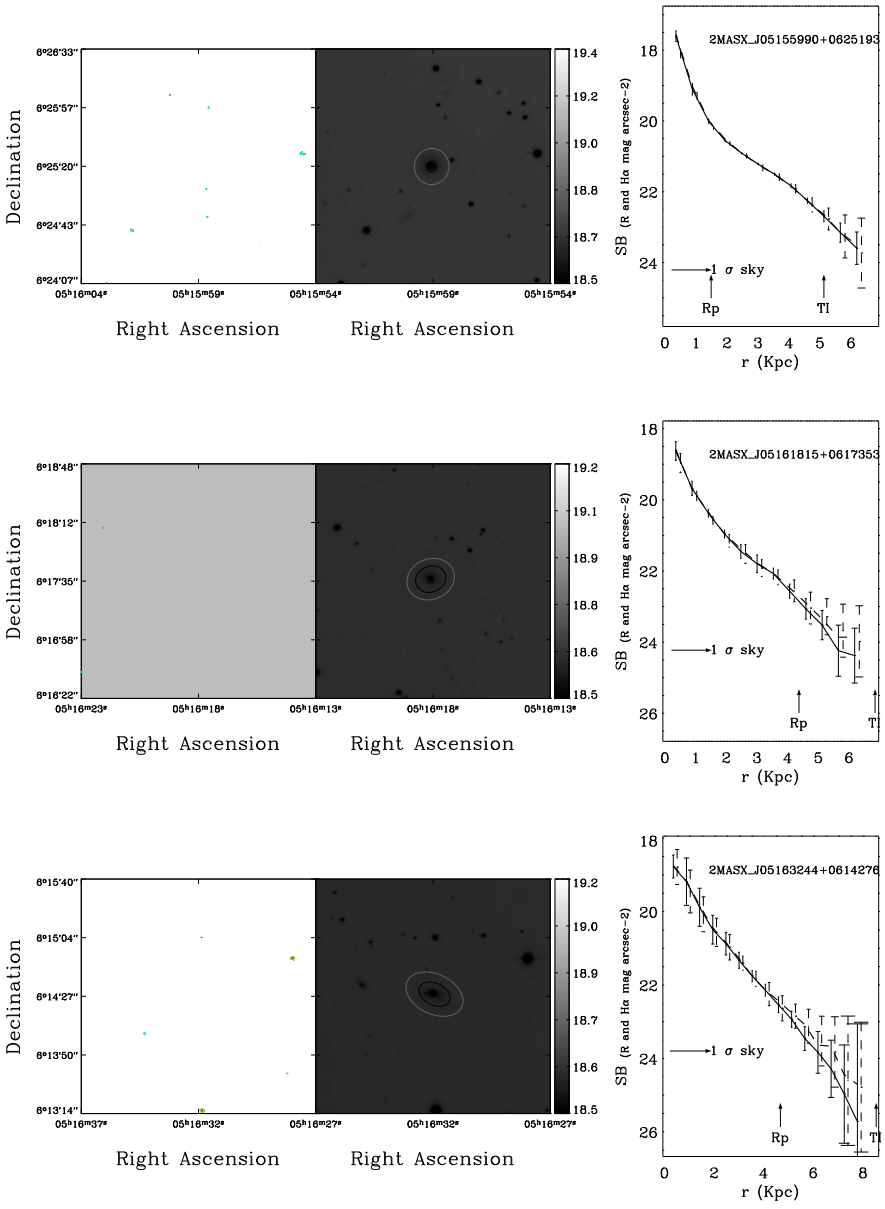
Declination
Right Ascension
Right Ascension
2MASX_J05155990+0625193
2MASX_J05161815+0617353
2MASX_J05163244+0614276
SB (R and Hα mag arcsec−2)
r (Kpc)
1 σ sky
Rp
Tl

C.3 Abell 634

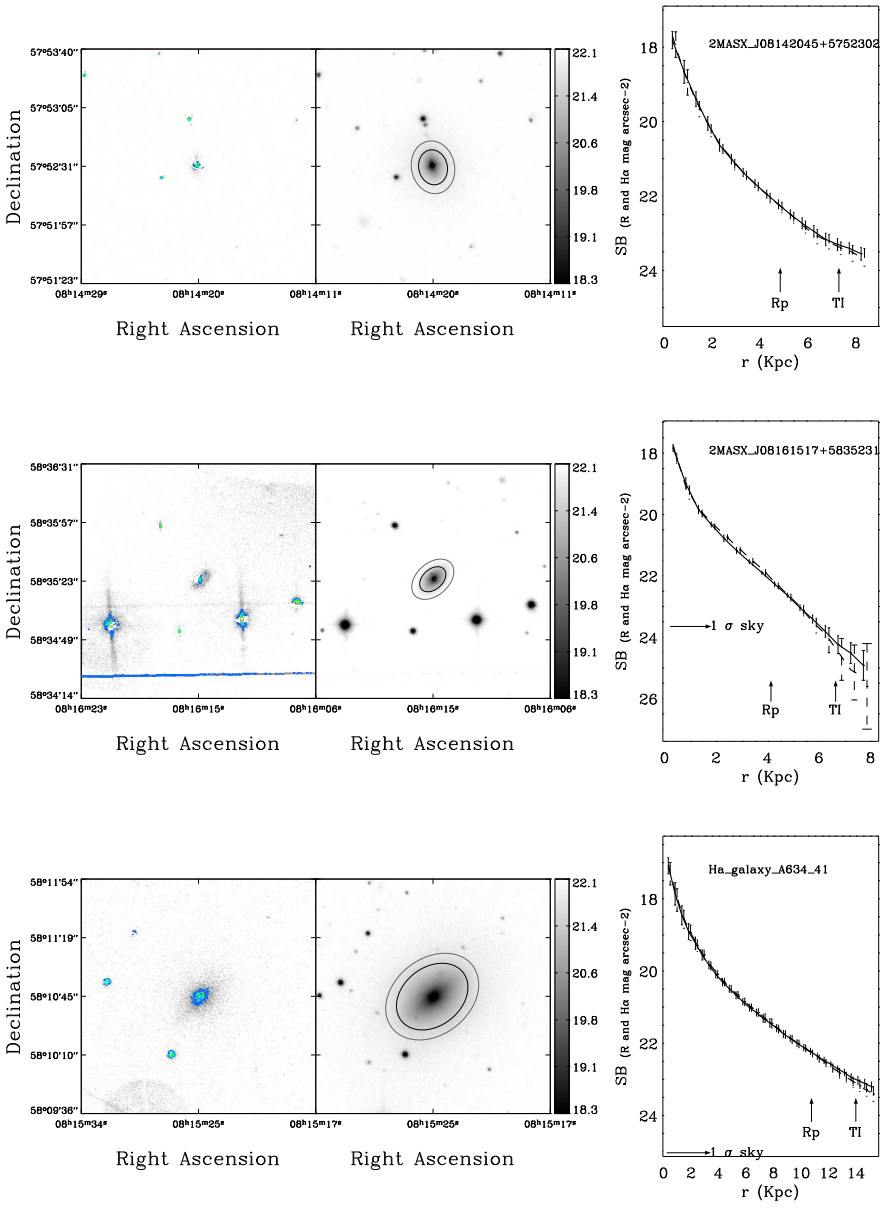
Declination
Right Ascension
Right Ascension
2MASX_J08142045+5752302
2MASX_J08161517+5835231
Ha_galaxy_A634_41
SB (R and Hα mag arcsec−2)
r (Kpc)
Rp
TI
1 σ sky

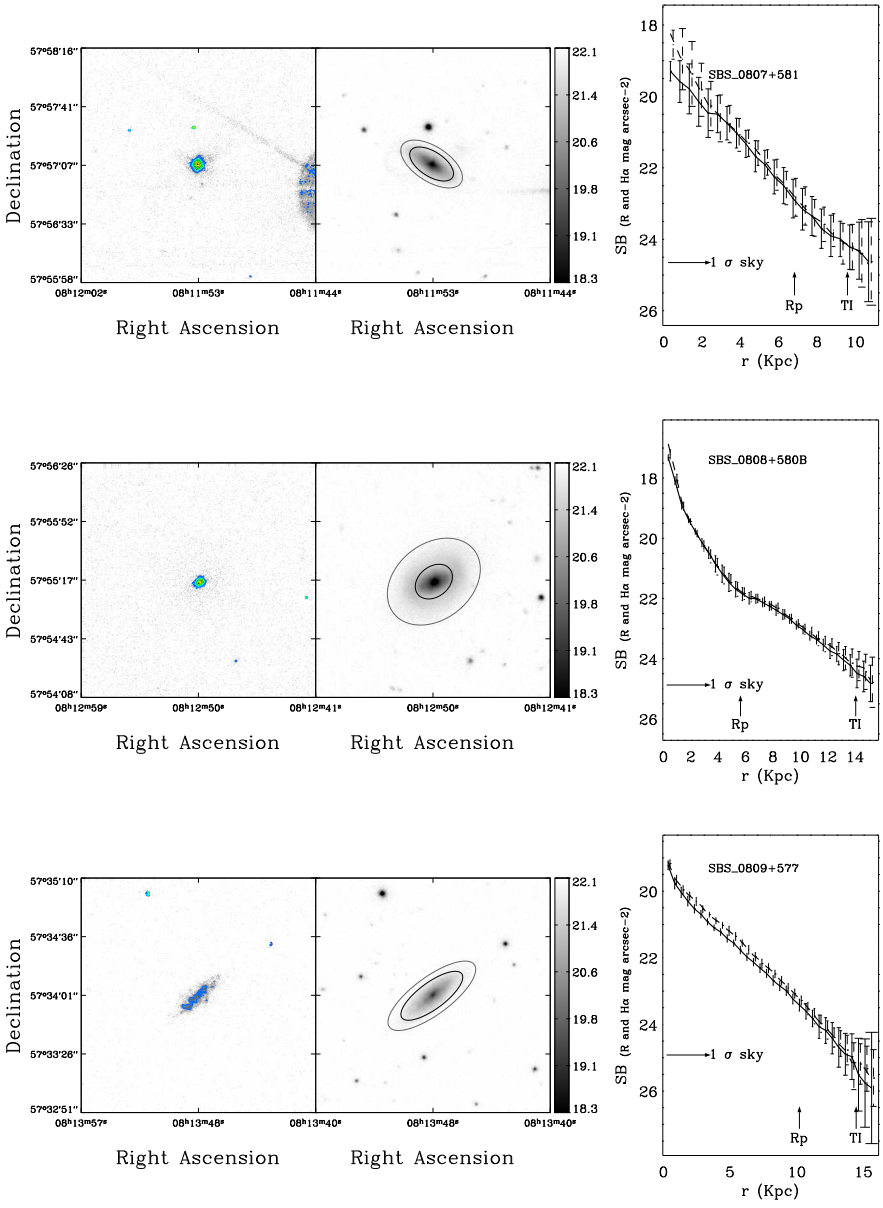
Declination
Right Ascension
Right Ascension
SBS_0807+581
SBS_0808+580B
SBS_0809+577
SB (R and Hα mag arcsec−2)
1 σ sky
Rp
TI
r (Kpc)

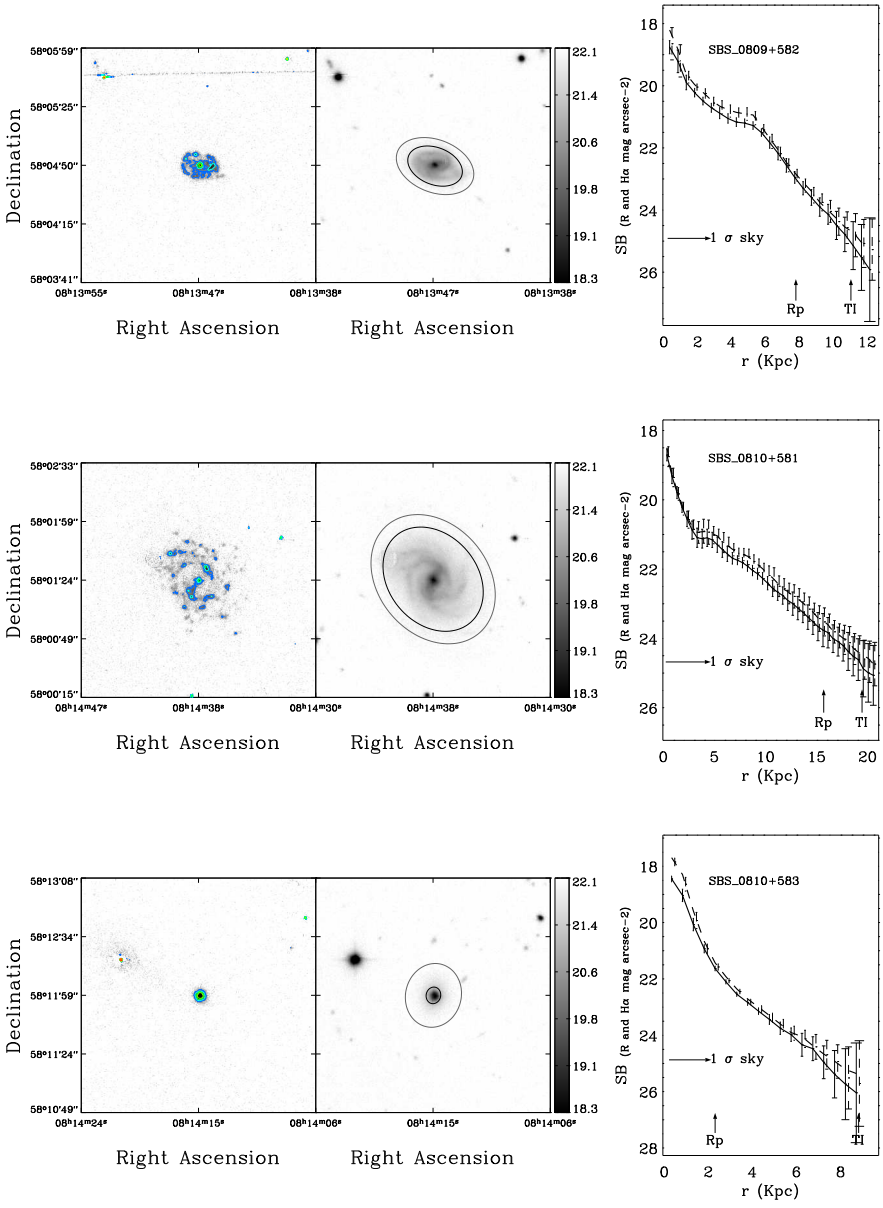
Declination
Right Ascension
Right Ascension
SB (R and Hα mag arcsec−2)
r (Kpc)
SBS_0809+582
SBS_0810+581
SBS_0810+583
1 σ sky
Rp
Tl

C.4 Abell 779

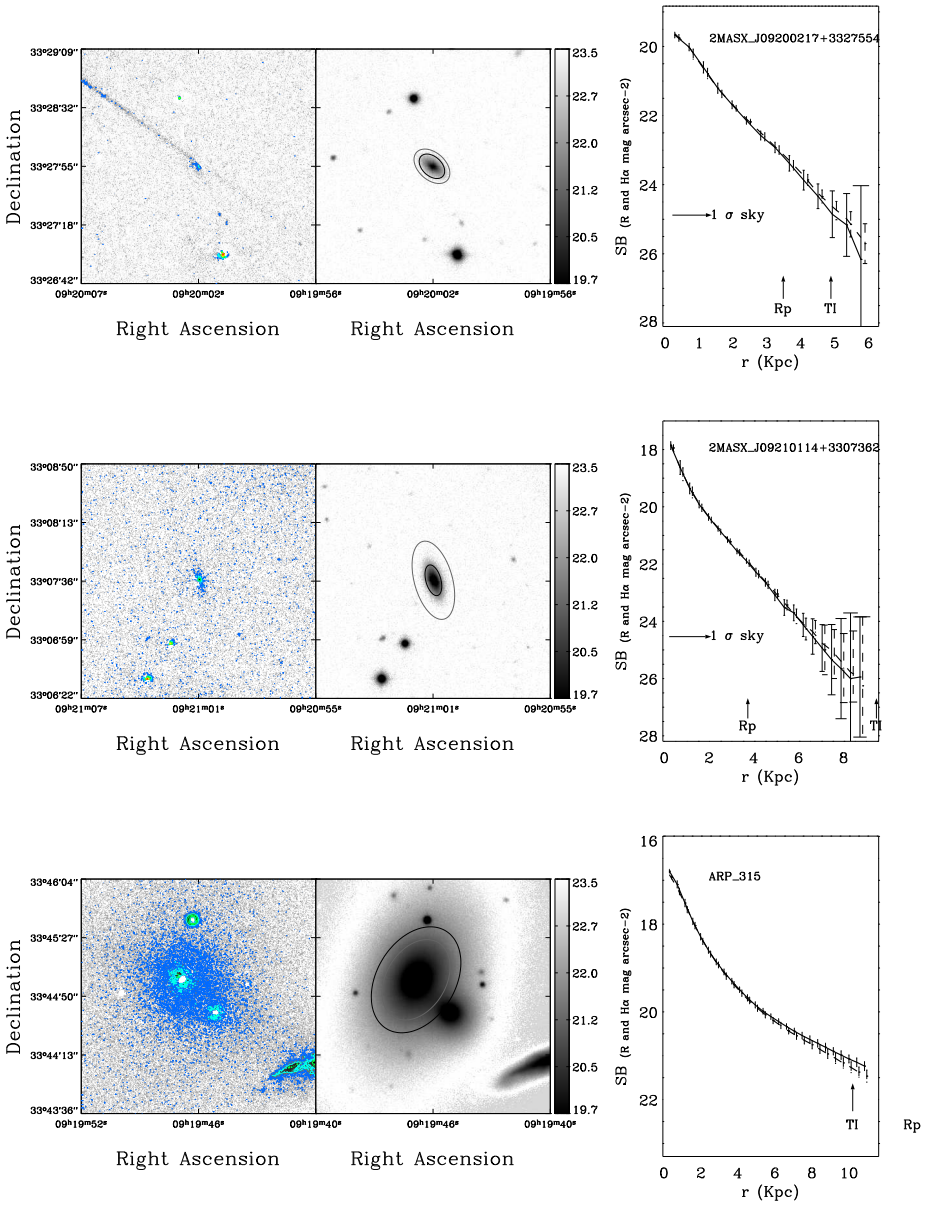
Declination
Right Ascension
Right Ascension
2MASX_J09200217+3327554
2MASX_J09210114+3307362
ARP_315
SB (R and Hα mag arcsec−2)
r (Kpc)
1 σ sky
Rp
Tl

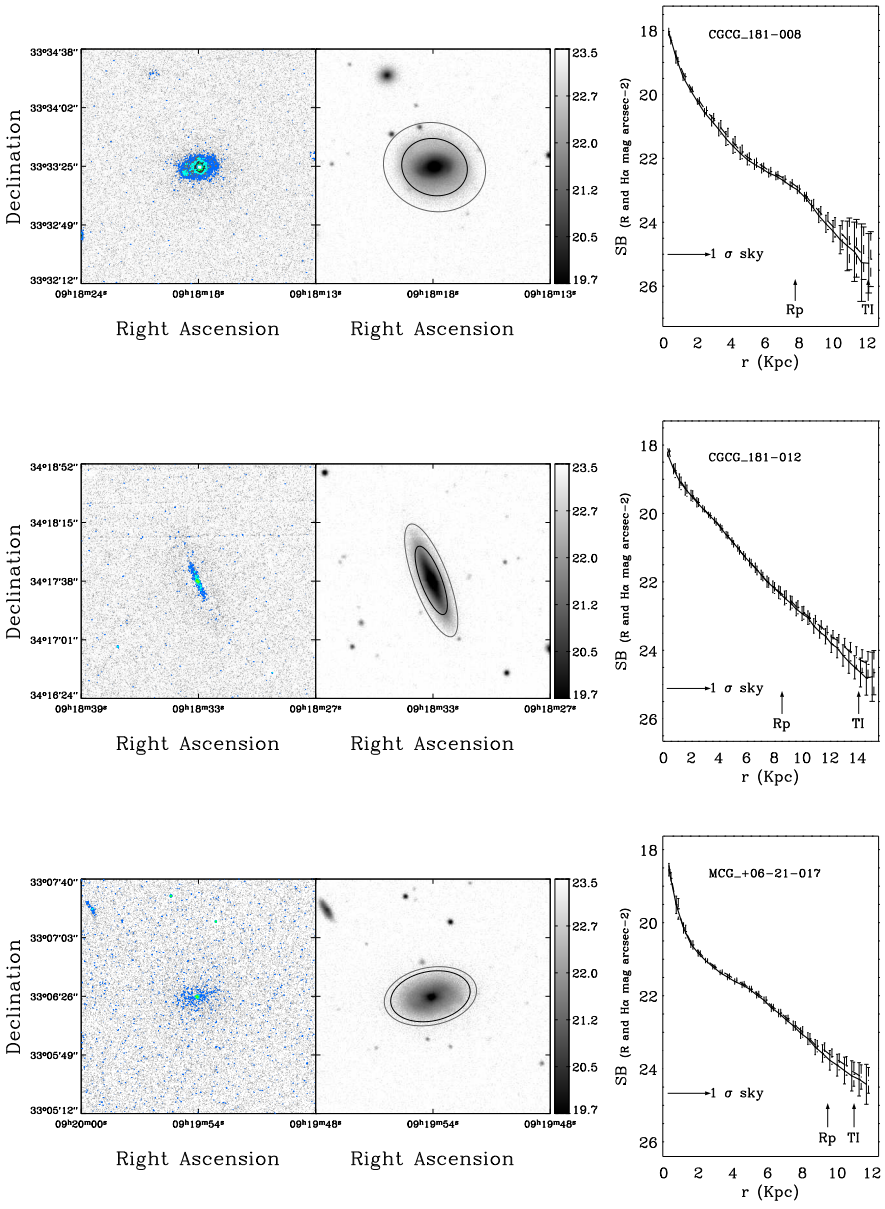
Declination
Right Ascension
Right Ascension
SB (R and Hα mag arcsec−2)
r (Kpc)
CGCG_181−008
CGCG_181−012
MCG_+06−21−017
1 σ sky
Rp
Tl

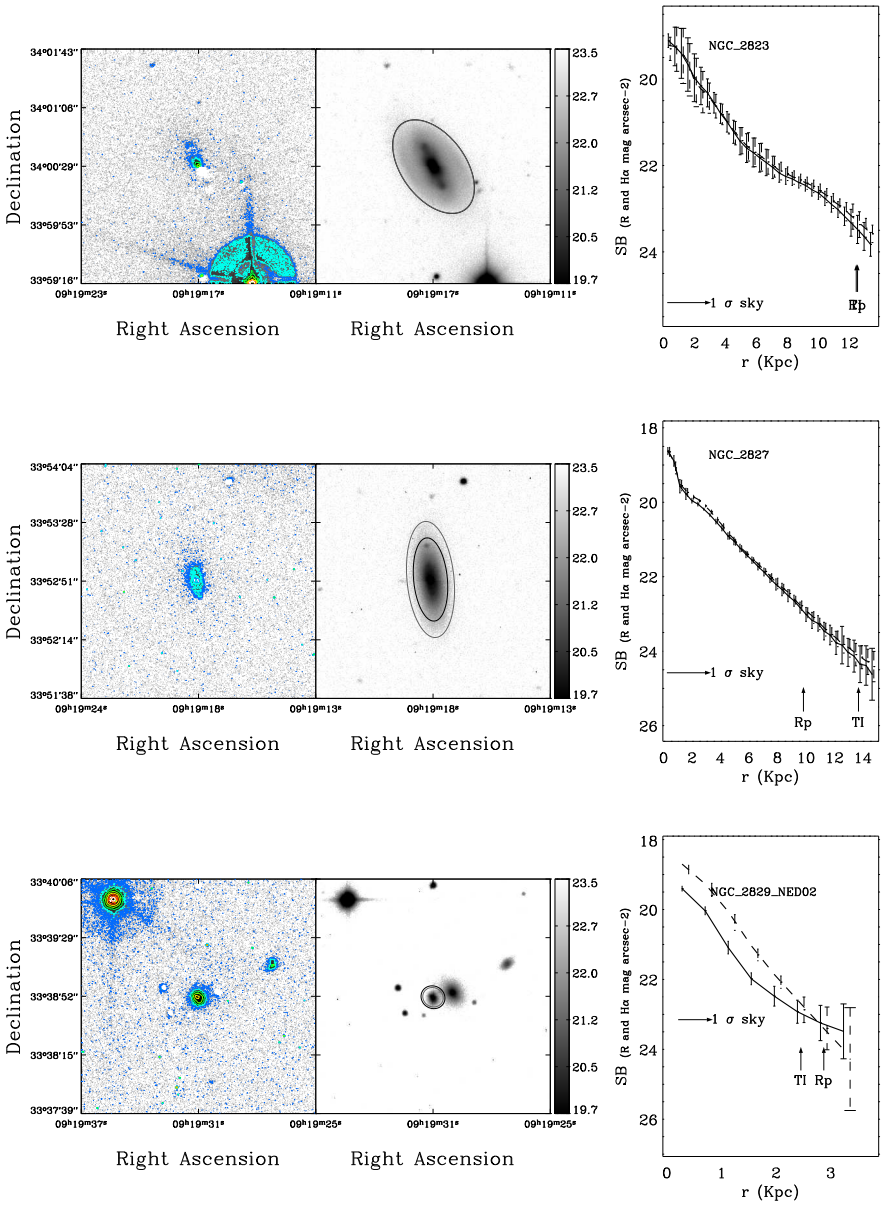
Declination
Right Ascension
Right Ascension
NGC_2823
NGC_2827
NGC_2829_NED02
SB (R and Hα mag arcsec−2)
r (Kpc)
1 σ sky
Rp
TI

C.5 Abell 2666

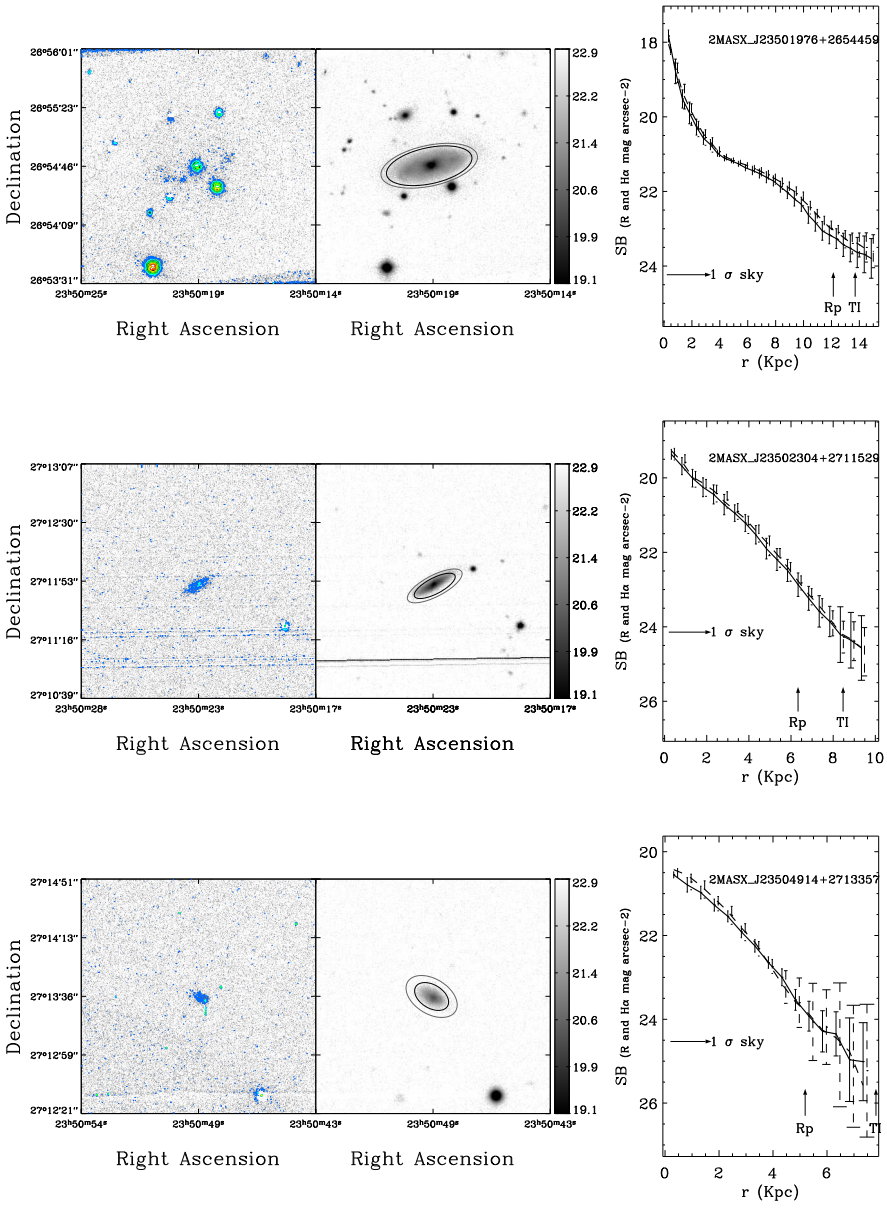
Declination
Right Ascension
Right Ascension
2MASX_J23501976+2654459
2MASX_J23502304+2711529
2MASX_J23504914+2713357
SB (R and Hα mag arcsec−2)
r (Kpc)
1 σ sky
Rp
TI

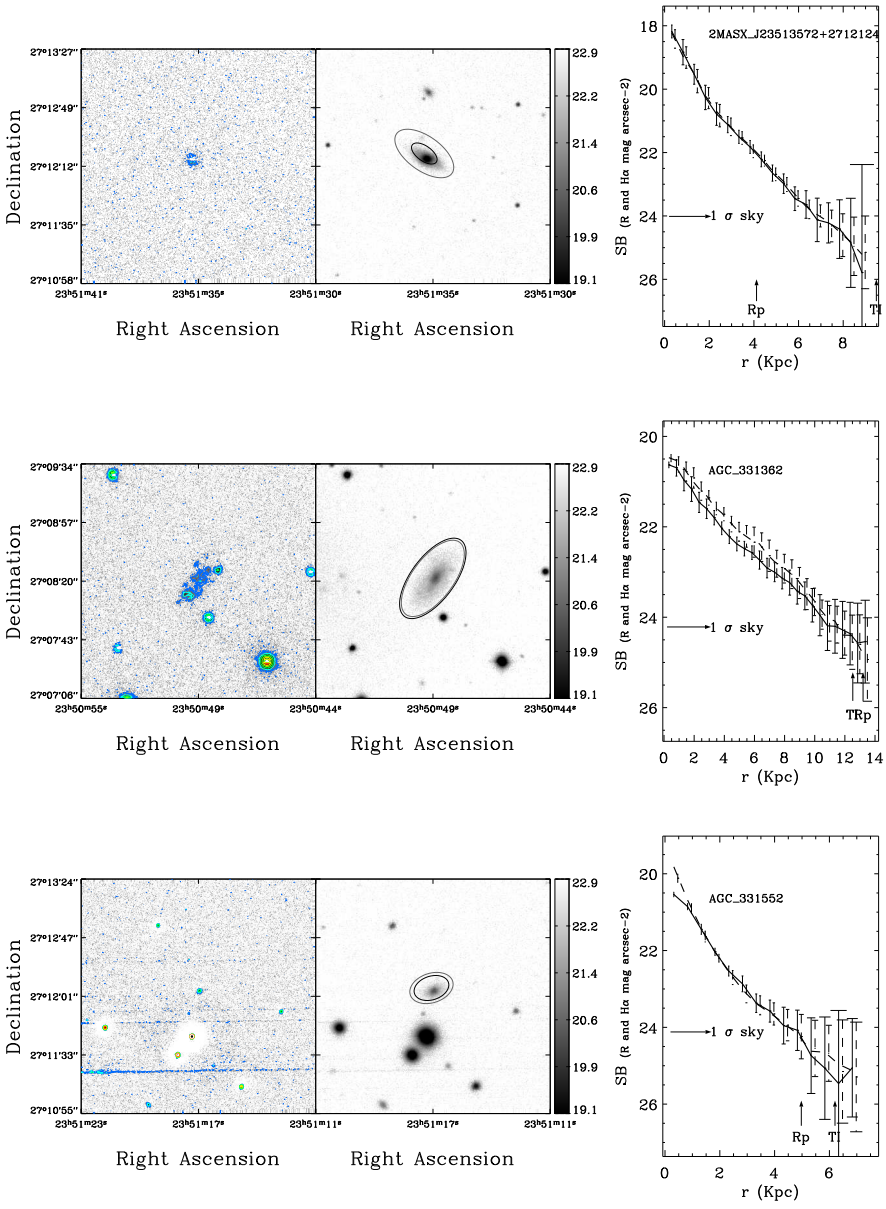
Declination
Right Ascension
Right Ascension
2MASX_J23513572+2712124
SB (R and Hα mag arcsec−2)
1 σ sky
Rp
Tl
r (Kpc)
AGC_331362
TRp
AGC_331552

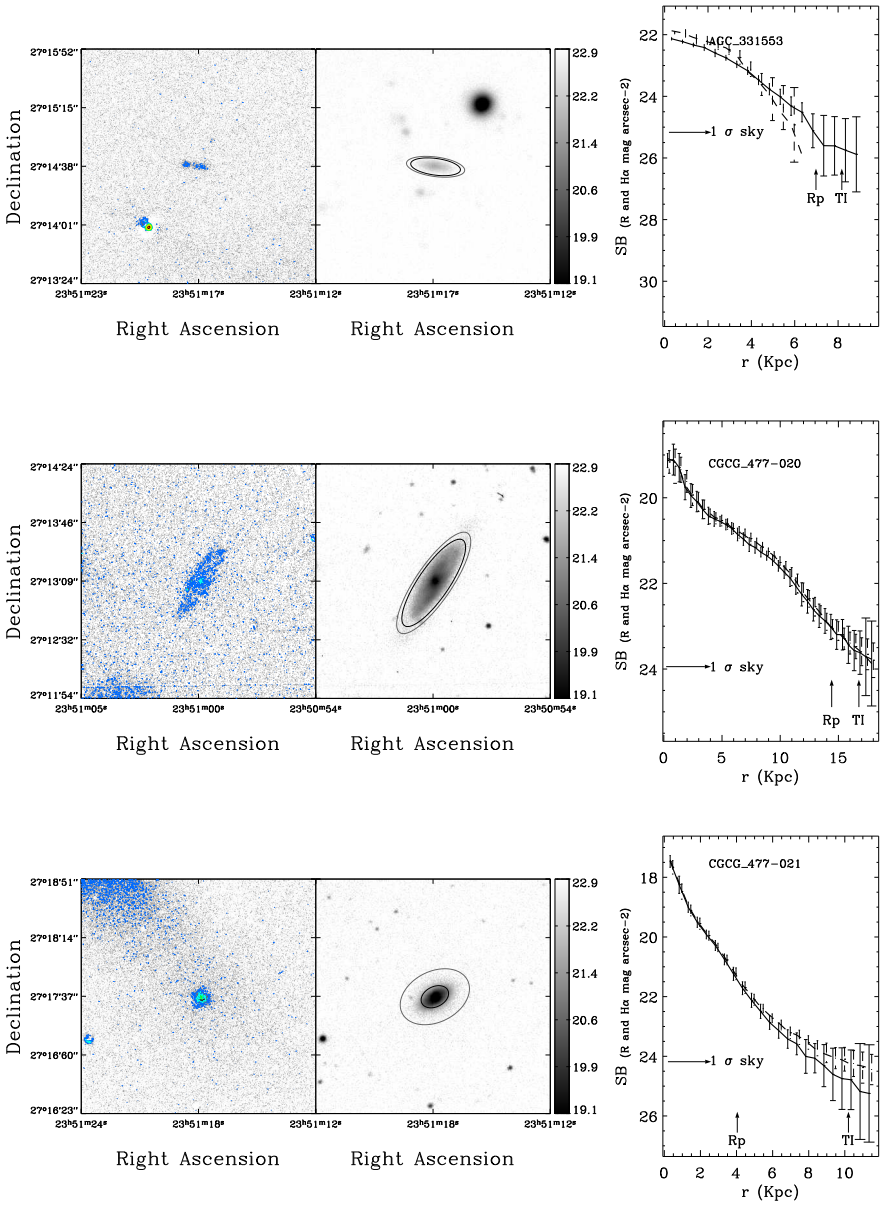
Declination
Right Ascension
Right Ascension
22.9
22.2
21.4
20.6
19.9
19.1
AGC_331553
CGCG_477-020
CGCG_477-021
1 σ sky
Rp
TI
SB (R and Hα mag arcsec−2)
r (Kpc)

BIBLIOGRAPHY

Abraham, R. G., van den Bergh, S., Glazebrook, K., et al. 1996, ApJS, 107, 1

Andreon, S. & Cuillandre, J.-C. 2002, ApJ, 569, 144

Balogh, M., Eke, V., Miller, C., et al. 2004, MNRAS, 348, 1355

Balogh, M. L., Morris, S. L., Yee, H. K. C., Carlberg, R. G., & Ellingson, E. 1997, ApJ, 488, L75+

Balogh, M. L., Schade, D., Morris, S. L., et al. 1998, ApJ, 504, L75+

Bekki, K. & Couch, W. J. 2003, ApJ, 596, L13

Benítez, N., Ford, H., Bouwens, R., et al. 2004, ApJS, 150, 1

Bernstein, R. A., Freedman, W. L., & Madore, B. F. 2002, ApJ, 571, 56

Bershady, M. A., Jangren, A., & Conselice, C. J. 2000, AJ, 119, 2645

Bershady, M. A., Lowenthal, J. D., & Koo, D. C. 1998, ApJ, 505, 50

Bertin, E. & Arnouts, S. 1996, A&AS, 117, 393

Boselli, A. & Gavazzi, G. 2002, A&A, 386, 124

Boselli, A. & Gavazzi, G. 2006, PASP, 118, 517

Bruzual, G. & Charlot, S. 2003, MNRAS, 344, 1000

Butcher, H. & Oemler, Jr., A. 1978, ApJ, 226, 559

Butcher, H. & Oemler, Jr., A. 1984, ApJ, 285, 426

Cardelli, J. A., Clayton, G. C., & Mathis, J. S. 1989, ApJ, 345, 245

Conselice, C. J. 1997, PASP, 109, 1251

Conselice, C. J. 2003, ApJS, 147, 1

Conselice, C. J., Bershady, M. A., & Jangren, A. 2000, ApJ, 529, 886

Corbin, M. R., Vacca, W. D., Cid Fernandes, R., et al. 2006, ApJ, 651, 861

Cortese, L., Boselli, A., Buat, V., et al. 2006, ApJ, 637, 242

Cortese, L., Gavazzi, G., Boselli, A., & Iglesias-Paramo, J. 2004, A&A, 416, 119

Cortese, L., Gavazzi, G., Iglesias-Paramo, J., Boselli, A., & Carrasco, L. 2003, A&A, 401, 471

Couch, W. J., Balogh, M. L., Bower, R. G., et al. 2001, ApJ, 549, 820

Couch, W. J. & Sharples, R. M. 1987, MNRAS, 229, 423

Cristóbal-Hornillos, D., Balcells, M., Prieto, M., et al. 2003, ApJ, 595, 71

Delgado, R. M. G., Cerviño, M., Martins, L. P., Leitherer, C., & Hauschildt, P. H. 2005, MNRAS, 357, 945

Dressler, A. 1980, ApJS, 42, 565

Dressler, A. & Gunn, J. E. 1982, ApJ, 263, 533

Dressler, A. & Gunn, J. E. 1983, ApJ, 270, 7

Dressler, A. & Gunn, J. E. 1992, ApJS, 78, 1

Dressler, A., Oemler, A. J., Couch, W. J., et al. 1997, ApJ, 490, 577

Dressler, A., Oemler, A. J., Poggianti, B. M., et al. 2004, ApJ, 617, 867

Dressler, A., Smail, I., Poggianti, B. M., et al. 1999, ApJS, 122, 51

Drinkwater, M. J., Gregg, M. D., Couch, W. J., et al. 2004, Publications of the Astronomical Society of Australia, 21, 375

Drinkwater, M. J., Gregg, M. D., Holman, B. A., & Brown, M. J. I. 2001, MNRAS, 326, 1076

Driver, S. P., Liske, J., Cross, N. J. G., De Propris, R., & Allen, P. D. 2005, MNRAS, 360, 81

Duc, P.-A., Brinks, E., Springel, V., et al. 2000, AJ, 120, 1238

Duc, P.-A., Cayatte, V., Balkowski, C., et al. 2001, A&A, 369, 763

Duc, P.-A., Papaderos, P., Balkowski, C., et al. 1999, A&AS, 136, 539

Elmegreen, B. G., Kaufman, M., & Thomasson, M. 1993, ApJ, 412, 90

Finlator, K., Ivezić, Ž., Fan, X., et al. 2000, AJ, 120, 2615

Finn, R. A., Zaritsky, D., & McCarthy, Jr., D. W. 2004, ApJ, 604, 141

Finn, R. A., Zaritsky, D., McCarthy, Jr., D. W., et al. 2005, ApJ, 630, 206

Frei, Z., Guhathakurta, P., Gunn, J. E., & Tyson, J. A. 1996, AJ, 111, 174

Fukugita, M., Ichikawa, T., Gunn, J. E., et al. 1996, AJ, 111, 1748

Fukugita, M., Shimasaku, K., & Ichikawa, T. 1995, PASP, 107, 945

Gal, R. R., de Carvalho, R. R., Lopes, P. A. A., et al. 2003, AJ, 125, 2064

Gallego, J., Zamorano, J., Rego, M., & Vitores, A. G. 1997, ApJ, 475, 502

Gavazzi, G., Boselli, A., Donati, A., Franzetti, P., & Scodeggio, M. 2003a, A&A, 400, 451

Gavazzi, G., Boselli, A., Mayer, L., et al. 2001a, ApJ, 563, L23

Gavazzi, G., Boselli, A., Pedotti, P., Gallazzi, A., & Carrasco, L. 2002, A&A, 396, 449

Gavazzi, G., Catinella, B., Carrasco, L., Boselli, A., & Contursi, A. 1998, AJ, 115, 1745

Gavazzi, G., Cortese, L., Boselli, A., et al. 2003b, ApJ, 597, 210

Gavazzi, G., Marcelin, M., Boselli, A., et al. 2001b, A&A, 377, 745

Gerhard, O., Arnaboldi, M., Freeman, K. C., & Okamura, S. 2002, ApJ, 580, L121

Girardi, L., Groenewegen, M. A. T., Hatziminaoglou, E., & da Costa, L. 2005, A&A, 436, 895

Haines, C. P., Gargiulo, A., La Barbera, F., et al. 2007, MNRAS, 381, 7

Haines, C. P., La Barbera, F., Mercurio, A., Merluzzi, P., & Busarello, G. 2006, ApJ, 647, L21

Helmboldt, J. F., Walterbos, R. A. M., Bothun, G. D., O'Neil, K., & de Blok, W. J. G. 2004, ApJ, 613, 914

Hippelein, H., Maier, C., Meisenheimer, K., et al. 2003, A&A, 402, 65

Homeier, N. L., Demarco, R., Rosati, P., et al. 2005, ApJ, 621, 651

Hopkins, A. M. 2004, ApJ, 615, 209

Hopkins, A. M., Irwin, M. J., & Connolly, A. J. 2001, ApJ, 558, L31

Hummer, D. G. & Storey, P. J. 1987, MNRAS, 224, 801

Hunter, D. A. & Elmegreen, B. G. 2004, AJ, 128, 2170

Iglesias-Páramo, J., Boselli, A., Cortese, L., Vílchez, J. M., & Gavazzi, G. 2002, A&A, 384, 383

Iglesias-Páramo, J., Boselli, A., Gavazzi, G., Cortese, L., & Vílchez, J. M. 2003a, A&A, 397, 421

Iglesias-Páramo, J., van Driel, W., Duc, P.-A., et al. 2003b, A&A, 406, 453

Iglesias-Páramo, J. & Vílchez, J. M. 2001, ApJ, 550, 204

James, P. A., Shane, N. S., Beckman, J. E., et al. 2004, A&A, 414, 23

Jansen, R. A., Fabricant, D., Franx, M., & Caldwell, N. 2000, ApJS, 126, 331

Jones, J. B., Drinkwater, M. J., Jurek, R., et al. 2006, AJ, 131, 312

Kennicutt, Jr., R. C. 1992, ApJ, 388, 310

Kennicutt, Jr., R. C. 1998, ARA&A, 36, 189

Kennicutt, Jr., R. C., Bothun, G. D., & Schommer, R. A. 1984, AJ, 89, 1279

Kennicutt, Jr., R. C., Edgar, B. K., & Hodge, P. W. 1989, ApJ, 337, 761

Kennicutt, Jr., R. C. & Kent, S. M. 1983, AJ, 88, 1094

Kent, S. M. 1979, PhD thesis, AA(California Inst. of Tech., Pasadena.)

Kewley, L. J., Dopita, M. A., Sutherland, R. S., Heisler, C. A., & Trevena, J. 2001, ApJ, 556, 121

Kewley, L. J., Jansen, R. A., & Geller, M. J. 2005, PASP, 117, 227

Kodama, T., Balogh, M. L., Smail, I., Bower, R. G., & Nakata, F. 2004, MNRAS, 354, 1103

Kodama, T. & Bower, R. G. 2001, Astrophysics and Space Science Supplement, 277, 597

Koopmann, R. A. 1997, PhD thesis, AA(YALE UNIVERSITY)

Koopmann, R. A. & Kenney, J. D. P. 2004a, ApJ, 613, 866

Koopmann, R. A. & Kenney, J. D. P. 2004b, ApJ, 613, 851

Kunth, D. & Östlin, G. 2000, A&A Rev., 10, 1

Lauger, S., Burgarella, D., & Buat, V. 2005, A&A, 434, 77

Leitherer, C., Schaerer, D., Goldader, J. D., et al. 1999, ApJS, 123, 3

Lewis, I., Balogh, M., De Propris, R., et al. 2002, MNRAS, 334, 673

Lilly, S. J., Le Fevre, O., Hammer, F., & Crampton, D. 1996, ApJ, 460, L1+

Liske, J., Driver, S. P., Allen, P. D., Cross, N. J. G., & De Propris, R. 2006, MNRAS, 369, 1547

Madau, P., Pozzetti, L., & Dickinson, M. 1998, ApJ, 498, 106

Margoniner, V. E. & de Carvalho, R. R. 2000, AJ, 119, 1562

Margoniner, V. E., de Carvalho, R. R., Gal, R. R., & Djorgovski, S. G. 2001, ApJ, 548, L143

Martinez, M. A., Del Olmo, A., Focardi, P., & Perea, J. 2007, in IAU Symposium, Vol. 235, IAU Symposium, ed. F. Combes & J. Palous, 222–222

Martini, P., Kelson, D. D., Kim, E., Mulchaey, J. S., & Athey, A. A. 2006, ApJ, 644, 116

McCall, M. L., Rybski, P. M., & Shields, G. A. 1985, ApJS, 57, 1

McGaugh, S. 2000, BAAS, 32, 1496

Mendes de Oliveira, C., Cypriano, E. S., Sodré, Jr., L., & Balkowski, C. 2004, ApJ, 605, L17

Mieske, S., Hilker, M., Infante, L., & Jordán, A. 2006, AJ, 131, 2442

Mirabel, I. F., Dottori, H., & Lutz, D. 1992, A&A, 256, L19

Moran, S. M., Ellis, R. S., Treu, T., et al. 2005, ApJ, 634, 977

Mori, M. & Burkert, A. 2000, ApJ, 538, 559

Moss, C., Irwin, M. J., & Whittle, M. 1988, MNRAS, 232, 381

Moss, C. & Whittle, M. 1993, ApJ, 407, L17

Moss, C. & Whittle, M. 2000, MNRAS, 317, 667

Moustakas, J. & Kennicutt, Jr., R. C. 2006, ApJS, 164, 81

Nakata, F., Bower, R. G., Balogh, M. L., & Wilman, D. J. 2005, MNRAS, 357, 679

Noeske, K. G., Papaderos, P., Cairós, L. M., & Fricke, K. J. 2003, A&A, 410, 481

Osterbrock, D. E. 1974, Astrophysics of gaseous nebulae (Research supported by the Research Corp., Wisconsin Alumni Research Foundation, John Simon Guggenheim Memorial Foundation, Institute for Advanced Studies, and National Science Foundation. San Francisco, W. H. Freeman and Co., 1974. 263 p.)

Pascual, S., Gallego, J., & Zamorano, J. 2007, PASP, 119, 30

Pierini, D. & Tuffs, R. J. 1999, A&A, 343, 751

Pilyugin, L. S., Vílchez, J. M., & Contini, T. 2004, A&A, 425, 849

Poggianti, B. M., Smail, I., Dressler, A., et al. 1999, ApJ, 518, 576

Popesso, P. & Biviano, A. 2006, A&A, 460, L23

Rines, K., Geller, M. J., Kurtz, M. J., & Diaferio, A. 2003, AJ, 126, 2152

Rines, K., Geller, M. J., Kurtz, M. J., & Diaferio, A. 2005, AJ, 130, 1482

Sakai, S., Kennicutt, Jr., R. C., van der Hulst, J. M., & Moss, C. 2002, ApJ, 578, 842

Salpeter, E. E. 1955, ApJ, 121, 161

Schlegel, D. J., Finkbeiner, D. P., & Davis, M. 1998, ApJ, 500, 525

Schombert, J. M. 2006, AJ, 131, 296

Smail, I., Edge, A. C., Ellis, R. S., & Blandford, R. D. 1998, MNRAS, 293, 124

Struble, M. F. & Rood, H. J. 1999, ApJS, 125, 35

Swaters, R. A. 1999, PhD thesis, , Rijksuniversiteit Groningen, (1999)

Tanaka, M., Goto, T., Okamura, S., Shimasaku, K., & Brinkmann, J. 2004, AJ, 128, 2677

Terlevich, R., Melnick, J., Masegosa, J., Moles, M., & Copetti, M. V. F. 1991, A&AS, 91, 285

Umeda, K., Yagi, M., Yamada, S. F., et al. 2004, ApJ, 601, 805

Väisänen, P., Mattila, S., Kniazev, A., et al. 2008, MNRAS, 384, 886

Vilchez, J. M. 1995, AJ, 110, 1090

Vilchez, J. M. 1997, in Revista Mexicana de Astronomia y Astrofisica, vol. 27, Vol. 6, Revista Mexicana de Astronomia y Astrofisica Conference Series, ed. J. Franco, R. Terlevich, & A. Serrano, 30–+

White, D. A., Jones, C., & Forman, W. 1997, MNRAS, 292, 419

Wilman, D. J., Balogh, M. L., Bower, R. G., et al. 2005, MNRAS, 358, 88

Yagi, M., Nakamura, Y., Doi, M., Shimasaku, K., & Okamura, S. 2006, MNRAS, 368, 211

Ziegler, B. L., Böhm, A., Fricke, K. J., et al. 2002, ApJ, 564, L69